UNIVERSITY COLLEGE LONDON

DOCTORAL THESIS

Strong-Field Interference of Quantum Trajectories with Coulomb Distortion and Electron Correlation

Author:
Andrew S MAXWELL

Supervisor:
Prof. Carla Figueira de Morisson FARIA

A thesis submitted in fulfilment of the requirements
for the degree of Doctor of Philosophy

in the

AMOPP group
Physics and Astronomy

December 10, 2018

Declaration of Authorship

I, Andrew S MAXWELL, confirm that the work presented in this thesis, titled "Strong-Field Interference of Quantum Trajectories with Coulomb Distortion and Electron Correlation", is my own. Where information has been derived from other sources, I confirm that this has been indicated in the thesis.

The following parts of this thesis have been published in journals:

1. **Chapter 5**: A. S. Maxwell, A. Al-Jawahiry, T. Das, and C. Figueira de Morisson Faria, "Coulomb-corrected quantum interference in above-threshold ionization: Working towards multi-trajectory electron holography", Phys. Rev. A **96**, 023420 (2017)

2. **Chapter 6**: A. S. Maxwell, A. Al-Jawahiry, X. Y. Lai, and C. Figueira de Morisson Faria, "Analytic quantum-interference conditions in Coulomb corrected photoelectron holography", J. Phys. B At. Mol. Opt. Phys. **51**, 044004 (2018)

3. **Chapter 7**: A. S. Maxwell and C. Figueira de Morisson Faria, "Coulomb-free and Coulomb-distorted recolliding quantum orbits in photoelectron holography", J. Phys. B At. Mol. Phys. **51**, 124001 (2018)

4. **Chapter 10**: A. S. Maxwell and C. Figueira de Morisson Faria, "Quantum interference in time-delayed nonsequential double ionization", Phys. Rev. A **92**, 023421 (2015)

5. **Chapter 11**: A. S. Maxwell and C. Figueira de Morisson Faria, "Controlling Below-Threshold Nonsequential Double Ionization via Quantum Interference", Phys. Rev. Lett. **116**, 143001 (2016)

Signed:

_____

Date: December 10, 2018

_____

"*Mathematics began to seem too much like puzzle solving. Physics is puzzle solving, too, but of puzzles created by nature, not by the mind of man.*"

Maria Goeppert-Mayer, 1906-1972

"*My methods are really methods of working and thinking; this is why they have crept in everywhere anonymously.*"

Emmy Noether, 1882-1935

"*There is a theory which states that if ever anyone discovers exactly what the Universe is for and why it is here, it will instantly disappear and be replaced by something even more bizarre and inexplicable. There is another theory which states that this has already happened.*"

Douglas Adams, 1952-2001

Abstract

This thesis explores quantum interference patterns present in the strong-field phenomena of above-threshold ionisation and non-sequential double ionisation, which correspond to one and two ionisation processes, respectively. For above-threshold ionisation a new model is explored that uses Coulomb-distorted quantum trajectories to produce the transition amplitude of the process. This method is one of only a few semi-analytic models to account for the Coulomb potential for electrons in the continuum. The quantum trajectories utilised in this model lead to a myriad of interference patterns, some of which have never been identified before and the signature of most can be found in experimental results or *ab-initio* solutions of the time dependent Schrödinger equation. Given the recent interest in using such interferences for holographic imaging of atoms and molecules, conditions and an analytic model are formulated to better understand the potential of this new imaging process. The role of recollision is also investigated and how trajectories in this new model relate to well known direct and rescattered trajectories from above-threshold ionisation models employing the strong field approximation. Subsequently, interference is examined for the case of non-sequential double ionisation for the recollision with subsequent ionisation mechanism using the strong field approximation. Many types of interference patterns are found, where previously it was expected that interference would not play a role. These patterns are investigated in detail and conditions formulated for them. The model is extended to different lengths of laser pulses by incorporating a particular superposition of intermediate excited states in the process in order to replicated experimental data, opening up the possibility of using experimental data to reconstruct the intermediate excited state of the second electron in the non-sequential double ionisation process.

Impact Statement

The strong field processes studied in this thesis involve manipulation of electrons over a few-hundred attoseconds (10^{-18} s), which are some of the fastest accessible timescales in nature. Better understanding and control of this will not just benefit the strong field community but physics and society in general.

This work has already impacted the strong field community by providing significant contributions and adding to a framework for understanding interference and predicting new patterns in one and two electron systems. Over the next few years these approaches could be applied to many-body systems, finding use in multielectron dynamics and ionisation of molecular targets. This will allow ultrafast imaging or sensing of molecules, which would have commercial interest to companies wishing to image fast dynamics of small molecules. The methodology could benefit physics as a whole as it provides faster solutions, which scale better with the number of degrees of freedom than solving the full time-dependent Schrödinger equation. Additionally, these methods are nonperturbative, with regards to the external field, so ideas could be exchanged with other areas of physics that deal with nonperturbative dynamics such as nonlinear quantum electrodynamics or chromodynamics and condensed matter problems.

Above-threshold ionisation and non-sequential double ionisation are both interesting processes that can be used to explore fundamental physics. In this thesis tunnelling and interference both play a role, allowing for in depth study of these processes and the interplay between them. Additionally, they are a case study for quantum-classical correspondence, as despite the aforementioned quantum effects they are often well described by semi-classical descriptions. Over the next few decades the application to ultrafast imaging could allow unprecedented access to molecular dynamics in chemical reactions. This could lead to advances over a wide range of industries. Additionally, the increasing control of electrons over short the timescales that strong-field processes allow could lead to new devices such as ultrafast electronics.

Acknowledgements

First, I would like to give my warmest thanks to my supervisor Prof Carla Faria, for guiding and supporting me through my PhD. Next, I would like to acknowledge Prof Sergey Popruzenhko, Prof Alessio Serafini, Prof Sougato Bose, Prof Stephen Hogan, Dr Sergey Yurchenko, Dr Xaunyang Lai, Dr Boris Bergues, Prof Maciej Lewenstein, Prof Jens Beigart and Dr Emilio Pisanty for fruitful collaborations and interesting discussions. I would also like to thank past and present co-workers from my group Dr Toni Das, Ahmed Al-Jawahiry, Heloise Chomet, Dr Carlos Zagoya and Abbie Bray. Additionally, I would like to thank the support and friendship of many fellow PhD students, Thomas Galley, Richard Juggins, Harry Banks, Jacob Lang, Thomas Meltzer, Carlo Sparaciari and many more who have made my time at UCL very enjoyable.

Some of my biggest thanks goes to my partner Katy Chubb and of course my Mum, Dad, Sister and Granny. Additionally, I can not underestimate the support of my closest friends and I am lucky to have so many that support me.

Contents

List of Figures

List of Tables

List of Abbreviations

SFA	**S**trong **F**ield **A**pproximation
CQSFA	**C**oulomb **Q**uantum-orbit **S**trong **F**ield **A**pproximation
TDSE	**T**ime-**D**ependent **S**chrödinger **E**quation
ATI	**A**bove-**T**hreshold **I**onisation
DATI	**D**irect **A**bove-**T**hreshold **I**onisation
HATI	**H**igh-order **A**bove-**T**hreshold **I**onisation
HHG	**H**igh-**H**armonic **G**eneration
NSDI	**N**on-**S**equential **D**ouble **I**onisation
NSMI	**N**on-**S**equential **M**ultiple **I**onisation
SDI	**S**equential **D**ouble **I**onisation
COLTRIMS	**COL**d-**T**arget **R**ecoil **I**on **M**omentum **S**pectroscopy
EI	**E**lectron-**I**mpact (in the context of NSDI)
RESI	**R**ecollision **E**xcitation with **S**ubsequent **I**onisation
SPA	**S**addle **P**oint **A**pproximation
PAD	**P**hotoelectron **A**ngular **D**istribution
LES	**L**ow-**E**nergy **S**tructure
VLES	**V**ery **L**ow-**E**nergy **S**tructure
NZES	**N**ear **Z**ero **E**nergy **S**tructure
QTMC	**Q**uantum-**T**rajectory **M**onte **C**arlo (model)
TCSFA	**T**rajectory-based **C**oulomb-corrected **S**trong-**F**ield **A**pproximation
CCSFA	**C**oulomb-**C**orrected **S**trong-**F**ield **A**pproximation
EVA	**E**ikonal-**V**olkov **A**pproximation
ARM	**A**nalytical **R**-**M**atrix (method)
CVA	**C**oulomb-**V**olkov **A**pproximation
QRS	**Q**uantitative **R**e**S**cattering (theory)

STSM **S**emiclassical **T**wo-**S**tep **M**odel

ADK **A**mmosov-**D**elone-**K**rainov (in the context of tunnelling)

Dedicated to Grambo

Chapter 1

Historical Overview

Light matter interaction has a long history in physics, starting before the modern era that brought quantum mechanics and relativity. Breakthroughs in the understanding of light matter interaction have gone hand in hand with revolutions in physics. For example Young's double slit experiment in 1801 and Maxwell's classical equations for electromagnetism in 1873 helped sediment the belief that light was a purely wave-like entity. However, following Planck's idea that black body radiation was emitted in energy quanta in 1901 and Einstein's application of this to the photoelectric effect [1, 2][1] in 1905, the modern quantum picture of light was adopted[2]. Note that this insight occurred through the study of light matter interaction and was a key part in developing quantum theory as a whole. A brief overview of this history is included in [3, 4].

Adopting the idea of a photon allowed for a powerful description of the interaction of light with matter and also immediately opened up the possibility of multiphoton effects, which was even suggested by Einstein in the photoelectric paper [1, 2]. Multiphoton effects will occur when the number of photons per unit area is sufficiently large, for example 10^{20} photons per cm^2 in the early experiment [5], this corresponded to an intensity of $I = 2 \times 10^5$ W/cm^2. Two-photon transitions, the simplest example of multiphoton effects, were first investigated in detail by Maria Goeppert-Mayer [6, 7][1] in 1931. Experimental confirmation of this process was not possible for sometime because of the high intensities required, but the invention of the laser in 1960 [8] allowed such intensities to be reached. Then, in 1961 two-photon excitation of CaF_2 crystals

[1] The second reference is an English translation of the first.

[2] It has since been shown the photoelectric effect can also be explained with classical light [3], so it pointed towards a photon picture of light but was not conclusive evidence for it. However, processes such as antibunching are conclusive evidence for the photon nature of light.

doped with Europium was observed [5] via fluorescence. Later additional multiphoton effects, such as the nonlinear ionisation of gases [9, 10] in 1963, were observed. Throughout this time perturbation theory was commonly used to describe light matter interaction. In perturbation theory the system is represented as a power series about a small perturbative parameter that describes the size of the interaction. This is used to calculate 'corrections' to the energy and eigenstates of the interacting system using the eigenstates of the unperturbed system as a basis. The perturbative series will have terms of increasing powers, which correspond to the 'order' of the interaction and the number of photons involved. This series will be truncated at an order appropriate to the system and more intense fields will require higher orders. A first-order truncation describes linear/ single photon transitions and anything above this is refers to nonlinear or multiphoton transitions.

For a very large number of photons the perturbation picture will break down. With large laser intensities the system will become distorted and the unperturbed eigenstates will no longer facilitate a good description of an electron transition/ or ionisation. This is called the nonperturbative/ strong-field regime. Before laser intensities had even reached a point where this would become important, a solution was proposed, a theory was suggested that used the solution of an electron in a plane electromagnetic wave, known as a Volkov state, as a final solution for the electron in the laser field [11–13]. This provided the first step to a new type of approach that ultimately yielded a new interpretation of ionisation. For strong low-frequency fields photons can be neglected as there is a high enough density such that the light will act like a classical field[3]. For particularly high fields intensities (around 10^{13} W/cm^2 for a wavelength of about 800 nm) the Coulomb potential of an atom will be distorted sufficiently by the incident laser field so that the bound electron will be able to escape via quantum tunnelling, see figure 1.1. This is known as tunnel ionisation. An approach which could account for this effect [14] was published in 1965 by Keldysh. This was long before laser intensities were sufficient to cause tunnel ionisation, which led to slow adoption of the theory initially and was compounded by the fact that the theory neglected the Coulomb potential for continuum electrons, which caused discrepancies with measured photoelectron angular

[3] This is dependant on what the light is interacting with, in this case we are considering valence electrons in atoms or molecules.

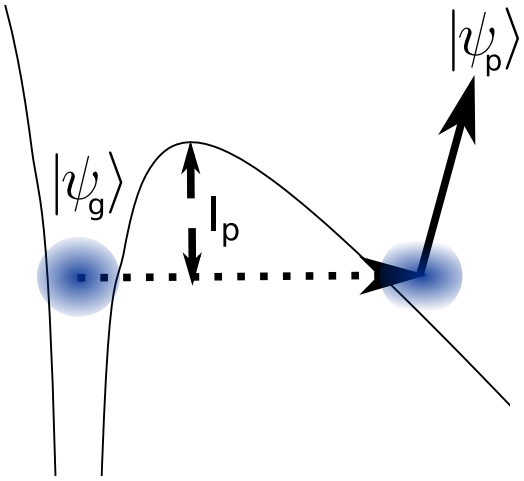

FIGURE 1.1: The combined effect of the Coulomb potential and laser field, leading to a distorted potential, through which the electron may escape via quantum ionisation. The ionisation potential of the system is denoted $\mathrm{I_p}$, the ground state by $|\psi_g\rangle$ and the final continuum state by $|\psi_p\rangle$, where p refers to the final momentum of the electron.

distributions. For example the experiments [15, 16] gave inconsistent results with the theory developed by Keldysh, although this should be expected as the results are not in the regime where tunnelling is the appropriate mechanism. In the late 1980s, however, laser intensities rose to a point where a tunnelling description became applicable and theories of this kind were widely adopted to explain phenomena in the strong-field regime, more details on the main successes are given in Chapter 3. The approaches developed around that time to model this effect following the methodology of Keldysh are often called KFR theories after Keldysh, Faisal and Reiss, who published seminal contributions [14, 17, 18] that have been widely used.

In order to understand when it is appropriate to describe ionisation in terms of tunnelling and thus whether KFR theory will apply, a few parameters will be introduce that can be used as a guide[4]. Firstly, in this work we will often consider an electron in a laser field. Thus, the concept of the ponderomotive energy of the electron will be used, this is defined as: "*the cycle-averaged quiver energy of a "free" electron in the laser field*" [4]. In other words, the ponderomotive energy, denoted $\mathrm{U_p}$, gives the energy of the oscillations of the electron due to the field, averaged over a cycle. This does not include kinetic energy due to the drift velocity of the electron. It is given by $\mathrm{U_p} = q_e^2 E_0/(4m_e\omega_0^2)$, where

[4]Such parameters are often deceptively simple and may not account for all necessary features. Thus it should be stressed they only provide a *guide* to the theories.

q_e is the charge of the electron, E_0 is the linearly polarised electric field amplitude of the laser, m_e is the mass of the electron and ω_0 is the angular frequency of the laser. In this work we will be considering 'low-frequency fields'. This means the photon energy is low in comparison to the ionisation potential of the bound state $\mathrm{I_p}$. The multiquantum parameter can be used to determine if this is the case, given by $K_0 = \mathrm{I_p}/(\hbar\omega_0)$. If $K_0 \gg 1$, this is the multiquantum regime [19], where many photons are required for ionisation, while for $K_0 \approx 1$ and $K_0 \ll 1$, these are the few-quantum and single-quantum regimes, respectively. However, K_0 does not determine if tunnel ionisation is a reasonable description, as it does not take into account the strength of the field. This can be determined by the Keldysh parameter, denoted γ, this uses the ionisation potential, frequency and field strength to give an idea of the applicability of tunnelling, it is given by $\gamma = \sqrt{2m_e\mathrm{I_p}}\omega/(eE_0)$. This can also be expressed in terms of just the ponderomotive energy and ionisation potential $\gamma = \sqrt{\mathrm{I_p}/(2\mathrm{U_p})}$. If $\gamma \ll 1$ this is considered the tunnelling domain, this is the strong-field regime that is considered throughout this work, while if $\gamma \gg 1$ this is called the multiphoton domain, in this regime a tunnelling picture/ KFR theory is not expected to give good results.

In this thesis a detailed analysis of interference effects is performed for two different processes in strong field physics, above-threshold ionisation (ATI) in Part I and non-sequential double ionisation (NSDI) in Part II. ATI and NSDI are one and two electron ionisation processes, respectively. In NSDI there is also strong electron correlation between the two electrons. They are both well described by a semi-classical nonperturbative description of light matter interaction and the general framework common to both is given in Chapter 2. In Part I a new model for describing ATI is explored, known as the Coulomb quantum-orbit strong field approximation (CQSFA), which accounts for the Coulomb potential for continuum electrons by including both a phase and considering Coulomb distortion of the trajectories. An introduction to ATI is given in Chapter 3 then the theory required to understand ATI in terms of the CQSFA is given in Chapter 4. The CQSFA produces a significant number of previously unexplored interference patterns (Chapters 5 and 7) most of which can be identified in experimental results. In Chapter 6 conditions and an analytic model are explored in order to investigate using

this interference for electron holography[5]. The topic of recollision is also covered in Chapter 7 in order to better understand how it fits in with this new CQSFA model and what the effects are on the interference patterns. In Part II the more complex two electron process of NSDI is investigated in the context of interference, however this time using the simpler 'work horse' of strong field physics, the strong field approximation (SFA). An introduction to NSDI is given in Chapter 8, followed by the theory required to understand NSDI in terms of the SFA in Chapter 9. Many of the interference patterns found, like in the previous part, have not been studied before, so in Chapter 10 a thorough analysis of such patterns is performed. In fact, this work is some of the first to consider the possibility of interference in NSDI as it was previously not expected to play a role. The model is also extended to consider few-cycle laser pulses (Chapter 11) and this is used to work backwards from experimental data to reconstruct an intermediate excited state of the second electron in the time-delayed NSDI process.

[5]Electron holography is a form of interferometric measurement using the ionised electron upon the parent ion.

Chapter 2

Underlying Framework and Theory

In this chapter we will define the general theoretical framework used throughout the thesis, starting with an introduction to strong field physics from first principles, for more details on this see [20]. All approximations that are used will be discussed and approaches employed to solve these problems that are relevant to this thesis are briefly mentioned. The saddle point approximation (SPA) and how it leads to quantum trajectories is discussed in detail. This methodology provides a powerful tool for studying interference.

2.1 Light Matter Interaction

In all this work relativistic effects can be ignored as the speeds of the particles and energies of the fields are not high enough. Additionally, the light-matter regime of interest is accurately described by a classical fields without quantisation, due to the high intensity and low frequency of the field relative to the atomic ionisation potentials. Thus, in any process a large number of photons will be involved. Furthermore, given the high intensity of the field, it is reasonable to neglect any backreaction of the electron(s) on the field, so the dynamics of the field will be fixed and will not depend on the motion of the electron(s). Given these assumptions, the Hamiltonian for a single electron in a Coulomb potential and strong laser field is given by

$$\hat{H}^{(c)} = \frac{1}{2m_e}\left(\hat{\mathbf{p}} - q_e\mathbf{A}(\hat{\mathbf{r}},t)\right)^2 + V(\hat{\mathbf{r}}), \tag{2.1}$$

this is given in the Coulomb gauge, where the gauge fixing $\nabla \cdot \mathbf{A} = 0$ is used. Here $\mathbf{A}(\hat{\mathbf{r}}, t)$ is the classical vector potential, $V(\hat{\mathbf{r}})$ is the Coulomb potential and $\hat{\mathbf{r}}$ and $\hat{\mathbf{p}}$ denote the position and momentum operators, respectively. The symbol m_e denotes the mass of the electron and q_e the charge. Now we present various considerations/ approximations that lead to more specific Hamiltonians. This leads to the framework that are more commonly employed in the literature and that will be used in this thesis.

2.1.1 Atomic Units

From this point and throughout the rest of this thesis atomic units will be used, unless specified otherwise. This means that $\hbar = k_e = m_e = e = 1$, where $\hbar$ is the reduced Planck's constant, $k_e = 1/(2\pi\epsilon_0)$ is the electric force constant and e is the elementary charge. Note from Eq. (2.2) $q_e = -e = -1$. This means that units of time, space, energy, momentum, charge, electric field strength and all others can be given by atomic units, denoted a.u. for all quantities. The speed of light in these units is given by $c = 137.03600$. In atomic units Eq. (2.1) reads

$$\hat{H}^{(c)} = \frac{1}{2}\left(\hat{\mathbf{p}} + \mathbf{A}(\hat{\mathbf{r}}, t)\right)^2 + V(\hat{\mathbf{r}}). \tag{2.2}$$

2.1.2 Dipole approximation and Velocity Gauge

The wavelength of the field, often around around 800 nm in this work, will be much larger than size of the system d (typically 1 a.u. $\approx 5.30 \times 10^{-2}$ nm for hydrogen) or even the electron excursion, which will be about 10 nm for a few laser cycles. Thus, the spatial part of the vector potential is neglected in the dipole approximation, $\mathbf{A}(\hat{\mathbf{r}}, t) \approx \mathbf{A}(t)$, which will be use throughout. Now Eq. (2.2) becomes

$$\hat{H}^{(v)} = \frac{1}{2}(\hat{\mathbf{p}} + \mathbf{A}(t))^2 + V(\hat{\mathbf{r}}), \tag{2.3}$$

this form of the Hamiltonian is known as the velocity gauge[1]. This change makes the Hamiltonian easier to solve without significantly affecting accuracy for the parameters ranges of interest. As previously stated the region where this approximation is valid is

[1] Some authors also refer to the Coulomb gauge as the velocity gauge [21]

defined by $\lambda \gg d$, where d is the size of the system. However, the dipole approximation also amounts to neglecting the magnetic field, given that $\mathbf{B} = \nabla \times \mathbf{A}(\mathbf{r}, t)$, which gives zero if there are no spatial components. Thus, we must ensure that the displacement due to the magnetic field is much smaller than the system size. Using a first order approximation for the magnetic field this leads to the following condition upon the electric field strength

$$|E_0| \ll \sqrt{\frac{dc\omega^3}{2\pi}}, \tag{2.4}$$

where ω is the angular frequency of the laser field given by $\omega = 2\pi c/\lambda$, where $c = 137.036$ a.u. is the speed of light and E_0 is the electric field strength. This gives a limit on the size of the electric field strength beyond which the magnetic field must be considered. This means that for very low frequency fields the large velocities picked up by the electrons leads to sufficient interaction with the magnetic field such that the dipole approximation will break down. For typical fields (for example in [22]), $\lambda = 800$ nm and $I = 2 \times 10^{14}$ W/cm^2, the left hand side and right hand side of Eq. (2.4) are 7.5×10^{-4} and 6.3×10^{-2}, respectively, thus the dipole approximation is valid. For the very long far infrared wavelengths used in [23], $\lambda = 16$ μm and $I = 3.4 \times 10^{11}$ W/cm^2 the left hand side and right hand side of Eq. (2.4) are 3.1×10^{-5} and 7.1×10^{-4}, respectively, at this point one may start having to consider account for the magnetic field for certain process. Recent study have investigated the break down of the dipole approximation for low-frequency fields and in NSDI [24–30]. Throughout this thesis all parameters will be well within what is required for the dipole approximation.

2.1.3 Other Transformations

From the form of the Hamiltonian, given in Eq. (2.3), transformations are often applied for convenience. For a general unitary transformation $\mathcal{U}$ the Hamiltonian transforms in the following way

$$\hat{H}^{(2)} = \mathcal{U}\hat{H}^{(1)}\mathcal{U}^\dagger + i\frac{\mathrm{d}\mathcal{U}}{\mathrm{d}t}\mathcal{U}^\dagger, \tag{2.5}$$

which can be derived from the time dependent Schrödinger equation. If the following form is given for unitary transformation $G = \exp(iF(\mathbf{r}, \mathbf{A}, t))$ this changes the transformation equation to

$$\hat{H}^{(2)} = G\hat{H}^{(1)}G^{\dagger} + \frac{\partial F}{\partial t}. \tag{2.6}$$

We can obtain the length gauge by applying the unitary transformation

$$G^{(vl)} = \exp(i\mathbf{A} \cdot \mathbf{r}) \tag{2.7}$$

to Eq. (2.3) and using the gauge field $\chi = -\hat{\mathbf{r}} \cdot \mathbf{A}(t)$ to transform the potentials. This gives the length-gauge Hamiltonian as

$$\hat{H}^{(l)} = \frac{1}{2}\hat{\mathbf{p}}^2 - \hat{\mathbf{r}} \cdot \mathbf{E}(t) + V(\hat{\mathbf{r}}), \tag{2.8}$$

where $\mathbf{E}(t)$ is the electric field of the external laser field and $\mathbf{E}(t) = -\partial\mathbf{A}(t)/\partial t$. Also sometimes used is the unitary Kramers-Henneberger's transformation given by

$$G^{(la)} = \exp\left(i\,\dot{\mathbf{r}} \cdot \int^{t} \mathbf{A}(\tau)\mathrm{d}\tau\right), \tag{2.9}$$

which gives the Hamiltonian

$$H^{(a)} = \frac{1}{2}\left(\hat{\mathbf{p}}^2 + \mathbf{A}(t)^2\right) + V\left(\hat{\mathbf{r}} + \int^{t} \mathbf{A}(\tau)\mathrm{d}\tau\right). \tag{2.10}$$

This is often called the acceleration frame. This is because the frame follows the motion of a classical electron in the laser field.

2.2 S-Matrix Approach

Now that we have various forms of the Hamiltonian we can write the time-dependent Schrödinger equation

$$i\partial_t|\psi(t)\rangle = \hat{H}(t)|\psi(t)\rangle\,, \tag{2.11}$$

which describes the evolution of an electron under the influence of the binding potential and the external field. The Hamiltonian may be split into $\hat{H}(t) = \hat{H}_a + \hat{H}_I(t)$, where

$$H_a = \frac{\hat{\mathbf{p}}^2}{2} + V(\hat{\mathbf{r}}) \tag{2.12}$$

gives the field-free one-electron atomic Hamiltonian. As previously stated $V(\hat{\mathbf{r}})$ is a Coulomb-type potential

$$V(\hat{\mathbf{r}}) = -\frac{C}{\sqrt{\hat{\mathbf{r}} \cdot \hat{\mathbf{r}}}}, \tag{2.13}$$

where $0 \leq C \leq 1$ is an effective coupling, and $H_I(t)$ gives the interaction with the external field. In the length and velocity gauge, $\hat{H}_I(t) = -\hat{\mathbf{r}} \cdot \mathbf{E}(t)$ and $\hat{H}_I(t) = \hat{\mathbf{p}} \cdot \mathbf{A}(t) + \mathbf{A}(t)^2/2$, respectively. Like most strongly interacting systems Eq. (2.11) can not be solved analytically. It is possible to solve this numerically and with today's resources it is not too computationally expensive for single/ few-particle systems, but this will scale badly for systems with more particles. Additionally, direct numerical solutions are not well suited to laser fields of longer wavelength as the larger excursions of the electron means that bigger grids are required. In this work we intend to probe analytically the dynamics of the system, particularly we are interested in probing interferences. An alternative approach to solving the Schrödinger equation directly is to write the problem as an S-matrix transition amplitude, a technique often using in scattering problems. This means that the transition amplitude of the electron ionising with momentum $\mathbf{p}$ can be written

$$M(\mathbf{p}) = \lim_{\substack{t\to\infty \\ t_0\to-\infty}} \langle \psi_{\mathbf{p}}(t)|U(t,t_0)|\psi(t_0)\rangle \,, \tag{2.14}$$

$|\psi_{\mathbf{p}}\rangle$ is a final unbound state of the electron far from the Coulomb potential after the laser has been turned off with a momentum $\mathbf{p}$ and $|\psi(t_0)\rangle$ is an initial bound state before the laser has been turned on. The time-evolution operator is given by

$$U(t,t_0) = \hat{\mathcal{T}} \exp\left[-i\int_{t_0}^{t} \hat{H}(t')\mathrm{d}t'\right], \tag{2.15}$$

where $\hat{\mathcal{T}}$ denotes time-ordering, relates to the full Hamiltonian $\hat{H}(t)$ evolving from an initial time t_0 to a final time t. The time-evolution operator is currently in an unhelpful form as it tells us little about the system and is difficult/ impossible to compute

analytically. We can improve this by using the Dyson equation

$$U(t,t_0) = U_a(t,t_0) - i\int_{t_0}^{t} U(t,t')H_I(t')U_a(t',t_0)\mathrm{d}t' \,, \tag{2.16}$$

where $U_a(t,t_0) = \exp[iH_a(t-t_0)]$ is the time-evolution operator associated with the field-free Hamiltonian. This yields an intermediate time that is integrated over, ultimately this will be interpreted as the time of ionisation.

Substituting Eq. (2.16) into Eq. (2.15) leads to the formally exact[2] ionisation amplitude

$$M(\mathbf{p}) = -i\lim_{t\to\infty}\int_{-\infty}^{t} \mathrm{d}t' \left\langle \psi_{\mathbf{p}}(t)|U(t,t')H_I(t')|\psi_0(t')\right\rangle \,, \tag{2.17}$$

with $|\psi_0(t')\rangle = \exp[iI_p t']\,|\psi_0\rangle$, where I_p is the ionisation potential. Note the first term from Eq. (2.16) gives zero when substituted into Eq. (2.15) as bound states are considered to have no overlap with the final momentum states. Now we have written the S-matrix transition amplitude in a form that is easier to to interpret. However, the time-evolution operator within this equation is still very tricky to compute. Below we present some tools that make it easier to evaluate this expression.

2.2.1 Volkov states and operators

The Volkov state is the solution of an electron in an oscillating electric field, which has an exact solution and is given in the length gauge by,

$$|\psi_{\mathrm{v}}(t)\rangle = e^{-iS_{\mathbf{p}}(t)}\,|\mathbf{p}+\mathbf{A}(t)\rangle \tag{2.18}$$

where,

$$S_{\mathbf{p}}(t) = \frac{1}{2}\int_{t_0}^{t} \mathrm{d}\tau(\mathbf{p}+\mathbf{A}(\tau))^2, \tag{2.19}$$

here t_0 is some arbitrary initial time that just contributes to the phase. Then the Volkov time-evolution operator is given by,

$$U^{(V)}(t,t') = e^{-\frac{i}{2}\int_t^{t'} \mathrm{d}\tau(\mathbf{p}+\mathbf{A}(\tau))^2}\,|\mathbf{p}+\mathbf{A}(t')\rangle\,\langle\mathbf{p}+\mathbf{A}(t)| \tag{2.20}$$

[2]This is exact in the context of the previously discussed approximations.

In the strong field approximation and related KFR approaches the solution of the electron in the continuum is given by a Volkov state. This means that the Coulomb potential is neglected for electrons in the continuum and the time-evolution operator in Eq. (2.17) can be replaced by Eq. (2.20).

2.2.2 Path Integral Approach

Another approach, which is one of the key parts of Chapters 3-7, is to use path integrals to evaluate the time-evolution operator. For further reference on path integrals in non-relativistic quantum mechanics see [31].

In our case it is most useful to look at the path integral representation of the transition amplitude from one momentum $|\mathbf{p}_i\rangle$ state to another $|\mathbf{p}_f\rangle$, which takes the form

$$\langle \mathbf{p}_f | U(t_f, t_i) | \mathbf{p}_i \rangle \,. \tag{2.21}$$

This will allow the time-evolution operator in Eq. (2.17) to be written in terms of a path integral. Now the main steps to get to the path integral formulation will be sketched out. First the time-evolution operator is expressed as a product of many time-evolution operators each covering a small time interval. This is called time slicing and the full time-evolution operator can be written as

$$U(t_f, t_i) = \prod_{n=1}^{N+1} U(t_n, t_{n-1}), \tag{2.22}$$

where $t_{N+1} = t_f$ and $t_0 = t_i$. Then we can approximate each sliced time-evolution operator by

$$U(t_n, t_{n-1}) \approx \exp\left[-i\hat{T}(t_n)\Delta t\right] \exp\left[-i\hat{V}\Delta t\right], \tag{2.23}$$

where $\Delta t = t_n - t_{n-1}$, and $\hat{T}(t_n)$ and $\hat{V}$ are the kinetic and potential energy operators from the Hamiltonian. The Baker-Campbell-Hausdorff formula has been used on Eq (2.15) to split $\hat{T}(t_n)$ and $\hat{V}$ apart into products. Terms of order $\mathcal{O}(\Delta t^2)$ and above have been neglected. In the limit that the number of time slices goes to infinity, then $\Delta t \to 0$ and this approximation will become exact. The next step is to add to each sliced

time-evolution operator resolutions of the identity in momentum and space given by

$$\mathbb{1} = \int \mathrm{d}\mathbf{p}_n \int \mathrm{d}\mathbf{r}_n \left|\mathbf{p}_n\right\rangle \left\langle \mathbf{p}_n|\mathbf{r}_n\right\rangle \left\langle \mathbf{r}_n\right|, \tag{2.24}$$

inserting this in between the kinetic and potential exponent leads to

$$U(t_n, t_{n-1}) = \int \mathrm{d}\mathbf{p}_n \int \mathrm{d}\mathbf{r}_n \exp\left[-i\hat{T}(t_n)\Delta t\right] \left|\mathbf{p}_n\right\rangle \left\langle \mathbf{p}_n|\mathbf{r}_n\right\rangle \left\langle \mathbf{r}_n\right| \exp\left[-i\hat{V}\Delta t\right]. \tag{2.25}$$

The operators can act on the states, giving the eigenvalues in their place. This effectively means the kinetic and potential energy operators are replaced by their classical counterparts

$$U(t_n, t_{n-1}) = \int \mathrm{d}\mathbf{p}_n \int \frac{\mathrm{d}\mathbf{r}_n}{(2\pi)^3} \exp\left[-iT(t_n)\Delta t\right] \exp\left[-iV\Delta t\right] \exp\left[-i\mathbf{p}_n \cdot \mathbf{r}_n\right] \left|\mathbf{p}_n\right\rangle \left\langle \mathbf{r}_n\right|, \tag{2.26}$$

where the identity for a plane wave $\langle \mathbf{p}_n|\mathbf{r}_n\rangle = \exp(-i\mathbf{p}_n \cdot \mathbf{r}_n)t)/(2\pi)^{3/2}$ was used. This result for the sliced time-evolution operator can added back into the full time-evolution operator, Eq. (2.22), to give

$$U(t_f, t_i) = \prod_{n=1}^{N+1} \left(\int \mathrm{d}\mathbf{p}_n \int \frac{\mathrm{d}\mathbf{r}_n}{(2\pi)^3} \exp\left[-iT(t_n)\Delta t\right] \exp\left[-iV\Delta t\right] \exp\left[-i\mathbf{p}_n \cdot \mathbf{r}_n\right] \left|\mathbf{p}_n\right\rangle \left\langle \mathbf{r}_n\right| \right). \tag{2.27}$$

This in turn can be substituted into Eq. (2.21) to give the transition amplitude

$$\left\langle \mathbf{p}_f|U(t_f, t_i)|\mathbf{p}_i\right\rangle = \prod_{n=1}^{N+1} \left(\int \mathrm{d}\mathbf{p}_n \right) \overbrace{\left\langle \mathbf{p}_f|\mathbf{p}_{N+1}\right\rangle}^{\delta(\mathbf{p}_f - \mathbf{p}_{N+1})} \prod_{n=1}^{N+1} \left(\int \frac{\mathrm{d}\mathbf{r}_n}{(2\pi)^{3/2}} \right) \tag{2.28}$$

$$\times \prod_{n=1}^{N} \left\{ \exp\left[-i\Delta t \left(T(t_n) + V + \frac{\mathbf{p}_n \cdot \mathbf{r}_n}{\Delta t} \right)\right] \left\langle \mathbf{r}_n|\mathbf{p}_{n-1}\right\rangle \right\}, \tag{2.29}$$

then using $\langle \mathbf{r}_n|\mathbf{p}_{n-1}\rangle = \exp(i\mathbf{p}_{n-1} \cdot \mathbf{r}_n)t)/(2\pi)^{3/2}$ yields

$$\left\langle \mathbf{p}_f|U(t_f, t_i)|\mathbf{p}_i\right\rangle = \prod_{n=1}^{N} \left(\int \mathrm{d}\mathbf{p}_n \right) \prod_{n=1}^{N+1} \left(\int \frac{\mathrm{d}\mathbf{r}_n}{(2\pi)^3} \right) \tag{2.30}$$

$$\times \exp\left[-i \sum_{n=1}^{N} \left\{ \Delta t \left(T(t_n) + V + \frac{\mathbf{p}_n - \mathbf{p}_{n-1}}{\Delta t} \cdot \mathbf{r}_n \right) \right\} \right]. \tag{2.31}$$

Now we take the limit that $N \to \infty$ and $\Delta t \to 0$, this leads to,

$$\prod_{n=1}^{N} \left(\int \mathrm{d}\mathbf{p}_n \right) \to \int \mathcal{D}'\mathbf{p}, \tag{2.32}$$

$$\prod_{n=1}^{N+1} \left(\int \frac{\mathrm{d}\mathbf{r}_n}{(2\pi)^3} \right) \to \int \frac{\mathcal{D}\mathbf{r}}{(2\pi)^3}, \tag{2.33}$$

$$\sum_{n=1}^{N} \Delta t \to \int_{t_i}^{t_f} \mathrm{d}\tau, \tag{2.34}$$

$$\frac{\mathbf{p}_n - \mathbf{p}_{n-1}}{\Delta t} \to \dot{\mathbf{p}}. \tag{2.35}$$

Now we can write the final form of the path integral equation for the momentum S-matrix amplitude, given in terms of a phase space action

$$\langle \mathbf{p}_f | U(t_f, t_i) | \mathbf{p}_i \rangle = \int \mathcal{D}'\mathbf{p} \int \frac{\mathcal{D}\mathbf{r}}{(2\pi)^3} \exp\left(i\mathcal{A}(\mathbf{p}, \mathbf{r}) \right), \tag{2.36}$$

where the classical action is given by

$$\mathcal{A}(\mathbf{p}, \mathbf{r}) = -\int_{t_i}^{t_f} \mathrm{d}\tau \left(\dot{\mathbf{p}} \cdot \mathbf{r} + H(\mathbf{p}, \mathbf{r}, t) \right) \tag{2.37}$$

and the $H(\mathbf{p}, \mathbf{r}, t)$ is the classical Hamiltonian of the system and the integrand in the Lagrangian.

2.3 The Saddle Point Approximation

The saddle point approximation, also known as the method of steepest descent or stationary phase method, is an approximate method of calculating integrals. In order to compute integrals such as that given in Eq. (2.36) the saddle point approximation is very useful. For quantum mechanics problems formulated in terms of an action, it has the added bonus of providing semi-classical equations of motion that lead to 'quantum trajectories', which arise from finding stationary action with respect to the integration variables. For this reason it is sometimes called the semi-classical approximation, particularly when applied to path integrals. It can be applied to ordinary integrals written

in the form

$$I(\lambda) = \int_{-\infty}^{\infty} \mathrm{d}x F(x) \exp\left[i\lambda S(x)\right]. \tag{2.38}$$

If λ is large and the function $F(x)$ is slowly varying in comparison to the rest of the integrand then the saddle point approximation will be valid. The saddle point approximation proceeds by Taylor expanding the function $S(x)$ about its saddle(s) i.e. $S'(x_s) = 0$, to second order[3]. So that

$$S(x) \approx S(x_s) + \frac{S''(x_s)}{2}(x - x_s)^2 \tag{2.39}$$

Inserting this into Eq. (2.38) leads to

$$I(\lambda) \approx F(x_s) \exp\left[i\lambda S(x_s)\right] \int_{-\infty}^{\infty} \mathrm{d}x \exp\left[i\lambda \frac{S''(x_s)}{2}(x - x_s)^2\right]. \tag{2.40}$$

The above Gaussian integral can be performed analytically to give

$$I(\lambda) \approx \sqrt{\frac{2\pi}{i\lambda S''(x_s)}} F(x_s) \exp\left[i\lambda S(x_s)\right], \tag{2.41}$$

which can be generalised to include many saddle-points solutions

$$I(\lambda) \approx \sum_s \sqrt{\frac{2\pi}{i\lambda S''(x_s)}} F(x_s) \exp\left[i\lambda S(x_s)\right]. \tag{2.42}$$

In this work the first term, $\sqrt{\frac{2\pi}{i\lambda S''(x_s)}} F(x_s)$ will often be singled out and called the prefactor. If the action is integrated over many variables there is a multivariable version. Then the integral takes the form

$$I(\lambda) = \prod_{n=1}^{N} \left(\int_{-\infty}^{\infty} \mathrm{d}x \right) F(x_1, \ldots, x_N) \exp\left[i\lambda S(x_1, \ldots, x_N)\right]. \tag{2.43}$$

[3]There is no linear term as the expansion is around a stationary point

In this case there are N saddle point equations/ equations of motion

$$\frac{\partial S}{\partial x_1} = 0, \ \ldots, \ \frac{\partial S}{\partial x_N} = 0. \tag{2.44}$$

Expanding in a multivariable Taylor expansion and computing N Gaussian integrals leads to

$$I(\lambda) \approx \left(\frac{2\pi}{i\lambda}\right)^{\frac{N}{2}} \sum_s \left(\det[S''(x_{1s}, \ldots, x_{Ns})]\right)^{-1/2} F(x_{1s}, \ldots, x_{Ns}) \exp\left[i\lambda S(x_{1s}, \ldots, x_{Ns})\right], \tag{2.45}$$

where $S''(x_{1s}, \ldots, x_{Ns})$ denotes the Hessian matrix of the multivariate action. In order to generalise this for path integrals we must consider an infinite dimensional version of Eq. (2.43), this can be written in functional form as,

$$I(\lambda) = \int \mathcal{D}x F[x] \exp\left(i\lambda S[x]\right) \tag{2.46}$$

The saddle point equations can now be written as $\delta S[x_s] = 0$, which using calculus of variations will yield the Euler-Lagrange equations or Hamilton's equations. The action must now be expanded in terms of a second-order functional Taylor expansion given by

$$S[x(t)] \approx S[x_s(t)] + \frac{1}{2} \iint \mathrm{d}t\mathrm{d}t' \delta x(t) \frac{\delta^2 S}{\delta x(t) \delta x(t')} \delta x(t'), \tag{2.47}$$

where $\delta x_s(t) = x(t) - x_s(t)$, the derivatives here are functional derivatives and as before there is no linear terms due the saddle point equation $\delta S[x_s] = 0$. Inserting this into Eq. (2.46) yields

$$I(\lambda) \approx \sum_s F[x_s] \exp\left(i\lambda S[x_s]\right) \int \mathcal{D}x \exp\left[i\frac{1}{2} \iint \mathrm{d}t\mathrm{d}t' \delta x(t) \frac{\delta^2 S}{\delta x(t) \delta x(t')} \delta x(t')\right]. \tag{2.48}$$

The Gaussian functional integral can then be calculated in a similar way to the multivariable case to give

$$I(\lambda) \approx \sum_s F[x_s] \left[\det\left(\frac{\delta^2 S}{\delta x(t) \delta x(t')}\right)\right]^{-1/2} \exp\left(i\lambda S[x_s]\right). \tag{2.49}$$

The functional derivative inside the determinant will reduce to a differential operator. It is not easy to compute this but luckily if we are dealing with an action for a real system with meaningful definitions for position and momentum the above equation can be written as

$$I(\lambda) \approx \sum_s F[x_s] \left[\det\left(-\frac{\partial p_s(t_f)}{\partial x_s(t_i)}\right)\right]^{1/2} \exp\left(i\lambda S[x_s]\right), \tag{2.50}$$

where the subscripts i and f denote initial and final, respectively. This expression is much easier to calculate as the determinant is of a 3×3 matrix for a system with 3 spatial coordinates. This can be applied to the phase space path integral matrix element given by Eq. (2.36) which results in

$$\langle \mathbf{p}_f | U(t_f, t_i) | \mathbf{p}_i \rangle \approx \sum_s \left[\det\left(-\frac{\partial \mathbf{p}_s(t_f)}{\partial \mathbf{r}_s(t_i)}\right)\right] \exp\left[i\mathcal{A}(\mathbf{p}_s, \mathbf{r}_s)\right]. \tag{2.51}$$

Aside from the requirement of a fast varying action and slow varying prefactors, for the SPA to be applicable the solutions of the saddle point equations must not become degenerate (or nearly degenerate) i.e. $S[x_s] = S[x_{s'}]$ if $s \neq s'$ otherwise the SPA will fail. This can be issue can be rectified if a higher order expansion of the action is used. One extension of the SPA that does this is called the uniform approximation and will be discussed in Chapter 9, however this is in relation to the SPA in the SFA where only ordinary integrals are used. No such expansion has been applied to the CQSFA as similar extension are more difficult for functional integrals.

2.4 Quantum Trajectories

Solving the stationary action/ saddle point equations returns solutions known as to *quantum* trajectories. They are called this as they can account for inherently quantum behaviour, such as interference and tunnelling, despite the fact they are governed by classical equations of motion. The interference is possible because each quantum trajectory leads to a complex valued amplitude that when combined with the amplitude due to another quantum trajectory may lead to interference effects. Tunnelling is possible because the solutions of the classical equations must often be extended to the complex

plane leading to non-classical effects. In the case of tunnel ionisation (and most other semi-classical descriptions of tunnelling), the time (of ionisation) is complex and propagation parallel to the imaginary axis to get (to the real time axis) is what results in the tunnelling of the electron.

Quantum trajectories provide a useful self consistent '*physical*' picture of what is going on. However, the trajectories are not observable so are not themselves '*physical*'. Only the final transition amplitude that is combination of all the possible trajectories is physical. This is no different to the fact that the wavefunction itself is not completely physical, so one should not exclude quantum trajectories from being used to interpret results.

2.5 Quantum Interference

A description of quantum interference when employing the SPA to give quantum trajectories is very easy and intuitive. The probability distribution for two interfering transition amplitudes can be easily simplified when using the SPA,

$$\Omega = |M_1 + M_2|^2 \tag{2.52}$$

$$= |e^{iS_1} + e^{iS_2}|^2 \tag{2.53}$$

$$= |\exp(iS_1)|^2 |1 + \exp(i\Delta S_{12})|, \tag{2.54}$$

where $\Delta S_{12} = S_2 - S_1$. For a real ΔS_{12} this simplifies to

$$= 4|\exp(iS_1)|^2 \cos(\Delta S_{12}^2/2), \tag{2.55}$$

this clearly gives interference fringes. The maxima are given by equating $\Delta S_{12}^2/2 = 2\pi n$, where n is an integer. In this formulation we have neglected the prefactors, often the phase of the prefactors is slowly varying and their effect can easily be understood in terms of shaping the final momentum distributions. A more general version of Eq. (2.55) can be formulated without assuming real action, considering an arbitrary number of

trajectories and the prefactors,

$$\Omega = \sum_{s=1}^{N} V_s \exp(iS_s) \tag{2.56}$$

$$= \underbrace{V_s |\exp(iS_1)|^2}_{\text{shaping}} \left(1 + \sum_{s=2}^{N} \underbrace{\frac{V_s}{V_1} \exp\left(i\text{Im}[\Delta S_{1s}]\right)}_{\text{switching}} \underbrace{\exp\left(i\text{Re}[\Delta S_{1s}]\right)}_{\text{interference}} \right). \tag{2.57}$$

The labels shaping, switching and interference give the dominant role of each term: To shape the overall distribution, to switch interference on/ off and to form the interference fringes, respectively. The minima and maxima of the fringes can be found by an analysis of the argument of the *interference* exponential, in a similar manner to that above. This is not a fully rigorous analysis but gives a flavour of the type of analysis that is used to understand the different interference patterns present in this thesis.

Part I

Above Threshold Ionisation

Chapter 3

Introduction

Above-Threshold Ionisation (ATI) is the removal of an electron from an atom, molecule, or any other target with at least one bound electron, with more energy than required by the ionisation potential. A detailed account of the different theories that are typically used to describe this process can be found in [32] and a brief history is given in [33].

3.1 Background

ATI was originally observed in 1979 [34] as a multi-photon effect in the ionisation of xenon atoms by a strong laser field (8×10^{12} W/cm^2). In this experiment it was found some photoelectrons were ionised with an additional photon's worth of kinetic energy than expected, see Fig. (3.1). The observation of ATI was enabled by the measurement of the relative yield across photoelectron energies, as opposed to just the overall yield for different laser intensities. This original observation of ATI can be described as perturbative with regard to the laser field, as it can be understood in terms of a few photons, however later there was the first evidence of non-perturbative ATI [35]. In these results multiple ATI orders, i.e. many peaks in the photoelectron yield each corresponding to the absorption of an additional photon, were observed. It was reported that peaks corresponding to the absorption up to 19 photons (11 in ionisation and 8 in the continuum) were observed. Additionally, there was an unexpected decrease in the yield for low energy photoelectrons for increased laser intensity. This effect was described by channel closure, where increasing the laser intensity also increased the effective atomic binding potential through Stark shifting, closing off the lowest order ATI channel, which translates to the lowest energy peak in the photoelectron yield being suppressed. However,

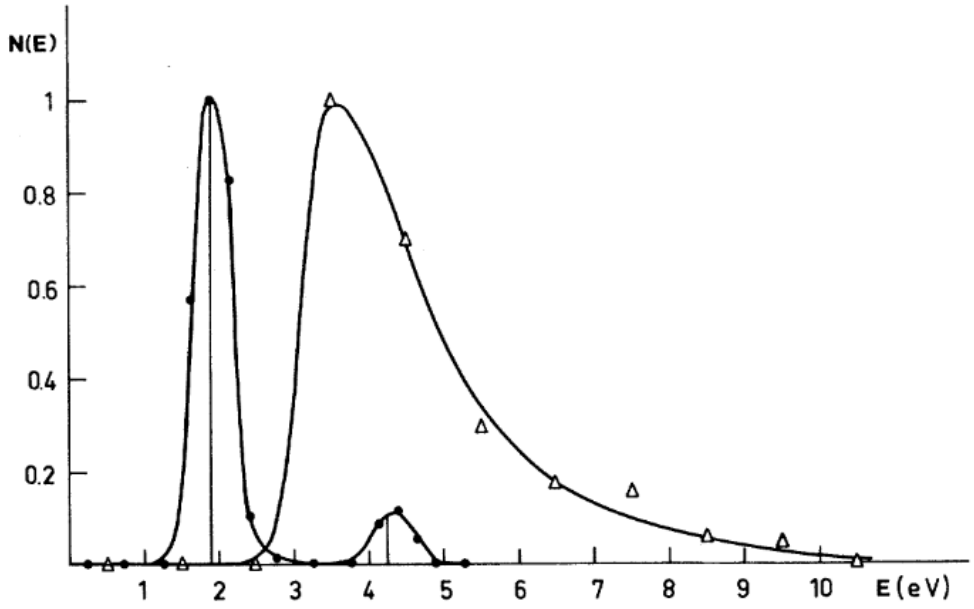

FIGURE 3.1: Energy spectra of emitted electrons in above-threshold ionisation of xenon, taken from [34]. The circles show results taken for a laser field with a photon energy of $\hbar\omega = 2.34$ eV and intensity $I = 8 \times 10^{12}$ W/cm^2, which shows a secondary peak resulting from the absorption of an additional photon beyond that required for ionisation. Note the gap between the two peaks is equal to the photon energy. The triangles show results from a different wavelength, $\hbar\omega = 1.17$ eV, and intensity, $I = 4 \times 10^{13}$ W/cm^2, where ATI was not observed.

the photon energy, $\hbar\omega$, was still high enough and the intensity low enough such that perturbation theory was applicable and able to explain these results.

With the advancement of CO_2 lasers in the 1980s, wavelengths of $10\ \mu$m became possible for intense fields (greater than around 10^{13} W/cm^2). Now the ATI tunnelling regime could be explored. The first experimental demonstration of tunnel ionisation was observed for xenon in 1985 [36], see Fig. (3.2). Requiring nearly 100 photons to ionise xenon at these frequencies, the multi-photon picture breaks down here. The application of standard perturbation theory is practically impossible. The Keldysh tunnelling picture/ KFR (Keldysh Faisal Reiss) theory [14, 17, 18, 37] had been developed in the previous couple of decades and was valid for this low frequency, high intensity situation. It gave good results for ionisation yields and photoelectron energy spectra and thus it was steadily adopted. Reviews on this topic are given in [19, 38]. It should be noted that although KFR and the related strong field approximation (SFA) approaches replaced perturbation theory as descriptions for strong field ionisation, these methods

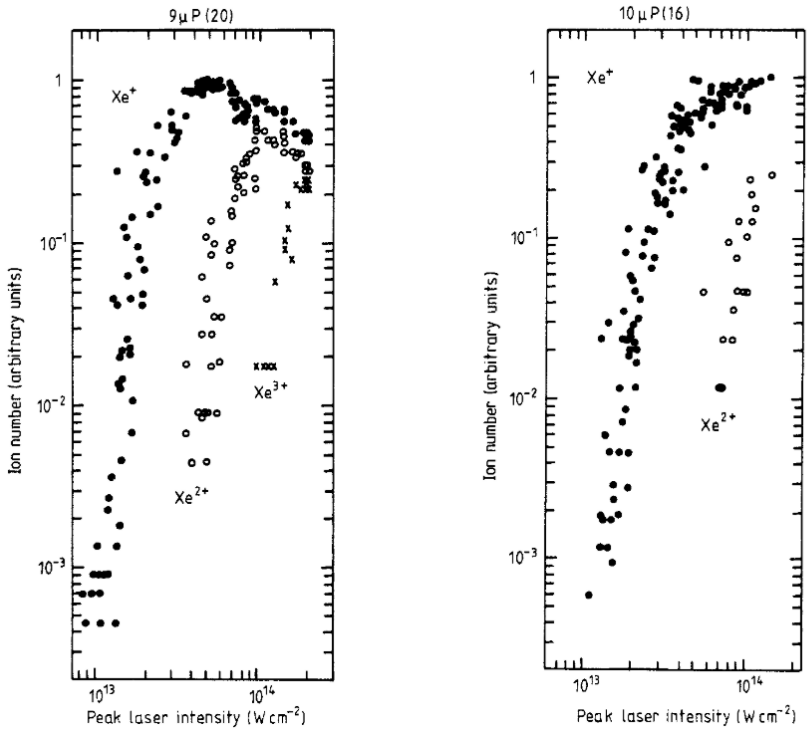

FIGURE 3.2: Ionisation yield of xenon vs laser intensity at two different laser wavelengths, $\lambda = 9\ \mu\mathrm{m}$ (left) and $\lambda = 10\ \mu\mathrm{m}$ (right), taken from [36]. The lack of resonance in the two ionisation curves and their similarity is consistent with the behaviour expected from tunnelling theory [14, 37].

still use perturbative expansions, most notably, they typically use a zero-order expansion in a Born series (or equivalent approximation) of the Coulomb field for continuum electron states and a first order expansion about the laser field for bound states.

KFR-type tunnelling theories had much success in the late 80s and 90s, providing successful descriptions to various new strong field phenomena, such as a plateau [39, 40] and a cut-off [41] in the spectra from photons released in high harmonic generation (HHG) and the plateau in rescattered ATI [41] known as high-order above-threshold ionisation (HATI). The plateau in HATI for a monochromatic, linearly polarised field, or a long enough pulse, may extend to a photoelectron energy of up to $10U_p$, and consists of ATI peaks with comparable intensities, see Fig. (3.3). It results from a hard elastic collision of an electron, which is backscattered by its parent ion [41, 42], for reviews see [33, 43]. These successes made the tunnelling picture central to strong field physics. Strong field phenomena were intuitively understood in terms of the behaviour of semi-classical trajectories, such as those in the three-step model [44] for HATI and HHG.

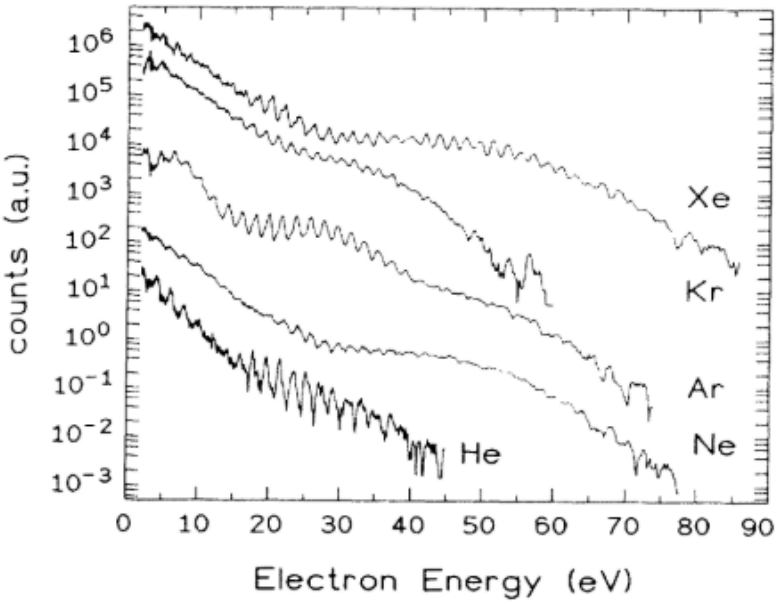

FIGURE 3.3: ATI spectra of all[1]rare gases, taken from [41]. This shows the ATI plateau, which can be explained by the three-step model [44]. The intensities are 3×10^{14} W/cm^2 for He and 2×10^{14} W/cm^2 for all the others.

What is now typically called the SFA was initially developed from KFR-type theories to explain phenomena in HHG and ATI [42, 45, 46]. One particularly powerful addition was the use of the saddle point approximation (SPA) to obtain semi-classical trajectories/ orbits and this also makes it a very numerically inexpensive method in comparison to *ab-initio* methods. Other variants of KFR-type theories use methods such as Bessel function expansions [47] instead of applying the SPA. For a given final electron momentum there may be multiple orbits that the active electron may follow. From each orbit one can calculate a transition amplitude. The transition amplitudes from paths leading to the same final momentum can be combined and will interfere. Using this technique interference based features such as the ATI rings [42] may be reproduced. For a qualitative description of strong-field dynamics in ATI, particularly when focusing just on overall yields, the SFA description works quite well and has enjoyed many successes in ATI [42, 48], HHG [45, 49, 50] and non-sequential double ionisation [51, 52] discussed in Part II. However, the approximation to neglect the binding potential in the electron propagation and approximate the continuum by field-dressed plane waves

leads to discrepancies with experiment.

3.2 The Effect of the Coulomb Potential

From the mid-2000s many features not captured by the SFA that stem from the interplay between the residual binding potential and the laser field have been identified in experiments. Observations of these features were made possible by the development of the cold-target recoil ion momentum spectroscopy (COLTRIMS) technique [24, 53], which provides the ionisation yields over the momentum components parallel and perpendicular to the laser field polarisation, see Fig. (3.5) for an example. Examples of such features are (i) the low-energy enhancements/ low-energy structure (LES) in ATI spectra (see Fig. (3.4)) [54–64], (ii) the fan-shaped structure in angular resolved ATI electron momentum distributions (see Fig. (3.5)) [22, 65, 66], and (iii) the species dependency in nonsequential double ionisation (NSDI) with circularly polarised fields [67].

The example (i), the LES is an unexpected increase in the yield for ATI photoelectron spectra in the low energy region that differed from the results of KFR-type theories, see Fig. (3.4). This jump in yield has been linked to the Coulomb potential, specifically it can be explained by forward scattered classical electron orbits [54, 56–59, 62–64]. Subsequently even lower energy structures have been found, the very low energy structure (VLES) [60] and the near-zero energy structure (NZES) [24, 62, 68, 69]. While examples (i) and (iii) may be explained by classical methods [54, 56–60, 63, 64, 67], (ii) is a quantum-interference effect that occurs near the ionisation threshold. Studies of near-threshold ATI using the SFA [70, 71] have shown that the interference of events separated by at most half a cycle leads to nearly vertical fringes, whose distortion by the Coulomb potential leads to the fan-shaped structure see Fig. (3.5). This relationship has been investigated by modifying the final electron scattering state [71, 72], comparing the full solution of the time-dependent Schrödinger equation (TDSE) for short- and long-range potentials [72], and performing classical-trajectory computations which relate the fringes to laser-dressed Kepler hyperbolae with neighbouring angular momenta

[1] This is all the non-radioactive rare gases, so does not include radon or oganesson (which was only first synthesised in 2002).

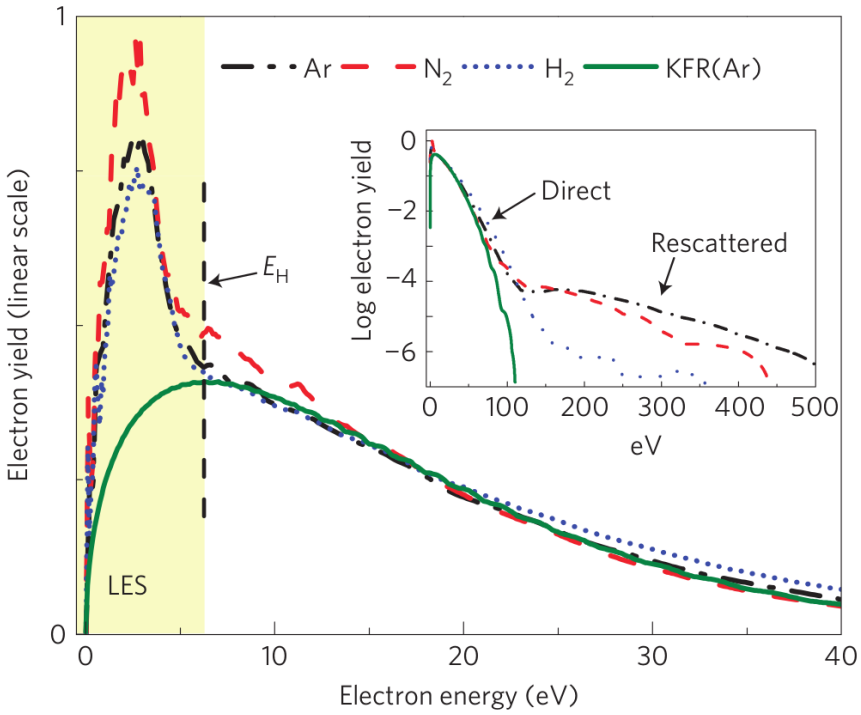

FIGURE 3.4: ATI spectra of argon showing the low-energy structure (LES), taken from [55], with an intensity of 1.5×10^{14} W/cm^2 and wavelengths of 2 μm.

[73, 74]. One should also note that, in strong-field photodetachment of negative ions, i.e. for short-range binding potentials, there is a very good agreement between the SFA and the full solution of the TDSE [75–77] and experimental results [78], with approximately vertical fringes instead of a fan. It should be noted, in a study with relatively short laser wavelengths $\lambda = 400 - 800$ nm [22], some of the features of the fan-like structure were related to Freeman resonances, although this sort of explanation could not explain all the features at these wavelengths. Freeman resonances would be expected in few-photon ionisation, which is consistent with the fact the aforementioned study used shorter wavelengths.

The combined effect of the long-range binding potential and the external driving field on the electron trajectories is important. For instance, it has been shown, using the model that will be introduced in the next chapter, the Coulomb-quantum orbit strong-field approximation (CQSFA) [79], that the fan-shaped structure results from the interference of trajectories that reach the detector directly with those that are forward-deflected by the core without undergoing hard collisions [80]. It was shown that the fan-like fringes are caused by the fact that the Coulomb potential distorts the deflected

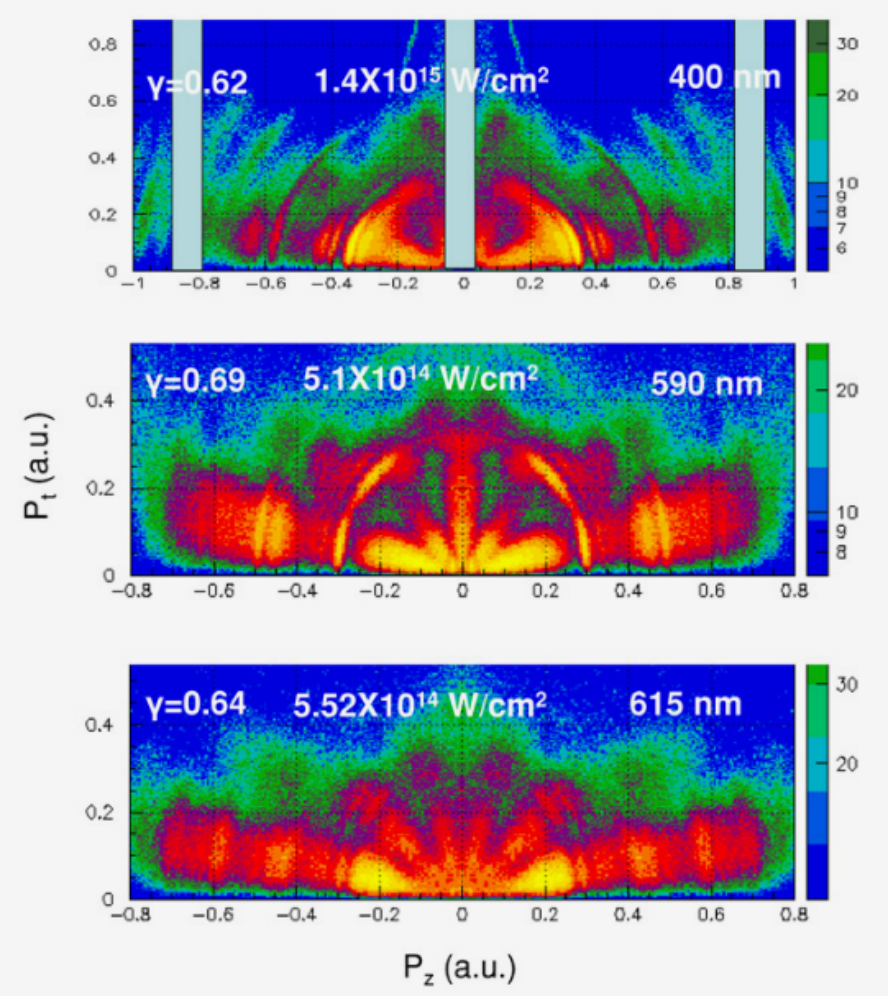

FIGURE 3.5: ATI photoelectron angular distributions (PADs), where p_z and p_t denote the momenta parallel and perpendicular to the laser field polarisation, of argon showing the fan-shaped structure, taken from [22]. The intensity and wavelength are marked on the panels.

trajectories unequally for different scattering angles and electron momenta. The phase difference between the two interfering types of trajectories is dependent on the electron scattering angle. This causes distortions in the intra-cycle fringes obtained from the SFA, which then form the fan-shaped pattern. Whilst this structure is widely studied and known to occur for long-range potentials, in most cases methods have been used that are unable to give a good explanation of how these patterns *form*. These include the numerical solution of the time-dependent Schrödinger equation for short- and long-range potentials, for which specific sets of orbits cannot be disentangled, or classical-trajectory methods, for which quantum interference does not occur [72–74]. Hence, there is a need for a quantum-orbit based method that exploit the saddle point approximation in a similar way to the SFA but includes the effect of the Coulomb potential. Models like this can be used to disentangle interference effects, which is important when considering imaging processes like electron holography. Thus, a few models along these lines have been developed:

1. **Coulomb-Volkov Approximation (CVA) and Quantitative Rescattering theory (QRS):** The CVA [70, 71, 74] uses a Coulomb-Volkov wave function, which assumes the laser distorts the Coulomb continuum state adiabatically. The resultant wavefunction is the product of a Coulomb continuum state and a laser dressed state. It does not make use of the SPA so there are no quantum trajectories with which to understand the interference in electron holography. It was one of the first models to compare with SFA and TDSE distributions [74] in order to understand Coulomb effects. QRS [81–86] uses a particular factorisation of the probability distribution that be can be used to describe processes with returning electron such as HHG, HATI and NSDI. The factorisation contains a transition dipole term and a flux term (of a returning wavefunction). It is shown the flux term can be treated accurately by the SFA while the dipole term uses a Coulomb-Volkov state to account for Coulomb corrections.

2. **The Eikonal-Volkov Approximation (EVA) and Analytical R-Matrix (ARM) Method:** The EVA [87–89] uses the eikonal approximation, an alternative semi-classical

approximation to the SPA, where the wavefunction is written in terms of exponentiated eikonal, which plays a similar role to the action in the SPA. The ARM method [90–92], splits the space into an inner and outer region, near and away from the atom/ molecule, respectively. In the inner region exact *ab-initio* methods are used, while in the outer region the EVA is employed. This has the capacity to give very accurate results, while retaining the concept of quantum trajectories. This has given very good results for the case of circularly polarised fields leading to interpreting ionisation times in a phenomena known as the attoclock [93]. Furthermore, it was used to show that including the imaginary part of the complex trajectories improves agreement with *ab-initio* solutions of the TDSE and can be related to wave-packet deceleration by the Coulomb potential [94]. However, these methods have not been applied to the interference structures present for linearly polarised fields such as the aforementioned fan-like structure. Possibly this is due to the fact that large deflections by the potential near the atomic core occur for these structures. The EVA assumes small changes in momentum during scattering so cannot account for such trajectories. The ARM can definitely account for such dynamics near the core but quantum trajectories are not used for the inner region so it may be difficult to disentangle such interferences.

3. **Coulomb-Corrected SFA (CCSFA):** The CCSFA [95–97] introduces the Coulomb effects perturbatively as a phase correction to the SFA in the action. The semi-classical trajectories are unaffected by the Coulomb potential. The Coulomb phase was added for both the continuum and tunnelling parts, even up to the Coulomb singularity. The singularity was regularised using a procedure where the asymptotic form of the initial wavefunction is matched to the action. A similar variant of this procedure was applied to the EVA [87] and the CQSFA [98]. This method is in theory very quick to calculate but is somewhat limited by a perturbative inclusion of the Coulomb potential. Additionally, there are branch cuts due to the complex trajectories, which can present quite a problem for this method, although some solutions have been found [61, 98].

4. **Trajectory-Based Coulomb SFA (TCSFA):** In the TCSFA [99, 100] the CCSFA is

built on by including equations of motion that include the Coulomb potential for continuum trajectories. This led to the categorisation, which is used in this thesis [99], of four possible contributing trajectories for each final momentum point. This method differs from the SFA, CCSFA and CQSFA in that it specifies the initial rather than final momentum and then the resulting final momenta are binned in a shooting method, similar to some Monte Carlo approaches. This procedure requires large numbers of trajectories (around 10^9) to get convergent results and suffers from caustics and defects in the PADs. It neglects a $\dot{\mathbf{p}} \cdot \mathbf{r}$ term in the action due to using a phase space action. Branch cuts are avoided by taking real trajectories in the continuum but as shown in [94, 101] complex trajectories should be used throughout.

5. **Coulomb Quantum-Orbit SFA (CQSFA):** The CQSFA [79, 80, 102–104] is the method of interest for this part of the thesis. It is the only method to use the functional integral representation of the time evolution operator from a Feynman path integral formulation, although many methods are 'in the spirit of' the sum over all paths. This formalism means that Newton's equations of motion arise as a result of the SPA as opposed to being an assumption of the method. This also naturally leads to the essential $\dot{\mathbf{p}} \cdot \mathbf{r}$ term for considering a phase-space action. Additionally, there is an additional prefactor term, relating to computing the momentum and space functional integrals in the SPA, not present in any other method, which improves agreement with solutions of the TDSE. This method like the TCSFA only solves the full Coulombic equations of motion in the continuum and neglects the Coulomb effects on the trajectories (but not the phase) during tunnelling. The continuum trajectories are forced to be real to avoid branch cuts, although complex trajectories have been explored in [98]. However, unlike the TCSFA (but like the SFA and CCSFA) the trajectories are solved starting from the final momenta and solving the inverse problem to get the initial momenta. This method is quick to solve in comparison to the TDSE and TCSFA (as it requires much fewer trajectories) and can explain a wide range of interference phenomena and electron dynamics.

6. **Quantum-Trajectory Monte Carlo (QTMC):** The QTMC [105, 106] uses the quasi-static Ammosov-Delone-Krainov (ADK) tunnelling theory to describe the first step of ionisation. Then initial conditions are randomly chosen, in the Monte Carlo fashion, weighting them with the probability distribution calculated by the ADK tunnelling rate [107]. These trajectories are propagated using Newton's equations of motion and the Coulomb phase is included in the action. The use of the ADK rate removes the caustics that were present in the TCSFA. However, it will also limit the applicability to longer wavelengths.

7. **Semiclassical Two-Step Model (STSM):** In the STSM [108, 109] a similar approach to the QTMC is used, with a tunnelling rate calculated by ADK theory. This is applied to populate initial conditions for trajectories that are used in a semiclassical theory. However, there is a difference with the QTMC in that although weights from the tunnelling rates are provided by the ADK theory, some of the initial conditions are provided by the SFA. This gives improved results when compared to the TDSE. In this work [108] a careful analysis of the action in different representations (e.g. position space and phase-space) was presented. This analysis leads to the derivation of the $\dot{\mathbf{p}} \cdot \mathbf{r}$ term that was neglected in other works.

3.3 Photoelectron Holography

In photoelectron holography of ATI, the interference of the different paths that the electron may take to the detector is exploited to 'image' the residual ion, see Fig. (3.6). Similar to other types of holography there is typically a probe and a reference signal, which are associated with two (or more) distinct types of orbits; the probe will have a stronger interaction with the core, while the reference signal is associated with an electron trajectory less strongly influenced by the potential. These trajectories will be semi-classical; for other types of trajectories in ATI, see [110–113]. The original concept of using the interference of two types of electron trajectories to perform electron holography was suggested in [66], where the trajectories were envisaged to be direct and rescattered. This idea was adapted from similar strong field imaging concepts such as electron diffraction [114], which used a high energy rescattered trajectory of the

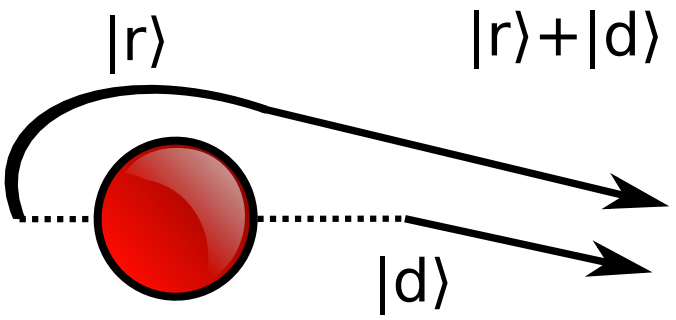

FIGURE 3.6: Two interfering paths of an ionised electron, resulting in electron holography. One path is more strongly affected by the Coulomb potential, the rescattered path, denoted $|r\rangle$, than the other direct path, denoted $|d\rangle$. The electron paths have tunnelled on opposite sides of the ion (red filled circle) but they both start from the centre of the ion.

ionised electron to probe the structure of the remaining ion/ molecule, or in HHG imaging [115–117], where the high energy photons that are released were used to provide tomographic information, using the fact that the harmonics generated are sensitive the alignment or dynamics of the molecule. Ultimately all these imaging procedures aim to provide ultrafast (sub-femtosecond), high resolution imaging capabilities for molecules in order to get unprecedented access to the electron dynamics during reactions and interactions.

In ATI there are a range of possible intra-cycle interferences, most of which can be considered holographic and it has not yet been properly investigated how the Coulomb potential distorts these holographic interference patterns. In previous holography studies [23, 63, 66, 118–123], typically only two types of trajectories are considered at any time. However, given that there are multiple types of interfering trajectories, could one generalise photoelectron holography in order to incorporate these orbits? Or alternatively can these orbits be preferentially selected for different imaging criteria? Interference structures that have been identified in ATI include: the ATI rings, caused by the interference of trajectories separated by a full number of cycles (a.k.a. intercycle interference), the carpet-like patterns observed in ATI angular distributions for electron emission perpendicular to the driving-field polarisation [75] and various holographic interference structures. Specifically, the different types of the latter are: 1) The previously mentioned fan-like structure, caused by the interference of direct and forward-deflected trajectories [22, 65, 80, 102], see Fig. (3.5). This structure was not originally considered holographic but in [102, 124] it was shown the influence of the Coulomb potential

on the two trajectories was integral to forming the fans straight fringes and thus it can be viewed as a holographic structure[2]. 2) The spider-like pattern, which results from the interference of different types of forward-scattered trajectories [23, 63, 66, 114, 118–120, 122, 123] that forms near the polarisation axis and extends up to high photoelectron energies, see Fig. (3.7). The first fringe of this structure lies on the axes parallel to the laser field polarisation and is the thickest of all the fringes. This is often referred to on its own as the side lobes [66, 102], due to the large rounded lobes on either side of the axis perpendicular to the laser field polarisation, see Fig. (3.7). 3) The fishbone-like structure observed caused by the interference of direct and backscattered electron wavepackets [66, 118].

Analytic conditions have been derived for some of these structures. However, the overwhelming majority of these conditions neglect the Coulomb potential in the electron propagation or have a limited range of validity. They are mostly based on the SFA, or on its classical counterpart. Coulomb-corrected conditions are only provided for specific scattering angles, and consider mainly sub-barrier corrections [100]. Still, such models have been able to reproduce key features. For instance, simplified models have shown that the spider-like structure stems from the interference between different types of deflected trajectories leaving within the same half cycle [23, 66, 105, 121]. One study employing the Coulomb corrected SFA [100] shows that the Coulomb potential introduces phase shifts and thus modifies interference patterns in ATI. Therein, analytic interference conditions are provided for electron emission parallel and perpendicular to the laser-field polarisation within the low-frequency limit and are only provided for specific scattering angles. These conditions are based on only two types of trajectories, neglecting two others that may occur [79, 99], and assumes the absolute value of the transition amplitudes are the same. Results in the following chapters will show that in general this does not hold.

The above-stated examples show that Coulomb effects are under-estimated and poorly understood within photoelectron holography. However, simplifications do have the advantage of leading to intuitive analytic conditions that describe the key features

[2]There is still some debate over whether this is a holographic structure as the signal trajectory does not include a hard collision with the core. But as we will show in Chapter 7 hard collision are an approximation due to using the Born expansion, hence this line of reasoning is only valid when using approximations such as the SFA.

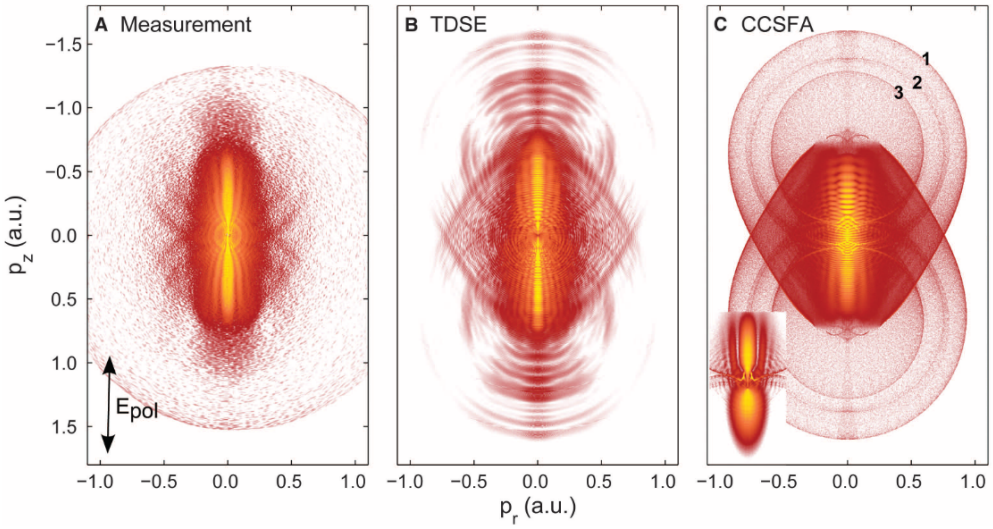

FIGURE 3.7: The spider-like structure in (A) experiment, (B) a TDSE solution and (C) a Coulomb-Corrected SFA model. Taken from [66]. The experiment was performed with a wavelength of $\lambda = 7\ \mu$m and an intensity of $I = 7.1^{11}$ W/cm^2 for a xenon target in a metastable excited state with an ionisation potential of $\mathrm{I_p} = 0.14$ a.u.

in several holographic patterns. This invites the following questions: Is it possible to derive more general expressions than in previous models, which account for the Coulomb potential, but are transparent enough to highlight the key features? If so, what is their range of validity?

These questions will be addressed in Chapters 5 and 6, where the following issues will be tackled: 1) Using the CQSFA model, we will perform a direct, quantum-orbit analysis of how the Coulomb potential influences ATI photoelectron distributions. This will cover all inter- and intra-cycle interferences, including the fan- and spider-like structures. 2) We provide analytic estimates for interference maxima and minima, and investigate to what extent the assumptions in [100] hold. We also assess how specific patterns form, and whether one must go beyond only two types of orbits. 3) We will seek analytic expressions so that the fan- and spider-like holographic patterns are reproduced for a wide range of driving-field parameters. For the analysis in 3) the same Keldysh parameter $\gamma = \sqrt{I_p/(2U_p)}$, where I_p and U_p denote the ionisation potential and the ponderomotive energy, will be used. Traditionally, the Keldysh parameter is a good indicator of the ionisation dynamics. Furthermore, there is experimental evidence that, for approximately the same γ, the spider-shaped structure becomes more important with increasing wavelength, dominating over the fan-shaped pattern, and

that the number of maxima in the fan changes [22]. As much as possible, we will justify the behaviours encountered in terms of interfering trajectories. Throughout, we will use the orbit classification introduced in [99, 100], where the closely related TCSFA is employed. This classification is based on the initial and final momentum components parallel and perpendicular to the driving-field polarisation, and has been used in our previous publications [79, 80, 102]. It singles out four types of orbits, all of which were found to influence the final momentum distributions in the parameter ranges used. Our results will be compared with the outcome of the CQSFA, and with the time-dependent Schrödinger equation (TDSE), which is solved using the freely available software Qprop [125]. Solutions of the TDSE provide the best comparison for such trajectory models as there are no uncertainties in the field parameters or other subtleties (such as focal averaging) found in experiment that make a comparison with experiments more difficult. Thus, any discrepancies must be due to approximations in the model (CQSFA) rather than experimental considerations.

3.4 Recollision and Orbit types

Laser-induced recollisions have played a vital role in ATI for over two decades [44]. The quintessential example of a recollision-induced effect being the aforementioned ATI plateau. Rescattering in ATI has been described in the context of the SFA by expanding the Coulomb potential in a Born expansion. Then the zeroth order term leads to so-called direct ATI, while the first-order term leads to rescattered ATI. this means that the additional rescattering is in terms of an instantaneous 'hard collision'. Up until recently, it was accepted knowledge that scattering in ATI was only important for intermediate and high photoelectron energy ranges. For energies up to around $2U_p$, the ATI plateau is obfuscated by the contribution from the so-called direct electrons, which result from strong-field ionisation in the absence of recollision with the core.

Recently, however, this has been called into question [64, 126, 127], in which it has been shown, within the framework of the Strong-Field Approximation (SFA), that rescattering is also important for much lower photoelectron energy. This has been attributed to the large scattering cross section that is specific to the Coulomb potential for

solutions of the ATI transition amplitude that had been previously overlooked. Among these, the importance of forward-scattered trajectories has been highlighted. In particular, low-energy rescattering events lead to a wide range of structures in photoelectron velocity maps that have been previously identified in experiments, such as a cusp-like, low-energy structure [54, 55], a fork-like structure [126] and a pronounced V-shaped structure [68].

The quantum interference of rescattered with direct electrons, or of trajectories associated with different types of rescattering, has been paramount for the development of time-resolved photoelectron holography. However, the very concept of “direct" and “rescattered" electrons has been defined either using classical models, for which the residual binding potentials are neglected during the electron propagation, or the strong-field approximation, for which the continuum is approximated by field-dressed plane waves and the core by a single point at the origin. This implies that such models allow for the existence of either hard collisions, or no collisions at all. In a realistic situation, however, the residual binding potential does influence the electron propagation in the continuum. Thus, the difference between direct and rescattered electron trajectories is blurred, and there may be direct trajectories, deflected trajectories, soft and hard collisions. A key question is how to determine whether a specific electron orbit should be viewed as “direct" or “rescattered", using the terminology implicit in the SFA, and what types of rescattering can be identified. Only in the case of low-energy structures have soft collisions been categorised in terms of phase-space criteria [58, 128, 129].

In Chapter 7 the role of rescattering is investigated for the Coulomb-corrected orbits encountered in the CQSFA, in comparison with the standard SFA. We will focus on the low- and intermediate photoelectron energy ranges investigated in [64], due to the rich structures encountered in this regime. We will also address how different types of trajectories in the CQSFA relate to their Coulomb-free, SFA counterparts.

In this part of the thesis, the material covered in each chapter is as follows: In Chapter 4, the theory required to understand the CQSFA and the SFA, is introduced. In Chapter 5, the properties of the four orbits in the CQSFA are investigated, the photoelectrons angular distributions (PADs) for each orbits are plotted, the PADs for combinations of orbits are plotted and related to holographic interference structures. Additionally, a

comparison with a full solution of the TDSE is made with PADs produced from all the relevant orbits in the CQSFA. In Chapter 6, analytic interference conditions are derived for the interference patterns, a semi-analytic model is derived for orbits 1-3 and it is used to probe the importance of soft recollision in orbit 3. In Chapter 7, the issue of recollision is investigated for the CQSFA. Parameters are introduced that qualify which type of recollision occurs an orbit, direct (no recollision), softly-recolliding and hard-recollision. The CQSFA orbits are then compared with direct ATI orbits (with no collisions) and rescattered ATI orbits (with a hard collision) and it found that the CQSFA describes both types at low and high scattering angles, respectively. Additionally, new trajectories are introduced, which suggest that the characterisation provided in [99] is too coarse.

Chapter 4

ATI Theory

In this section all the theory necessary to understanding above-threshold ionisation (ATI) and electron holography in terms of both the strong field approximation (SFA) and the Coulomb quantum-orbit strong field approximation (CQSFA) is presented. In Sec. 2.2 we presented the S-matrix framework for formulating transition amplitudes for a system and then, in Sec. 2.3, how to solve it using the saddle point approximation (SPA). This is the formalism that is used throughout this thesis. Now using Eq. (2.17) as a starting point we will derive the SFA and CQSFA transition amplitudes.

4.1 Strong Field Approximation

The SFA transition amplitude for ATI is obtained if, in Eq. (2.17), the full time evolution operator is replaced by the Volkov time evolution operator $U^{(V)}(t,t')$, as given by Eq. (2.20). Then the exponentiated terms from the continuum evolution and bound state evolution can be collected together into a semi-classical action. More details are provided in [130, 131] and in the review article [19]. The main advantage is that this operator can be computed analytically. This, however, approximates the continuum by field-dressed plane waves, and thus eliminates the influence of the binding potential in the electron propagation. Hence, within the SFA, the transition amplitude for direct ATI from the initial bound state $|\psi_0\rangle$ to a final Volkov state with drift momentum $\mathbf{p}$ is given by [14, 17, 18, 43, 132]:

$$M_d(\mathbf{p}) = -i\int_{-\infty}^{\infty} \mathrm{d}t' \langle \mathbf{p} + \mathbf{A}(t')|H_I(t')|\Psi_0\rangle e^{iS_d(\mathbf{p},t')}, \tag{4.1}$$

where

$$S_d(\mathbf{p}, t') = -\frac{1}{2}\int_{t'}^{\infty}(\mathbf{p} + \mathbf{A}(\tau))^2 \mathrm{d}\tau + I_p t' \tag{4.2}$$

is the semiclassical action, which describes the propagation of an electron from the ionisation time t' to the end of the pulse, which is taken to be infinitely long. The electron's continuum state $|\mathbf{p} + \mathbf{A}(t')\rangle$ is a field-dressed plane wave with momentum $\mathbf{p}+\mathbf{A}(t')$, obtained by back propagating the final state $|\psi_{\mathbf{p}}(t)\rangle$ from t to t' with $U^{(V)}(t', t)$. In Eq. (4.2), I_p denotes the ionisation potential. We use the length gauge Hamiltonian for $H_I(t')$, and employ the steepest descent method. This means that we seek t' for which Eq (4.2) is stationary, which gives the saddle point equation

$$\frac{\partial S(t')}{\partial t'} = 0 \implies \frac{[\mathbf{p} + \mathbf{A}(t')]^2}{2} + I_p = 0. \tag{4.3}$$

Physically, Eq. (4.3) ensures the conservation of energy upon tunnel ionisation at time t' for the electron. Because tunnelling has no classical counterpart, this equation has only complex solutions. Eq. (4.3) can be explicitly inverted to give the time in terms of the momenta,

$$t_s = \frac{2\pi n}{\omega} \pm \frac{1}{\omega}\arccos\left(\frac{-p_{\parallel} \mp i\sqrt{2I_{\mathrm{p}} + p_{\perp}^2}}{2\sqrt{U_{\mathrm{p}}}}\right), \tag{4.4}$$

where n is any integer and $p_{\parallel}$ and $p_{\perp}$ are momenta parallel and perpendicular to the laser field polarisation. In terms of the solutions t_s of Eq. (4.3), the transition amplitude can be approximated by

$$M_d(\mathbf{p}) = \sum_s \mathcal{C}(t_s) e^{iS_d(\mathbf{p}, t_s)}, \tag{4.5}$$

where

$$\mathcal{C}(t_s) = \sqrt{\frac{2\pi i}{\partial^2 S(\mathbf{p}, t_s)/\partial t_s^2}}\langle \mathbf{p} + \mathbf{A}(t_s)|H_I(t_s)|\Psi_0\rangle. \tag{4.6}$$

The prefactor $\mathcal{C}(t_s)$ is expected to vary much more slowly than the action for the saddle point approximation to hold [133]. According to Eq. (4.5), there are, in principle, many orbits along which the electron may be freed. This means that, for the same final momentum, the corresponding transition amplitudes will interfere. The theory for the SFA with a single act of rescattering is presented in Chapter 7, where the CQSFA is

compared with both direct and rescattered SFA results.

4.2 Coulomb Quantum-Orbit Strong Field Approximation

Now, from the same starting point as the SFA, Eq. (2.17), we will derive the transition amplitude for the CQSFA. In this model we would like to include the effect of the Coulomb potential for ionised electrons. However, we do not have a useful form for the time evolution operator. In Sec. 2.2.2 we showed that amplitudes of the form $\langle \mathbf{p}_f | U(t_f, t_i) | \mathbf{p}_i \rangle$ may be written in terms of a path integral formulation. This is a convenient formalism as immediately it leads to a semi-classical action, which, when approximated by the SPA, leads to '*quantum-trajectories*' that may be interpreted similarly to the SFA orbits. This allows for useful comparisons and these trajectories can be used to make holographic interference patterns. We will now insert the closure relation $\int d\tilde{\mathbf{p}}_0 |\tilde{\mathbf{p}}_0\rangle\langle\tilde{\mathbf{p}}_0| = 1$ in Eq. (2.17). This yields

$$M(\mathbf{p}_f) \;=\; -i \lim_{t\to\infty} \int_{-\infty}^{t} \mathrm{d}t' \int \mathrm{d}\tilde{\mathbf{p}}_0 \left\langle \tilde{\mathbf{p}}_f(t) | U(t,t') | \tilde{\mathbf{p}}_0 \right\rangle \left\langle \tilde{\mathbf{p}}_0 | H_I(t') | \psi_0(t') \right\rangle , \qquad (4.7)$$

where $|\tilde{\mathbf{p}}_f(t)\rangle = |\psi_{\mathbf{p}}(t)\rangle$, which give the final momentum state measured at the detector. The variables $\tilde{\mathbf{p}}_0 = \mathbf{p}_0 + \mathbf{A}(t')$ and $\tilde{\mathbf{p}}_f(t) = \mathbf{p}_f + \mathbf{A}(t)$ give the initial and final velocity of the electron at the times t' and t, respectively. This leads to the amplitude $\langle \tilde{\mathbf{p}}_f | U(t,t') | \tilde{\mathbf{p}}_0 \rangle$, which can be computed using path-integral methods [31, 134]. This will work well for propagation, from t' to t, of the continuum electrons in a laser field and Coulomb potential, but one should note that the bound states of the system have not been explicitly included in the above-stated closure relation. Despite the fact that the momentum basis is complete, this formalism will break down when describing electron motion very close to the core, such as that in low-lying bound states. Hence, not explicitly including the bound states physically amounts to ignoring any transitions to bound states beyond the initial state. However, it may be the case that high lying Rydberg states that act quasi-classically are described reasonably well by this formalism, especially as in the presence of the field they will be strongly coupled with the continuum.

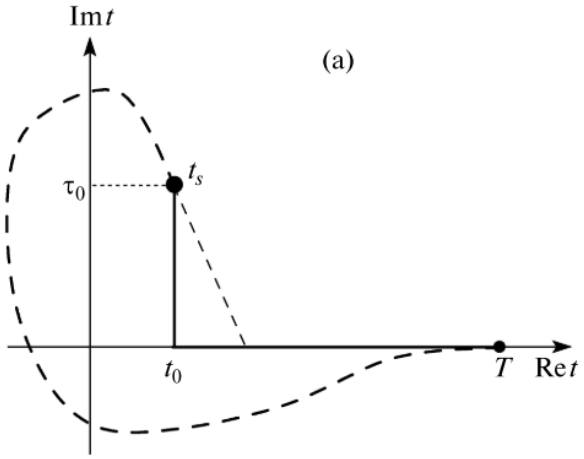

FIGURE 4.1: The integration contour in complex time, parallel to the imaginary axis and then along the real axis, is shown by the solid black line. An alternative valid contour is shown by the dashed line. Figure taken from [101].

After inserting the path integral given in Eq. (2.36), the CQSFA transition amplitude then becomes

$$M(\mathbf{p}_f) = -i \lim_{t\to\infty} \int_{-\infty}^{t} \mathrm{d}t' \int \mathrm{d}\tilde{\mathbf{p}}_0 \int_{\tilde{\mathbf{p}}_0}^{\tilde{\mathbf{p}}_f(t)} \mathcal{D}'\tilde{\mathbf{p}} \int \frac{\mathcal{D}\mathbf{r}}{(2\pi)^3} e^{iS(\tilde{\mathbf{p}},\mathbf{r},t,t')} \langle \tilde{\mathbf{p}}_0 | H_I(t') | \psi_0 \rangle \,, \quad (4.8)$$

where $\mathcal{D}'\tilde{\mathbf{p}}$ and $\mathcal{D}\mathbf{r}$ are the integration measures for the path integrals [31, 79], and the prime indicates a restriction upon the momentum integral, so all paths start and end with the initial and final momenta $\mathbf{p}_0$ and $\mathbf{p}_f$, respectively. These functional integrals can be thought of as a sum over all possible paths that the electron can take in position and momentum, between the initial and final states. The action in Eq. (4.8) is given by

$$S(\tilde{\mathbf{p}}, \mathbf{r}, t, t') = I_p t' - \int_{t'}^{t} [\dot{\mathbf{p}}(\tau) \cdot \mathbf{r}(\tau) + H(\mathbf{r}(\tau), \mathbf{p}(\tau), \tau)] \mathrm{d}\tau, \quad (4.9)$$

and the Hamiltonian by

$$H(\mathbf{r}(\tau), \mathbf{p}(\tau), \tau) = \frac{1}{2} [\mathbf{p}(\tau) + \mathbf{A}(\tau)]^2 + V(\mathbf{r}(\tau)). \quad (4.10)$$

Given that the time t' will be complex, as it is in the SFA, we must choose a contour that connects t' to the real final time t, see Fig. (4.1). We compute the action along a two-pronged contour, and perform a series of approximations. The first part of the

contour is taken to be parallel to the imaginary-time axis, going from $t' = t'_r + it'_i$ to t'_r. The second part of the contour is chosen to be along the real time axis, from t'_r to t. Physically, the former and the latter arm of the contour describe tunnel ionisation and the continuum propagation, respectively. The action then reads

$$S(\tilde{\mathbf{p}}, \mathbf{r}, t, t') = S^{\mathrm{tun}}(\tilde{\mathbf{p}}, \mathbf{r}, t'_r, t') + S^{\mathrm{prop}}(\tilde{\mathbf{p}}, \mathbf{r}, t, t'_r), \tag{4.11}$$

where $S^{\mathrm{tun}}(\tilde{\mathbf{p}}, \mathbf{r}, t'_r, t')$ and $S^{\mathrm{prop}}(\tilde{\mathbf{p}}, \mathbf{r}, t, t'_r)$ give the action along the first and second part of the contour, respectively. The final solution should not depend on the contour in complex time, however, due to necessary approximations this will end up being the case. Further details on the contour and related issues such as the emergence of branch cuts can be found in the literature [61, 90, 94, 96, 100, 101]. We assume the electrons momentum $\mathbf{p}_0$ to be approximately constant in the first arm of the contour. We make this approximation due to the difficulty of solving the equations of motion for the tunnel trajectory, which requires complex trajectories that may encounter branch cuts and has divergent initial conditions. The explicit expressions for S^{tun} and S^{prop} are

$$S^{\mathrm{tun}}(\tilde{\mathbf{p}}, \mathbf{r}, t'_r, t') = I_p(it'_i) - \frac{1}{2}\int_{t'}^{t'_r} [\mathbf{p}_0 + \mathbf{A}(\tau)]^2 \, \mathrm{d}\tau - \int_{t'}^{t'_r} V(\mathbf{r}_0(\tau))\mathrm{d}\tau, \tag{4.12}$$

where $\mathbf{r}_0$ is defined by

$$\mathbf{r}_0(\tau) = \int_{t'}^{\tau} (\mathbf{p}_0 + \mathbf{A}(\tau'))\mathrm{d}\tau', \tag{4.13}$$

and

$$S^{\mathrm{prop}}(\tilde{\mathbf{p}}, \mathbf{r}, t, t'_r) = I_p(t'_r) - \frac{1}{2}\int_{t'_r}^{t} [\mathbf{p}(\tau) + \mathbf{A}(\tau)]^2 \, \mathrm{d}\tau - \int_{t'_r}^{t} [\dot{\mathbf{p}} \cdot \mathbf{r} + V(\mathbf{r}(\tau))]\mathrm{d}\tau, \tag{4.14}$$

respectively. The contour for $S^{\mathrm{tun}}(\tilde{\mathbf{p}}, \mathbf{r}, t'_r, t')$ inside the barrier will be computed from the origin until the tunnel exit, which is chosen as

$$z_0 = \mathrm{Re}[r_{0\|}(t'_r)], \tag{4.15}$$

as given in [135]. In this formulation the tunnel exit is always restricted to the polarisation axis of the laser, $r_{\parallel}$. This gives the following for the continuum electron trajectory

$$\mathbf{r}(\tau) = \int_{t_r'}^{\tau} (\mathbf{p}(\tau') + \mathbf{A}(\tau'))\mathrm{d}\tau' + z_0\hat{e}_{\parallel}, \tag{4.16}$$

where $\hat{e}_{\parallel}$ is the unit vector in the direction of the laser field polarisation. It should be noted that in Eq. (4.12) the path $\mathbf{r}_0(\tau)$ approaches zero at $\tau = t'$. Hence, the singular potential will diverge. This divergence can be treated by a regularisation procedure introduced in [19, 96, 101], where the action can be matched to the asymptotic form of the atomic wavefunction.

The above-stated equation will be solved by the stationary-phase method. In the CQSFA, we must seek solutions not only for the ionisation time t' but also for the intermediate position and momentum $\mathbf{r}(\tau)$ and $\mathbf{p}(\tau)$, so that the action given by Eq. (4.9) is stationary. This gives the equation

$$\frac{[\mathbf{p}(t') + \mathbf{A}(t')]^2}{2} + \dot{\mathbf{p}}(t') \cdot \mathbf{r}(t') + V(\mathbf{r}(t')) = -I_p, \tag{4.17}$$

related to the energy conservation upon tunnel ionisation, and

$$\nabla_r S(\tilde{\mathbf{p}}, \mathbf{r}, t, t') = 0 \implies \qquad \dot{\mathbf{p}} = -\nabla_r V(\mathbf{r}(\tau)), \tag{4.18}$$

$$\nabla_p S(\tilde{\mathbf{p}}, \mathbf{r}, t, t') = 0 \implies \qquad \dot{\mathbf{r}} = \mathbf{p} + A(\tau), \tag{4.19}$$

which describe the dynamics of the electron in the continuum from t_r' to t.

In our publication [102], we found a simplification to the action based on the fact we were using the Coulomb potential. Given that $V(r) = -C/r$ we find

$$\mathbf{r} \cdot \dot{\mathbf{p}} = -\mathbf{r} \cdot \nabla_r V(r) = V(r). \tag{4.20}$$

Hence, Eq. (4.20) can be substituted into Eq. (4.14) to simplify it. This yields

$$S^{\mathrm{prop}}(\tilde{\mathbf{p}}, \mathbf{r}, t, t_r') = I_p(t_r) - \frac{1}{2}\int_{t_r'}^{t} [\mathbf{p}(\tau) + \mathbf{A}(\tau)]^2 \, d\tau - 2\int_{t_r'}^{t} V(\mathbf{r}(\tau)))d\tau. \tag{4.21}$$

This resembles the virial theorem, for which an analogous relationship between kinetic

and potential energy can be derived. A similar result was obtained in [108]. Similarly, in Eq. (4.17) the potential is problematic as it is divergent but we can substitute it for $\dot{\mathbf{p}}(t') \cdot \mathbf{r}(t')$,

$$\frac{[\mathbf{p}(t') + \mathbf{A}(t')]^2}{2} + 2\dot{\mathbf{p}}(t') \cdot \mathbf{r}(t') = -I_p, \tag{4.22}$$

where $\mathbf{p}_0 = \mathbf{p}(t')$ is the initial momenta. Then, as given in Eq. (4.12), we have approximated the momentum to be fixed. This means $\dot{\mathbf{p}}(t') \to 0$ in Eq. (4.22), which leads to

$$\frac{1}{2}\left[\mathbf{p}_0 + \mathbf{A}(t')\right]^2 + I_p = 0. \tag{4.23}$$

Despite the fact the potential is not in the ionisation equation, it is included in the equations of motion (4.18) and (4.19) and in the action (4.14), which are solved for a specific final momentum $\mathbf{p}_f$ and $t \to \infty$. The ionisation time t'_{ec} associated with an event e occurring in a cycle c is obtained analytically by solving the saddle-point Eq. (4.23). For clarity, we will employ this notation instead of the index s in the SFA times in Eq. (4.4). As before we can invert the ionisation equation, Eq. (4.23), and obtain an explicit solution for time. This yields

$$t'_{ec} = \frac{2\pi c}{\omega} \pm \frac{1}{\omega} \arccos\left(\frac{-p_{0\parallel} \mp i\sqrt{2I_\mathrm{p} + p_{0\perp}^2}}{2\sqrt{U_\mathrm{p}}}\right), \tag{4.24}$$

where $p_{0\parallel}$ and $p_{0\perp}$ denote the components of the initial momentum parallel and perpendicular to the laser-field polarisation, respectively. Within a field cycle, each event e may be associated with a specific type of orbit. The specific solutions for orbits 1 - 4 within a particular field cycle c and parallel momentum component $p_{f\parallel} > 0$ are

$$t'_{ec} = \frac{2\pi(c+1)}{\omega} - \frac{1}{\omega} \arccos\left(\frac{-p_{0\parallel} + i\sqrt{2I_\mathrm{p} + p_{0\perp}^2}}{2\sqrt{U_\mathrm{p}}}\right), \tag{4.25}$$

$$t'_{e'c} = \frac{2\pi c}{\omega} + \frac{1}{\omega} \arccos\left(\frac{-p_{0\parallel} - i\sqrt{2I_\mathrm{p} + p_{0\perp}^2}}{2\sqrt{U_\mathrm{p}}}\right) \tag{4.26}$$

with $e = 1, 4$ and $e' = 2, 3$. One should note that although t_{1c} and t_{4c} are given by the same equation, Eq. (4.25), and also t_{2c} and t_{3c} are given by Eq. (4.26), the times differ, due to the distinct *initial* momenta within each pair. For $p_{f\parallel} < 0$, the situation reverses,

so that t'_{ec} is given by Eq. (4.26) and the remaining times by Eq. (4.25).

The initial momenta are computed by solving Eqs. (4.18) and (4.19), with the tunnel exit as an initial position and the final momenta as a "limit" condition. This method does not explicitly parametrise the initial momenta in terms of the final, but enables each orbit's initial momentum to be calculated for any given final momentum. This makes it much easier to disentangle the momentum distributions for each orbit, which gives a unique insight into the dynamics.

Using the SPA for path integrals, as presented in Sec. 2.3, the Coulomb corrected transition amplitude becomes

$$M(\mathbf{p}_f) \propto -i \lim_{t\to\infty} \sum_s \left\{ \det \left[\frac{\partial \mathbf{p}_s(t)}{\partial \mathbf{r}_s(t_s)} \right] \right\}^{-1/2} \mathcal{C}(t_s) e^{iS(\tilde{\mathbf{p}}_s, \mathbf{r}_s, t, t_s))}, \tag{4.27}$$

where t_s, $\mathbf{p}_s$ and $\mathbf{r}_s$ are determined by Eqs. (4.18)-(4.23) and $\mathcal{C}(t_s)$ is given by Eq. (4.6). In practice, we employ the stability factor $\partial \mathbf{p}_s(t)/\partial \mathbf{p}_s(t_s)$, which is obtained using a Legendre transformation. The action will remain the same as long as the electron starts from the origin. Eq. (4.27) is normalised so that the SFA transition amplitude is obtained in the limit of vanishing binding potential. Throughout, we consider the electron to be initially bound in a $1s$-state. For details, we refer to [79].

4.2.1 Solution Method

Given that we solve the inverse problem, where all parameters are found by specifying the final momentum as a limit condition, this makes finding a solution tricky and very precise initial starting guesses are required for the solver. This issue is tackled by using a couple of approaches. A step-by-step account of how the problem is solved is given below:

1. **Iteratively solve using SFA as starting point:** For some specific starting point(s), which have been determined to be 'well behaved' we solve the problem iteratively. First, we set the Coulomb coupling C to zero and use solutions of the SFA as a starting point for the saddle point equations, incrementally increasing the Coulomb coupling, inputting the previous solution as a initial guesses for each iteration.

2. **Propagate initial conditions through momentum grid:** Solutions of the saddle point equations are propagated through the radial grid of final momenta by using points that have already been solved as initial starting guesses for adjacent points in a grid and iterating this process. Degeneracies in the CQSFA orbits can be exploited to make this process easier and enable the solutions of one orbit be used as initial guesses for another. This will be described in more detail in Chapter 7.

3. **Calculate Action:** Using the grid of the now fully solved saddle-point-equation solutions, we use these values to calculate the integrals in the action. Care must be taken about the Coulomb singularity.

4. **Calculate and combine amplitudes using the saddle-point approximation:** Now plugging the action into the saddle-point approximation, the prefactors and transition amplitudes can be computed for each orbit and these can be added together in any combination to investigated the interference patterns. The final transition amplitude is a combination of all the transition amplitudes relating to each orbit.

Despite the difficulty in finding solutions, this problem is very parallelisable and without much optimisation can produce PADs much more quickly than equivalent highly optimised software that solves the full TDSE [125].

Chapter 5

Interference in the CQSFA - Electron Holography

In this chapter, all orbits are solved and investigated and a full analysis of all the types of holographic interference is performed along with an in-depth comparison with results obtained by solving the *ab-initio* solution to the TDSE. These results were originally presented in the papers [102, 104]. The chapter layout is as follows. In Sec. 5.1 the main types of orbits in the CQSFA are studied and analytic estimates for the PAD side-lobes (5.1.1) are provided, showing they are not just part of the interference structure of the spider-like pattern. In Sec. 5.2, an analysis of the near-threshold patterns in ATI is performed and linked to several intra-cycle holographic structures (Sec. 5.2.1). Then, in Sec. 5.3 a comparison is made with PADs solved using the full TDSE solution. Finally, in Sec. 5.4 the main conclusions are stated.

Orbit	$z_0 p_{f\parallel}$	$p_{f\perp} p_{0\perp}$
1	+	+
2	-	+
3	-	-
4	+	-

TABLE 5.1: Summary of the main types of orbits identified for Coulomb-corrected strong-field approaches. The + and - signs on each cell indicate a positive or negative product, respectively.

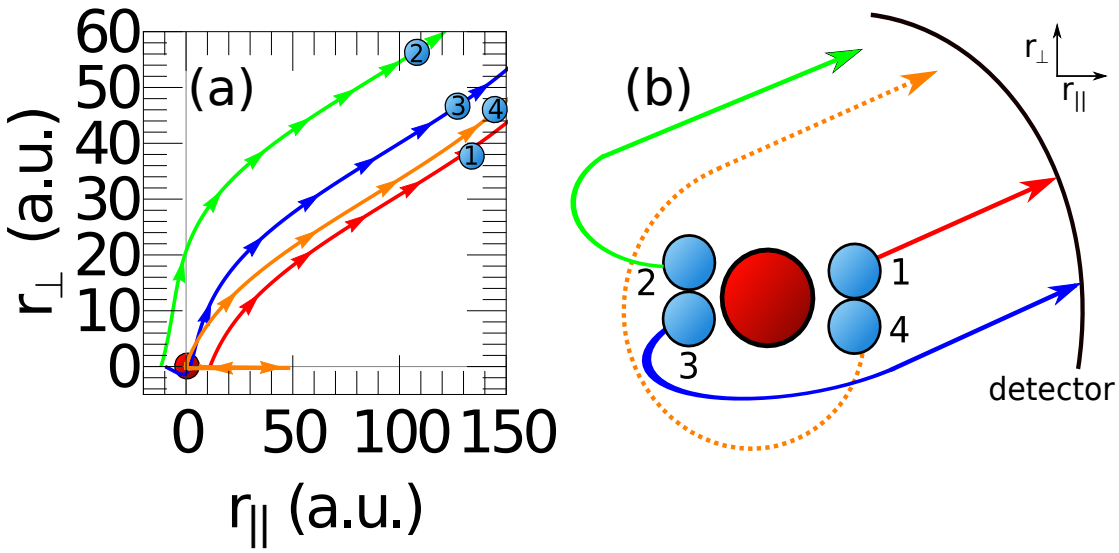

FIGURE 5.1: Panel (a) shows the trajectory after the tunnel exit for each orbit, for a final momentum of $\mathbf{p}_f = (1.66, 0.702)$ a.u. Panel (b) shows a schematic representation of the four orbit's trajectories, where the features have been exaggerated for emphasis. The ion has been marked with a red circle.

5.1 Orbit Types and Characteristics

In the following we will have a closer look at the orbits that exist in the CQSFA. In Coulomb corrected models of ATI, such as the CQSFA, there are four types of orbits for any given momenta. Example trajectories after the tunnel exit and a schematic representation are shown in Fig. (5.1). The standard characterisation is based on the tunnel exit z_0 and the initial transverse momenta $p_{0\perp}$ with regard to the final parallel and transverse momenta $p_{f||}$ and $p_{f\perp}$, respectively [99]. For orbit 1, z_0 and the electron's final momentum $p_{f||}$ point in the same direction, i.e., $z_0 p_{f||} > 0$, and its initial and final transverse momenta have the same sign, i.e., $p_{0\perp} p_{f\perp} > 0$. Orbits 2 and 3 have their tunnel exit on the opposite side, so that $z_0 p_{f\perp} < 0$. Orbit 2 has its initial transverse momentum in the same direction as the final momentum ($p_{0\perp} p_{f\perp} > 0$), while for orbit 3 these momentum components point in opposite directions ($p_{0\perp} p_{f\perp} < 0$). Finally, orbit 4 has its tunnel exit on the same side as $p_{f||}$, but the initial and final transverse momenta are in opposite directions, i.e., $p_{0\perp} p_{f\perp} < 0$. This characterisation leads to a discontinuity in the solution of t_{ec} associated with each orbit, see Fig. (5.2) panel (a). However, keeping t_{ec} continuous would change the behaviour of the orbits according to this classification, which we would like to avoid. A summary of these conditions is

provided in Table 5.1.

One of the main differences between the SFA and CQSFA is that momenta do not remain constant in the latter. Hence, one can no longer assume that two orbits with the same initial momenta will interfere, as they may reach the detector with different final momenta.

In Eq. (4.24) the ionisation times have been explicitly parametrised in terms of the initial momenta. For $p_{f\parallel} > 0$, the times t_{1c} associated with orbit 1 and 4 are given by Eq. (4.26), while those related to orbits 2 and 3 are given by Eq. (4.25). Differences between the times t_{1c} & t_{4c}, and t_{2c} & t_{3c} come from the fact that the trajectories have different initial momenta. For $p_{f\parallel} < 0$, the situation reverses, i.e., t_{1c} and t_{4c} are given by Eq. (4.25) and the remaining times by Eq. (4.26).

In Fig. (5.2)(a), we display the real parts of the ionisation times as functions of the electron's final momentum $p_{f\parallel}$ parallel to the laser-field polarisation, which are associated to the classical trajectories of an electron in the field. We can see from Fig. (5.2)(a) that the real part of the time of ionisation for the CQSFA is quite similar to the SFA but is shifted down. Physically, this can be understood as follows: For orbit 1, the electron is decelerated by the Coulomb potential, so that it will need a higher momentum $\mathbf{p}_0$ to escape and reach the detector with a specific momentum $\mathbf{p}_f$. This means that the laser field must compensate the above-mentioned deceleration and that the electron's release time t_{1c} will move away from the field extremum towards the crossing. In contrast, for orbits 2 and 3 the Coulomb potential accelerates the electron and it must acquire less energy from the field to achieve a final momentum $\mathbf{p}_f$. Thus, the electron is released with a lower momentum and its release times must approach the previous field extremum. For orbit 4, the situation is totally different, as the orbit undergoes a very close return to the Coulomb potential. This means that small differences in the initial momenta lead to large differences in the final momentum. This is due to the scattering off the core, which will cause all initial values to be very flat when plotted with respect to the final momenta. Given that the initial momenta does not vary significantly with the final momentum the real part of the ionisation time will not either, as it is computed using the initial momenta. As $|p_{f\parallel}|$ increases, the first three times tend in different ways to their SFA counterparts, while orbit 4 does not do this at all. In fact orbit 4 becomes

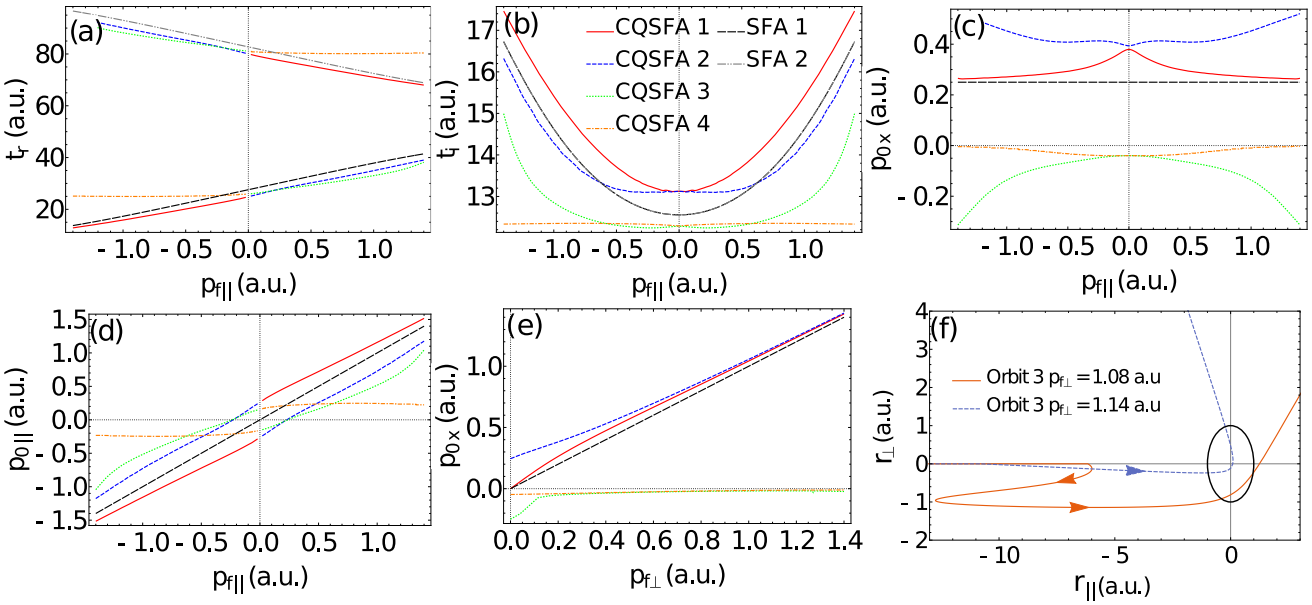

FIGURE 5.2: In panels (a) and (b), we plot the real and imaginary part of the ionisation times obtained for the CQSFA orbits as functions of the final momentum component $p_{f\parallel}$ parallel to the laser-field polarisation, compared with their SFA counterpart (black and grey lines in the figure). Panels (c) and (d) show the initial perpendicular and parallel momentum components $p_{0\perp}$ and $p_{0\parallel}$ for all the CQSFA orbits, respectively, as functions of the final parallel momentum $p_{f\parallel}$. In panels (a) to (d), the final perpendicular momentum was chosen as $p_{f\perp} = 0.25$ a.u.. Panel (e) presents the initial perpendicular momentum $p_{0\perp}$ as a function of the final perpendicular momenta $p_{f\perp}^{(i)}$, $i = 1, 2, 3, 4$, for a fixed value of $p_{f\parallel} = 0.25$ a.u. Note, the plot legend in panel (b) also applies to panels (a), (c), (d) and (e), for reference, from panels (a) to (e) the SFA solution is provided as the black dotted-dashed line. Panel (f) shows orbit 3 for two values of the initial perpendicular momentum. For a final momentum $(p_{f\parallel}, p_{f\perp}) = (0.668 \text{ a.u.}, 1.082 \text{ a.u.})$ and an initial momentum of $(p_{0\parallel}, p_{0\perp}) = (0.563 \text{ a.u.}, -0.043 \text{ a.u.})$ (solid orange line), the electron deflected by the potential, while for $(p_{f\parallel}, p_{f\perp}) = (0.672 \text{ a.u.}, 1.144 \text{ a.u.})$ and an initial momentum of $(p_{0\parallel}, p_{0\perp}) = (2.713 \text{ a.u.}, -0.041 \text{ a.u.})$ (dashed blue line), the electron undergoes a hard collision with the core. The black circle in the figure marks the region for which the collision occurs. Electron momentum distributions computed with the SFA for hydrogen (I_p = 0.5 a.u.) in a driving field of intensity $I = 2 \times 10^{14}$ W/cm^2 and wavelength of $\lambda = 800$ nm, which gives an angular frequency $\omega = 0.057$ a.u.

more like a rescattered SFA orbit, we will discuss this in more detail in Chapter 7. The time t_{1c} tends monotonically towards the SFA value, while the ionisation times t_{2c} and t_{3c} first deviate from their SFA counterparts. This is because an electron along orbit 1 may escape with vanishing transverse momentum $p_{0\perp} = 0$, while for orbits 2 and 3 this would either trap the electron or lead to a hard rescattering with the core in case the $p_{0\|}$ is low.

In Fig. (5.2)(b), we show the imaginary parts $\mathrm{Im}[t_{ec}]$, with $e = 1, 2, 3, 4$, of these solutions. An overall feature is that they are no longer identical as in the SFA. This is expected, as $\mathrm{Im}[t_{ec}]$ is roughly related to the width of the effective potential barrier through which the electron tunnels [136]. The Coulomb potential will make this barrier different for orbits 1, 2, 3 and 4, while in the SFA it is determined solely by the field. Qualitatively, $\mathrm{Im}[t_{1c}]$ behaves in the same way for the SFA and CQSFA, with a clear minimum at $p_{f\|} = 0$. This is not surprising, as the topology of orbit 1 is similar in both cases. In contrast, for orbit 2, $\mathrm{Im}[t_{2c}]$ exhibits a maximum at $p_{f\|} = 0$ and two symmetric minima at non-vanishing momenta. This effect is quite robust, and contributes to the appearance of side-lobes in the PADs. For orbit 3, $\mathrm{Im}[t_{3c}]$ is much flatter and smaller than for the other two orbits, which indicates a high escape probability over a large momentum range. This is consistent with the electron being accelerated for a longer time, in comparison to orbit 2. Similar to what occurs for orbit 2, $\mathrm{Im}[t_{3c}]$ exhibits a local maximum for $p_{f\|} = 0$ and two symmetric minima at $p_{f\|} \neq 0$. There is however a sharp increase in $\mathrm{Im}[t]$ for higher parallel momenta, as hard collisions with the core start to take place [see Fig. (5.2)(f)]. This regime will be discussed in more detail in Chapter 7. The behaviour of orbit 4 is more extreme than that of orbit 3, as $\mathrm{Im}[t_{4c}]$ is almost totally flat also with a very slight minimum.

In Fig. (5.2)(c), we plot the initial perpendicular momenta as functions of the final parallel momentum. For orbit 1, if the electron escapes along the polarisation axis, it will need an initial momentum corresponding to the classical escape velocity $\sqrt{2C/|z_0|}$, determined by setting $|V(z_0)| = v_{0\|}^2/2$. For non-vanishing transverse momentum, analytical estimates for the escape velocity are non-trivial. However, the figure clearly shows a monotonic decrease in $p_{0\perp}^{(1)}$. This is because for $p_{f\|} = 0$, the orbit will also have nearly zero initial parallel momenta and must compensate in the initial perpendicular in

order to escape. Orbits 2 and 3, go around the core from behind in opposite directions. Thus, orbit 2 has a positive initial perpendicular momenta while, for orbit 3 it is negative. Orbits 2 and 3, need a much lower momentum to escape and reach the detector along the polarisation axis as they are accelerated by passing the Coulomb potential. Thus, $|p_{0\perp}|$ increases with final parallel momentum. Orbit 4 like orbit 3 has a negative initial perpendicular momentum. It remains quite flat as with the other parameters, slightly decreasing with the final parallel momenta. It does this because a lower initial perpendicular momenta leads to a closer pass by the Coulomb potential giving the orbit a higher final parallel momenta.

Similar features are observed in Fig. (5.2)(d), where $p_{0\parallel}^{(e)}$, $e = 1, 2, 3, 4$ are displayed as functions of $p_{f\parallel}$. Importantly, orbit 1 never crosses the $p_{f\parallel}$ axis. This is because the electron starts with the atomic potential directly behind it. Hence, it must have a large enough initial parallel velocity ($\sqrt{2C/|z_0|}$) to be able to escape. Furthermore, for orbits 2 and 3, the SFA solution $p_{0\parallel} = p_{f\parallel}$ is approached from below, while for orbit 1 it is approached from above. This is a consequence of the electron being accelerated by the potential along the two former orbits, and decelerated along the latter. The acceleration is more significant for orbit 3, in agreement with the previous plots. The critical behaviour of this orbit is also shown in Fig. (5.2)(e) in which $p_{0\perp}$ is plotted as function of its final value $p_{f\perp}$. For orbit 4 $p_{0\parallel}$ remains approximately constant, this value of $p_{0\parallel}$ will lead to a laser driven collision. Note that $p_{0\parallel}$ for orbit 4 is always less than the value for orbit 1, which escapes the influence of the potential. As long it is small enough so that a laser driven recollision occurs, the initial parallel momentum $p_{0\parallel}$ has less effect on the final momenta than the initial perpendicular momentum $p_{0\perp}$ for orbit 4. This is because changing $p_{0\parallel}$ slightly alters the velocity with which the orbit recollides, but $p_{0\parallel}$ is small with respect to the recollision velocity picked up in the laser field and the Coulomb potential. In contrast, $p_{0\perp}$ controls how close the orbit passes by the Coulomb potential, thus can strongly effect the final momenta. For orbits 1 and 2, the SFA value is reached when the momentum increases, but this does not happen for orbit 3 or 4. The recolliding nature of orbits 3 and 4 and the link between the CQSFA orbits and both direct and high-order ATI trajectories will be investigated in more detail in Sec. 7.

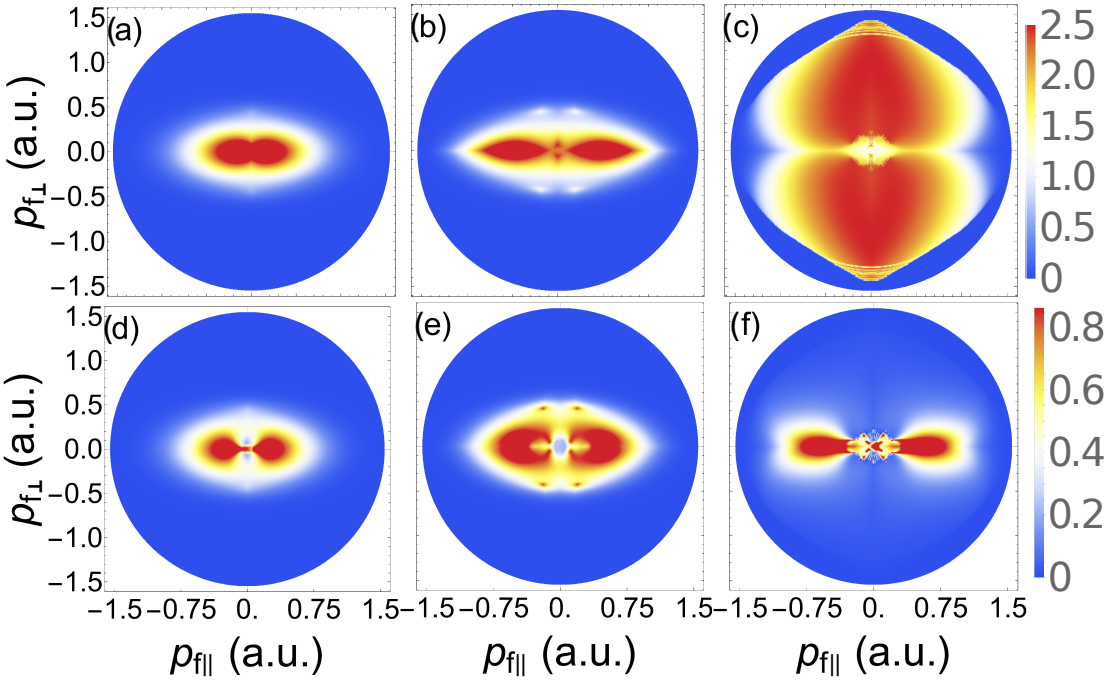

FIGURE 5.3: Single-orbit angle-resolved probability distributions plotted in arbitrary units and computed for the same field and atomic parameters as in Fig. (5.2). The left, middle and right columns correspond to orbit 1, 2 and 3, respectively. The upper panels have been computed using solely the actions, while in the lower panels we have included the prefactors.

5.1.1 Single-orbit distributions and side-lobes

In Fig. (5.3) and (5.4) we plot the PADs computed using a single orbit. In Fig. (5.3) we consider orbits 1-3, the upper panels include only the influence of the action, while in the lower panels we include the whole prefactor, given by the stability factor multiplied by $\mathcal{C}(t_s)$ in Eq. (4.27). Overall, we see the presence of side-lobes for the contributions of orbits 1 and 2. They mainly stem from the imaginary part of the action [Figs. (5.3)(a) and (b)] but are enhanced by the prefactors [Figs. (5.3)(d) and (e)]. Furthermore, in Fig. (5.3)(c), one can see that the contributions of orbit 3 decay more slowly than those of the two other orbits. Around 1.2 a.u. there is a sharp decay in probability, as above a certain energy an electron leaving along orbit 3 starts to backscatter. This prominence is however obfuscated by the influence of the prefactor, which causes a huge suppression of the probability density away from the $p_{f\parallel}$ axis [Figs. (5.3)(f)]. This led to this orbit being neglected in previous studies on the CQSFA [80]. In Fig. (5.4) we plot the single orbit PADs for only orbit 4, without and with the prefactor, panel (a) and (b), respectively. The contribution of orbit 4 decays even more slowly than orbit

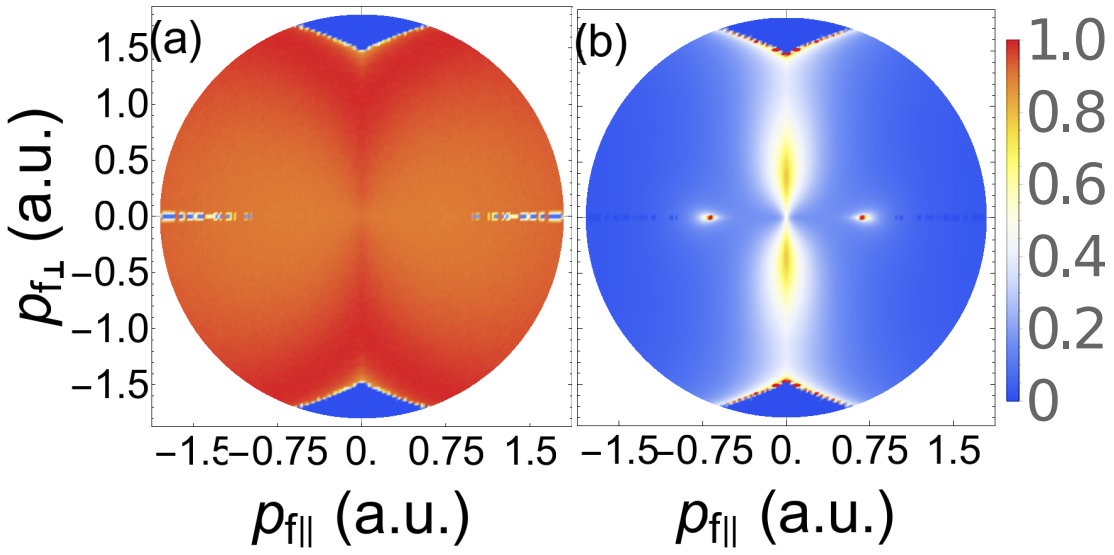

FIGURE 5.4: Single-orbit angle-resolved probability distributions, for orbit 4, plotted in arbitrary units and computed for the same field and atomic parameters as in as in Fig. (5.2). The left panel (a) was computed using solely the action, while the right panel (b) includes the prefactor. The panels are normalised with respect to their peak value. In panel (a) the peak value is 1.41 times that for orbit 1 in Fig. (5.3) panel (a), while for panel (b) the peak yield is 0.103 of that for orbit 1 in Fig. (5.3) panel (d).

3, so much so that it has almost no visible structure without considering the prefactor. Similar to orbit 3 there is a boundary/ cutoff for very high $p_{f\perp}$, where the probability decays very sharply. Once the prefactor is applied the PAD radically changes to lie almost entirely on the $p_{f\perp}$ axis with two off-centre spots on the $p_{f\parallel}$ axis. This will mean that the contributions orbit 3 and 4 will have little overlap so any interference will be quite weak.

The single orbit PADs are governed entirely by the imaginary part of the action, which is related to the tunnelling dynamics, and the prefactor. In the CQSFA, the imaginary part of the action reads

$$S^{\mathrm{Im}}(t',\mathbf{p},\mathbf{r}) = \left(\mathrm{I_p} + \mathrm{U_p} + \frac{1}{2}\mathbf{p}_0^2\right) t_i' + \frac{2p_{0\parallel}\sqrt{\mathrm{U_p}}\cos(\omega t_r')\sinh(\omega t_i')}{\omega} + \frac{\mathrm{U_p}\cos(2\omega t_r')\sinh(2\omega t_i')}{2\omega} - \int_{t'}^{t_r'} \mathrm{Im}[V(\mathbf{r}_0(\tau))]\mathrm{d}\tau. \tag{5.1}$$

Eq. (5.1) is plotted in Fig. (5.5)(a), for orbits 1, 2 and 3. In general, its behaviour mirrors that observed for the imaginary parts of the ionisation times. This includes it being much smaller and flatter for orbit 3 and the local minima outside the origin for

orbit 2.

The mirroring behaviour can be seen from Eq. (6.16) if one applies the low-frequency approximation [100]. This gives $\sinh(\omega t_i') \simeq \omega t_i'$ and $\sinh(2\omega t_i') \simeq 2\omega t_i'$, which are in the dominant terms. Within the same approximation, the integral over $V(\mathbf{r}_0(\tau))$ leads to an algebraic term, which may be viewed as a modified prefactor and whose influence is secondary as far as the side-lobes are concerned. It does however play an important role in the overall shape of the distributions. The calculation of the full action using the low frequency approximation is given Chapter 6.

In Fig. (5.5)(b), we plot the action $S^{\mathrm{Im}}(t_{2c}, \mathbf{p}, \mathbf{r})$ associated with orbit 2, with and without the integral over $V(\mathbf{r}_0(\tau))$ in the low-frequency approximation. In all cases, the two minima are present. Examples of single-orbit PADs computed analytically are provided in Figs. (5.5)(c) and (d). Both figures show clear side-lobes and resemble the single-orbit distribution in Fig. (5.3)(b), which has been computed numerically. However, inclusion of the integral over the binding potential in the low-frequency approximation renders the numerical and analytical single-orbit distributions strikingly similar. This similarity includes the broader shape and secondary peaks.

5.2 Interference Types

We have calculated four different types of orbit in the CQSFA, so there are six pair-wise combinations that will each give rise to different interference patterns. On top of that, restrictions on these combinations can be imposed to give rise to further interference types. These types were first presented for the CQSFA in [102, 104]. In Fig. (5.6) we show the interference types in terms of the real part t_r' of the times of ionisation. The first type, denoted A or B interference, occurs between pairs of orbits with their tunnel exit on opposite sides of the atom. This means that for $p_{f\parallel} = 0$ the difference between the values for t_r' for the two orbits will be half a laser cycle, this difference will increase or decrease for non zero $p_{f\parallel}$, see Fig. (5.6). So these interference types occur for the following combinations of orbits, 1 & 2, 1 & 3, 4 & 2 and 4 & 3. If the difference between the real part of the times of ionisation in these pairs is less than half a cycle the interference is type A, while if it is more than half a cycle the interference is type

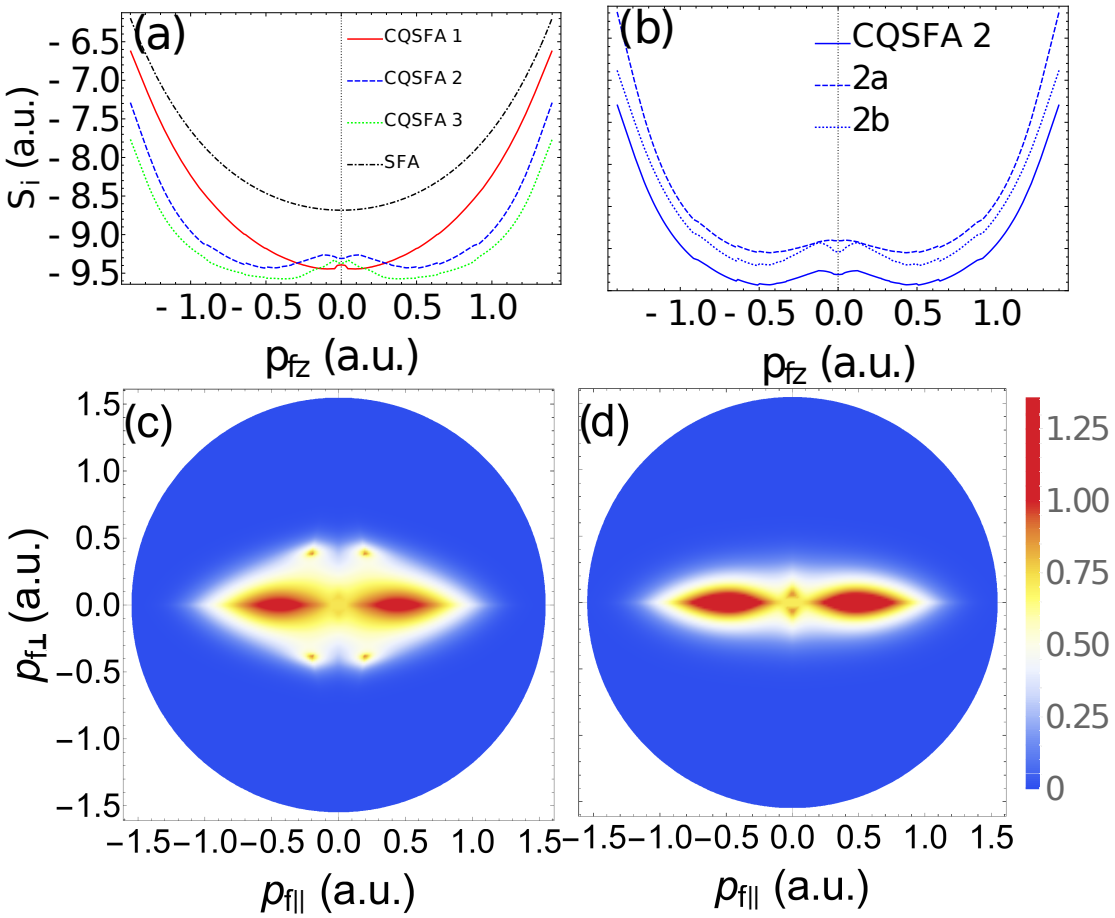

FIGURE 5.5: Panel (a) shows the imaginary parts of the actions S_i (i=1,2,3) associated to the orbits 1, 2 and 3 of the CQSFA, as functions of the final parallel momentum, computed directly from Eq. (5.1) for perpendicular momentum $p_{f\perp} = 0.05$ a.u.. For comparison, the SFA counterpart has been included. Panel (b) displays the approximate expressions obtained for orbit 2, as functions of the final parallel momentum, for the same perpendicular momentum as panel (a). The dotted line, labelled 2b, corresponds to the single-orbit action without the integral over the binding potential, and the dashed lines, labelled 2a, include this integral in the long-wavelength approximation. The solid line gives the numerical expression for Eq. (5.1). Panels (c) and (d) illustrate the PADs computed for orbit 2 without the prefactors, with and without the integral over $V(\mathbf{r}_0(\tau))$ in the long-wavelength approximation, respectively. The atomic and field parameters are the same as in the previous figures in this chapter.

Interference Type	$z_{0i}z_{0j}$	$\omega\left\|t'_{ri}-t'_{rj}\right\|$
unrestricted/ AB	$-$	$(0,2\pi)$
A	$-$	$(0,\pi)$
B	$-$	$(\pi,2\pi)$
No prime	$+$	$(0,\pi/2)$
Prime	$+$	$(3\pi/2,2\pi)$

TABLE 5.2: The different interference type possible between two orbits in the CQSFA. The first column gives the type, the second column gives a condition on the tunnel exits of the two orbits and the third column gives the restriction of the difference of ionisation times for the two orbits.

B. These two cases are both marked on Fig. (5.6). If no restrictions are applied to the above pairs then there will be a mixture of A and B interference, the type will change with the sign of $\mathbf{p}_{f\parallel}$.

For the remaining two pairs of orbits, 1 & 4 and 2 & 3 the orbits tunnel exits are on the same side and thus ionisation occurs at similar times (in the same quarter cycle). This means that the same kind of classification can not be applied as the difference is always less than half a cycle. However, an alternative type of intracycle interference exists. One of the orbits in each pair will have real part of time of ionisation time that is less than the other, e.g., in Fig. (5.6) orbit 1 ionises before orbit 4. So if this orbit (orbit 1) is delayed by a field cycle the difference between the times of ionisation will still be under a field cycle so the combination will give intracycle interference. This type of interference will be indicated by adding a prime to the label of the orbit that has been delayed by a field cycle. A brief summary of the interference types is given in Table 5.2. We consider these different types of interference for two reasons:

1. Symmetrisation sometimes performed in experiments or theory (e.g. reflection about the $p_\perp$ axis) effectively imposes such temporal restrictions (type A/ B), thus showing all case makes our result comparable to others.

2. Some interference types for a particular pair of orbits reveal structures that are obscured in the other interference types of the same pair.

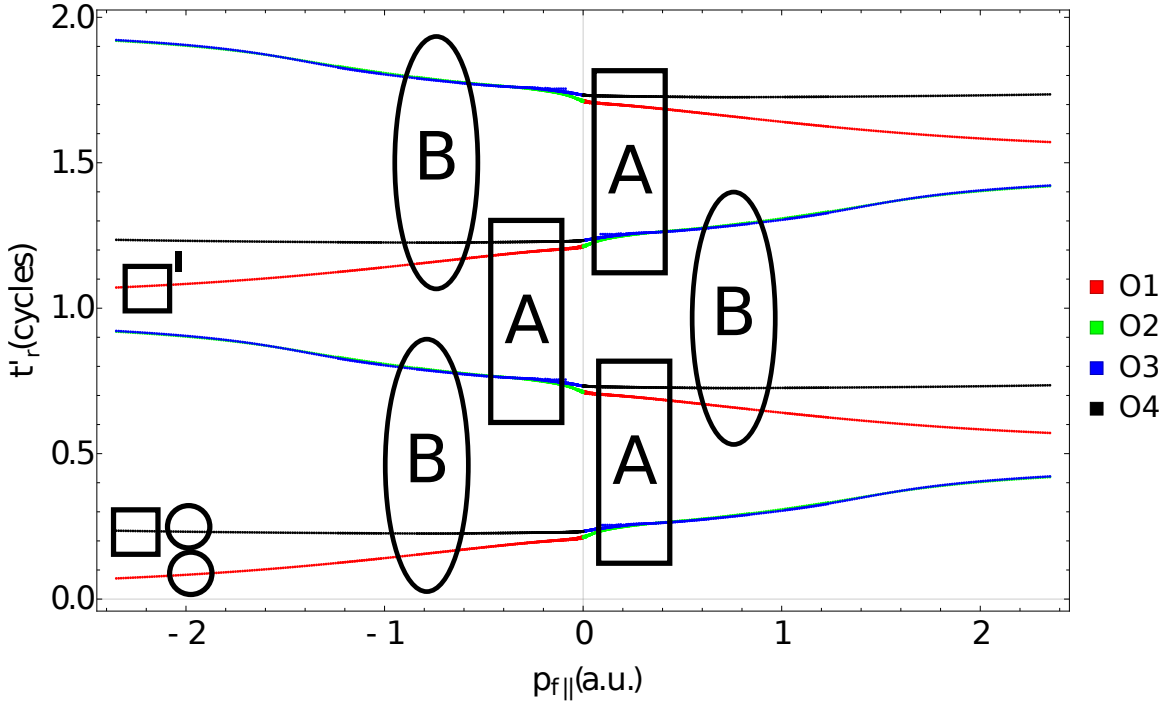

FIGURE 5.6: Schematic of the real part of the time of ionisation for all four of the orbits over two laser cycles. This is plotted against the momentum component parallel to the laser field polarisation. The orbits are labelled in the legend by Oi, where i refers to the specific orbit number. The rectangles with an A inside show example combinations of orbits that give rise to interference of type A. The ovals with a B inside show example combinations of orbits that give rise to interference of type B. The circles show an example combination of orbits that have their tunnel exit on the same side. The squares (with one primed) show an example combination of prime interference (where the primed orbit has been delayed by a field cycle). The atomic and field parameters are the same as in the previous figures in this chapter.

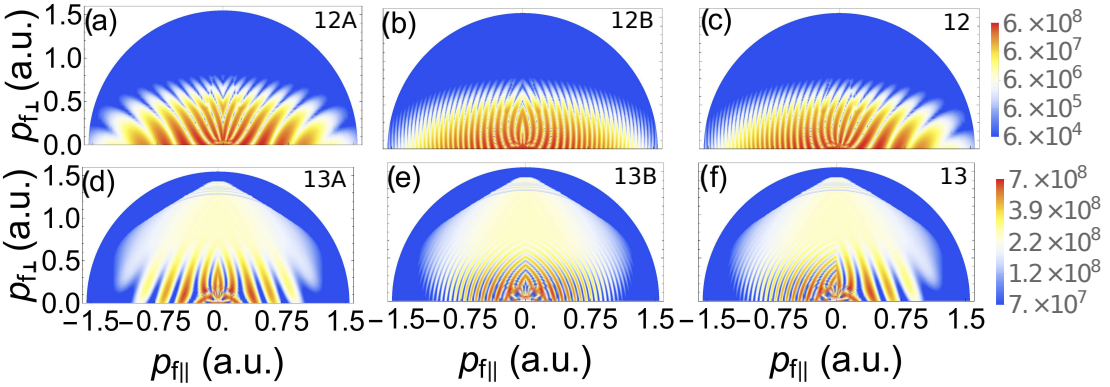

FIGURE 5.7: Photoelectron angular distributions computed in the CQSFA for times within a single cycle of the laser field and the same parameters as in the previous figures in this chapter, neglecting the prefactors. The upper and bottom row includes orbits 1 and 2, and orbits 1 and 3 as interfering trajectories, respectively. Panels (a) and (d) show type A intra-cycle interference, panels (b), and (e) present type B intra-cycle interference and panels (c), and (f) exhibit both types of interference. The PADs have been plotted in a logarithmic scale.

5.2.1 Orbits 1 to 3

Here we analyse the interference effects of the first three orbits, these have the highest overall signal so should form the main features in the final PAD. Figs. (5.7) and (5.8) exemplify the types of interference that occur in the CQSFA, with and without the full prefactor, respectively. The left, middle and right panels in both figures refer to type A, type B and no restrictions where both types will occur intracycle interference, respectively, computed as described above. The patterns obtained are more complex than those seen in the SFA, such as the distributions presented in [102], as here we are considering three interfering types of orbits. Furthermore, since the imaginary parts Im$[t_{ec}]$ differ for each type of orbit, the fringes may become blurred in specific momentum regions.

If only orbits 1 and 2 are taken [upper panels of Figs. (5.7) and (5.8)], the fringes are sharp and the fringe spacing is similar to that observed in the SFA. This is expected, as Im$[t_{1c}]$ and Im$[t_{2c}]$ are comparable and Re$[t_{1c}]$ and Re$[t_{2c}]$ follow the SFA solutions closely. The shapes of the distributions, however, are different. Specifically, for type A intra-cycle interference, we see a fan-shaped structure spreading from the origin $(p_{f\parallel}, p_{f\perp}) = (0, 0)$ [Figs. (5.7)(a) and 5.8(a)]. This structure is well known, both theoretically and experimentally. This highlights the importance of forming these

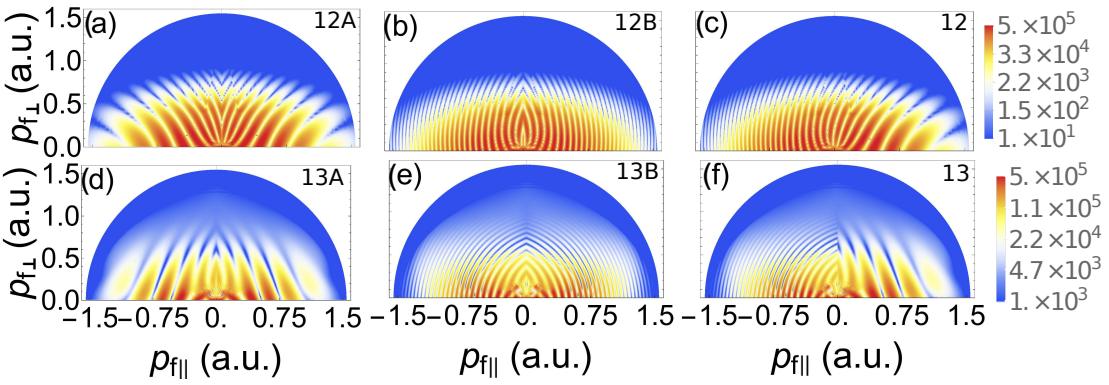

FIGURE 5.8: Photoelectron angular distributions computed in the CQSFA for times within a single cycle of the laser field and the same parameters as in the previous figures in this chapter, including the prefactors. The upper and bottom row includes orbits 1 and 2, and orbits 1 and 3 as interfering trajectories, respectively. Panels (a) and (d) show type A intra-cycle interference, panels (b), and (e) present type B intra-cycle interference and panels (c), and (f) exhibit both types of interference. The PADs have been plotted in a logarithmic scale.

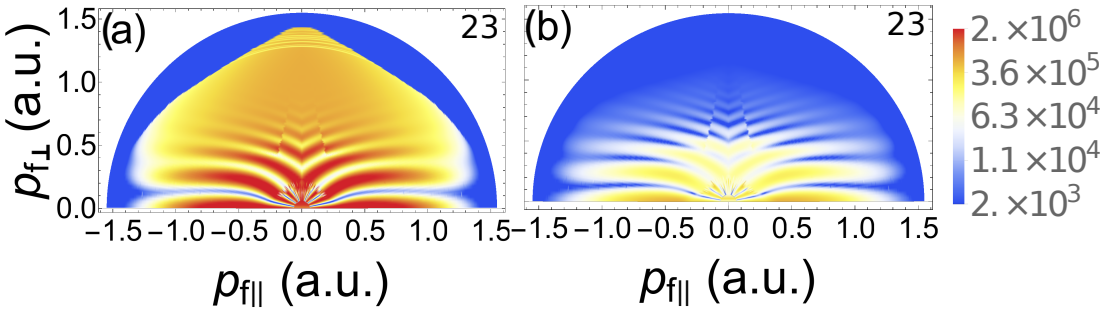

FIGURE 5.9: Photoelectron angular distributions computed in the CQSFA using orbits 2 and 3 for the same parameters as in Figs. (5.7) and (5.8) without and with prefactor [panels (a) and (b), respectively]. The PADs have been plotted in a logarithmic scale.

interference types and many experiments and theoretical results show only type A for the fan. Type B interference, shown in Figs. (5.7)(b) and 5.8(b), exhibits sharp, nearly vertical fringes, which resemble those observed for the SFA but also become distorted for low momentum regions. If both types of interference are considered, the fringes become increasingly thicker as the momenta move from the negative to the positive $p_{f\parallel}$ region. The presence of the prefactor enhances the side-lobes, but does not change these features.

The interference between orbits 1 and 3, shown in the lower panels of Figs. (5.7) and (5.8), behaves in a different way. First, the shapes of the fringes do not resemble the finger-shaped structures or those from the SFA and the side-lobes are absent. Second, if the prefactors are absent [Fig. (5.7)], they are only sharp near the $p_{f\parallel}$ axis and up to $p_{f\perp} \simeq 0.5$ a.u. For higher perpendicular momenta, the fringes are blurred and the PADs acquire the shape of the single-orbit distribution in Fig. (5.3)(c). This is due to the high probability of an electron leaving along orbit 3. In Fig. (5.8), however, one can see that the prefactor outweighs this high probability and suppresses the contribution of orbit 3 away from the $p_{f\parallel}$ axis. If the intra-cycle interference between orbits 2 and 3 is considered, Fig. (5.9), we observe a set of prominent, almost horizontal fringes diverging from a spider-like structure near the origin. A similar structure has been observed in [105] using the QTMC method. This is the spider-like structure, seen in various experimental studies [23, 66, 121–123]. The prefactor restricts the relevance of this structure to a relatively narrow momentum range close to the $p_{f\parallel}$ axis. One should note that, since these specific orbits leave in the same half cycle, the classification in A and B type interference is not applicable.

The real parts of the actions are displayed in Fig. (5.10)(a) for the three CQSFA orbits as functions of $p_{f\parallel}$. The figure shows a similar behaviour as for the SFA, with type A and B interference corresponding to thicker and finer fringes, respectively. One should note that type A interference is more sensitive to the Coulomb potential, and that, for large positive momentum, the action related to orbit 3 tends to that related orbit 1. This leads to very thick fringes in this momentum region. The real parts of ΔS_{ij}, plotted in Fig. (5.10) as a function of the deflection angle, confirms the above-mentioned trends. First, the action difference ΔS_{12} between orbit 1 and 2 tends to

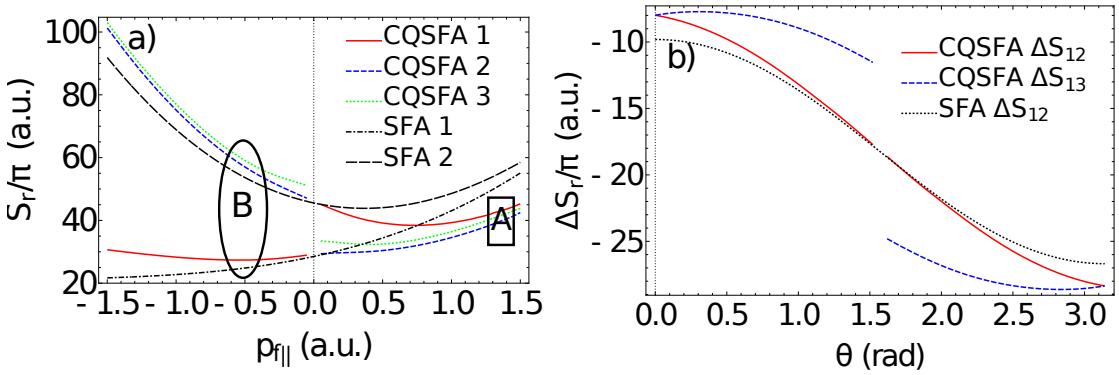

FIGURE 5.10: Panel (a) shows the real part of the action for the first three CQSFA orbits, together with their SFA counterparts, plotted as functions of the final momentum $p_{f\|}$, computed for perpendicular final momentum of $p_{f\perp} = 0.25$ a.u. As in Fig. (5.6), type A and B intra-cycle interference is indicated by squares and circles, respectively. Panel (b) displays the real part of the action differences ΔS_{12} and ΔS_{13}, together with its SFA counterpart, as functions of the deflection angle θ and energy 0.1 a.u.. The remaining parameters are the same as in the previous figures.

the SFA for perpendicular photoelectron emission, but deviates from it for other angles. This causes the vertical structures in the SFA to be distorted into a fan. In contrast, the difference ΔS_{13} agrees with its SFA counterpart at the polarisation axis, but increases with the scattering angle. This leads to the convergent fringes seen in Fig. (5.7)(d) and (5.8)(d). In all cases, there is a decrease in ΔS_{ij} as the polarisation axis is approached, which manifests itself as thicker interference fringes.

5.2.2 Adding orbit 4

Now we introduce interference effects from combing orbit 4 with all other orbits, the overall signal for orbit 4 is slightly lower so the interference fringes will be somewhat weaker. In Fig. (5.11) we plot interference patterns from combining each orbit with orbit 4, which have been neglected until now. Panel (a) shows interference between orbits 3 and 4, which gives rise to a spiral-like pattern. Including the prefactors, as shown in panel (d), causes the signal from orbit 3 to be mainly located on the $p_{f\|}$ axis and that from orbit 4 to be mostly along the $p_{f\perp}$ axis. Since there is not much overlap between these regions, the interference fringes are relatively faint.

The fringes' faintness, along with the fact they could be confused with intercycle interference rings, may explain why they have been overlooked in experiments or other theoretical computations. In panel (b) we see the interference pattern that arises from

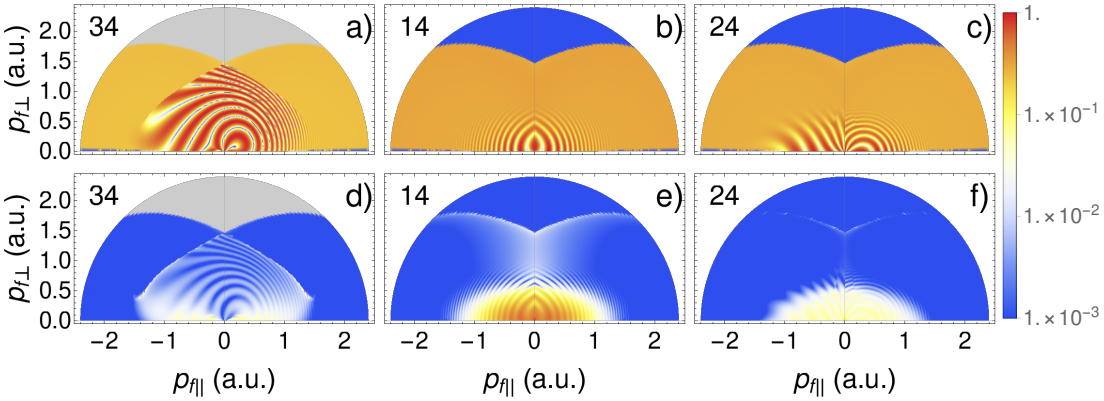

FIGURE 5.11: Photoelectron angular distributions computed using pairwise combinations of the first three types of orbits with orbit 4 to produce interference patterns. The orbit combinations are labelled in the top left corner. The upper and the lower panels neglect and incorporate prefactors, respectively. The left, middle and right column employ orbits 3 and 4, 1 and 4, and 2 and 4, respectively. All distributions are normalised by their peak intensity. A logarithmic scale has been used. The same field and atomic parameters have been used as the previous figures in this chapter. No restrictions have been assumed upon the ionisation times.

orbits 1 and 4. Once prefactors have been included (panel (e)), the V-shaped structure is very distinctive. The interference fringes are truncated circles, which also may be confused with ATI rings. Interference between orbits 2 and 4 (panels (c) and (f)) also leads to a faint V-shaped structure. The fringes for the mid-energy orbit 4 trajectories plot are fan-like on the left side and resemble off centre circles on the right. One should note that in Fig. (5.11) no restrictions have been imposed upon the ionisation times and no symmetrisation has been used. It is however common in the literature that holographic patterns are obtained by imposing such restrictions [109, 118]. In Chapter 7, we present all possible combinations of these interference types and describe them in terms of the orbit dynamics and properties such as being direct or undergoing a recollision.

5.3 Comparison with the Time-Dependent Schrödinger Equation

If the first three orbits are combined (Fig. (5.12)), a more complex pattern arises and several types of fringes are superimposed. In Figs. (5.12)(a) and (d), computed within a

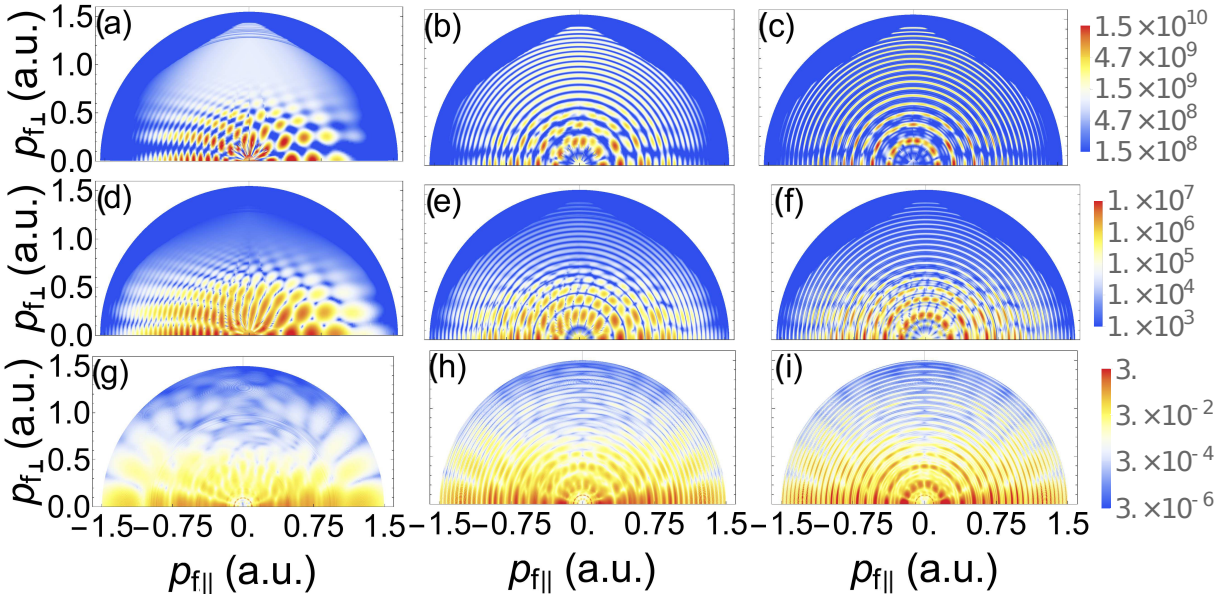

FIGURE 5.12: Photoelectron angular distributions computed in the CQSFA (first and second row) and with the TDSE (third row) for comparison. Calculated over one, two and four cycles [left, middle and right panels, respectively]. The CQSFA was calculated using orbits 1, 2 and 3 without symmetrizing with respect to the origin. The first and second panels have been computed without and with prefactors, respectively. The TDSE was calculated using the freely available software qprop [137], where a window operator was used to compute the PADs. We considered a trapezoidal pulse with a half-cycle ramp on and off and, from left to right, one, two and four cycles of constant amplitude. The remaining field and atomic parameters are the same as in the previous figures in this chapter. The panels have been plotted in a logarithmic scale.

cycle of the driving field, we see type B and type A intra-cycle interference for negative and positive parallel momentum $p_{f\parallel}$, respectively. Particularly visible are the nearly horizontal fringes caused by the interference of type 2 and 3 trajectories (the spider-like structure), and the structures related to the interference of orbits 1 and 2. This holds both in the presence and in the absence of prefactors, whose main effect is to introduce a bias towards the $p_{f\parallel}$ axis. Traces of the patterns caused by the interference of type 1 and 3 trajectories can also be identified, but they are much less prominent. This is possibly caused by their contrast being poorer than that of the other patterns [see Figs. (5.7)(f) and (5.8)(f)].

If more cycles are included [middle and right columns of Fig. (5.12)], there will be circular inter-cycle fringes dictated by Eq. (6.4), which tend towards a Dirac delta comb as the number of cycles increase. In addition, intra-cycle fringes may be either washed out or reinforced. For instance, the convergent structure due to the interference of orbits 1 and 3 is no longer visible, and the nearly horizontal fringes related to the interference of orbits 2 and 3 is weakened. In contrast, the fan-shaped structure from the interference of orbits 1 and 2, and the spider-like structure near the origin from the interference of orbits 2 and 3 are very clear, and even seem to reinforce each other. The patterns become increasingly symmetric as more cycles are included in the computation. This can be seen by comparing Figs. (5.12)(b) and (c), which has been computed for two cycles, with Figs. (5.12)(e) and (f), for which four cycles have been incorporated.

When comparing the full CQSFA results with the TDSE [bottom row of Fig. (5.12)] we find good qualitative agreement for near-threshold and intermediate energies. For instance, the CQSFA reproduces the fan-shaped structure very well. Comparing panels (f) and (i), one can see that the inner ring at around 0.3 a.u. has the same number of fringes in both the CQSFA and TDSE. The subsequent rings further out also match and display very similar structure, although the TDSE fringes are slightly more blurred. This good agreement is expected as there are no hard collisions or irregular behaviour for the orbits leading to this pattern.

The spider-like patterns from the CQSFA and the TDSE also match for lower values of $p_{f\parallel}$. In fact, by comparing Figs. (5.12)(d) and (g) one can see that, for $p_{f\parallel} = -0.5$ a.u. the maxima both occur at $p_{f\perp} = 0$, 0.25, and 0.4 a.u.. However, for $|p_{f\parallel}| > 0.8$ a.u.

the TDSE fringes bend upwards while the CQSFA fringes bend slightly down. We have verified that the main reason for this difference is due to the fact that we force the trajectories in the continuum to be real, despite the fact that the during tunnelling there is a complex component. If some approximate imaginary part is included[1] in the continuum trajectories the angle of the spider- and fan-like structures agrees much better with the TDSE results. However, due to the nature of the approximation used, the signal in orbit 3 and 4 is much too high so the overall agreement gets worse. Furthermore, complex trajectories will lead to branch cuts for orbits 2, 3 and 4 in the corresponding transition amplitude [61]. These have not been properly accounted for in the current treatment, which may also contribute to the above-mentioned discrepancies. We have verified that these branch cuts also occur in the high-energy regime, for which hard collisions occur. In [61], it was shown that a correct treatment of these branch cuts is essential for modelling the low energy softly recolliding orbits that are responsible for the low-energy structure (LES) and very low-energy structure (VLES). The issue of complex trajectories and branch cuts is tackled in more detail in [98], where branch cuts are corrected for both Coulomb-free (e.g. SFA) and Coulomb-distorted (e.g. CQSFA) models, which fixes defects in the PADs. However for now, the region $|\mathbf{p}_f| < 0.1$ a.u. has been left out of the CQSFA results. In the TDSE results, a low-energy ring at around 0.1 a.u. can be seen, which can be associated with the VLES.

In addition to this there are some other features of the model that may contribute to such discrepancies. The spider-like pattern arises from the interference between orbits 2 and 3, orbit 3 is a forward scattered trajectory that may interact strongly with the core. For higher $p_{f\parallel}$ the closest approach of orbit 3 gets smaller, hence there is a larger interaction with the core, where the path integral approach is expected to break down somewhat. Furthermore, the momentum is fixed for the tunnel trajectory, hence the full effect of the atomic potential is not accounted for. In studies using much lower frequencies [23, 66, 121], the bending does not occur and the agreement with the CQSFA improves markedly.

Finally, in Fig. (5.12)(i) some faint V-shaped structures can be made out above $p_{f\perp} = 0.5$, which are not visible in the CQSFA. Previously, these fringes have been associated

[1] We kept the imaginary part constant beyond the tunnel exit, which is how it behaves in the SFA trajectories.

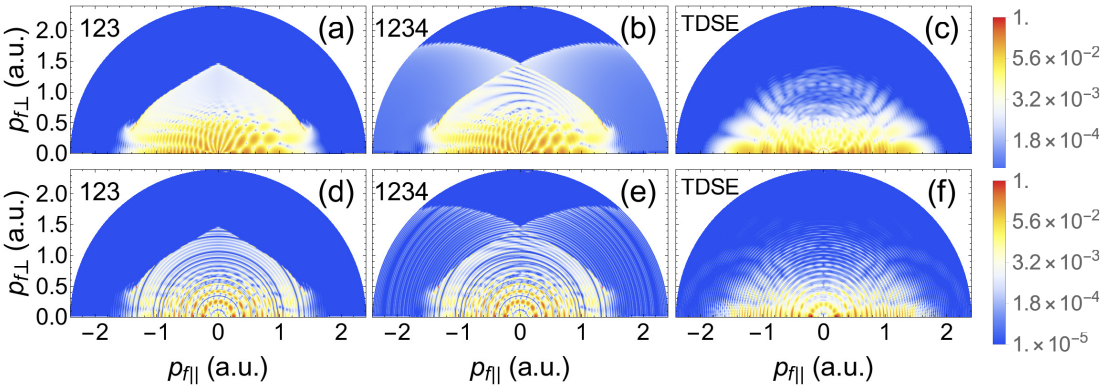

FIGURE 5.13: Full CQSFA photoelectron angular distributions calculated excluding and including orbit 4 (left and middle columns, respectively), compared with the TDSE solution (right column). The distributions in the top and bottom row have been calculated over a single and four laser cycles, respectively. The orbits included in each distribution are marked in the top left, and the prefactors have been included in all cases. The freely available software Qprop [125] was used to perform the TDSE calculation. All distributions are normalised by their peak intensity. A logarithmic scale has been used. The same field and atomic parameters have been used as in Fig. (7.1).

with interference between trajectories that may be similar to orbits 3 and 4 [64]. This suggests that orbit 4 may have some role to play in the high-energy domain, even if it is less significant than the other orbits. Some features in the TDSE such as the VLES are strongly dependent on the pulse envelope used. However, the features we focus on, namely the fan-shaped and spider-like fringes, do not change significantly with the pulse envelope.

5.3.1 Including orbit 4

If we compute the photoelectron angular distributions combining all orbits and compare them to those obtained with the coherent superposition of the first three, we can see what effect orbit 4 has. This has been done in Fig. (5.13) for one and four laser cycles, in which the CQSFA is also compared with the *ab-initio* solution of the time-dependent Schrödinger equation (TDSE) [125]. Comparing panels (a) and (b) we can see that adding orbit 4 does little to change the central fringes that are dominated by the fan- and spider-like structures. As previously mentioned, these structures are mainly due to the interference of orbits 1 and 2, and 2 and 3, respectively. However, above this

region there are clear spiral fringes, which are also visible near the $p_{f\perp}$ axis for the ab-initio solutions (see panel (c)). Additionally, the V-shaped structure is very visible in the high-energy region near the $p_{f\perp}$ axis for the CQSFA.

If four laser cycles are taken into account, as shown in panels (d) and (e), again there is little change to the main fringes. However, the coherent superposition of the spiral-like patterns and ATI rings causes chopped up fringes that appear to be interlocking. This more closely matches solutions from the TDSE in this region, shown in panel (f), where the ATI rings are not solid but exhibit some interlocking gaps. The V-shaped structure is not explicitly identifiable in the TDSE results. However, the inclusion of orbit 4 introduces a faint signal in the very high energy regions, and improves the agreement with the TDSE results.

5.4 Discussion

Using the Coulomb quantum-orbit strong-field approximation (CQSFA) [79], we have isolated many types of interference patterns and other qualitative features present in ATI momentum distributions. Apart from the widely studied near-threshold fan-shaped structure, the inter-cycle ATI interference rings and the ATI side-lobes, these features include many types of intra-cycle interference that have been overlooked in the literature. We provide direct evidence of how these patterns form, and show that they may be viewed as holographic type structures arising from different types of interfering trajectories. We follow the notation in [79, 80, 99, 100], which classifies the trajectories that reach the detector directly as type 1 orbits, those that leave from the opposite side and are deflected by the core as type 2 and 3 orbits and those that leave from the same side as the detector but are driven in the other direction towards the ion and backscatter as orbit 4. Previously overlooked holographic patterns that have been studied in this work include finer structures that arise from the intra-cycle interference of events separated by more than half a cycle, and a converging structure caused by the interference of type 1 and 3 trajectories and also interferences with newly solved orbit 4. Within many field cycles, some of these structures may be weakened, washed out or reinforced.

We have found that both orbit 3 and 4 are pivotal for many ATI features and have provided a systematic analysis of their effects. In previous studies [80, 100] orbit 3 has been neglected, possibly because the corresponding prefactor strongly reduces the overall signal. Our studies show that, outside the $p_{f\|}$ axis, this counteracts the fact that ionisation probability along this orbit is quite high. However, two peaks remain located on the $p_{f\|}$ axis which contribute to the side-lobes identified in [66]. Interference between orbits 2 and 3 produces a spider-like pattern, which can be seen superimposed on the fan-like interference pattern that occurs due to interference between orbits 1 and 2. The same spider-like pattern is seen in [105, 106], in which the quantum-trajectory Monte Carlo (QTMC) model is applied to mid-IR fields, and experimentally in [118, 121], and it is attributed to these forward scattered trajectories. The on-axis contribution of orbit 3 to the overall PADs improves the agreement with the time-dependent Schrödinger equation (TDSE) [80, 100, 118] and with experiments [22, 121, 123, 138], and can be seen in Coulomb-corrected computations in which orbit 3 has been included implicitly [106, 108]. We also provide a more rigorous discussion of the side-lobes, which are often linked with the spider-like structure and show that they are mainly determined by the behaviour of orbits 2 and 3. In particular, the imaginary part of the action mirrors the behaviour of those of the ionisation times t_{2c} and t_{3c}, which exhibit minima for non-vanishing parallel momenta. This is both verified numerically and analytically using the long-wavelength approximation. This demonstrates the side-lobes are not solely a holographic interference structure as previously supposed.

Orbit 4 was also previously neglected in the literature [80, 100, 102, 103], not only because the prefactor strongly suppresses this orbit's contribution to the $p_\perp$ axis but also due to the high precision needed in the starting guess for the initial conditions, that are required in order for the saddle point equations to converge to orbit 4. This requires the degeneracy between the orbits at particular angles to be exploited. It is found that the interference between orbits 3 and 4 gives rises to a totally new, previously neglected structure, that we have dubbed the spiral-like structure, due to its spiral shape. This structure has not been mentioned in the literature for experiments or *ab-initio* solutions of the TDSE. This could be due to the fact that the fringes are fairly weak and occur for high $p_\perp$, where ATI rings are often quite visible and it may be difficult to tell the two

apart. However, in our comparison the inclusion of orbit 4 with the other orbits gives a clear improvement with the solution of the TDSE by providing an explantation for gaps in the ATI rings that seem to be caused by the interplay of the spiral-like structure and ATI rings. This structure has a lot of scope to be used in electron holography as orbits 3 and 4 have the two highest interactions with the residual ion. These orbits will recollide with the target from different sides as well, so when applying this method to molecules the spider-like structure could be used to probe structural information. There is also a V-shaped cusp in the very highest energy region spanned by orbit 4, that cannot be seen with the same prominence in the TDSE results. However, a similar V-shaped structure was found in [64], even though, therein, this feature occurs in a different parameter range.

It is also worth noting that classical soft forward-scattered trajectories associated with the LES [58] are the same type of trajectories as orbit 3 and 4. This correspondence is possible because we are solving Newton's equations of motion for the continuum. Hence, all our orbits in the continuum have direct classical counterparts. Thus, classical or quasi-classical methods may be built from the CQSFA by performing incoherent sums over trajectories, neglecting or approximating prefactors, and ignoring sub-barrier corrections.

Furthermore, we make a detailed assessment of intra-cycle interference, and the quantum-orbit analysis in this work strongly suggests that the conditions derived in [100] are only valid for high momenta and orbits 1 and 2. This is because, in [100], the imaginary parts of the times related to orbits 1 and 2 are set to be equal and their momenta at the tunnel exit is chosen to be equal to their final momenta. These assumptions hold in the SFA and are good approximations for high momenta, as fast electrons are less influenced by the Coulomb potential. This is consistent with our analysis, which shows that the initial momenta $\mathbf{p}_0^{(1)}$, $\mathbf{p}_0^{(2)}$ and the ionisation times t_{1c} and t_{2c} tend to their SFA counterparts in this regime. For momenta close to the threshold, however, these assumptions no longer hold. Additionally, one should be careful considering interference between orbit 1 and 2 when $p_{0\perp} = 0$, as orbit 2 cannot have zero initial perpendicular momenta or it will undergo a hard collision with the parent ion. For orbit 3 and 4, the conditions in [100] are not applicable in any momentum range, as they behave in

a very different way. Apart from having much larger tunnel probabilities throughout, which implies a much smaller $\mathrm{Im}[t_{3c}]$ and $\mathrm{Im}[t_{4c}]$, they do not tend to the SFA as the momentum increases. However, the prefactors suppress the orbits over a wide range of scattering angles, leaving most of the signal concentrated near to the $p_{f\parallel}$ axis for orbit 3 and near to the $p_{f\perp}$ axis for orbit 4.

This analysis is greatly facilitated by how the CQSFA is implemented. While our method is similar to other approaches such as the trajectory-based Coulomb-corrected strong-field approximation (TCSFA) [99, 100] and the QTMC model [105, 106, 108], there are some key differences. The TCSFA and the QTMC method solve the forward problem. Since it is not known what the final momentum will be, given a particular starting momentum, one must use large initial momentum regions in order to ensure the final momentum region of interest is completely covered by orbits of all types. Additionally, the final momenta must be binned in order to determine which orbits will interfere. Thus, a high density of trajectories with different initial momenta must be used to ensure a sufficient number of trajectories of each type end up in each bin. This means that many trajectories, typically $10^8 - 10^9$, with different initial momenta must be run before each bin is sufficiently populated and interference patterns can be resolved. Furthermore, a uniform spread of initial momenta may under sample specific types of trajectories. This is particularly true for type 3 and 4 orbits, whose initial momenta are strongly bunched close to the parallel momentum axis. In contrast, the CQSFA solves the inverse problem, so that for each point in final momentum there are four well defined orbits and we only need to calculate as many points as the resolution dictates. This method is more in-keeping with a calculation of a quantum transition amplitude, where first the initial and final states are selected and can be calculated by summing all the relevant paths between the two states, as opposed to setting an ensemble initial conditions and semi-classically propagating it to a final state and then summing solutions that are close to the final state selected. In addition, the TCSFA has caustics that are made worse both by including sub-barrier Coulomb corrections and when orbit 3 or 4 are included, and which make the interference patterns less clear [100]. This could be due to orbits 3 and 4 becoming more chaotic for low momenta, which may be problematic if a forward mapping is performed. The CQSFA does not suffer from this despite

considering sub-barrier Coulomb corrections and orbit 3 and 4. The QTMC methods do not contain caustics but are less general as they either disregard sub-barrier corrections [108] or they use quasi-static tunnelling rates [105, 106], which will not be valid for higher frequencies [80].

In the CQSFA, the momentum is approximated to be constant in the sub-barrier part of the contour, as originally done in [99, 100]. One of the main issues with this region is that one must integrate the potential up to its singularity. In practice, often one can determine a lower bound of integration before the singularity for which there are no qualitative changes in the PADs. However, this introduces some ambiguity so that no quantitative statements can be made about total ionisation rates. So, alternatively, it is possible to use the asymptotic form of the Coulomb wavefunction to match to the singularity and regularise the result. A detailed account of this approach is given in [19, 96, 98]. We have found that this method regularises the CQSFA such that the overall value of the probability is within range[2] of the TDSE solutions. However, there is no qualitative change in the distribution, so we did not use this regularisation for this qualitative analysis. Furthermore, the tunnel trajectory end point is fixed by the tunnel exit derived in [139], which takes a perturbative approach. Improvements to this contour have been reported in [61] in the context of low-energy structures.

A direct comparison with the TDSE shows that our approach works best for near-threshold and moderate photoelectron energies. Discrepancies have been observed for very low and very high energies, and may be due to the following issues. First, we have neglected the imaginary parts of the trajectories in the continuum. In [90, 94, 101] it is shown it is essential to include the imaginary components throughout and the inclusion leads to better agreement with the TDSE. In fact it was shown that the imaginary parts can be linked to the deceleration of the electronic wavepacket [94]. The inclusion of the imaginary parts in the CQSFA would require solving Newton's equations of motion for complex valued trajectories. Given the Coulomb potential will contain branch cuts, this presents a very difficult problem, which is discussed in [61, 98]. Second, by inserting a closure relation in the ATI transition amplitude, we have eliminated the contributions from excited bound states in Eq. (4.7). These contributions may play a role for very

[2]Within range here means approximately one order of magnitude, note that previously the total values were out by more than ten of orders of magnitude due to the divergence of the Coulomb potential.

low energy, by providing additional pathways for the electron to reach the continuum. Finally, the assumption that the under-the-barrier momentum is constant may break down in cases for which there is substantial acceleration.

Nonetheless, the CQSFA can qualitatively reproduce many features in the ATI momentum distribution, including the number of nodes on each ATI ring. In [100] it is stated how sub-barrier corrections rectify the number of nodes on the second ring but those on the first remain incorrect. This is attributed to the tunnel contour approximation being insufficient. However, we do obtain the correct number of fringes using the same approximation. It is more likely that this discrepancy is due to the $\dot{\mathbf{p}} \cdot \mathbf{r}$ term, that derives from using a phase space action in our expression, which is absent in [100]. In previous publications it has been found this this term is important for a good agreement with the TDSE [79, 80]. Similar results have also been reported in [108].

The holographic interference patterns discussed in this chapter provide rich structure that has the potential to yield a lot of tomographic and dynamical information on targets such as molecules. Recent work [140] has shown that by adding a weak secondary harmonic to the laser field, polarised orthogonally to the original field, adds a control parameter that modifies the phase of orbits in such a way that useful information can be extracted. By focusing on the spider-like structure visible in experimental PADs and using a simple Coulomb-corrected SFA (CCSFA) model to analyse it, ionisation times could be extracted from the interference sub-structure. A theoretical study with a similar field set-up demonstrated holographic patterns could be used to extract the field intensity. Another study [141] demonstrated theoretically that holographic interference could be used to trace the charge migration of an electron. This study employed an adiabatic semi-classical model [142] to calculate the phase. All these studies require a corresponding semi-classical model in order to translate phase differences between orbits into something useful. Note that care should be used when tracing back parameters using semi-classical models as this assumes some ontology about them. However, in such models the only 'real' part is the final observable, in our case the final momentum $\mathbf{p}_f$. The semi-classical models used are typically quite simple including the Coulomb potential only as a phase in the action, but often not in the tunnelling part and not including it at all in the equations of motion. The CQSFA is well placed to provide this kind

of analysis given the inclusion of the Coulomb potential in the orbits and the action. Additionally, the CQSFA has very low computational demand and could be easily extended to more complex systems such as multi-electron targets or two-colour fields. Possibilities for extending this method for a multi-electron system include effective potentials, imposing a spatial boundary inside which the multi-electron dynamics are incorporated and the field is treated approximately, such as in the analytical R-Matrix Theory (ARM) [90], and perturbative multielectron expansions around the one-electron CQSFA [143–147]. If the present formulation is considered, a method of extending an effective potential to the complex plane would be necessary for computing the tunnel trajectory. At least for simpler targets such at diatomic molecules effective potentials can be described in terms of elementary functions such $\exp$, for which extension to the complex plane is trivial, and non-trivial parts such as the Coulomb-like $1/r$ terms, for which the extension to the complex plane and examination of resulting branch cuts has already been investigated [61, 90, 98, 101]. In fact, in initial tests, including simple diatomic effective potentials in the CQSFA, it was found the orbits could be calculated without much difficulty. Hence, in the future this method could be essential for extracting detailed and accurate information, from the high resolution PADs that can be produced in experiments for molecular targets, exploiting control parameters such as a secondary orthogonal field.

Chapter 6

Analytic Computations

In the previous chapter we investigated all the possible interference patterns in the CQSFA. Now in this chapter we will derive analytic conditions and a semi-analytic model for these patterns. This is so we can work towards generalised holographic conditions that could be used to interpret experimental results. It also enables a deep analysis of the interference in the CQSFA, in that it gives us the ability to separate any part from the rest or change what contributions are included. We also use a larger range of parameters in this section, using wavelengths between 590 nm and 1300 nm, while keeping the Keldysh parameter (an indication of tunnelling) the same at round $\gamma \approx 0.75$, where $\gamma = \sqrt{\mathrm{I_p}/2\mathrm{U_p}}$. This enables comparison with a wider range of the literature and tests the CQSFA for different wavelengths. The results in this section draw from our publications [102, 103]. The chapter is organised as follows. In Sec. 6.1 holographic conditions are derived for the ATI rings and interference involving orbits 1-3. In Sec. 6.2, using the CQSFA as a starting point, we derive further analytic expressions that will be subsequently used to model ATI PADs and to describe several types of interference. In Sec. 6.3, we perform a detailed analysis of such expressions. This includes a comparison with the CQSFA and solutions of the TDSE, and an in-depth study of the physical causes of key features in several types of holographic structures, including the fan and the spider. Finally, in Sec. 6.4, we provide the main conclusions to be taken from this work.

6.1 Generalised Holographic Conditions

If the prefactors are neglected, one may write the ATI photoelectron probability density for N_c cycles of the driving field and a number n_e of relevant events per cycle as

$$\Omega(\mathbf{p}_f) = \left| \sum_{e=1}^{n_e} \sum_{c=1}^{N_c} \exp[iS_{ec}] \right|^2 , \tag{6.1}$$

where S_{ec} is the action associated to the e-th event in the c-th cycle and $\mathbf{p}_f$ the momentum at the detector. Here the single sum over s in Eq. (4.27) has been replaced by a double sum in the indices e and c.

For a monochromatic field the difference between the actions related to the same type of orbit but a different cycle is independent of the orbit and is given by the following equation,

$$S_{ec'} - S_{ec} = \frac{2\pi i(c'-c)}{\omega} \left(\mathrm{I_p} + \mathrm{U_p} + \frac{1}{2}\mathbf{p}_f^2 \right) := S_{\mathrm{inter}}^{(\mathrm{SFA})}. \tag{6.2}$$

This has been shown many times for the SFA but we will show it is also true for the CQSFA. This renders Eq. (6.1) factorisable and given by

$$\Omega(\mathbf{p}_f) = \Omega_{n_e}(\mathbf{p}_f)\Omega_{N_c}(\mathbf{p}_f), \tag{6.3}$$

where $\Omega_{n_e}(\mathbf{p}_f)$ is the probability associated with intra-cycle interference and

$$\Omega_{N_c}(\mathbf{p}_f) = \frac{\cos\left[\frac{2\pi N_c}{\omega}\left(\mathrm{I_p} + \mathrm{U_p} + \frac{1}{2}\mathbf{p}_f^2\right)\right] - 1}{\cos\left[\frac{2\pi}{\omega}\left(\mathrm{I_p} + \mathrm{U_p} + \frac{1}{2}\mathbf{p}_f^2\right)\right] - 1} \tag{6.4}$$

is the probability related to inter-cycle interference. This can be shown in the following way,

$$\Omega(\mathbf{p}_f) = \left| \sum_{e=1}^{n_e} \sum_{c=0}^{N_c-1} \exp[iS_{ec}] \right|^2 \tag{6.5}$$

$$= \left| \sum_{e=1}^{n_e} \exp[iS_{e0}] \sum_{c=0}^{N_c-1} \exp[i(S_{ec} - S_{e0})] \right|^2 . \tag{6.6}$$

From Eq. (6.2) we can calculate $S_{ec} - S_{e0}$, which reads as

$$S_{ec} - S_{e0} = \frac{2\pi i c}{\omega} \underbrace{\left(\mathrm{I_p} + \mathrm{U_p} + \frac{1}{2}\mathbf{p}_f^2\right)}_{\alpha}. \tag{6.7}$$

The fact that we can pull out a factor S_{e0} and the remaining sum over c is not dependent on e means that we can factorise the two sums. This gives

$$\Omega(\mathbf{p}_f) = \underbrace{\left|\sum_{e=1}^{n_e} \exp[iS_{e0}]\right|^2}_{\Omega_{n_e}} \underbrace{\left|\sum_{c=0}^{N_c-1} \exp\left[\frac{2\pi i \alpha c}{\omega}\right]\right|^2}_{\Omega_{N_c}}, \tag{6.8}$$

We can further simplify $\Omega_{N_c}(\mathbf{p}_f)$, so that

$$\begin{aligned}\Omega_{N_c}(\mathbf{p}_f) &= \left|\frac{\exp\left[\frac{2\pi i\alpha(N_c-1)}{\omega}\right] - 1}{\exp\left[\frac{2\pi i\alpha}{\omega}\right] - 1}\right|^2 \\ &= \frac{\cos\left[\frac{2\pi N_c}{\omega}\alpha\right] - 1}{\cos\left[\frac{2\pi}{\omega}\alpha\right] - 1},\end{aligned} \tag{6.9}$$

which leads to Eq. (6.4).

In the limit of infinitely long pulses, Eq. (6.4) describes a Dirac delta comb, whose peaks are unequally spaced, and remains the same for the SFA and CQSFA. This condition agrees with the expression in [71].

The number n_e of relevant orbits per cycle will depend on the approach, and for simplicity we will use just the first three orbits in this chapter. Hence, we can write an expression for intra-cycle interference that is general enough to encapsulate all the effects discussed. Explicitly,

$$\Omega_{n_e}(\mathbf{p}_f) = e^{-2\mathrm{Im}[S_{1c}]}\left|1 + e^{-\Delta S_{12}^{\mathrm{Im}}} e^{i\Delta S_{12}^{\mathrm{Re}}} + e^{-\Delta S_{13}^{\mathrm{Im}}} e^{i\Delta S_{13}^{\mathrm{Re}}}\right|^2. \tag{6.10}$$

Here $\Delta S_{1j}^{\mathrm{Re}} = \mathrm{Re}[S_{jc} - S_{1c}]$ and $\Delta S_{1j}^{\mathrm{Im}} = \mathrm{Im}[S_{jc} - S_{1c}]$ with $j = 2, 3$. This is valid for all cycles c. The term $e^{-2\mathrm{Im}[S_{1c}]}$ shapes the momentum distribution, and gives rise to the side-lobes identified in ATI photoelectron momentum distributions [66]. This part is related purely to the tunnelling dynamics so we call it the tunnelling prefactor. The real parts of ΔS_{ij} lead to the interference fringes seen in ATI, while $\mathrm{Im}[\Delta S_{ij}]$ switch

interference on or off. If $\mathrm{Im}[\Delta S_{ij}]$ is small, then interference is on, whereas for large $\mathrm{Im}[\Delta S_{ij}]$ interference is off and one of the orbits prevails. Therefore, a full generalised holographic interference equations that describes all features in ATI, relating to the first three orbits can be written as follows,

$$\Omega(\mathbf{p}_f) = \frac{\cos\left[\frac{2\pi N_c}{\omega}\left(\mathrm{I_p} + \mathrm{U_p} + \frac{1}{2}\mathbf{p}_f^2\right)\right] - 1}{\cos\left[\frac{2\pi}{\omega}\left(\mathrm{I_p} + \mathrm{U_p} + \frac{1}{2}\mathbf{p}_f^2\right)\right] - 1} e^{-2\mathrm{Im}[S_{1c}]} \left|1 + e^{-\Delta S_{12}^{\mathrm{Im}}} e^{i\Delta S_{12}^{\mathrm{Re}}} + e^{-\Delta S_{13}^{\mathrm{Im}}} e^{i\Delta S_{13}^{\mathrm{Re}}}\right|^2 \tag{6.11}$$

So in order to fully describe the interference patterns one can compute all the action terms, which is what we will do via the long wavelength approximation in Sec. 6.2. Note the effect of orbit 4 can easily be include by adding the corresponding differences in the action with orbit 1. However, computing the action analytically for this orbit is particularly troublesome so we have left it out.

In order to help compute these action differences we write the action more explicitly for monochromatic fields. The tunnelling and propagation parts of the action in the CQSFA given in Eq. (4.12) and (4.21), respectively, can be rewritten as

$$\begin{aligned} S^{\mathrm{tun}}(\tilde{\mathbf{p}}, \mathbf{r}, t_r', t') = {} & i\left(\mathrm{I_p} + \frac{1}{2}\mathbf{p}_0^2 + \mathrm{U_p}\right) t_i' - \int_{t'}^{t_r'} V(\mathbf{r}_0(\tau))\mathrm{d}\tau \\ & + \frac{2\sqrt{\mathrm{U_p}} p_{0\parallel}}{\omega}\left[\sin(\omega t') - \sin(\omega t_r')\right] \\ & + \frac{\mathrm{U_p}}{2\omega}\left[\sin(2\omega t') - \sin(2\omega t_r')\right] \end{aligned} \tag{6.12}$$

and

$$\begin{aligned} S^{\mathrm{prop}}(\tilde{\mathbf{p}}, \mathbf{r}, t, t_r') = {} & \left(\mathrm{I_p} + \frac{1}{2}\mathbf{p}_f^2 + \mathrm{U_p}\right) t_r' + \frac{2\sqrt{\mathrm{U_p}} p_{f\parallel}}{\omega}\sin(\omega t_r') \\ & + \frac{\mathrm{U_p}}{2\omega}\sin(2\omega t_r') - \frac{1}{2}\int_{t_r'}^{t} \boldsymbol{\mathscr{P}}(\tau)\cdot(\boldsymbol{\mathscr{P}}(\tau) + 2\mathbf{p}_f)\mathrm{d}\tau \\ & - 2\sqrt{\mathrm{U_p}}\int_{t_r'}^{t} \mathscr{P}_{\parallel}(\tau)\cos(\omega\tau)\mathrm{d}\tau - 2\int_{t_r'}^{t} V(\mathbf{r}(\tau))\mathrm{d}\tau, \end{aligned} \tag{6.13}$$

where $p_{j\parallel}$, with $j = 0, f$, correspond to the electron momentum components parallel to the laser-field polarisation and

$$\mathbf{p}(\tau) = \boldsymbol{\mathscr{P}}(\tau) + \mathbf{p}_f. \tag{6.14}$$

This has been chosen so that all the integrands go to zero for large τ. Eqs. (6.12) and (6.13) can be combined to give a more explicit form of the action,

$$\begin{aligned} S(\tilde{\mathbf{p}}, \mathbf{r}, t, t') = {} & (\mathrm{I_p} + \mathrm{U_p})\, t' + \frac{1}{2}\mathbf{p}_f^2 t'_r + \frac{i}{2}\mathbf{p}_0^2 t'_i + \frac{\mathrm{U_p}}{2\omega}\sin(2\omega t') \\ & + \frac{2\sqrt{\mathrm{U_p}}}{\omega}\left[p_{0\parallel}\sin(\omega t') - (p_{0\parallel} - p_{f\parallel})\sin(\omega t'_r)\right] - \int_{t'}^{t'_r} V(\mathbf{r}_0(\tau))\mathrm{d}\tau \\ & - \frac{1}{2}\int_{t'_r}^{t} \boldsymbol{\mathscr{P}}(\tau)\cdot(\boldsymbol{\mathscr{P}}(\tau) + 2\mathbf{p}_f + 2\mathbf{A}(\tau))\mathrm{d}\tau - 2\int_{t'_r}^{t} V(\mathbf{r}(\tau))\mathrm{d}\tau. \end{aligned} \tag{6.15}$$

This equation can be considered general in that we will recover the SFA if the Coulomb coupling is reduced to zero, i.e., in the limit $C \to 0$. Then $V(\mathbf{r}) \to 0$, $\mathbf{p}_f \to \mathbf{p}_0 \to \mathbf{p}$ and $\boldsymbol{\mathscr{P}} \to 0$, which leaves us with the SFA action given in Eq. (4.2).

The dominant contributors to the overall shape of the electron-momentum distributions and to the interference patterns are the imaginary and real parts of the action, respectively. It is helpful to write the real and imaginary parts of the action in more explicit terms. The imaginary part of the action is directly related to the tunnelling probability density, and it is a good indicator of the width of the barrier. Specifically for Eq. (6.15), $\mathrm{Im}[S]$ reads

$$\begin{aligned} S_e^{\mathrm{Im}}(t'_e, \mathbf{p}_e, \mathbf{r}_e) = {} & \left(\mathrm{I_p} + \mathrm{U_p} + \tfrac{1}{2}\mathbf{p}_{e0}^2\right) t'_{ei} + \tfrac{2p_{e0\parallel}\sqrt{\mathrm{U_p}}}{\omega}\cos(\omega t'_{er})\sinh(\omega t'_{ei}) \\ & + \tfrac{\mathrm{U_p}}{2\omega}\cos(2\omega t'_{er})\sinh(2\omega t'_{ei}) - \textstyle\int_{t'_e}^{t'_{er}} \mathrm{Im}[V(\mathbf{r}_{e0}(\tau))]\mathrm{d}\tau, \end{aligned} \tag{6.16}$$

where $e = 1, 2, 3$. The real parts give the phase differences between different types of trajectories. For the action (6.15) and a specific orbit e, $\mathrm{Re}[S]$ is given by

$$\begin{aligned} S_e^{\mathrm{Re}}(t'_e, \mathbf{p}_e, \mathbf{r}_e) = {} & \left(I_p + U_p + \frac{1}{2}\mathbf{p}_f^2\right) t'_{er} + \frac{2\sqrt{U_p}}{\omega}\left(2p_{e0\parallel}\sinh\left(\frac{\omega t'_{ei}}{2}\right)^2 + p_{f\parallel}\right)\sin(\omega t'_{er}) \\ & + \frac{U_p}{2\omega}\mathrm{Re}[\sin(2\omega t'_e)] - \frac{1}{2}\int_{t'_{er}}^{t} f_e(\tau)\mathrm{d}\tau - \int_{t'_e}^{t'_{er}} \mathrm{Re}[V(\mathbf{r}_{e0}(\tau))]\mathrm{d}\tau \\ & - 2\int_{t'_{er}}^{t} V(\mathbf{r}_e(\tau))\mathrm{d}\tau, \end{aligned} \tag{6.17}$$

where $f_e(\tau) = \boldsymbol{\mathcal{P}}_e(\tau) \cdot (\boldsymbol{\mathcal{P}}_e(\tau) + 2\mathbf{p}_f + 2\mathbf{A}(\tau))$ and $\mathbf{p}_e(\tau) = \boldsymbol{\mathcal{P}}_e(\tau) + \mathbf{p}_f$. Prefactors will introduce additional biases, which do influence the shape of the PADS. They will however play a secondary role in quantum-interference effects as they vary much more slowly than the action.

6.1.1 Intercycle interference

In the following, we will show that the expression for intercycle interference remains the same for the CQSFA, provided the field is monochromatic. In the CQSFA action difference between two orbits of the same type in different field cycles may be written as

$$\Delta S_{\text{inter}} = S_{ec'} - S_{ec} = \Delta S_{\text{inter}}^{(\text{SFA})} + \Delta S_{cc'}, \tag{6.18}$$

where the $S_{\text{inter}}^{(\text{SFA})}$ is given by Eq. (6.2) with $\mathbf{p}$ replaced by $\mathbf{p}_f$, and $\Delta S_{cc'}$ are Coulomb corrections related to an orbit of the type e occurring in cycles c and c', so that the ionisation times satisfy $t'_{c'} = t'_c + 2\pi n_c/\omega$. The indices e are dropped as the condition refers to the same type of orbit. This action difference reads

$$\Delta S_{cc'} = \Delta S_{V_T} + \Delta S_{V_C} + \Delta S_p, \tag{6.19}$$

where ΔS_{V_T} and ΔS_{V_C} are the phase differences caused by the potential during tunnelling and continuum propagation, respectively, and ΔS_p is related to the change in momentum during the electron propagation. Explicitly,

$$\Delta S_{V_T} = \int_{t'_{c'}}^{t'_{c'r}} V(\mathbf{r}_{c'0}(\tau))\mathrm{d}\tau - \int_{t'_c}^{t'_{cr}} V(\mathbf{r}_{c0}(\tau))\mathrm{d}\tau, \tag{6.20}$$

where the subscripts r indicate the real parts of t'_c and $t'_{c'}$ and $\mathbf{r}_{0c}(\tau)$ is given by Eq. (4.13) with the lower bound replaced by t'_c. For a monochromatic field, $\mathbf{r}_{c'0}(\tau) = \mathbf{r}_{c0}(\tau - \frac{2\pi n}{\omega})$. Substituting this into Eq. (6.20) leads to

$$\Delta S_{V_T} = \int_{t'_{c'}}^{t'_{c'r}} V(\mathbf{r}_{c0}(\tau - \frac{2\pi n}{\omega}))\mathrm{d}\tau - \int_{t'_c}^{t'_{cr}} V(\mathbf{r}_{c0}(\tau))\mathrm{d}\tau \tag{6.21}$$

$$= \int_{t'_c+2\pi n_c/\omega}^{t'_{cr}+2\pi n_c/\omega} V(\mathbf{r}_{c0}(\tau - \frac{2\pi n}{\omega}))\mathrm{d}\tau - \int_{t'_c}^{t'_{cr}} V(\mathbf{r}_{c0}(\tau))\mathrm{d}\tau. \tag{6.22}$$

Transforming the first terms integration variable, $\tau' = \tau - \frac{2\pi n}{\omega}$, gives

$$= \int_{t'_c}^{t'_{cr}} V(\mathbf{r}_{c0}(\tau'))\mathrm{d}\tau' - \int_{t'_c}^{t'_{cr}} V(\mathbf{r}_{c0}(\tau))\mathrm{d}\tau. \tag{6.23}$$

Thus, the first and the second integrals cancel so that Eq. (6.20) vanishes.

The action difference

$$\Delta S_{V_C} = -2\int_{t'_{c'r}}^{t} V(\mathbf{r}_{c'}(\tau))\mathrm{d}\tau + 2\int_{t'_{cr}}^{t} V(\mathbf{r}_{c}(\tau))\mathrm{d}\tau \tag{6.24}$$

is handled in a similar way, using $\mathbf{r}_{c'}(\tau) = \mathbf{r}_c(\tau - \frac{2\pi n}{\omega})$. But this time as the upper integration limit t doesn't transform as before, so the term

$$\Delta S_{V_C} = 2\int_{t-2\pi/\omega}^{t} V(\mathbf{r}_{c}(\tau))\mathrm{d}\tau \tag{6.25}$$

is left, which vanishes in the limit of $t \to \infty$, given $r \to \infty$. The same procedure, together with the mapping $\mathbf{p}_{c'}(\tau) = \mathbf{p}_c(\tau - \frac{2\pi n}{\omega})$, can also be used to show that

$$\begin{aligned}\Delta S_p &= -\frac{1}{2}\int_{t'_{c'r}}^{t} \boldsymbol{\mathscr{P}}_{c'}(\tau)\cdot(\boldsymbol{\mathscr{P}}_{c'}(\tau) + 2\mathbf{p}_f + 2\mathbf{A}(\tau))\mathrm{d}\tau \\ &\quad + \frac{1}{2}\int_{t'_{cr}}^{t} \boldsymbol{\mathscr{P}}_{c}(\tau)\cdot(\boldsymbol{\mathscr{P}}_{c}(\tau) + 2\mathbf{p}_f + 2\mathbf{A}(\tau))\mathrm{d}\tau\end{aligned} \tag{6.26}$$

vanishes in this limit, given $\boldsymbol{\mathscr{P}}_c(\tau) \to \infty$ as $\tau \to \infty$. Hence, the Coulomb potential has no effect on the ATI rings, for a monochromatic field. For a short laser pulse, this will not hold.

6.2 Semi-Analytic Model

We will now provide analytic approximations for the remaining action terms that contribute to Eq. (6.11). This includes, sub-barrier dynamics and the continuum propagation. In order to make the imaginary and real parts of the action, Eqs. (6.16) and (6.17), analytically solvable, we employ the low-frequency approximation and some simplifying assumptions upon the intermediate momenta. The low-frequency approximation

has been used in [100] to derive sub-barrier corrections, and in [102, 103] for computing analytical single-orbit probability distributions from Eq. (6.16). The continuum terms contain integrals over trajectories that have no analytic solution. So in order to solve these integrals we must assume a particular physical form for these trajectories, using insight gained from examining the different orbit types. Thus, we describe this part as a semi-analytic model.

The quantities of interest are the under-the-barrier potential integral

$$\mathcal{I}_{V_T} = -\int_{t'_e}^{t'_{er}} V(\mathbf{r}_{e0}(\tau))\mathrm{d}\tau, \tag{6.27}$$

the potential integral

$$\mathcal{I}_{V_C} = -\int_{t'_{er}}^{t} V(\mathbf{r}_{e}(\tau))\mathrm{d}\tau \tag{6.28}$$

related to the continuum propagation, and the phase difference

$$\mathcal{I}_{\mathcal{P}_e} = -\frac{1}{2}\int_{t'_{er}}^{t} \boldsymbol{\mathcal{P}}_e(\tau)\cdot(\boldsymbol{\mathcal{P}}_e(\tau) + 2\mathbf{p}_f + 2\mathbf{A}(\tau))\mathrm{d}\tau \tag{6.29}$$

due to the electron's final and intermediate momentum being different, as it is accelerated by the residual binding potential.

6.2.1 The under-the-barrier integral and single-orbit distributions

We compute the integral over the binding potential for the imaginary part of the CQSFA action related to tunnel ionisation, Eq. (6.16), in the long wavelength approximation. For more details see, [102]. This integral is important in determining the shapes of single-orbit distributions, and influences their sidelobes. The tunnel trajectory can be written explicitly as

$$\mathbf{r}_0(\tau) = i\mathbf{p}_{e0}(\tau_i - t'_i) + i\int_{t'_i}^{\tau_i} \mathbf{A}(t_r + i\tau'_i)\mathrm{d}\tau'_i \tag{6.30}$$

Using the long wavelength approximation and expanding around the imaginary component to first order, the above-stated expression is approximated by

$$\mathbf{r}_0(\tau) = (\tau_i - t_i')\left[i(\mathbf{p}_0 + \mathbf{A}(t_r')) - \frac{1}{2}\dot{\mathbf{A}}(t_r')(\tau_i + t_i')\right], \tag{6.31}$$

where $\tau_i = \mathrm{Im}[\tau]$. This expression can be used to compute the indefinite integral

$$\begin{aligned}\int V(\mathbf{r}_0(\tau))\mathrm{d}\tau = \frac{iC}{\sqrt{-\mathbf{p}_{0\perp}^2 + \chi^2}}\Big[&\ln(\tau_i - t_i') \\ &- \ln\left(2[\chi\eta(\tau_i) - \mathbf{p}_{0\perp}^2] + 2\sqrt{-\mathbf{p}_{0\perp}^2 + \eta(\tau_i)^2}\sqrt{-\mathbf{p}_{0\perp}^2 + \chi^2}\right)\Big]\end{aligned} \tag{6.32}$$

where

$$\chi = i(p_{0\perp} + A(t_r')) - t_i'\dot{A}(t_r') \qquad \text{and} \tag{6.33}$$

$$\eta(\tau_i) = i(p_{0\parallel} + A(t_r')) - \frac{1}{2}(t_i' + \tau_i)\dot{A}(t_r'). \tag{6.34}$$

We are however interested in the definite integral from t' to t_r'. Care must be taken with the lower bound as it will lead to a divergence. For that reason, we take it as $t' - i\Delta\tau_i$, where $\Delta\tau_i$ is chosen to be an arbitrarily small real value. This gives

$$\begin{aligned}\mathcal{I}_{V_T} &= \int_{t'-i\Delta\tau_i}^{t_r'} V(\mathbf{r}_0(\tau))\mathrm{d}\tau \qquad (6.35)\\ &= i\ln\left[\left(\frac{t_i'\left(\chi\eta(t_i' - \Delta\tau_i) - p_{0\perp}^2 + \sqrt{-\mathbf{p}_{0\perp}^2 + \eta(t_i' - \Delta\tau_i)^2}\sqrt{-\mathbf{p}_{0\perp}^2 + \chi^2}\right)}{\Delta\tau_i\left(\chi\eta(0) - p_{0\perp}^2 + \sqrt{-\mathbf{p}_{0\perp}^2 + \eta(0)^2}\sqrt{-\mathbf{p}_{0\perp}^2 + \chi^2}\right)}\right)^{C/\sqrt{-\mathbf{p}_{0\perp}^2+\chi^2}}\right],\end{aligned}$$

so that $\exp[-i\mathcal{I}_{V_T}]$ will be a power of $C/\sqrt{-\mathbf{p}_{0\perp}^2 + \chi^2}$ and $\Delta\tau_i^{-C/\sqrt{-\mathbf{p}_{0\perp}^2+\chi^2}}$ will contribute as an orbit independent overall factor multiplying the whole transition amplitude. Eq. (6.35) agrees with numerical computations, in which $\Delta\tau_i$ is set to be small.

The parameter C is the effective Coulomb coupling, typically set to 1, and the subscripts e have been dropped for simplicity. The divergence, caused by the lower integration limit, can be brought out as a common factor and thus ignored. Eq. (6.35) can be split into a non-divergent and a divergent part, which can be treated separately. This

gives

$$\mathcal{I}_{V_T} = \widetilde{\mathcal{I}}_{V_T} + \mathcal{I}_{\rm div}, \tag{6.36}$$

with

$$\widetilde{\mathcal{I}}_{V_T} = \tag{6.37}$$
$$i \ln \left[\left(\frac{t_i' \left(\chi\eta(t_i' - \Delta\tau_i) - p_{0\perp}^2 + \sqrt{-\mathbf{p}_{0\perp}^2 + \eta(t_i' - \Delta\tau_i)^2}\sqrt{-\mathbf{p}_{0\perp}^2 + \chi^2} \right)}{\chi\eta(0) - p_{0\perp}^2 + \sqrt{-\mathbf{p}_{0\perp}^2 + \eta(0)^2}\sqrt{-\mathbf{p}_{0\perp}^2 + \chi^2}} \right)^{C/\sqrt{-\mathbf{p}_{0\perp}^2 + \chi^2}} \right]$$

and

$$\mathcal{I}_{\rm div} = -iC/\sqrt{-\mathbf{p}_{0\perp}^2 + \chi^2} \ln(\Delta\tau_i). \tag{6.38}$$

In Eq. (6.37), $\Delta\tau_i \to 0$ leads to $\eta(t_i' - \Delta\tau_i) \to \chi$, while Eq. (6.38), when added into the action, will act like a prefactor. Explicitly,

$$\begin{aligned} \exp(i\widetilde{\mathcal{I}}_{V_T} + i\mathcal{I}_{\rm div}) &= \exp(i\widetilde{\mathcal{I}}_{V_T}) \exp(C/\sqrt{-\mathbf{p}_{0\perp}^2 + \chi^2} \ln(\Delta\tau_i)) \\ &= \Delta\tau_i^{-C/\sqrt{-\mathbf{p}_{0\perp}^2 + \chi^2}} \exp(i\widetilde{\mathcal{I}}_{V_T}) \end{aligned} \tag{6.39}$$

To remove this factor from the expression we can use the freedom that we may tend $\Delta\tau_i$ to zero via any route. We can set $\Delta\tau_i = -\delta\sqrt{-\mathbf{p}_{0\perp}^2 + \chi^2}/C$, where δ is a parameter that can used for all orbits to tend $\Delta\tau_i$ to zero. This will lead to a common factor δ, which will affect the overall yield of all the orbits equally but will not affect not the interference patterns. Hence, it can be removed. This provides an argument as why it is OK to ignore this divergence for a qualitative analysis but does not constitute as a proper regularisation procedure. [1]

The regularised expression for Eq. (6.35) then reads

$$\mathcal{I}_{V_T} = iC/\sqrt{-\mathbf{p}_{0\perp}^2 + \chi^2} \ln \left[\underbrace{\left(\frac{2t_i' \left(\chi^2 - p_{0\perp}^2 \right)}{\chi\eta(0) - p_{0\perp}^2 + \sqrt{-\mathbf{p}_{0\perp}^2 + \eta(0)^2}\sqrt{-\mathbf{p}_{0\perp}^2 + \chi^2}} \right)}_{\mathcal{F}} \right]. \tag{6.40}$$

In Fig. (6.1), we plot single-orbit distributions computed for orbits 1 and 2 using the

[1] We also verified numerically that for small $\Delta\tau_i$ the qualitative behaviour does not change.

full CQSFA, and the analytic approximation given by Eq. (6.40). In order to facilitate a comparison, the prefactors have not been included. Overall, there is little discrepancy between the analytical approximation and the full CQSFA. This is because the single-orbit plots will vary only with the imaginary part of the action, which occurs exclusively along the tunnel trajectory. The momentum along the tunnel trajectory is already taken to be constant. Thus, the only difference between both models is the long wavelength approximation used to integrate the potential. This additional approximation is quite accurate along the tunnel trajectory, partly because the path along the imaginary time axis is relatively short, typically well under half a cycle. Furthermore, the trigonometric functions turn into hyperbolic functions, which are easily approximated. For both orbits, there is a double peaked structure in the analytic and full CQSFA solutions, and the yield becomes suppressed at the origin (see upper panels in Figs. (6.1)(a) to (f)). This indicates that, in the presence of the Coulomb potential, the electron must have a non-vanishing momentum to reach the continuum with a high probability [102]. For orbit 2, this structure is particularly visible and spreads to a larger momentum region as the driving-field frequency increases (see upper rows in Figs. (6.1)(b), (d) and (f)). Both the analytic and full CQSFA exhibit sharply focused spots in the PADs computed with orbit 2, which become more prominent as the laser frequency increases. The analytic expressions overestimate these spots. This can be seen by comparing panels F2 and A2 in Figs. (6.1)(b), (d) and (f).

Using the analytic model we can break down these effects to find their origin. The single-orbit distributions are entirely governed by the imaginary part of the action, which can be written as

$$S^{\mathrm{Im}}(\mathbf{p},\mathbf{r},t) = \frac{\mathrm{U_p}}{\omega}\mathcal{G}(\xi) - i\mathrm{Re}\left[\frac{C}{\sqrt{-\mathbf{p}_{0\perp}^2+\chi^2}}\ln\left(\mathcal{F}\right)\right], \tag{6.41}$$

$$\begin{aligned}\mathcal{G}(\xi) &= (1+2|\xi|^2)\arccos(\xi) - 4\xi_r\mathrm{Im}[\sqrt{1-\xi^2}] \\ &+ \mathrm{Im}[\xi\sqrt{1-\xi^2}]\end{aligned} \tag{6.42}$$

where $\mathcal{F}$ is equal to the argument of the logarithm in Eq. (6.40), related to the binding potential, $\mathcal{G}(\xi)$ is the unit-less SFA-like part of the action, associated with the laser-induced dynamics, and $\xi = \cos(\omega t_e')$ is a unit-less variables that has been used to replace

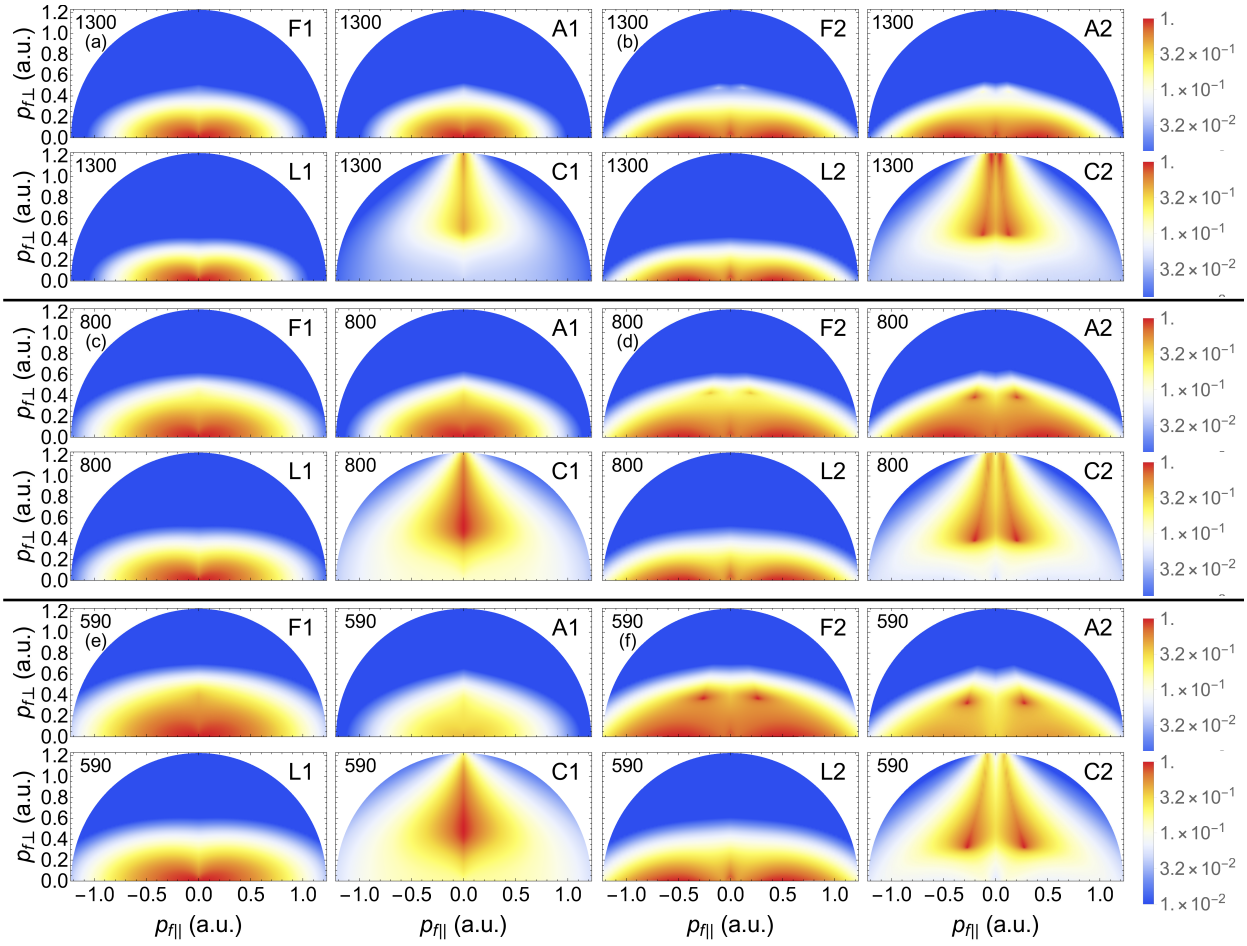

FIGURE 6.1: Single-orbit ATI photoelectron angle-resolved distributions (PADs) computed without prefactors for hydrogen ($I_p = 0.5$ a.u.) and orbits 1 and 2. The lower case letters on the top left corner correspond to the field parameters $(I, \lambda) = (7.5 \times 10^{13}\ \mathrm{W/cm^2}, 1300\ \mathrm{nm})$ [panels (a) and (b)], $(I, \lambda) = (2.0 \times 10^{14}\ \mathrm{W/cm^2}, 800\ \mathrm{nm})$ [panels (c) and (d)] and $(I, \lambda) = (3.75 \times 10^{14}\ \mathrm{W/cm^2}, 590\ \mathrm{nm})$ [panels (e) and (f)], where I and λ give the field intensity and wavelength, respectively. This yields a Keldysh parameter $\gamma \approx 0.75$. The acronyms Fn $(n = 1, 2)$, An $(n = 1, 2)$ on the right top corner indicate the full and analytic CQSFA solution for orbits 1 or 2, while Ln $(n = 1, 2)$ and Cn $(n = 1, 2)$ give the laser and Coulomb terms of the analytic expressions as defined in Eqs. (6.42) and (6.43). The numbers on the top left corner of each panel give the driving-field wavelengths. The density plots have been represented in a logarithmic scale and normalised to the highest yield in each panel. The thick horizontal lines separate panels with different field parameters.

	L_1 Max	C_1 Max	L_2 Max	C_2 Max
1300 nm	3.45×10^{-4}	1.44×10^{7}	3.11×10^{-4}	3.23×10^{7}
800 nm	1.02×10^{-3}	5.18×10^{4}	8.19×10^{-4}	1.20×10^{5}
590 nm	2.06×10^{-3}	4.38×10^{3}	7.25×10^{-4}	5.70×10^{3}

TABLE 6.1: Maximum signal for the laser and Coulomb related parts of the amplitude L_n and C_n for orbits 1 and 2.

initial momentum and time. We can separate these parts when we consider the single-orbit probability distribution, so that

$$\begin{aligned} |\exp(iS(\mathbf{p},\mathbf{r},t))|^2 &= \exp(-2S^{\mathrm{Im}}(\mathbf{p},\mathbf{r},t)) \\ &= \left|\mathcal{F}\frac{C}{\sqrt{-\mathbf{p}_{0\perp}^2+\chi^2}}\right|^2 \exp\left(-\frac{2\mathrm{U_p}}{\omega}\mathcal{G}(\xi)\right). \end{aligned} \tag{6.43}$$

The SFA-like part has a clear ω dependence and contributes the most to the final shape, hence the apparent overall scaling with ω seen in the upper parts of Figs. (6.1)(a)–(f) [panels An and Fn $(n = 1, 2)$]. The potential-dependent prefactor scales in a non-trivial way. The figure also shows that the contributions from the SFA-like terms and the potential integrals $\mathcal{I}_{V_T}$, plotted in panels Ln and Cn $(n = 1, 2)$, respectively, mostly occupy different momentum regions. The SFA-like part of the action is more located near the $p_\parallel$ axis, while the Coulomb contribution leads to an elongated structure near the $p_\perp$ axis. For orbit 1, this structure is single peaked, but for orbit 2 it exhibits a clear suppression at $p_\parallel = 0$, with two distinct maxima around this axis. This happens because there is a cusp at $p_{0||} = 0$ for both orbits 1 and 2. However, an electron along orbit 2 is accelerated by the Coulomb potential to a non-zero final momentum value, leading to the double maxima.

There is also a lower momentum bound for this structure, which decreases for higher frequencies. This will increase the overlap between the Coulomb and laser-field contributions for a shorter wavelength. This means that features such as the two spots in orbit 2, most visible for 590 nm, are due to an increasing overlap of these two parts. In Table 6.1 we list the peak values for the SFA-like and Coulomb terms. The Coulomb part is many orders of magnitude larger than the SFA-like part, which is expected as it involves the Coulomb singularity. Despite this difference, both will play a role as they are multiplied in Eq. (6.43). The Coulomb term's peak value actually increases with the

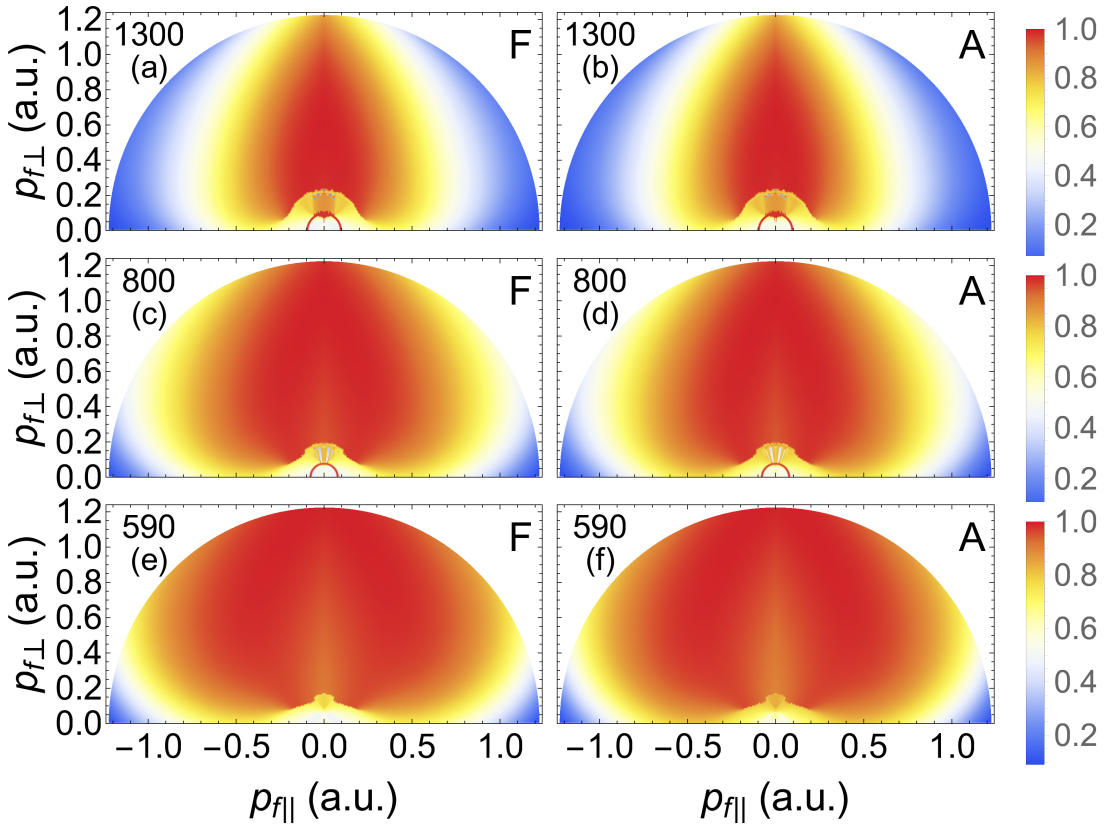

FIGURE 6.2: Single-orbit ATI PADs computed without prefactors for hydrogen ($I_p = 0.5$ a.u.) and orbit 3. The top, middle and bottom panels have been calculated for the field parameters $(I, \lambda) = (7.5 \times 10^{13}\ \mathrm{W/cm^2}, 1300\ \mathrm{nm})$ [panels (a) and (b)], $(I, \lambda) = (2.0 \times 10^{14}\ \mathrm{W/cm^2}, 800\ \mathrm{nm})$ [panels (c) and (d)] and $(I, \lambda) = (3.75 \times 10^{14}\ \mathrm{W/cm^2}, 590\ \mathrm{nm})$ [panels (e) and (f)], where I and λ give the field intensity and wavelength, respectively. The upper-case letters F and A on the right top corner of each panel indicate the full and analytic CQSFA solutions and the numbers on the top left corners give the driving-field wavelength. The density plots have been represented in a linear scale and normalised to the highest yield in each panel.

wavelength, despite the doubly peaked structure being more visible for shorter wavelengths in the full distributions. This shows that the overlap between the two terms is the most important factor in determining whether this structure shows up in the final distribution.

For orbit 3, we also find a very good agreement between the numeric and analytic results, as shown in Fig. (6.2). In particular, we observe that the single-orbit PADs occupy a broader momentum region for decreasing driving-field wavelength. One should note that the shape of the distributions remains similar. However, they scale with increasing frequencies. Hence, for the region of interest, longer wavelengths favour the

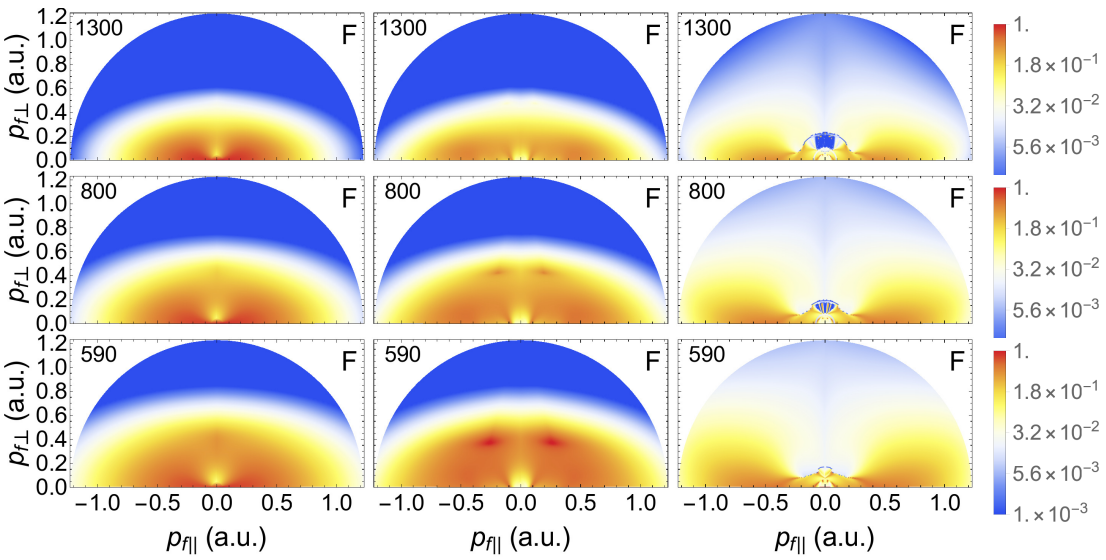

FIGURE 6.3: Single-orbit PADs for hydrogen ($I_p = 0.5$ a.u.), including all prefactors and using the full CQSFA, for orbits 1, 2 and 3 (left, middle and right columns, respectively). The top, middle and bottom panel have been calculated for the field parameters $(I, \lambda) = (7.5 \times 10^{13}\ \mathrm{W/cm^2}, 1300\ \mathrm{nm})$, $(I, \lambda) = (2.0 \times 10^{14}\ \mathrm{W/cm^2}, 800\ \mathrm{nm})$ and $(I, \lambda) = (3.75 \times 10^{14}\ \mathrm{W/cm^2}, 590\ \mathrm{nm})$, respectively. The PADs have been plotted in a logarithmic scale. The numbers on the left top corner of each panel give the driving-field wavelength, and the letters F in the top right corner indicate that this is the full CQSFA solution. All panels have been normalised with regard to their counterparts computed for orbit 1.

signal along the $p_\perp$ axis, and reduce the region along the $p_\parallel$ axis for which the probability density is significant. Inclusion of the prefactor (Fig. (6.3)) locates the distributions along the $p_\parallel$ axis for orbit 3 and reduces the off axis probability density. The effect of the prefactor is less dramatic for orbits 1 and 2, and the previously discussed features remain. However, it introduces a suppression in the yield around the origin for such orbits. Examples are the widening of the PADs in the $p_\perp$ direction with increasing frequency and the sharp spots caused by $\mathcal{I}_{V_T}$ that exist for orbit 2 (see the left and middle columns in Fig. (6.3)).

The under-the-barrier integral $\mathcal{I}_{V_T}$ does also contribute with a phase. Nonetheless, we have verified that this phase plays a secondary role and does not strongly alter the holographic patterns of interest. It does however cause discontinuities in the fringes due to branch cuts. For a detailed discussion of these problems see [19, 61, 98, 148].

6.2.2 The continuum propagation

We will now approximate the continuum propagation in order to obtain analytic expressions for the integrals of the potential and momentum in the continuum, Eqs. (6.28) and (6.29). The key idea is to use approximate functions for the intermediate momenta in conjunction with the low-frequency approximation applied around a physically relevant, specific time.

In the potential integral $\mathcal{I}_{V_C}$, we will assume that the momentum in the continuum trajectory, Eq. (4.16), is either constant or piecewise constant. This leads to the approximate expression

$$\mathcal{I}_{V_C} \approx -\sum_{j=1}^{n-1} \int_{t_j}^{t_{j+1}} V(\mathbf{r}_j(\tau))\mathrm{d}\tau \tag{6.44}$$

$$\mathbf{r}_j(\tau) \approx \int_{t_j}^{\tau} (\mathbf{p}_j + \mathbf{A}(\tau'))\mathrm{d}\tau' + \mathbf{c}_j, \tag{6.45}$$

where $n-1$ is the number of subintervals for which the momentum $\mathbf{p}_j$ is assumed to be constant, t_j is the lower bound for these intervals and the constants $\mathbf{c}_j$ account for initial conditions that may be introduced in each subinterval. These intervals start at the real part of the ionisation time, i.e., $t_1 = t'_r$ and finish at the time $t_n = t$, $t \to \infty$. Depending on the specific orbit and on the integration interval, the times t_j will carry different physical meanings, such as the time of ionisation, recollision, etc. Using the long wavelength approximation to zeroth order on the integrand of Eq. (6.45), one may write $\mathbf{A}(\tau') = \mathbf{A}(\widetilde{t})$ in Eq. (6.45), where $\widetilde{t}$ is the orbit-specific time for which the potential integral is the most significant. In general, we take $\widetilde{t}$ to be the time of closest approach between the electron and the core. However, if more than one orbit is taken into consideration, we must ensure that a common time $\widetilde{t}$ is taken so that both orbits are in the continuum. This yields

$$\mathbf{r}_j(\tau) \approx \mathbf{k}_j(\tau - t_j) + \mathbf{c}_j, \tag{6.46}$$

where $\mathbf{k}_j = (\mathbf{p}_j + \mathbf{A}(\widetilde{t}))$. The indefinite integral related to each term in Eq. (6.44) reads

$$\begin{aligned}\mathcal{I}(\Delta\tau_j) &= -\int V(\mathbf{r}_j(\Delta\tau_j))\mathrm{d}\Delta\tau_j \\ &= -\frac{C}{|\mathbf{k}_j|}\ln\left[-\mathbf{k}_j\cdot(\Delta\tau_j\mathbf{k}_j+\mathbf{c}_j)+|\mathbf{k}_j|\,|\Delta\tau_j\mathbf{k}_j+\mathbf{c}_j|\right], \end{aligned} \tag{6.47}$$

where $\Delta\tau_j = \tau - t_j$.

A different approximation is employed to compute the momentum correction Eq. (6.29). Thereby, we assume that, starting from a given initial time $\widetilde{t}$ whose physical meaning is orbit dependent, the difference $\boldsymbol{\mathcal{P}}$ between the current momentum $\mathbf{p}(\tau)$ and the final momentum $\mathbf{p}_f$ is exponentially decaying. This means that the variable intermediate momentum $\mathbf{p}(\tau)$ is replaced by an analytic function, $\mathbf{p}(\tau) = \mathcal{P}(\tau) + \mathbf{p}_f$, with

$$\mathcal{P}_\parallel(\tau) = (p_{f\parallel} - p_{j\parallel})\exp(a_\parallel(\tau-\widetilde{t})) \tag{6.48}$$

$$\mathcal{P}_\perp(\tau) = (p_{f\perp} - p_{j\perp})\exp(a_\perp(\tau-\widetilde{t})), \tag{6.49}$$

where the coefficients $a_\parallel$ and $a_\perp$ are computed using the assumptions specific to the problem at hand. For a monochromatic field, the integral over the momentum difference yields

$$\begin{aligned}\mathcal{I}_\mathcal{P} &= \frac{(p_{f\parallel}-p_{j\parallel})(p_{j\parallel}+3p_{f\parallel})}{4a_\parallel} + \frac{(p_{f\perp}-p_{j\perp})(p_{j\perp}+3p_{f\perp})}{4a_\perp} \\ &+ \frac{2\sqrt{\mathrm{U_p}}(p_{f\parallel}-p_{j\parallel})}{a_\parallel^2+\omega^2}\left(a_\parallel\cos(\omega\widetilde{t}) - \omega\sin(\omega\widetilde{t})\right). \end{aligned} \tag{6.50}$$

We will now apply the approximations discussed above to the three main orbits that lead to intra-cycle interference. For interference to occur, they must reach the detector with the same momentum, i.e., $\mathbf{p}_{1f} = \mathbf{p}_{2f} = \mathbf{p}_{3f} = \mathbf{p}_f$. In all cases, we extract the tunnel exits z_{e0} from Eq. (4.15) and the ionisation times t'_{er} from the full CQSFA according to Eqs. (4.26) and (4.25). For orbits 1 and 2, it suffices to assume that (i) $\mathbf{p} = \mathbf{p}_f$ during the continuum propagation in order to calculate the potential integral $\mathcal{I}_{V_C}$; (ii) from the ionisation time t'_r to the end of the pulse, the momentum will tend monotonically to its final value in order to compute the momentum correction $\mathcal{I}_\mathcal{P}$.

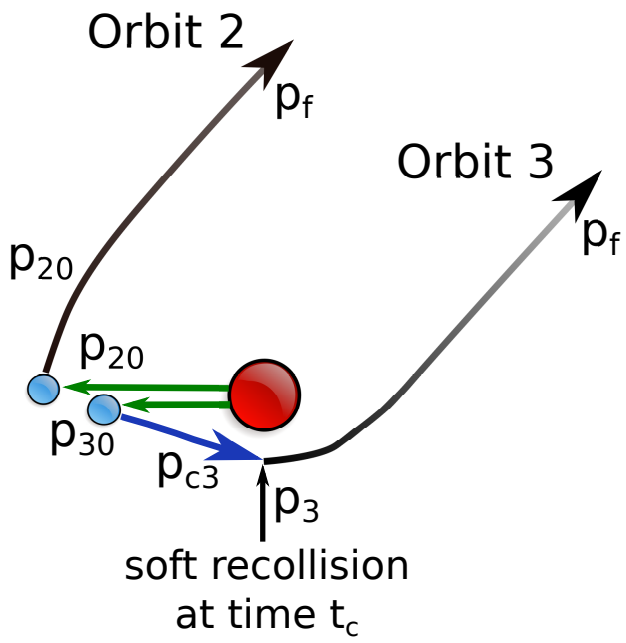

FIGURE 6.4: Schematic representation of the approximations employed in the analytic model for orbits 2 and 3. The first part of the path in green is the tunnel exit, which is modelled as a constant momentum region as in the CQSFA. Then for orbit 2 the field dressed momentum is modelled by exponential decay to the final momentum, the fading black line. For orbit 3 the next segment in blue refers to the also constant momentum $\mathbf{p}_{3c}$ and is chosen such that a soft recollision ($r_{\parallel}(t_c) = 0$) will occur at the same time as in the CQSFA denoted t_c. Then orbit 3 is also described by an exponential decay from momentum $\mathbf{p}_3$ to the final momentum $\mathbf{p}_f$. Here, $\mathbf{p}_3$ is calculated by assuming an elastic collision, that scatters in electron towards the direction of the final momentum $\mathbf{p}_f$.

In contrast, for orbit 3, one must incorporate a soft collision with the core in order to reproduce the spider-like structure[2]. Specifically, we assume that the electron will follow a constant-momentum trajectory with a momentum $\mathbf{p} = \mathbf{p}_{3c}$ up to the recollision, and that it will undergo a laser driven soft collision with the core at a time t_c. Immediately after the collision, the electron has a momentum $\mathbf{p}_3$, which is related to the collision momentum $\mathbf{p}_{3c}$ and the final momentum $\mathbf{p}_f$ using several approximations. A schematic representation of the approximations used in order to compute the integrals and phase differences for orbits is plotted in Fig. (6.4). More details are provided below.

[2]We have verified that the approximations employed for orbits 1 and 2 leads to the correct behaviour, for orbit 3 for high photoelectron momenta, but fails to reproduce the spider-like patterns in the intermediate momentum regions. An example will be provided in Fig. (6.10)

6.2.3 Orbits 1 and 2.

Using a monochromatic driving field, and assumptions (i) and (ii), the actions S_e ($e = 1, 2$) associated with orbits 1 and 2 read

$$\begin{aligned} S_e(\tilde{\mathbf{p}}, \mathbf{r}, t, t'_e) &= (\mathrm{I_p} + \mathrm{U_p})\, t'_e + \frac{1}{2}\mathbf{p}_f^2 t'_{er} + \frac{i}{2}\mathbf{p}_{e0}^2 t'_{ei} + \frac{\mathrm{U_p}}{2\omega}\sin(2\omega t'_e) \\ &\quad + \frac{2\sqrt{\mathrm{U_p}}}{\omega}\left[p_{e0\parallel}\sin(\omega t'_e) - (p_{e0\parallel} - p_{f\parallel})\sin(\omega t'_{er})\right] - \underbrace{\int_{t'_e}^{t'_{er}} V(\mathbf{r}_{e0}(\tau))\mathrm{d}\tau}_{\mathcal{I}_{V_T}^{(e)}} \\ &\quad \underbrace{-\frac{1}{2}\int_{t'_{er}}^{t} \boldsymbol{\mathcal{P}}_e(\tau)\cdot(\boldsymbol{\mathcal{P}}_e(\tau) + 2\mathbf{p}_f + 2\mathbf{A}(\tau))\mathrm{d}\tau}_{\mathcal{I}_{\mathcal{P}_e}} - \underbrace{\int_{t'_{er}}^{t} V(\mathbf{r}_{ec}(\tau))\mathrm{d}\tau}_{\mathcal{I}_{V_C}^{(e)}}. \end{aligned} \tag{6.51}$$

The integrals $\mathcal{I}_{V_T}^{(e)}$, $\mathcal{I}_{V_C}^{(e)}$ and $\mathcal{I}_{\mathcal{P}_e}$ are computed as stated below. Note that making $\mathbf{p}_e$ piecewise constant eliminates the term $\mathbf{r}\cdot\dot{\mathbf{p}}$ as given by Eq. (4.20), so that there is no longer a factor 2 multiplying $\mathcal{I}_{V_C}^{(e)}$.

For $\mathcal{I}_{V_C}^{(e)}$, there will be only one interval, i.e., the lower and upper limit are $t'_{er} = \mathrm{Re}[t'_e]$ and t in Eq. (6.44). In the approximated expression (6.46) we take $\mathbf{k}_j = \mathbf{p}_f + \mathbf{A}(\widetilde{t})$, $\mathbf{c}_j = z_{e0}\hat{e}_\parallel$ and $t_j = t'_{er}$, where z_{e0} ($e = 1, 2$) are the tunnel exits for orbits 1 and 2. The time $\widetilde{t}$ is chosen as common to orbits 1 and 2. Since it must guarantee that the Coulomb effects are significant and that both orbits are in the continuum, we consider the times of closest approach for orbits 1 and 2 and take the largest of the two.

One must then compute $\mathcal{I}_e(t - t'_r) - \mathcal{I}_e(0)$, with $t \to \infty$, where $\mathcal{I}_e$ is the indefinite integral given by Eq. (6.47) for $e = 1, 2$. The lower limit reads

$$\lim_{\Delta\tau_e \to 0} \mathcal{I}_e(\Delta\tau_e) = -\frac{C}{|\mathbf{k}_e|}\ln\left[-\mathbf{k}_e\cdot\mathbf{c}_e + |\mathbf{k}_e||\mathbf{c}_e|\right], \tag{6.52}$$

while the upper limit diverges. This divergence will however cancel out for the difference $\Delta\mathcal{I}_{V_C}^{(12)}$=$\mathcal{I}_{V_C}^{(1)}$- $\mathcal{I}_{V_C}^{(2)}$, which is the quantity of interest. The expression for this difference between the two lower limits is

$$\Delta\mathcal{I}_{V_C}^{(ee')} = -\frac{C}{|\mathbf{k}_e|}\ln\left[\frac{(-\mathbf{k}_{e'}\cdot(\mathbf{k}_{e'}\Delta\tau_{e'} + \mathbf{c}_{e'}) + |\mathbf{k}_{e'}||\mathbf{k}_{e'}\Delta\tau_{e'} + \mathbf{c}_{e'}|)}{(-\mathbf{k}_e\cdot(\mathbf{k}_e\Delta\tau_e + \mathbf{c}_e) + |\mathbf{k}_e||\mathbf{k}_e\Delta\tau_e + \mathbf{c}_e|)}\right], \tag{6.53}$$

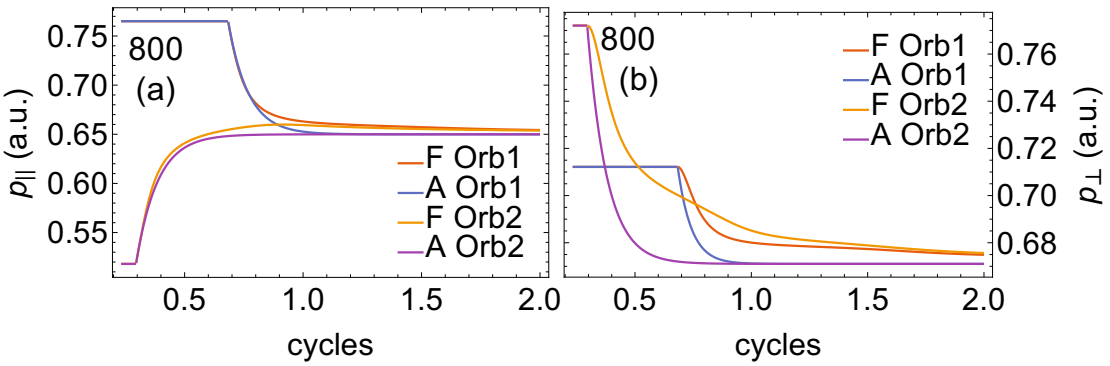

FIGURE 6.5: Exact and analytic intermediate momenta $\mathbf{p}_n$, $(n = 1, 2)$ for orbits 1 and 2 over two field cycles considering a field of intensity $I = 2.0 \times 10^{14}$ W/cm^2 and wavelength $\lambda = 800$ nm. Panels (a) and (b) give the parallel and perpendicular momentum components $p_{\parallel}$ and $p_{\perp}$, respectively. The capital letters F and A refer to the full CQSFA and the analytic approximation, respectively.

where $\Delta\tau_e = \tau - t'_{er}$. Specifically, the upper limit reads

$$\lim_{\tau\to\infty} \Delta\mathcal{I}_{V_C}^{(12)} = -\frac{2C}{|\mathbf{p}_f + \mathbf{A}(\widetilde{t})|} \ln\left(\frac{|z_{20}|}{|z_{10}|}\right), \tag{6.54}$$

which, together with the lower limit difference as stated in Eq. (6.53), is the dominant contribution to intra-cycle interference.

The momentum corrections $\mathcal{I}_{\mathcal{P}_e}$ are computed by taking $\widetilde{t} = t'_{er}$ and $\mathbf{p}_e = \mathbf{p}_{e0}$ $(e = 1, 2)$ in Eqs. (6.48) and (6.49). This is justified by the fact that, for orbits 1 and 2, the intermediate momentum tends monotonically towards the final momentum from the ionisation time to the end of the pulse (see Fig. (6.5)).

The coefficient $a_{e\parallel}$ is evaluated at the tunnel exit and in the parallel direction using the saddle point Eq. (4.19) and the approximate action (6.51). This gives

$$\dot{\mathcal{P}}_{e\parallel}(t'_{er}) = \dot{p}_{e\parallel}(t'_{er}) \implies a_{e\parallel} = -\frac{C}{z_{e0}^2(p_{e0\parallel} - p_{f\parallel})}. \tag{6.55}$$

In order to compute $a_{e\perp}$, one must bear in mind that the electron starts on the parallel axis. Thus, the right hand side of Eq. (4.19) $(\nabla V(\mathbf{r}_0) \cdot \hat{e}_{\perp})$ is zero as $x(t'_r) = 0$. Hence, we take the derivative with respect to time of both sides instead. This yields

$$\ddot{\mathcal{P}}_{e\perp}(t'_{er}) = \ddot{p}_{e\perp}(t'_{er}) \implies a_{e\perp} = -\sqrt{\frac{C p_{e0\perp}}{|z_{e0}|^3(p_{e0\perp} - p_{f\parallel})}}. \tag{6.56}$$

These coefficients are then used in Eq. (6.50) and in the phase difference

$$\Delta\mathcal{I}_{\mathcal{P}_{12}} = \mathcal{I}_{\mathcal{P}_1} - \mathcal{I}_{\mathcal{P}_2}. \tag{6.57}$$

6.2.4 Orbit 3 and rescattering.

Below we discuss the approximations performed for orbit 3. The initial momentum, used in the under-the-barrier trajectories and in $\mathcal{I}^{(3)}_{V_T}$, is p_{30}, and the final (given) momentum is $\mathbf{p}_f$. The continuum propagation will require two subintervals: (i) from the ionisation time $t'_{3r} = \mathrm{Re}[t'_3]$ to a real time t_c for which a soft collision with the core occurs, and (ii) from the recollision time t_c to the final time t, $t \to \infty$. The time t_c is calculated by solving $z(t_c) = 0$ for the CQSFA, and, in agreement with the approximations in this work, is the time $\widetilde{t}$ of closest approach from the core for orbit 3. The collision being soft implies that $x(t_c) \neq 0$. We consider that, from t'_{3r} to t_c, the perpendicular momentum component remains the same, i.e., $p_{3c\perp} = p_{30\perp}$ and the parallel component $p_{3c\parallel}$ is given by

$$\int_{t'_r}^{t_c} (p_{3c\parallel} + A(\tau))\mathrm{d}\tau + z_{30} = 0. \tag{6.58}$$

One should note that the initial parallel momentum $\mathbf{p}_{30\parallel}$ cannot be chosen for this segment. Although the laser is the main driving force for the collision, some electron trajectories additionally require the attraction of the core to collide. Furthermore, the momentum $p_{3c\parallel}$ described by Eq. (6.58) ensures that scattering off the core occurs at the correct time t_c as determined by the CQSFA.

Upon recollision, we assume that the electron momentum changes instantaneously from $\mathbf{p}_{3c}$ to $\mathbf{p}_3$. The latter can be fully determined using the following simplifications: (i) elastic scattering at t_c, i.e., $|\mathbf{p}_{3c}+\mathbf{A}(t_c)|^2 = |\mathbf{p}_3+\mathbf{A}(t_c)|^2$; (ii) the scattering angle remains the same until the end of the pulse, i.e., $p_{3\parallel}/p_{3\perp} = p_{f\parallel}/p_{f\perp}$. Physically, assumption (ii) implies that most of the angular changes occur during the collision and not subsequently. The intermediate momentum $\mathbf{p}_3$ computed as stated above will be employed in the momentum corrections $\mathcal{I}_{\mathcal{P}_3}$, but will not be used in the potential integrals $\mathcal{I}^{(3)}_{V_C}$.

The approximate expression for the action along orbit 3 reads

$$\begin{aligned} S_3(\tilde{\mathbf{p}},\mathbf{r},t,t_3') &= (\mathrm{I_p}+\mathrm{U_p})\,t_3' + \frac{1}{2}(p_{3c\parallel}^2 - p_{30\parallel}^2)t_{3r}' + \frac{1}{2}(\mathbf{p}_f^2 - \mathbf{p}_{3c}^2)t_c + \frac{\mathrm{U_p}}{2\omega}\sin(2\omega t_3') \\ &+ \frac{2\sqrt{\mathrm{U_p}}}{\omega}\left[p_{30\parallel}\sin(\omega t_3') - (p_{30\parallel}-p_{3c\parallel})\sin(\omega t_{3r}') - (p_{3c\parallel}-p_{f\parallel})\sin(\omega t_c)\right] \\ &+ \mathcal{I}_{\mathcal{P}_3} + \mathcal{I}_{V_T}^{(3)} + \mathcal{I}_{V_C}^{(3)}, \end{aligned} \tag{6.59}$$

where the first two lines give a SFA-like action, and the remaining terms yield the corrections. One should note that the above-stated equation differs from Eq. (6.17) in the sense that the change of momentum at the scattering time t_c has been incorporated. This is consistent with the fact that orbit 3 lies beyond the scope of the SFA transition amplitude for direct ATI electrons [79, 99].

The tunnel integral

$$\mathcal{I}_{V_T}^{(3)} = -\int_{t_3'}^{t_{3r}'} V(\mathbf{r}_{30}(\tau))\mathrm{d}\tau \tag{6.60}$$

is approximated by Eq. (6.40). The Coulomb integral $\mathcal{I}_{V_C}^{(3)}$ in the continuum must be considered within two subintervals: (i) from the ionisation time t_r' to the collision time t_c, and (ii) from the collision time t_c to the final time t, $t\to\infty$. Explicitly,

$$\mathcal{I}_{V_C}^{(3)} = -\int_{t_{3r}'}^{t_c} V(\mathbf{r}_{3c}(\tau))\mathrm{d}\tau - \int_{t_c}^{t} V(\mathbf{r}_{3f}(\tau))\mathrm{d}\tau, \tag{6.61}$$

where

$$\mathbf{r}_{3c}(\tau) = \int_{t_{er}'}^{\tau}(\mathbf{p}_{3c}+\mathbf{A}(\tau'))\mathrm{d}\tau' + \underbrace{\mathrm{Re}[\mathbf{r}_{30}(t_{3r}')]}_{z_{30}\hat{e}_\parallel} \tag{6.62}$$

and

$$\mathbf{r}_{3\mathrm{f}}(\tau) = \int_{t_c}^{\tau}(\mathbf{p}_f+\mathbf{A}(\tau'))\mathrm{d}\tau' + \mathbf{r}_{3c}(t_c). \tag{6.63}$$

For both integrals we take $A(\tau')\approx A(t_c)$, as the collision time is when the contributions of the binding potential are expected to be most relevant. This is again using the long wavelength approximation to zeroth order, and gives $\mathbf{k}_{3f}=\mathbf{p}_f+\mathbf{A}(t_c)$ for Eq. (6.63). In order to compute the continuum phase differences, it is convenient to rewrite Eq. (6.62) using the assumptions stated above. Eq. (6.58) provides us with the tunnel exit z_{30},

which, if combined with the parallel component of $\mathbf{r}_{3c}(\tau)$ gives

$$r_{3c\parallel}(\tau) = \int_{t_c}^{\tau} [p_{3c\parallel} + A(\tau')]\mathrm{d}\tau' \approx [p_{3c\parallel} + A(t_c)](\tau - t_c). \tag{6.64}$$

Constant $p_{3\perp}$ between ionisation and recollision times, i.e., $p_{3c\perp} = p_{30\perp}$, then yields

$$\mathbf{r}_{3c}(\tau) = [p_{3c\parallel} + A(t_c)](\tau - t_c)\hat{e}_{\parallel} + p_{0\perp}(\tau - t'_r)\hat{e}_{\perp}, \tag{6.65}$$

which can be rewritten as

$$\mathbf{r}_{3c}(\tau) = \mathbf{k}_{3c}(\tau - t_c) + \mathbf{c}_3, \tag{6.66}$$

with $\mathbf{k}_{3c} = \mathbf{p}_{3c} + \mathbf{A}(t_c)$ and $\mathbf{c}_3 = p_{30\perp}(t_c - t'_{3r})\hat{e}_{\perp}$. Similarly,

$$\mathbf{r}_{3f}(\tau) = \mathbf{k}_f(\tau - t_c) + \mathbf{c}_3, \tag{6.67}$$

with $\mathbf{k}_f = \mathbf{p}_f + \mathbf{A}(t_c)$. We will now use Eq. (6.47) to solve the two integrals in Eq. (6.61). For the first subinterval, we have

$$\mathcal{I}_{\mathrm{col}} = -\int_{t'_{3r}}^{t_c} V(\mathbf{r}_{3c}(\tau))\mathrm{d}\tau = \lim_{\Delta\tau_c \to 0} \mathcal{I}_3(\Delta\tau_c) - \mathcal{I}_3(t'_{3r} - t_c). \tag{6.68}$$

This gives

$$\mathcal{I}_{\mathrm{col}} = -\frac{C}{|\mathbf{k}_{3c}|} \ln\left[\frac{-\mathbf{k}_{3c}\cdot\mathbf{c}_{3c} + |\mathbf{k}_{3c}||\mathbf{c}_{3c}|}{-\mathbf{k}_{3c}\cdot(\mathbf{k}_{3c}(t'_r - t_c) + \mathbf{c}_{3c}) + |\mathbf{k}_{3c}||\mathbf{k}_{3c}(t'_r - t_c) + \mathbf{c}_{3c}|}\right], \tag{6.69}$$

which can be simplified further to

$$\begin{aligned}\mathcal{I}_{\mathrm{col}} &= -\frac{C}{|\mathbf{k}_{3c}|} \ln\left[\frac{-p_{30\perp}^2(t_c - t'_{3r}) + |p_{30\perp}||k_{3c}||t_c - t'_{3r}|}{(p_{3c\parallel} + A(t_c))^2(t_c - t'_{3r}) + |k_{3c}||p_{3c\parallel} + A(t_c)||t_c - t'_{3r}|}\right] \\ &= -\frac{C}{|\mathbf{k}_{3c}|} \ln\left[\frac{-p_{30\perp}^2 + |\mathbf{k}_{3c}||p_{30\perp}|}{(p_{3c\parallel} + A(t_c))^2 + |\mathbf{k}_{3c}||p_{3c\parallel} + A(t_c)|}\right].\end{aligned} \tag{6.70}$$

The second integral is computed in a similar way as those in Sec. 6.2.3, with the difference that the common time will be the recollision time t_c for orbit 3. Explicitly, the upper limit for the Coulomb phase difference between orbit 3 and one of the other two

orbits, as discussed in Sec. 6.2.3, will be

$$\lim_{\tau\to\infty}\Delta\mathcal{I}_{V_C}^{(e3)} = -\frac{2C}{|\mathbf{k}_f|}\ln\left(\frac{p_{30\perp}^2(p_{f\parallel}+A_\parallel(t_c))^2(t_c-t'_{3r})^2}{p_{f\perp}^2 z_{e0}^2}\right), \tag{6.71}$$

with $e = 1, 2$. The lower limit can be computed from Eq. (6.52) and Eq. (6.70) directly. The momentum integral $\mathcal{I}_{\mathcal{P}_3}$ is computed assuming an exponential decay from the recollision time t_c to the final time $t \to \infty$. Prior to that, the momentum $\mathbf{p}_3$ is assumed to be constant and equal to $(p_{3\parallel}, p_{3\perp}) = (p_{3c\parallel}, p_{30\perp})$ and the resulting phase shift is incorporated in the SFA-like part of the action. This means that, in Eq. (6.48)-(6.50), $\mathbf{p}_j = \mathbf{p}_3$, which is determined according to the simplification (ii) specified above, and the closest approach time is taken as $\widetilde{t} = t_c$. A further subtlety is that, in order to obtain the coefficient $a_{3\parallel}$ from the action (6.59), one must use the derivative of Eq. (4.19) as $z(t_c) = 0$, so that

$$\ddot{\mathcal{P}}_{3\parallel}(t_c) = \ddot{p}_{3\parallel}(t_c) \implies a_{3\parallel} = -\sqrt{\frac{Cp_{3\parallel}}{|p_{30\perp}|^3|p_{3\parallel}-p_{3f\parallel}|(t_c-t'_{3r})^3}}. \tag{6.72}$$

Finally, for the perpendicular direction,

$$\dot{\mathcal{P}}_{3\perp}(t_c) = \dot{p}_{3\perp}(t_c) \implies a_{3\perp} = -\frac{C}{p_{30\perp}^2(p_{3\perp}-p_{3f\perp})(t_c-t'_{er})^2}. \tag{6.73}$$

One should note that, in the above-stated equation, it was not necessary to take the time derivative of Eq. (4.19) as the transverse component $x(t_c) \neq 0$. Phase differences due to the momentum changes are then computed by taking $\Delta\mathcal{I}_{\mathcal{P}_{e3}} = \mathcal{I}_{\mathcal{P}_e} - \mathcal{I}_{\mathcal{P}_3}$, with $e = 1, 2$. Now all parts have been computed necessary to calculating the action in the semi-analytic model for orbits 1-3. So we can use this to compute PADs and compare with the full CQSFA and solutions of the TDSE.

6.3 Replicating Holographic Structures

In Fig. (6.6), we compare PADs computed using different means over four driving-field cycles. This includes the full CQSFA spectra with and without prefactors, the full solution of the time-dependent Schrödinger equation (TDSE), computed with the freely available

software Qprop [125], and the analytic expressions derived in the previous sections. All PADs exhibit a myriad of patterns, including the rings caused by inter-cycle interference, the spider-like patterns near the polarisation axis that result from the interference of orbits 2 and 3, and the near-threshold, fan-shaped structures caused by the interference of orbits 1 and 2.

In general, the full CQSFA and TDSE solutions, shown in the second right [panels (c), (g) and (k)] and right [panels (d), (h) and (l)] columns, exhibit a very good agreement. However, the CQSFA underestimates the signal near the origin and the polarisation axis, differs from the full TSDE solution around the $p_\perp$ axis and leads to different slopes for the spider. The discrepancy near the origin may be attributed to several approximations made in the CQSFA, such as neglecting bound-state depletion and ionisation pathways involving excited states. Furthermore, one assumes that the main ionisation mechanism is tunnel ionisation. For that reason, the Keldysh parameter $\gamma = \sqrt{I_p/(2U_p)}$ has been kept fixed and well within the tunnelling regime. However, this only indicates the prevalent ionisation mechanism, but it does not rule out above-the-barrier or multiphoton ionisation. The agreement between the slopes of the spider-like patterns worsens for decreasing driving-field wavelength. It is quite good for $\lambda = 1300$ nm [panels (c), and (d)], reasonable for $\lambda = 800$ nm [panels (g) and (h)] and poor for $\lambda = 590$ nm. As the wavelength decreases, the TDSE slope moves away from the polarisation axis, while its CQSFA counterpart remains nearly horizontal. This is likely to be caused by the longer electron excursion amplitudes in the mid-IR regime, which increase the influence of the driving field and reduce the role of the Coulomb potential. Finally, orbit 4 has not been included in our computations and will play a role near the $p_\perp$ axis, with the spiral-like fringes interplaying with the ATI rings.

In the two left panels of Fig. (6.6), we compare the full CQSFA and the analytic approximation as derived in Sec. 6.2. This comparison can only be performed if one leaves out the prefactors, as they have not been included in the approximate expressions. They play a secondary, but important role in the PADs, by determining the relative weight between the orbits, their stability and wave-packet spreading. This makes all PADs more uniformly distributed in momentum space, instead of concentrated around the polarisation axis, and modifies the interference patterns. In the absence of prefactors, the

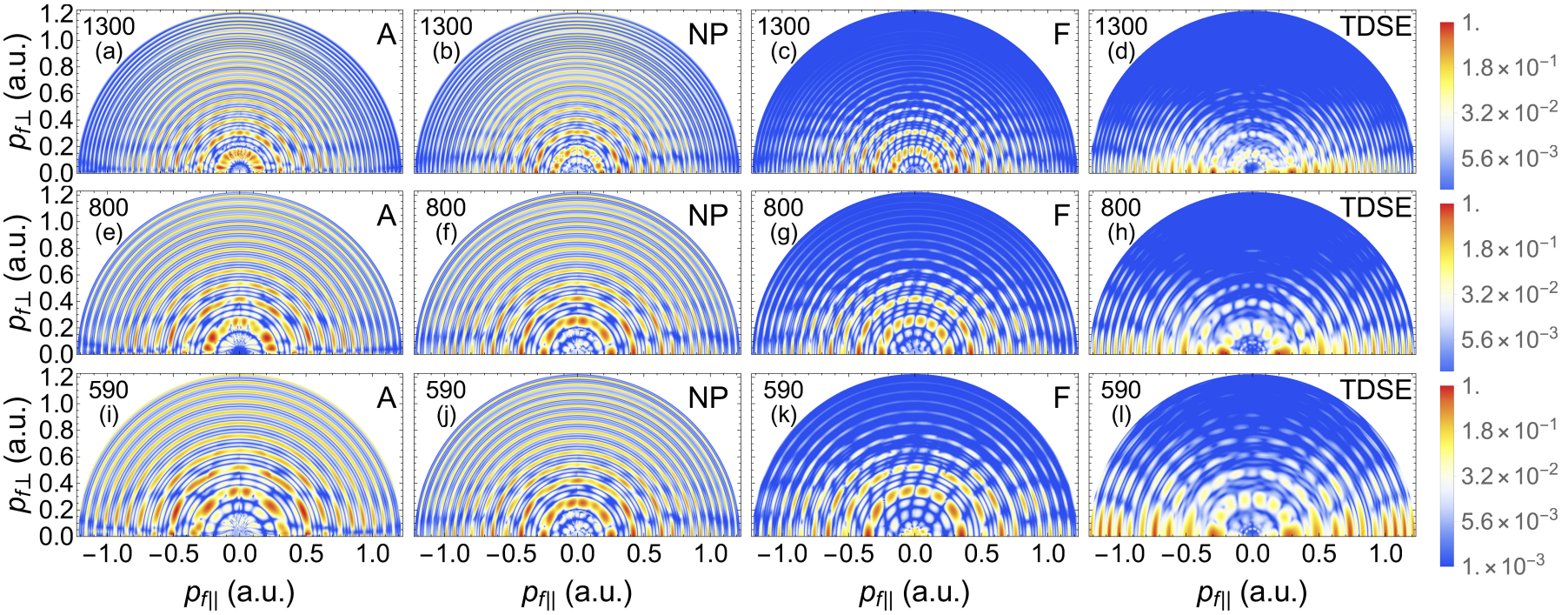

FIGURE 6.6: ATI PADs computed with the analytic condition (left column, denoted by (A), the CQSFA solution without prefactors (second left column, denoted by NP), the full CQSFA solution (second right column, denoted by (F) and the TDSE (right column, denoted by TDSE) for hydrogen ($I_p = 0.5$ a.u.) over four driving-field cycles. A trapezium envelope was used for the TDSE results, where the flat top part was four cycles with a half-cycle ramp on and off. The lower case letters on the top left corner [panels (a) to (l)] correspond to the field parameters $(I, \lambda) = (7.5\times10^{13}\ \mathrm{W/cm^2}, 1300\ \mathrm{nm})$ [panels (a) to (d)], $(I, \lambda) = (2.0\times10^{14}\ \mathrm{W/cm^2}, 800\ \mathrm{nm})$ [panels (e) to (h)] and $(I, \lambda) = (3.75\times10^{14}\ \mathrm{W/cm^2}, 590\ \mathrm{nm})$ [panels (i) to (l)], where I and λ give the field intensity and wavelength, respectively. The density plots have been plotted in a logarithmic scale and normalised to the highest yield in each panel. The numbers on the top left corner of each panel give the driving-field wavelength.

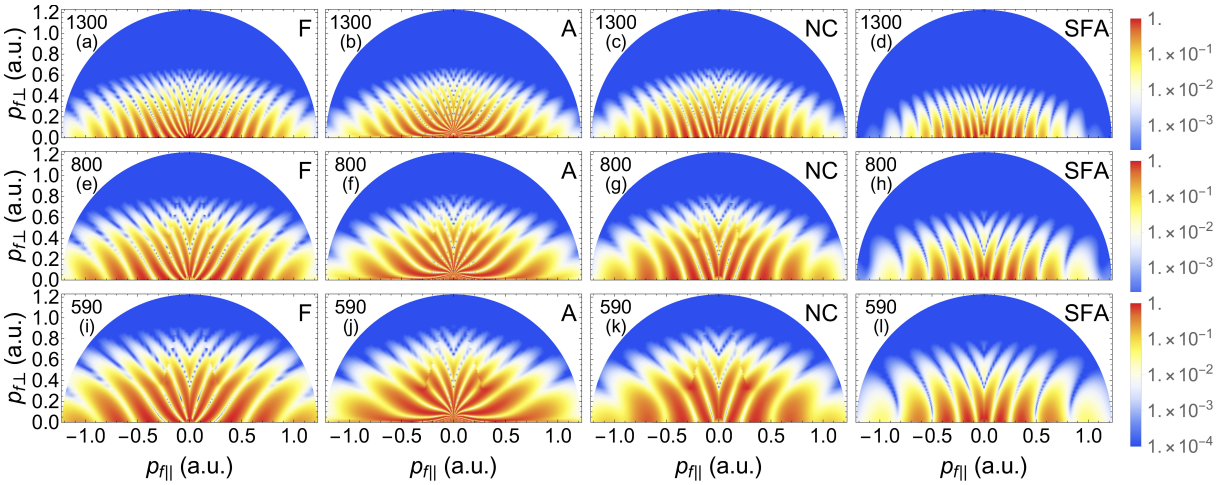

FIGURE 6.7: Fan-shaped holographic structures computed for hydrogen using orbits 1 and 2 and symmetrising upon $p_{\parallel} = 0$ so that $\mathrm{Re}[t_1 - t_2]$ is smaller than or at most equal to half a field cycle. The left columns [panels (a), (e) and (i)] provide the numerical CQSFA solution without prefactor, the second left column [panels (b), (f) and (j)] show the analytical approximations, the second right column [panels (c), (g) and (k)] display the analytical model without the Coulomb phases $\mathcal{I}_{V_C}$, and the far right column [panels (d), (h) and (l)] show the equivalent patterns for the SFA-like term in the action. The field parameters for the first, second and third row are the same as in Fig. (6.6). The probability densities have been normalised to the maximum yield in each panel and plotted in a logarithmic scale. The upper-case letters F, A, NC and SFA on the top right corners of each panel mean full CQSFA, analytic CQSFA, CQSFA with no Coulomb integral and the SFA-like part of the transition amplitude, where the integral corrections are not included, respectively. The numbers on the top left corner of each panel indicate the driving-field wavelength.

CSQFA fringes appear more blurred and blotched, and there is good agreement with the analytic expressions for a wide range of driving-field parameters. Thus, the additional approximations carried out in the previous section can be used in analysing specific holographic patterns more closely.

Coulomb effects in intra-cycle interference

We will next employ the analytic approximations to assess what influence the propagation integrals $\mathcal{I}_{V_C}$ and $\mathcal{I}_{\mathcal{P}}$, in addition to the SFA-like terms, have on intra-cycle interference patterns. Fig. (6.7) displays the fan-shaped structure, which, in Chapter 5, was shown to result from the intra-cycle interference of types 1 and 2 orbits [80, 102], provided that $\mathrm{Re}[t_{2c} - t_{1c}] \leq \pi/\omega$. The figure shows that the analytic model overestimates the diverging behaviour of this structure due to the Coulomb phase, in comparison to

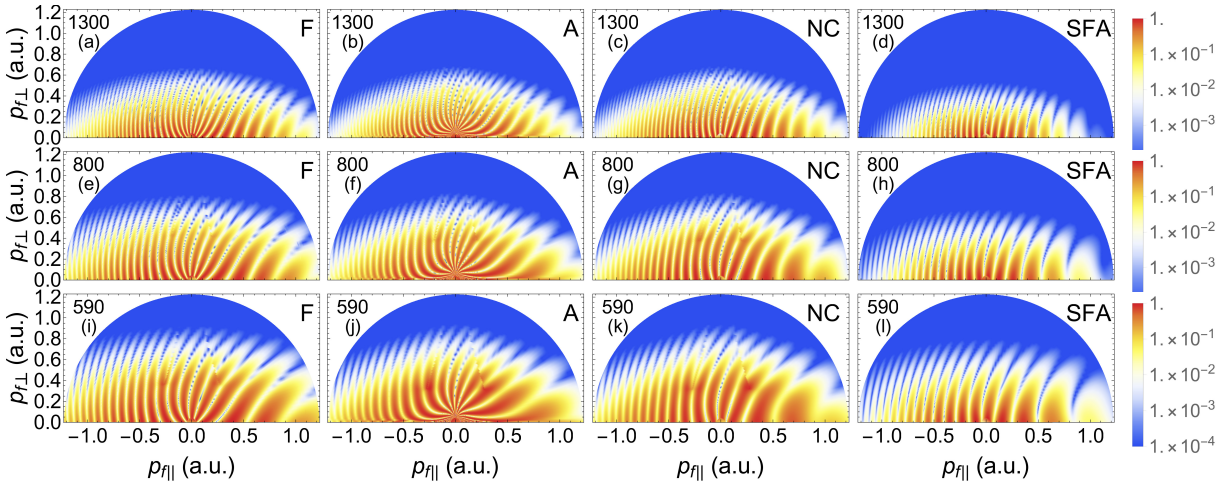

FIGURE 6.8: Holographic structures stemming from the interference of orbits 1 and 2 computed without symmetrisation and relaxing the restriction upon the ionisation times t_1 and t_2. We use the same field and atomic parameters, and the same notation as in Fig. (6.7). The probability densities have been normalised to the maximum yield in each panel and plotted in a logarithmic scale.

the full CQSFA for a wide range of field parameters. This is expected, as it has been constructed around the times $\widetilde{t}$ for which the Coulomb potential is most important, whose long tail causes the fringes to diverge. A legitimate question is where this influence is the most critical: is it via the Coulomb phase difference Eq. (6.54) or via the momentum corrections Eq. (6.57)? In Figs. (6.7) (c), (g) and (k), we remove the Coulomb phase difference from the analytic expressions, and find that the slope of the distributions changes considerably. Furthermore, the Coulomb phase causes a narrowing of the fringes near the origin, where the effect of the Coulomb potential is the largest, which is lost when this term is removed. This can be observed to lesser extent in the full CQSFA plots, Figs. (6.7) (a), (e) and (i). Still, both the momentum and Coulomb integrals contribute as the PADs computed using Eq. (6.51) without such integrals, displayed in the far right panels of the figure, are markedly different. This shows that all corrections are important in forming the fan, but that $\mathcal{I}_{V_C}^{(12)}$ is the most important contribution.

This situation persists if the restriction $\mathrm{Re}[t_{2c} - t_{1c}] \leq \pi/\omega$ is relaxed and other types of intra-cycle interference between orbit 1 and 2 are present. This can be seen in Fig. (6.8), which shows that the absence of the Coulomb phase $\mathcal{I}_{V_C}^{(12)}$ causes the interference patterns to become much closer to those obtained with the SFA. Overall, we also see that the fringes become thicker as the driving-field wavelength decreases.

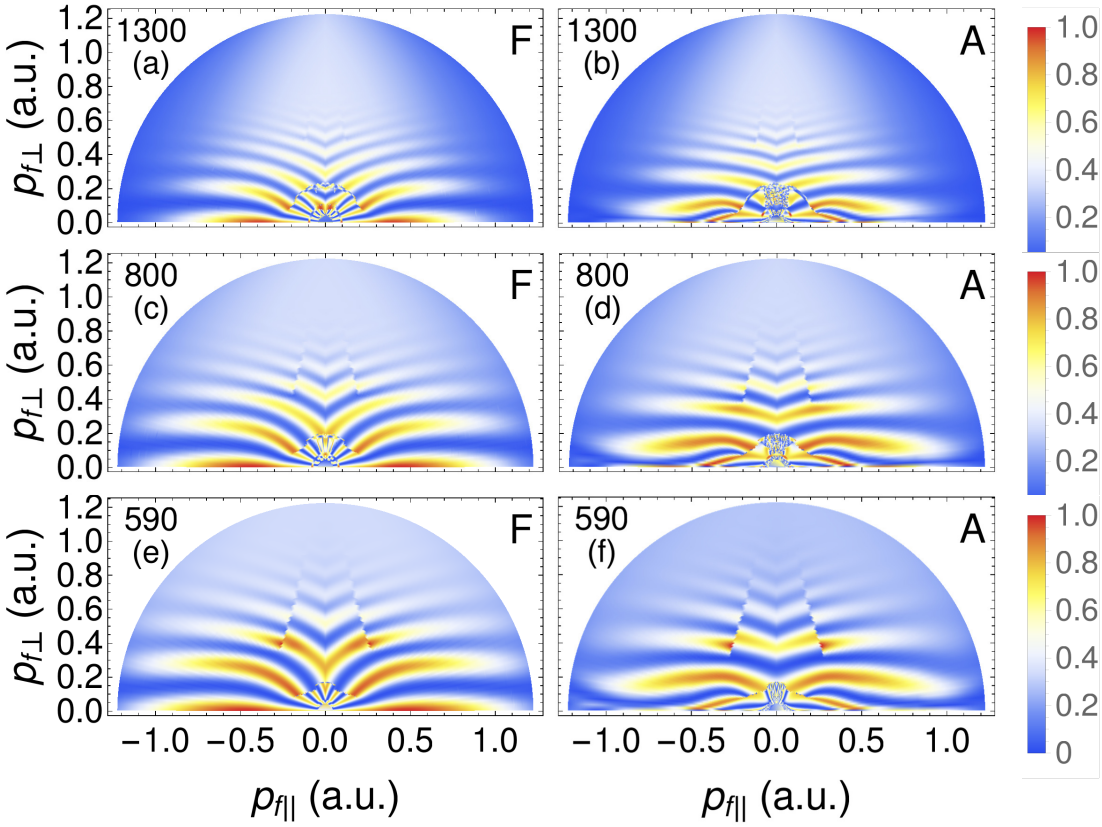

FIGURE 6.9: Spider-like structures stemming from the interference of orbits 1 and 2, computed for the same field and atomic parameters, no prefactors, and using the same notation as in Figs. (6.7) and (6.8). The left and the right column have been computed using the full CQSFA and its analytical counterpart, respectively. This is indicated by the capital letters F and A in the top right corner of each panel. The probability densities have been normalised to the maximum yield in each panel and plotted in a linear scale.

Physically, this is consistent with the fact that, for longer wavelengths, the electron excursion lengths in the continuum are larger. This clearly plays a role in increasing the phase difference as orbits 1 and 2 start in different half cycles of the field.

Fig. (6.9) shows the spider-like structures computed with the full and analytic CQSFA. Overall, we see that the slope of the full solution is nearly horizontal, while the slope of the analytic solution is somewhat distorted. This is consistent with the fact that the bending is caused by the Coulomb phases in the continuum, which are overestimated in the analytic model. The figure also shows a series of features, which are in agreement with existing experiments [23]. For instance, the fringes broaden for increasing frequency. There is also a scaling behaviour, which gives the impression that the spider-like fringes are “zoomed" out for increasing wavelength.

Interestingly, the fringe spacing in Fig. (6.9) changes by half the amount of the remaining holographic patterns with the driving-field wavelength. In fact, if the wavelength is changed from 1300 nm to 590 nm, the fringe spacing doubles for the fan and for the interference patterns stemming from orbits 1 and 3. This is due to the fact that orbits 2 and 3 start in the same half cycle of the field. However, the change in fringe spacing for the spider-like structure is still comparable to the experimental findings. An example can seen in [23], where the spider fringe spacing changes by around 60% when the frequency is doubled, compared to a change of around 50% in the CQSFA as the frequency is increased by a factor of 2.2. The difference may be due to the fact that [23] uses a much longer wavelength 8 μm - 16 μm, which leads to a much lower Keldysh parameter.

Another noteworthy feature is that, near the origin, there are secondary spider-like structures in the full CQSFA, which are associated with multiple scattering events. They are particularly clear in Fig. (6.9)(a) for a wavelength of 1300 nm. This can be associated with the number of field cycles before rescattering; 1, 3 and 5 cycles relate to the outer, inner and "inner-inner" spider patterns, respectively [61, 106, 121]. The splitting is partially recovered in the analytic model, but cannot be fully accounted for as it only allows one 'soft-scattering'/close return of the electron. Such soft scattering trajectories have been directly related to the low energy structure (LES) [58, 61, 64]. In the full CQSFA, the splitting is clearly visible. There is however room for improvement in the treatment of orbits with multiple passes, whose nature is irregular. In addition to that, there are discontinuities in the fringes near the transverse momentum axis, which are more prominent in the high-frequency regime. These are artefacts of the model due to branch cuts in our contour. We have verified this by removing the under-the-barrier Coulomb integral in the analytic model, which removes the discontinuities. These discontinuities play only a secondary role in the full CQSFA PADs, as the yield related to orbits 2 and 3 is strongly suppressed near the perpendicular momentum axis when the prefactor is included.

Fig. (6.10) provides additional insight on how the Coulomb potential affects the spider. Its influence occurs in three main ways: (i) It contributes to the Coulomb phases and to the phase difference $\mathcal{I}_{V_C}^{(23)}$; (ii) it accelerates the electron, which within our model

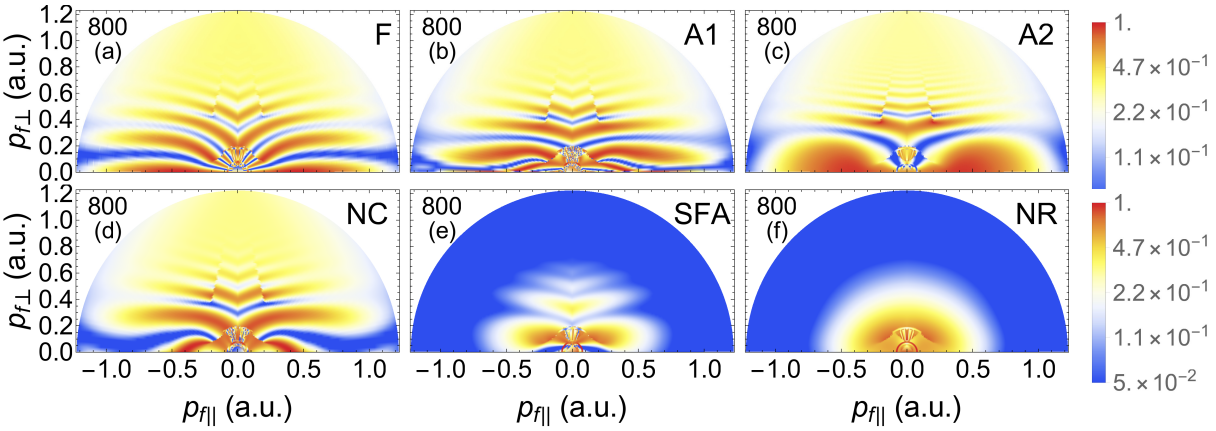

FIGURE 6.10: Spider-like structures computed for hydrogen in a field of intensity $I = 2.0 \times 10^{14}$ W/cm^2 and wavelength $\lambda = 800$ nm using the full CQSFA [panel (a); indicated by F], the analytic CQSFA model with and without rescattering [panels (b) and (c); indicated by A1 and A2, respectively], the CQSFA without the Coulomb phases $\mathcal{I}_{V_C}$ [panel (d); indicated by NC], the SFA-like part of the action, for which the potential and momentum integrals in the have been neglected in the continuum propagation [panel (e); indicated by SFA] and the SFA-like part of the action without rescattering [panel (f); indicated by NR]. The probability densities have been normalised to the maximum yield in each panel and plotted in a logarithmic scale.

is taken into account in the momentum integral $\mathcal{I}_{\mathcal{P}}$ and the phase difference $\mathcal{I}_{\mathcal{P}_{23}}$; (iii) it causes the electron along orbit 3 to rescatter with the core. The main effect of the Coulomb phase in (i) is to bring the fringes of the spider upwards. This can be readily seen by comparing Figs. (6.10)(b) and (d), for which these integrals are present and absent, respectively. If the influence of the Coulomb potential is accounted for only as (ii) and (iii) the spider fringes bend downwards, and even cross the $p_{\parallel}$ axis. Fig. (6.10)(c) models orbit 3 within the CQSFA in a similar way as for orbits 1 and 2, i.e., incorporating the Coulomb potential but without rescattering. In this case, the fringes near the axis and the central part of the spider vanish. This shows that considering the binding potential only via (i) and (ii) does not suffice for a correct description of orbit 3. Furthermore, the spider will only extend towards high photoelectron momenta if the acceleration by the potential as described in (ii) is incorporated. This is clearly seen in Fig. (6.10)(e), for which both the Coulomb and the momentum integral are absent. In this case, only the central part of the spider is present, and the photoelectron energy extends to roughly $2U_p = 0.88$ a.u., which is the direct ATI cutoff as given by the SFA. Finally, if neither rescattering for orbit 3 nor the corrections $\mathcal{I}_{V_C}$ and $\mathcal{I}_{\mathcal{P}}$ are present, the

distribution resembles what is obtained for a single-orbit direct ATI PAD in the standard SFA, i.e., a single peak around $(p_{\parallel}, p_{\perp}) = (0, 0)$, which extends to the maximum energy of around $2U_p$. Physically, this could be loosely understood as an SFA-like model with two long orbits, which carry slightly different ionisation times and momenta. This very small difference would lead to very thick interference fringes, which will lie beyond the cutoff energy.

6.4 Discussion

In this chapter, we derived conditions for interference patterns, which are kept as general as possible with regard to the number of field cycles and events per cycle, and provide an analytic expression determining the overall shapes of the distributions. Using properties related to the field being monochromatic, we show analytically that the intercycle interference condition is the same for both the SFA and CQSFA. The shape of the distributions and other features will however be affected by the Coulomb potential. The sub-barrier integral over the binding potential is also computed analytically, and is shown to exert a strong influence on the shapes of the PADs.

We also provide analytic expressions for Coulomb corrected above-threshold ionisation (ATI) dynamics based on the previously developed Coulomb quantum orbit strong-field approximation (CQSFA) [79, 80, 102], which allows a direct computation of quantum-interference patterns in photoelectron angular distributions (PADs). This approach is more refined than the analytic methods existing in the literature, as it includes the Coulomb potential in the ionisation and continuum propagation dynamics. The former is important in determining the shapes of the electron-momentum distributions, and the latter allows us to reproduce patterns commonly encountered in photoelectron holography, such as the fan- and spider-like structures. In the ionisation dynamics, the main piece of information are the times and the momenta with which the electron reaches the continuum, and how this alters the electron momentum distribution. In the continuum dynamics, the influence of the Coulomb potential manifests itself as (a) a Coulomb phase, which is accumulated during the electron propagation; (b) phase differences due to changes in the electron momentum caused by the residual potential,

from the instance of ionisation to the time at which it reaches the detector; (c) in some cases, rescattering does play a role and must be incorporated. This goes beyond most analytic models for holographic photoelectron structures, which are fully classical [66, 106, 121] and/or are SFA-based include at most hard collisions [64, 149]. More sophisticated models focus on the low-energy structures, but do not aim at reproducing holographic patterns [58, 61].

In contrast, we incorporate the effects (a)–(c) in the semiclassical action, which is directly used to computed the PADs and photoelectron patterns. Key approximations consist of assuming that the intermediate electron momenta are piecewise constant when computing the Coulomb phase (a), and monotonically decaying towards its final value when computing the momentum corrections (b). We also expand the external field around the times for which the electron is closest to the core, which are determined from the numerical solution of the CQSFA.

Overall, we reproduce key features observed in intra- and intercycle interference, and obtain a good agreement with the CQSFA, provided the prefactors are neglected. The latter include further momentum bias due to the shapes of the initial bound-states, wave-packet spreading and modify the stability of each type of orbit. In this chapter we used orbits 1-3, which are direct (orbit 1), and forward deflected (orbits 2 and 3). Orbits 1 and 2 exist in the standard strong-field approximation (SFA), for which the influence of the Coulomb potential is neglected in the continuum, while orbit 3 requires the residual Coulomb potential to be present [79, 99]. It behaves in a similar way to the forward scattered orbit present in the SFA model of high-order ATI [64, 149].

The analytic model allows a closer look at how the holographic structures form. For instance, we have previously shown that the fan-shaped structure that forms near the ionisation threshold stems from the interference of types 1 and 2 orbits. The fan arises due to an angle- and momentum dependent distortion caused by the Coulomb potential, which is maximal close to the polarisation axis [80, 102]. An open question was, however, whether this distortion occurred due to the Coulomb phase or the momentum changes caused by the Coulomb potential. In the present work, we find that all Coulomb corrections contribute to the fan. However, the most dramatic effect is caused by the Coulomb phase given by the integrals $\mathcal{I}_{V_C}$, which acts to both straighten and

narrow (near the origin) the fringes to give the characteristic fan shape. Our analytic computations also show that, when modelling orbits 1 and 2, it suffices to include corrections around a model which, in the limit of vanishing Coulomb potential, tends to the SFA without rescattering. This is consistent with the fact that orbits 1 and 2 have well-known SFA counterparts [79, 99] and tend to the SFA in the limit of very large photoelectron momenta [102].

The present results show that the spider-like pattern, caused by the interference of orbits 2 and 3, requires an appreciable acceleration of the electron in the continuum, the Coulomb phase and, above all, rescattering for orbit 3. In fact, analytical Coulomb corrected models similar to those developed by us for orbits 1 and 2 fail to reproduce this structure (see Fig. (6.10)). It was necessary to assume an abrupt momentum change at a rescattering time t_c, which led to a very distinct transition amplitude, see Eq. (6.59). Note that assuming a soft recollision leads to worse agreement in the region very close to the $p_{f\parallel}$ axis. This is due to the fact that orbit 3 undergoes the least interaction with the core near the $p_{f\parallel}$ axis and the orbit is deflected like orbit 2, rather than rescattered. In the limit of vanishing binding potential, Eq. (6.59) does not tend to the direct SFA. This is supported by the fact that an electron along orbit 3 gets much closer to the core and is accelerated for a longer time than for the remaining orbits. Furthermore, orbit 3 does not have an SFA counterpart in direct ATI nor exhibits any high-energy limit that can be traced back to the direct SFA [102]. However, there is some evidence that it could be approximated by a forward scattered SFA orbit in high-order ATI [64] and we will consider this in the next chapter for both orbits 3 and 4. It is indeed noteworthy that, in the full CQSFA, the distinction between direct and rescattered electrons is blurred. In contrast, the assumptions made upon the intermediate momenta in order to compute the corrections used in this work provide a higher degree of control over the presence, absence or nature of the rescattering events taking place. Hence, we can extract the importance of soft rescattering in orbit 3, despite the fact that this orbit can exhibit behaviour that varies between deflection and hard scattering.

Interestingly, the full CQSFA takes into account multiple scattering, which is left out in the analytic effect. This causes the spider-like fringes to split in the low momentum region, leading to several inner spiders. These structures have been reported in [121],

and are more visible for longer wavelengths. Additionally, our results indicate that the Coulomb phase in the continuum is underestimated in the full CQSFA, especially for shorter driving-field wavelengths. This can be seen in the slope of the spider-like structure, which is strongly influenced by the Coulomb phase.

For the CQSFA, the fringes forming the spider are nearly horizontal for all the parameters used, while in their TDSE counterparts the slopes in the mid-IR regime are in agreement with the CQSFA, but increase with the driving-field frequency. Physically, this is related to the fact that, the higher the frequency is, the smaller the electron excursion amplitude in the continuum will be. This means that the electron will spend more time near the core. A distortion in the slope is also observed for the analytical CQSFA model, which overestimates the Coulomb phase by expanding around the times of closest approach to the core [see Figs. (6.9) and (6.10)].

A shortcoming of our approach is that, in its current form, it is not a stand-alone model, as it uses the closest-approach times and initial momenta determined from the CQSFA. It is hence desirable to find an alternative, consistent criterium for determining such times and momenta. This model, however, has much similarity with the SFA model for direct ATI for orbits 1 and 2 and HATI for orbit 3, with the crucial difference that a soft recollision is used here as opposed to a hard one in HATI and in the kinetic energy part of the action the momentum is not constant. Otherwise the piecewise constant nature of the trajectories is very similar to those in direct ATI and HATI and the saddle point equations from these models, which are much simpler to solve than the CQSFA saddle point equations, could be used as starting point to provide the closest-approach times and initial momenta. Another shortcoming is that the regularisation procedure allows some freedom in the normalisation of the orbits, as the divergent part is only pulled out as a common factor for the transition amplitudes for all orbits and is not entirely removed. A preferable regularisation procedure would not have this freedom. It should also be noted that the approximation taken on the electron trajectory during recollision favours high energy collisions. Despite this it works well for the fan-shaped structure near the threshold and for the central part of the spider. These regions exhibit relatively low final momenta. This is due to the fact that, in both cases, the final momentum is low, but the momentum at the collision/closest approach time is often high enough. Further

important issues are how to incorporate multiple rescattering, improve the integration contours in order to avoid branch cuts and to establish a direct connection between the CQSFA, the analytic model and the rescattered ATI transition amplitude computed using the SFA, the latter will be covered in the next chapter. Nonetheless, the analytic approach discussed in this work provides deeper insight into how holographic structures form, and yields a consistent and numerically much cheaper way of computing ATI PADs in the presence of the residual binding potential.

Chapter 7

Recollision and Alternative Orbit Types

In the previous chapter the significance of soft recollision was shown for orbit 3, and some comparison to high-order above threshold ionisation (HATI) orbits was made. In this chapter we will investigate this connection further. We will show that the orbits in the CQSFA will either tend to direct ATI (DATI) or HATI orbits, in the limit of high energy, and this depends on the change in emission angle of the photoelectron orbit. Hence, the CQSFA trajectories are a generalisation of the strong field approximation (SFA) DATI and HATI orbits with these orbits being at the either extreme of a range of possible interactions with the core, from direct/ unaffected (i.e. DATI), to softly rescattered, to hard recollisions (i.e. HATI). We also show that there are additional solutions for the CQSFA orbits 3 and 4, some of which can be related to the softly scattering orbits related to the low-energy structure (LES) and very low-energy structure (VLES) [56, 58, 61, 128, 129]. This chapter is organised as follows. In Sec. 7.1, we perform a detailed analysis of the CQSFA orbits as compared to the DATI and HATI orbits that are present in the SFA. In Sec. 7.2 we refine the standard orbit classification employed in Coulomb-corrected models and we investigate the overall shapes present in single-orbit probability distributions. In particular, we and establish the momentum regions occupied for the CQSFA and rescattered SFA. In Sec. 7.3 we examine all possible interference types and understand them in the context of the orbit dynamics discussed above. Finally, in Sec. 7.4 we state our conclusions.

7.1 Recollision in the Strong Field Approximation

7.1.1 High Order Above Threshold Ionisation

We previously introduced the S-matrix transition amplitude for ATI within the SFA Eq. (4.1), if one incorporates up to a single act of rescattering this gives,

$$M_r(\mathbf{p}) = -\int_{-\infty}^{\infty} \mathrm{d}t \int_{-\infty}^{t} \mathrm{d}t' \, \langle \psi_{\mathbf{p}}^{v}(t)|VU^{v}(t,t')V|\psi_g(t')\rangle \,, \tag{7.1}$$

Where V denotes the Coulomb potential and $U^v(t,t')$ is the Volkov propagator given by Eq. (2.20). This equation would be the first order term in Born-expansion for V, while the DATI transition amplitude, given by Eq. (4.1) would correspond to the zeroth order term. Inserting the definition for the Volkov time evolution operator and rewriting in terms of a semi-classical action and prefactors gives

$$M_r(\mathbf{p}) = -\int_{-\infty}^{\infty} \mathrm{d}t \int_{-\infty}^{t} \mathrm{d}t' \int \mathrm{d}^3k \exp[iS_r(\mathbf{p},\mathbf{k},t,t')]V_{\mathbf{k}0}V_{\mathbf{pk}}, \tag{7.2}$$

where the action is given by

$$S_r(\mathbf{p},\mathbf{k},t,t') = -\frac{1}{2}\int_{t}^{\infty}[\mathbf{p}+\mathbf{A}(\tau)]^2\mathrm{d}\tau - \frac{1}{2}\int_{t'}^{t}[\mathbf{k}+\mathbf{A}(\tau)]^2\mathrm{d}\tau + \mathrm{I_p}t', \tag{7.3}$$

and all the influence of the core is incorporated in the ionisation prefactor

$$V_{\mathbf{k}0} = \langle \mathbf{k}+\mathbf{A}(t)| \, V \, |\Psi_0\rangle \,, \tag{7.4}$$

and in the rescattering prefactor

$$V_{\mathbf{pk}} = \langle \mathbf{p}+\mathbf{A}(t)| \, V \, |\mathbf{k}+\mathbf{A}(t)\rangle \,. \tag{7.5}$$

Eq. (7.2) includes the transition amplitudes associated with direct and rescattered electrons [130]. It is, however, more convenient to employ Eq. (4.1) instead to compute direct-electron contributions. Particularly clear in Eq. (7.2) is a process in which an

electron, initially in a bound state $|\Psi_0(t')\rangle$, is freed at time t', propagates in the continuum with an intermediate momentum $\mathbf{k}$ for $t' < \tau < t$ and recollides with its parent ion at a later time t. Upon recollision, it then acquires the final momentum $\mathbf{p}$. The direct and rescattered transition amplitudes, given by Eqs. (4.1) and (7.2), respectively, are solved using the steepest descent method. This method requires that the actions $S_d(\mathbf{p}, t')$ and $S_r(\mathbf{p}, \mathbf{k}, t, t')$ be stationary. The saddle-point equation obtained from the direct action $S_d(\mathbf{p}, t')$ reads

$$[\mathbf{p} + \mathbf{A}(t')]^2 = -2I_p t', \tag{7.6}$$

which expresses the kinetic energy conservation at the time of ionisation. One should note that Eq. (7.6) has no real solutions, which reflects the fact that tunnel ionisation has no classical counterpart. A formally identical equation is obtained by imposing the condition $\partial S_r(\mathbf{p}, \mathbf{k}, t, t')/\partial t' = 0$, with the final momentum $\mathbf{p}$ being replaced by the intermediate momentum $\mathbf{k}$. This gives

$$[\mathbf{k} + \mathbf{A}(t')]^2 = -2I_p t'. \tag{7.7}$$

The condition $\partial S_r(\mathbf{p}, \mathbf{k}, t, t')/\partial t = 0$ yields the conservation of energy

$$[\mathbf{p} + \mathbf{A}(t)]^2 = [\mathbf{k} + \mathbf{A}(t)]^2 \tag{7.8}$$

upon recollision, and $\partial S_r(\mathbf{p}, \mathbf{k}, t, t')/\partial \mathbf{k} = \mathbf{0}$ leads to the constraint upon the intermediate momentum $\mathbf{k}$

$$\mathbf{k} = -\frac{1}{t - t'} \int_t^{t'} \mathbf{A}(\tau) \mathrm{d}\tau, \tag{7.9}$$

such that it returns to the site of its release, i.e., the origin. Eqs. (7.8) and (7.9) in fact imply that the electron suffers a hard collision as it returns to the origin. These are the same equations employed in [64]. We compute the direct transition amplitude as given in Eq. (4.5) using the standard saddle point approximation, and the rescattering transition amplitude, Eq. (7.2), employing the specific uniform approximation discussed in [132]. Throughout, we will employ the acronyms DATI and HATI for direct and high-order, rescattered ATI, respectively.

7.1.2 Recollision in the CQSFA

We have developed an improved method of solving the saddle-point Eqs. (4.23), (4.19) and (4.18). This method exploits degeneracy between the two orbits in order to solve them. It has allowed us to solve orbit 4, enabling us to probe features like recollision and also find new types of trajectories for orbit 3 and 4, suggesting the orbit classification introduced in the Sec. 5 is too coarse. The gradual deformation of the orbits, that leads them to be degenerate at particular angles is shown in Fig. (7.1). This is achieved by keeping the initial conditions fixed for a particular orbit and varying the final angle θ_f at which the final momentum $\mathbf{p}_f$ is detected from 0 to 2π. The initial conditions are chosen so that the tunnel exit and the perpendicular initial momentum are positive, ($z_0 > 0$, $p_{0\perp} > 0$). This means that the tunnel 'velocity' of the orbits is always along the positive parallel axis and the angle θ_f represent the change in direction from this 'velocity' to the final continuum momentum $\mathbf{p}_f$. This means, following the classification used in [99], the orbits will be categorised as type 1, 2, 3 and 4 for $0 < \theta_f < \pi/2$, $\pi/2 < \theta_f < \pi$, $\pi < \theta_f < 3\pi/2$ and $3\pi/2 < \theta_f < 2\pi$, respectively.

As θ_f moves from one quadrant to the other, the electron trajectories change smoothly from 1 to 4. Hence, the orbits are degenerate precisely at the boundaries between quadrants, i.e. on the axes. In Fig. (7.1) these boundaries are crossed when the thick dashed arrows in the figure become vertical. In fact, a resemblance can be seen very clearly for orbits 1 and 2, as the boundary $\theta_f = \pi/2$ is crossed (see upper two far right panels in Fig. (7.1)). This also holds for orbits 2 and 3, as the boundary $\theta_f = \pi$ is crossed (see left panels for which $\theta_f = 0.957\pi$ and $\theta_f = 1.040\pi$), and for orbits 3 and 4, as the boundary $\theta = 3/2\pi$ is crossed (two lower far right panels). Orbits 1 and 4 cannot be degenerate at $p_{f||} = 0$, $\theta_f = 2\pi, 0$, despite the electron's initial and final momentum being in the same direction for the two orbits. This is because in orbit 4 the electron undergoes a full 2π rotation around the ion, making the orbits qualitatively different.

The degeneracy between the four types of orbits at the boundaries can be exploited when solving the saddle-point Eqs. (4.23), (4.19) and (4.18). Starting from orbit 1 up to orbit 4, one computes each orbit up to the boundary, and uses it to provide initial conditions for the subsequent orbit type. For example, orbit 1 can be used to provide initial conditions for orbit 2 in the neighbourhood of $\theta_f = \pi/2$. Next, orbit 2 may be used

near $\theta_f = \pi$ for solving orbit 3 and so on. This property is more useful with increasing orbit number, as the CQSFA orbits behave less like the DATI orbits in the standard SFA. In fact, this approach is essential for obtaining convergent solutions for orbit 4.

Given that the CQSFA spans these different orbit types, we would like to explore the idea that the CQSFA provides orbits that lie qualitatively between the two extremes of DATI (no collisions) and HATI (hard collisions). In Fig. (7.1) one can see that for low final angle θ_f the electron trajectories behave qualitatively similarly to DATI trajectories. The electron does not revisit the ion and the initial and final momentum are almost the same. For high θ_f the electron trajectories resemble HATI orbits. The electron revisits the core, passing very close to the origin and undergoing what looks like a "hard" collision. There is almost no perpendicular momentum during the collision, in agreement with the saddle-point Eq. (7.9) that gives the electron's intermediate momentum within the SFA. The orbits in-between these angles are less well defined and may be strongly deflected or undergo soft collisions such as those seen in [58, 61, 128]. As such, the CQSFA can be seen to blur the distinction between direct and re-scattered ATI and softly colliding orbits.

In addition, the CQSFA will behave more like the SFA for high energy orbits as there will be less interaction time with the core. We verified that the direct SFA is the high-energy limit of the CQSFA for orbits 1 and 2 in Chapter 5. The angle θ_f will determine whether the CQSFA orbit will tend towards its DATI (low angles) or HATI (high angles) counterpart. In the CQSFA, there can never be any truly "hard" collision (except in the limiting case $\theta_f = 2\pi$) as the electron trajectory will always miss the origin by some amount. In order to make a comparison with the DATI and HATI limits we have identified three important parameters, which determine the kind of collision we are dealing with:

(i) The Bohr radius, whose perimeter is marked on Fig. (7.1) as a solid black circle, and which is indicated in Figs. (7.2) (a) and (b) as a solid line.

(ii) A circle whose radius is the tunnel exit, displayed in Fig. (7.1) in dashed black. This radius is also plotted as the black dashed lines in Figs. (7.2) (a) and (b).

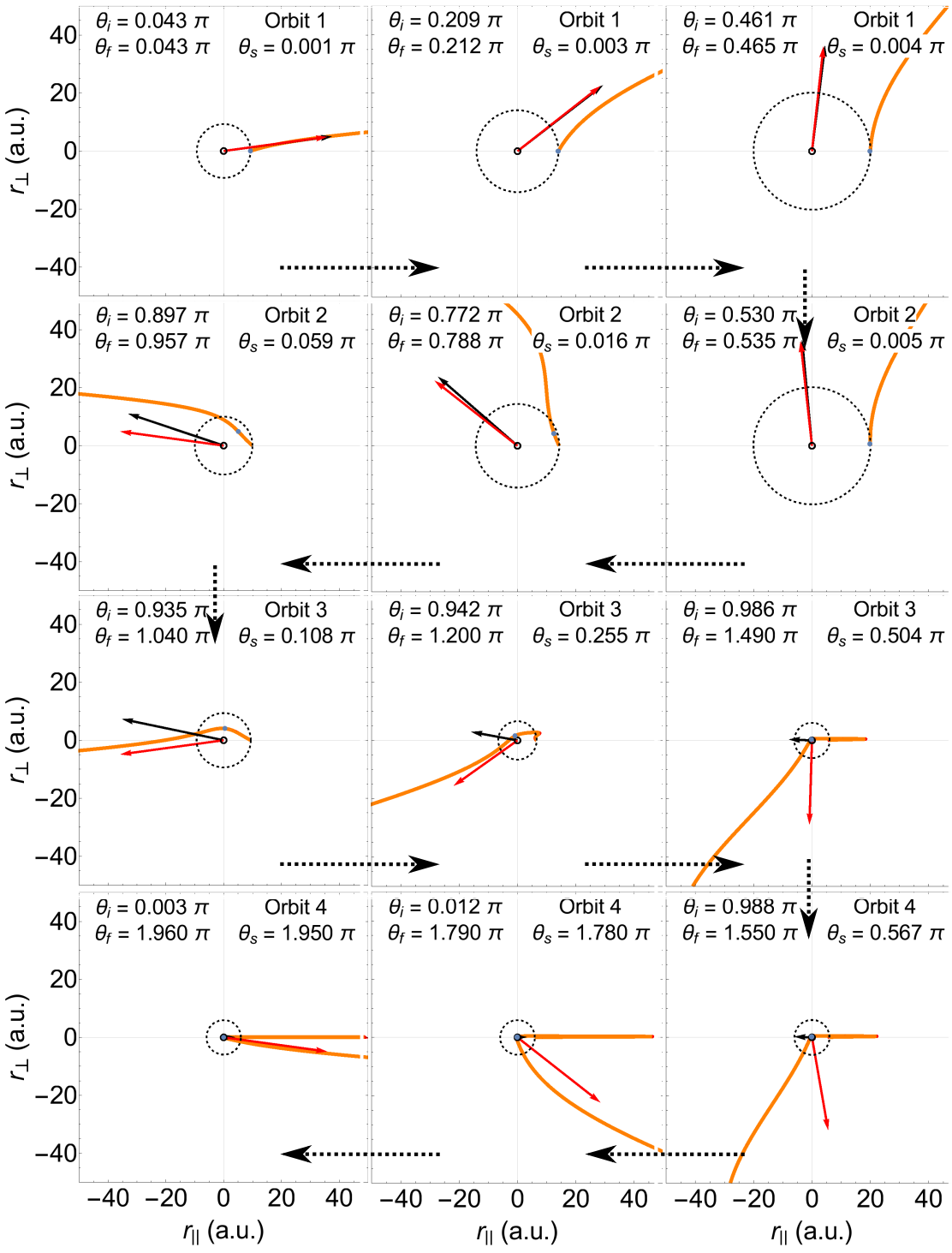

FIGURE 7.1: Electron trajectories calculated using Eqs. (4.19) and (4.18) for fixed energy, $E = 1.3$ a.u. or $E = 3\mathrm{U_p}$, and values of the angle θ_f associated with the final momenta in the range $0 < \theta_f < 2\pi$. Each orange line represents an electron trajectory after tunnelling, while the dotted arrows point in the direction of increasing θ_f. The initial and final momentum vectors are marked on the figure by black and red arrows, respectively. The angles related to the initial and final momentum are given by θ_i and θ_f (top left of each panel), while their difference is given by θ_s (top right of each panel). The orbit type is also marked in the top right corner of each panel. As guides, circles whose radii are the Bohr radius and the tunnel exit are marked in solid black and in dashed black, respectively. We consider a field of wavelength $\lambda = 800$ nm, intensity $I_0 = 2 \times 10^{14}$ W/cm^2 and a model atom with ionisation potential $\mathrm{I_p} = 0.5$ a.u. This gives a ponderomotive energy of $\mathrm{U_p} = 0.439$ a.u.

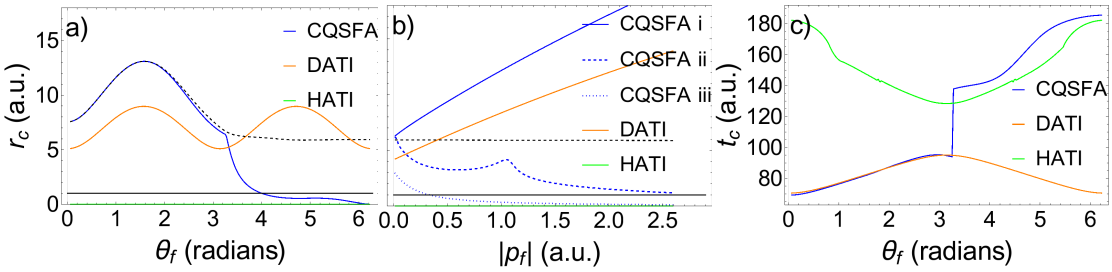

FIGURE 7.2: Distances r_c and time t_c of closest approach are plotted for the CQSFA, DATI and HATI. In panel (a), the distance of closest approach r_c is plotted for a fixed energy $E = 0.26$ a.u., and increasing angle θ_f. The tunnel exit for the CQSFA is plotted in a black dashed line and the Bohr radius is marked with a solid black line. In panel (b), r_c is plotted for three fixed angles for the CQSFA. The indices i, ii and iii correspond to the angles, 0.25π, 1.10π and 1.75π, respectively. The tunnel exit for the CQSFA in case iii is plotted with a black dashed line. For the DATI and HATI, r_c is plotted for a fixed angle of $\theta_f = 1.75\pi$. In panel (c), the time of closest approach t_c is plotted for a fixed energy of $E = 0.26$ a.u. for the CQSFA, DATI and HATI. The same field and atomic parameters have been used as in Fig. (7.1). For HATI we compute θ_f as given in [64].

(iii) The electron's distance r_c of closest approach after tunnelling, indicated in Fig. (7.1) by a blue spot.

If an electron trajectory goes within the region determined by the Bohr radius, we assume it will undergo a "hard" collision as then it will interact as strongly with the core as a bound electron. Furthermore, orbits that do not enter region (ii) can be called direct as outside this perimeter the laser field dominates strongly over the potential. Finally, if the electron's trajectory closest point as defined in (iii) is between regions (i), the Bohr radius, and (ii), the tunnel exit radius, one may view it as softly recolliding. Using these radii as a guide, one can see that orbit 1 may be always classified as a direct electron trajectory. In contrast, an electron along orbit 2 goes from direct to softly rescattered with increasing θ_f. Orbit 3 will change from softly recolliding to a hard collision. Finally, for the parameter range of the figure, orbit 4 always corresponds to a hard collision.

In addition to the above-stated parameters, one may also use the time t_c associated with r_c (the time of closest approach), the time of ionisation t' and the initial momentum $\mathbf{p}_0$ to compare the CQSFA orbits with the DATI and HATI models. These are presented in Figs. (7.2) and (7.3). In Fig. (7.2) (a), we plot r_c for fixed photoelectron energy as a function of the final angle θ_f. For the CQSFA at low angles, r_c (blue line) is the same as the tunnel exit (black dashed line) and the behaviour will mimic DATI (orange line).

However, at $\theta_f = \pi/2$, when the electron trajectory becomes a type 2 orbit, the distance of closest approach moves away from the tunnel exit as the electron goes into the softly recolliding region (see Fig. (7.1)). At $\theta_f \approx 1.1\pi$, there is a change in behaviour, marked by a discontinuous derivative in r_c. As θ_f increases further, the distance of closest approach falls rapidly, until it reaches the Bohr radius, where it levels off. This is not related to the change in orbit type from 2 to 3 at $\theta_f = \pi$. Instead, it is due to the nature of the orbit changing from deflection to hard collision. For $\pi < \theta_f < 1.1\pi$, the electron moves entirely through the soft recolliding region defined by (ii) and the trajectory has a similar initial and final momentum. In contrast, for $\theta_f > 1.3\pi$, the trajectory is initially moved outside of the softly recolliding region by the laser field. Subsequently, the field drives back the electron into the hard collision region. In this latter case, the initial and final momentum are quite different as the electron gains energy in the collision and is scattered through a larger angle. This kind of trajectory closely resembles HATI orbits. This transition can also be seen in the third row of Fig. (7.1). A similar behaviour is displayed for the time t_c of closest approach in Fig. (7.2) (c). For t_c at low angles the CQSFA very closely follows the DATI ionisation time, with a discontinuity for $\theta_f \approx 1.1\pi$. The time of closest approach jumps up at this point as the electron trajectory is now first taken away from the core before revisiting it. Hence, the closest approach occurs later in the orbit. After the transition, t_c follows the HATI recollision time.

The CQSFA distance of closest approach r_c is also plotted for three fixed angles over increasing photoelectron momenta in Fig. (7.2) (b). For $\theta_f = 0.25\pi$, the CQSFA follows the DATI curve and stays on its tunnel exit. For $\theta_f = 1.1\pi$, in the region where orbit 3 undergoes a transition, the CQSFA trajectory remains a softly colliding orbit for all energies staying just above the Bohr radius. For $\theta_f = 1.75\pi$, the CQSFA orbit behaves like a HATI orbit and quickly falls below the Bohr radius with increasing energy. Nonetheless, one should note that, for very low energy, this is a softly-colliding orbit. In this region it behaves similarly to the softly colliding orbits discussed in [58, 128] that are responsible for the low-energy structure (LES).

In Fig. (7.3) we plot the initial time and momentum components for the CQSFA, DATI and HATI (upper and lower panels, respectively). In panel (a), one can see that the real parts of the ionisation times t' are different for the three approaches. This is

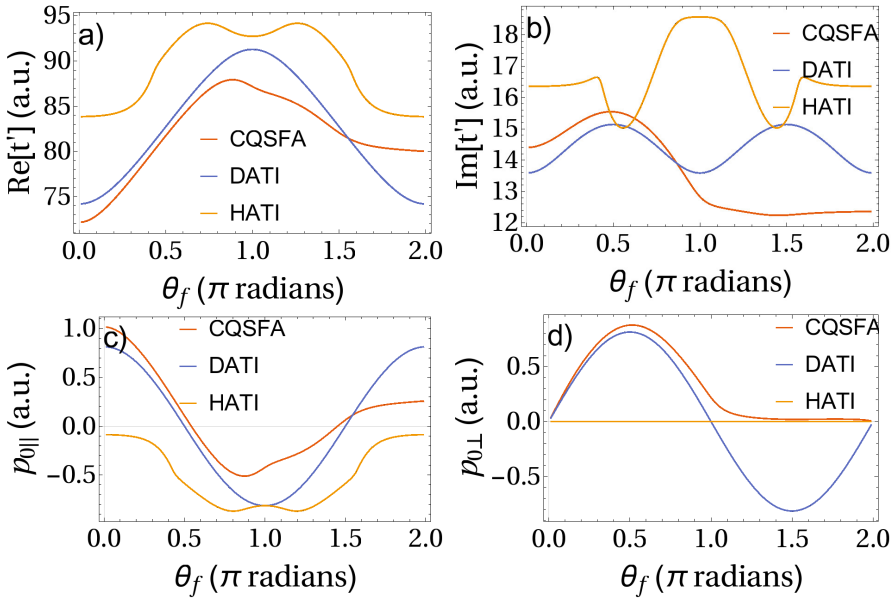

FIGURE 7.3: Ionisation times and initial momenta for the CQSFA, DATI and HATI, for a fixed photoelectron energy $E = 0.055$ a.u. and the same field and atomic parameters as in Fig. (7.1). In panels (a) and (b), the real and imaginary parts of the time of ionisation are plotted. In panels (c) and (d), we display the components of the initial momentum parallel and perpendicular to the laser-field polarisation.

due to the effect of the Coulomb potential, which favours shorter times for the CQSFA. However, as before, for low θ_f the CQSFA follows the DATI line, but as θ_f increases the behaviour tends towards the HATI curve. Similarly, in panel (b) $\mathrm{Im}[t']$ is different for the three approaches. This is because the Coulomb potential alters the tunnelling probability and hence shifts the imaginary component of the tunnelling time. Nonetheless, the qualitative behaviour of the CQSFA outcome also mirrors DATI for low angles and HATI for high angles. The same angular behaviour is present for the parallel and perpendicular initial momentum components $p_{0\parallel}$ and $p_{0\perp}$. In the perpendicular momentum case, the CQSFA momentum even tends asymptotically to its DATI and HATI counterparts as $\theta_f \to 0$ and $\theta_f \to 2\pi$, respectively. It is remarkable that this behaviour is already present for low photoelectron energy, such as that employed in Fig. (7.3). In all cases, we also see that the reflection symmetry about $\theta_f = \pi$ that exists in the Coulomb-free cases breaks for the CQSFA. This is expected as the dynamics of the system are no longer determined by the laser field alone.

7.2 Additional Orbit Types in the CQSFA

Other types of orbits that have been made accessible by the new method of solving outlined in Sec. 7.1.2 and which are important in the low-energy regime include those with multiple passes and/or trajectories whose dynamics are mainly determined by the Coulomb potential. In the previous chapter we stated that the soft-recolliding forward-scattered trajectories that form the inner spider [121] and low energy structure [58, 61, 128, 129] bear similarity to some type 3 orbits. Furthermore, we can make the same statement for softly colliding back-scattered trajectories and some type 4 orbits.

Fig. (7.4) in fact illustrates the fact that classifying orbits into type 3 or type 4 is an over-simplification. Therein, we show three examples of orbits with very distinct dynamics, that lead to the same final momenta and fall into the same classification introduced in Sec. 5.1. Apart from the standard case for these orbits, in panel (a), there are type 3 and 4 orbits that are driven past the core many times (multi-pass) before softly scattering (see panel (b)), and also directly recolliding trajectories that hard-scatter off the core before the laser field has time to change sign (see panel (c)). As these orbits will lead to the same final momentum, they will potentially interfere. However, combining these orbits would require a careful analysis of the orbits and potentially a new asymptotic expansion, which is beyond the scope of this work. The low energy (multi-pass) orbits are similar to longer HATI orbits that undergo a few passes before colliding with the core. In this way it seems possible to map each type of HATI long and short orbits onto single CQSFA orbits. The directly recolliding orbits may be loosely related to the L orbits in the SFA [150], as both undergo a collision before the laser field has changed sign. However, the underlying dynamics are fundamentally different as the acceleration by the Coulomb potential plays a key role in the CQSFA case.

Using our new method of solving the saddle point solutions (using previous orbit types to solve the next), we are able to carefully choose initial conditions such that we can probe these orbits deriving from different energy ranges. If we start the solver in a medium energy range, $|p_f| \approx 1.6\sqrt{\mathrm{U_p}}$, panel (a), we find the standard orbits that return after a single laser cycle and scatter off the core, as shown in Fig. (7.4). If we start the solver in a low energy region, $|p_f| \approx 0.3\sqrt{\mathrm{U_p}}$, panel (b), we find orbits that softly scatter

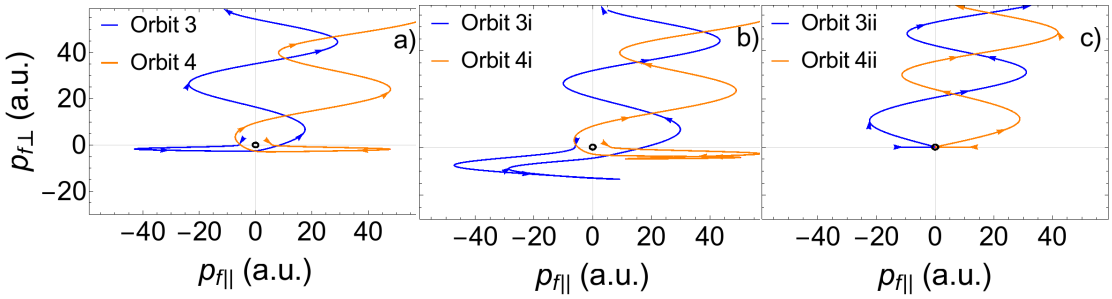

FIGURE 7.4: Different subtypes of orbit 3 and 4 that can occur for a final momentum $\mathbf{p}_f = (0.086, 0.22)$ a.u., computed using the CQSFA. Panel (a), (b) and (c) show the standard trajectories, the multi-pass orbits (denoted i) and the directly recolliding orbits (denoted ii), respectively. The Bohr radius is marked by a black circle. The same field and atomic parameters have been used as in Fig. (7.1).

after multiple laser cycles and are deflected or softly scattered by the core. However, if we start the solver in a high energy region, $|p_f| \approx 3.0\sqrt{\mathrm{U_p}}$, panel (c), we find the directly-recolliding orbits.

7.2.1 Cutoff Comparisons

In this section, we have a closer look at the contributions from different types of recolliding orbits to the photoelectron momentum distributions. This includes not only their shapes, but the momentum regions in which they are dominant or even present. Fig. (7.5) shows CQSFA single-orbit probability distributions computed for the three different types of orbit 3 and 4 presented in Fig. (7.4). This is a good indicator of the regions in which they are important. The grey areas in the figure mark drastic topological changes in the saddle-point solutions. At the boundaries of such areas, the solutions may no longer be present, coalesce, become degenerate, split or diverge. This type of behaviour is closely associated with, but is not the sole indicator of, cutoffs, and it is usually followed by a cusp. A direct consequence is that the present asymptotic expansion used in the CQSFA breaks down, and alternative expressions will be required. This situation is more complex, but bears some similarity to the nearly coalescent saddles followed by the Stokes transition encountered and described in earlier work on ATI [132].

Panels (a) to (f) show the contributions from the three variants of orbit 3. These contributions occupy a large momentum range, but are restricted for large transverse

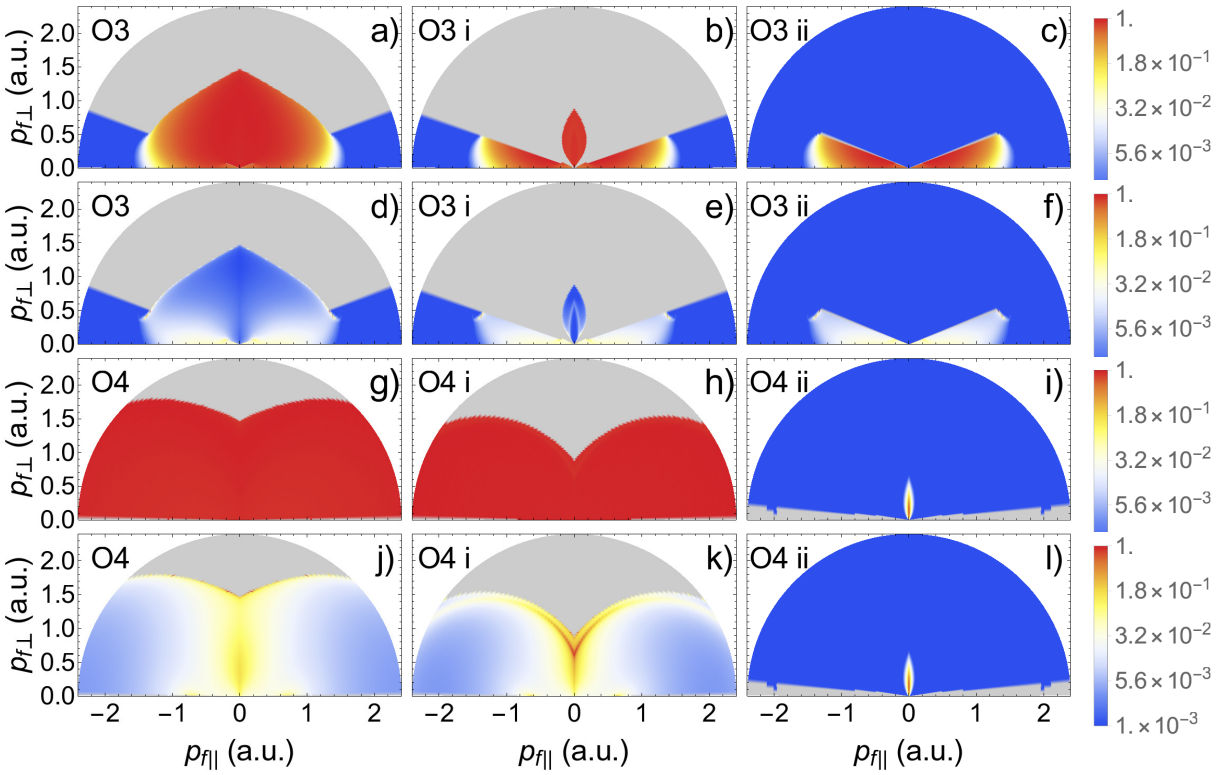

FIGURE 7.5: Single-orbit probability distributions for standard, multi-pass and directly recolliding orbits 3 and 4 (left, middle and right column, respectively). The orbit type is labelled in the top left corner of each panel. The first and second rows give the distributions related to orbit 3 without and with prefactors, respectively. The third and fourth rows show the distributions related to orbit 4 without and with prefactors, respectively. All distributions are normalised by their peak intensity. A logarithmic scale has been used. The same field and atomic parameters have been used as in Fig. (7.1).

momenta. The prefactor concentrates these distributions along the $p_{f\parallel}$ axis. If orbit 3 has two passes, the corresponding probability distributions occupy a much more restricted region close to the axes, whose V shape resembles the LES reported in [121]. Similar structures are also present for the contributions of single-pass or direct recolliding orbit 3 variants (see panels (a) and (c), respectively). The grey regions in panels (a) and (b) that start at the $\theta_f = 0.1\pi$ correspond to the transition from a soft recollision to a hard scattering event. In fact, if this angle is transformed such that $p_{0\perp} > 0$ and $z_0 > 0$, we find $\theta_f \approx 1.1\pi$, i.e. the same angle at which orbit 3 begins to qualitatively change to become more like HATI (see discussion in the Sec. 7.1.2). In panels (b) and (c), this angle marks a sharp cutoff. One should note, however, that despite the probability drop

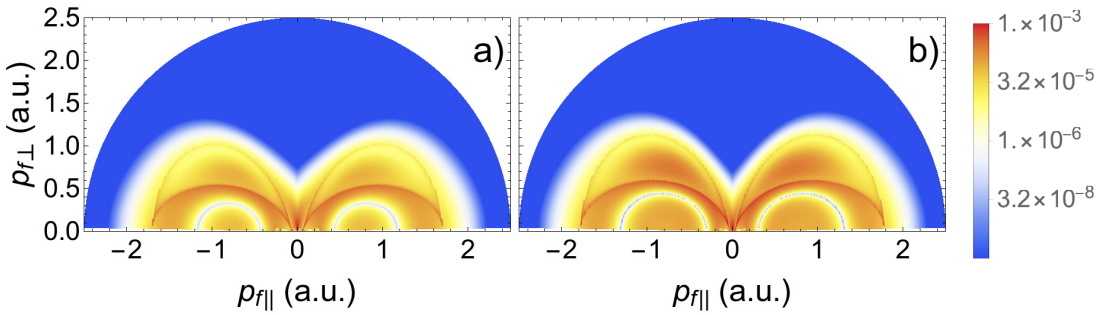

FIGURE 7.6: Probability distributions computed with the SFA using HATI backscattered orbits. Panel (a) and (b) correspond to the shortest and second shortest possible backscattered orbit pairs starting from the first half cycle. All distributions are normalised by their peak intensity. A logarithmic scale has been used. The same field and atomic parameters have been used as in Fig. (7.1).

there is no topological change in the directly recolliding type 3 orbits, whose contributions are displayed in panels (c) and (f). Physically, this may be understood to mean that hard scattering will always take place in this case, regardless of the photoelectron energy.

In panels (g) - (l) we present the single-orbit distribution for orbit 4. If the prefactors are excluded (panel (g)), the orbit has a very large flat probability distribution that extends beyond the parameter range of interest. Once the prefactors have been added (panel (j)), it is restricted to mainly around the $p_\perp$ axis, with some small spots on the $p_\parallel$ axis. There is a sharp V-shaped cutoff and cusp that is similar to those found for backscattered HATI orbits in [64]. The directly rescattering orbit 4 probability plots show only a small tulip shaped distribution with and without prefactors (panel (i) and (l)). This resembles the tulip shape in panel (b), for the probability plots associated with the multi-pass orbit 3. The tulip shapes that arise for both orbits 3 and 4 look similar to the cutoffs found for backscattered and forward scattered orbits in [64].

In order to compare the regions outlined by the single-orbit distributions in Fig. (7.5) with those from the HATI case, we combine pairs of orbits using the uniform approximation for the standard SFA, see [132] for more information. Since, in [64], it is emphasised that the Coulomb scattering cross section plays a very important role in this regime, we include the ionisation and rescattering prefactors associated with the Coulomb potential.

In Figs. (7.6) (a) and (b) we plot the probability densities obtained with the first

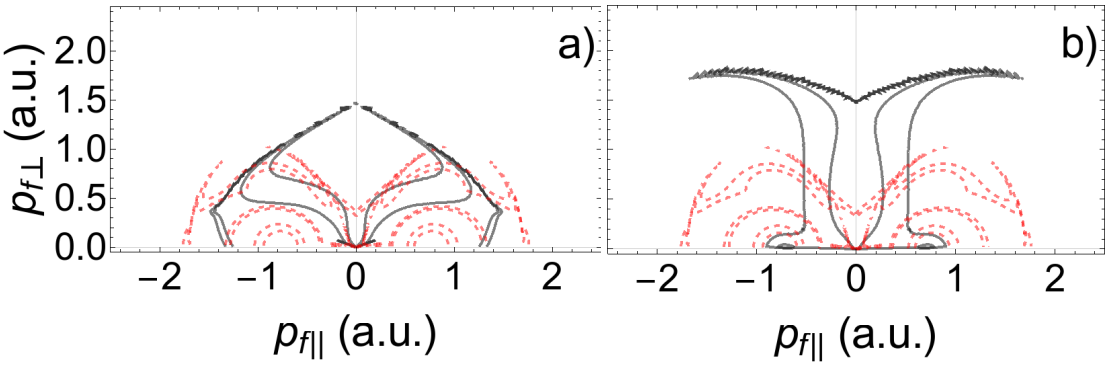

FIGURE 7.7: Comparison of CQSFA (black) and HATI (red dashed) contours, including the prefactors, using the HATI contours from Fig. (7.6) (a). Panels (a) and (b) relate to the standard orbits 3 and 4, respectively. The same field and atomic parameters have been used as in Fig. (7.1).

and second shortest HATI pair of backscattered orbits that are first sent in the opposite direction to the detector, respectively. This means that the resulting probability distributions will share features that are common to both orbits 3 and 4. Striking examples are the V-shaped structure near the $p_{f\perp}$ axis and cusps in the low-energy region. These distributions are compared in more detail in Fig. (7.7), where the contours related to the HATI distributions in Fig. (7.6) and the CQSFA orbit 3 and 4 distributions are plotted. Fig. (7.7)(a) shows that the shapes determined by the backscattered HATI orbits and orbit 3 from the CQSFA are not so different. They both have off-centre distorted ellipses/side-lobes along the parallel momentum axis. There is also a V-shaped structure where these distorted ellipses meet in both models. Despite the fact that orbit 3 is forward scattered and the HATI orbits are backscattered, one should note that both types of orbits are first displaced in the opposite direction to the detector. A striking feature is that the cusps near the origin are exactly at the same place. In HATI, the cusps are due to Stokes transitions, and if the Coulomb potential is taken into consideration, this corresponds to the region in which LES have been identified. This strongly suggests that the appropriate asymptotic expansion will change in this region for the CQSFA. In panel (b), one can clearly see that, despite being backscattered, orbit 4 leads to very different distributions than those obtained for HATI backscattered orbits. However, there is some similarity on the $p_{f||}$ axis in the form of two off-centre spots. This all indicates that the initial direction followed by the electron is more important than the type of scattering it undergoes.

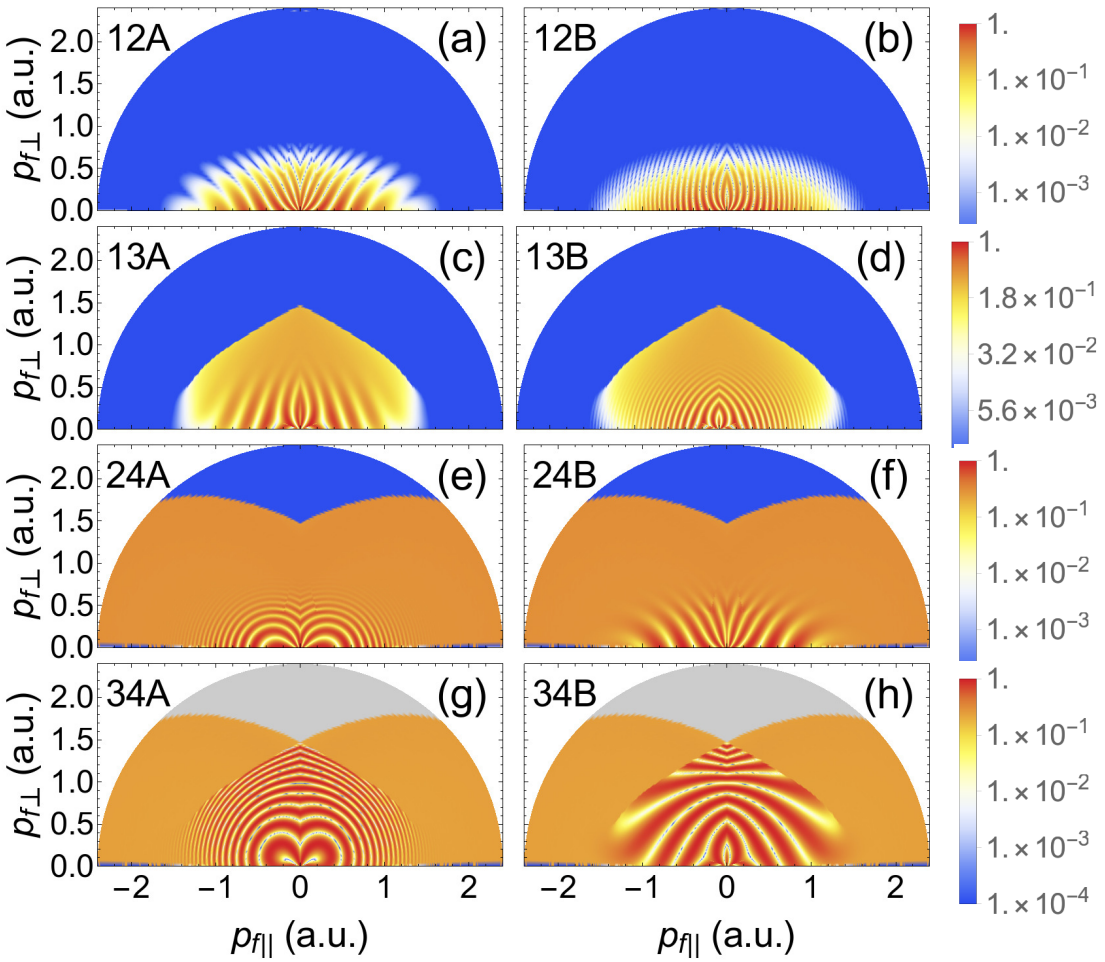

FIGURE 7.8: Photoelectron angular distributions computed using pairwise combinations symmetrised with regard to $p_{||} = 0$ with specific time restrictions, denoted by A and B and explained in the main text. The combination of orbits and interference types are given in the top left of each panel. The yield in each panel has been normalised to its peak value. A logarithmic scale has been used. The same field and atomic parameters have been used as in the previous figures in this chapter. No prefactors have been employed in the figure.

7.3 All Pairwise Interference Types

In Figs. (7.8) and (7.9), we plot all possible patterns that may be obtained by considering pairwise combinations of specific types of trajectories and well-defined ranges of ionisation times. In Fig. (7.8), we show the interference obtained using time differences of $0 < |\Delta t| < T/2$ (type A) and $T/2 < |\Delta t| < T$ (type B), where $T = 2\pi/\omega$ is a field cycle. The alternative classification is used in Fig. (7.9), in which both orbits' tunnel exit lies in the same direction, giving rise to similar ionisation times. The prime indicates that the ionisation time of a specific orbit has been delayed by a field cycle. Otherwise the orbits will leave within the same quarter cycle.

In both figures we identify two main types of patterns, diverging [Figs. (7.8)(a) and (f), and (7.9)(a) and (f)] or converging [all remaining panels except Fig. (7.8)(c) and (h)]. Diverging patterns include three fan-shaped structures and the well-known spider-like structure in Fig. (7.9)(a). They seem to be present when the time t_c of closest approach of both orbits are similar. For instance, for orbits 2 and 4, the ionisation time is delayed for orbit 2 by approximately half a cycle for type B interference [Fig. (7.8)(f)]. This delay compensates for the fact that orbit 4 is driven back towards the ion by the laser and then backscatters off the core, which takes approximately one field cycle. Orbit 2 ionises half a cycle after orbit 4 in type B interference, see Fig. (5.6), and is also turned by the laser field, which delays it approximately another half cycle. Hence, the two orbits will leave the influence of the core at approximately the same time. A similar scenario occurs for orbits 1 and 4, if the former is delayed by a cycle [Fig. (7.9)(f)]. No delays are required for orbits 1 and 2 [Fig. (7.8)(a)], and 2 and 3 [Fig. (7.9)(a)], as these orbits already leave the influence of the core at similar times. See [80, 102, 104] for more information on interference types. Each possible orbit pair has a single diverging pattern in one of the interference types. In the diverging pattern the fringes are the widest, which means that the difference between the action associated with each orbit is the smallest. Transformations to an orbit, such as temporal shifts, can change the difference between the action with another orbits, e.g. in ATI rings an orbit is temporally shifted by one laser cycle and the action difference with the original untransformed orbit leads to rings in momentum space. However, this is not revealing

difference in the orbit dynamics or interactions but just the presence of a time delay and hence different phases are picked up in the continuum. In diverging patterns transformations have been used to minimise the differences, this means the difference in actions is not due to time delays between the orbits but instead is due to the differences in the dynamics of the orbits and their interaction with core. Finding the smallest differences between the actions of two orbits amounts to finding the *essential* difference between the orbits that can not be removed by transformations, this should lead to interference that gives the most information about the interaction with the core for the two orbits. Converging patterns resemble different types of superimposed rings, and occur when the times of closest approach differ by at least half a cycle. That is, because two orbits spend different amounts of time propagating in the continuum, the *essential* interference features related to interaction with the potential get obfuscated by interference relating to the continuum propagation. Rings show the influence of the kinetic energy in the action. This parts sometimes can not be removed enough to make 'diverging' patterns, borderline cases are shown in Fig. (7.8)(c) and (h). In Table 7.1 all the diverging and converging patterns are marked for every interference type of all orbit combination.

Holographic patterns that are somewhat related to those in Figs. (7.8) and (7.9) have been studied in [118]. A direct comparison is however quite difficult due to underlying differences in the models. First, in [118], the tunnel exit is kept fixed and the trajectories are equally weighted, while in our model this does not hold. Thus, the interference may be blurred in the latter case. Second, our model includes the Coulomb potential, which is absent in [118]. This means that (i) the distinction between direct and rescattered orbits becomes blurred; (ii) in general a one-to-one time mapping for Coulomb-free and Coulomb-distorted orbits is not possible. For an extensive discussion of these issues see [109]. Nonetheless, loosely speaking some patterns are related in both models. For instance, Fig. (7.8)(c) is related to Fig. 3(b) in [118], but the ring pattern is more pronounced in the latter. This happens because in our results the residual Coulomb potential decelerates the direct orbit and accelerates the forward scattered trajectory. This leads to a smaller difference between the times of closest approach $t_c^{(1)}$ and $t_c^{(3)}$ of orbits 1 and 3 than in the Coulomb-free case.

Orbits	unrestricted	type A	type B	Prime
12	Mixed	**Diverging**	Converging	Converging†
13	Mixed	**Diverging**§	Converging	Converging†
24	Mixed	Converging	**Diverging**	Converging†
34	Mixed	Converging	**Diverging**§	Converging†
23	**Diverging**	N/A	N/A	Converging
14	Converging	N/A	N/A	**Diverging**

TABLE 7.1: Summary of the qualitative behaviour of the patterns (converging or diverging) for each interference type of all pairwise combinations of the orbits. For the first four combinations (12, 13, 24 and 34) the tunnel exits are on opposite sides, for these combinations the interference type prime will cause the difference in the times t_r' to be greater than a field cycle, thus this will not count as intracycle interference and they have not been plotted, these cases have marked by a † symbol. For the last two combination (23, 14) the tunnel exits are on the same side, for these combinations interference types A and B do not exist. Borderline cases, between diverging and converging, have been marked by a § symbol.

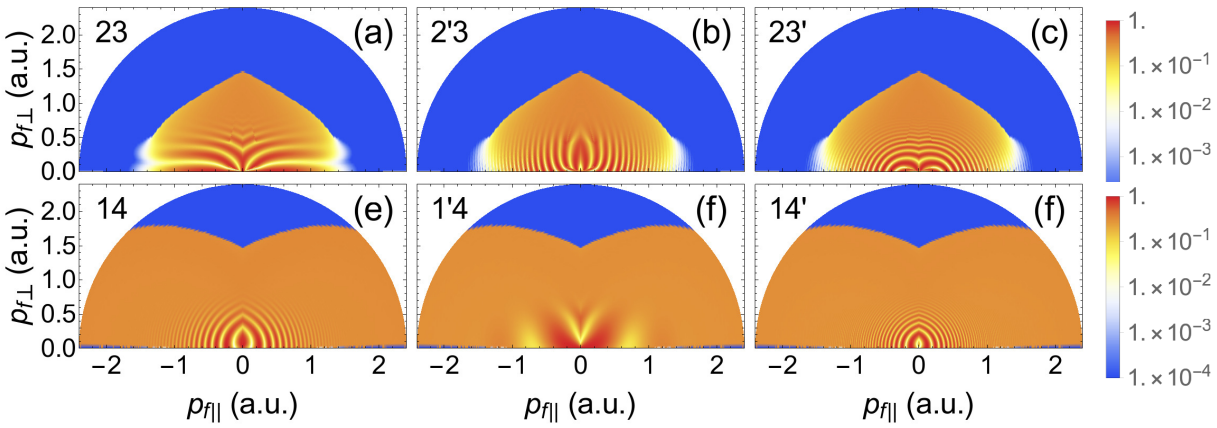

FIGURE 7.9: Photoelectron angular distributions computed using pairwise combinations of orbits starting in the same direction. The prime denotes orbits starting one cycle later, with regard to their counterparts, and the combinations of orbits are given in the top left of each panel.The yield in each panel has been normalised to its peak value. A logarithmic scale has been used. The same field and atomic parameters have been used as in the previous figures in this chapter. No prefactors have been employed in the figure.

7.4 Discussion

We have performed an in-depth analysis of recollision in the Coulomb distorted orbits that arise in the CQSFA model [79, 80, 99, 100, 102]. This includes (a) understanding the various types of collision that are present in the CQSFA orbits, (b) a comparison with direct and rescattered ATI orbits within the scope of the standard SFA, (c) an extensive discussion of additional types of back- and forward scattered trajectories.

We use the distance r_c of closest approach of an electron to the core to determine whether a specific Coulomb-distorted trajectory is a direct, softly recolliding or hard scattered orbit. If this distance is smaller than the Bohr radius, the collision is hard, and if r_c is between the Bohr radius and the tunnel exit, the collision is soft. The classification we use differs from that in [58, 128, 129], where the separation of zeros in the transverse coordinate determines the collision type. However we still yield the same class of softly recolliding orbits responsible for the LES and VLES as found in [56, 58, 61, 128, 129]. We find that some CQSFA orbits have analogues in direct and rescattered ATI. Thereby, the angle θ_f associated with the final momentum determines whether the CQSFA orbit will tend to direct or rescattered ATI in the high energy limit. Low and high values of θ_f will lead to direct and rescattered trajectories, respectively, while for angles in between we find softly colliding orbits. It is worth noticing that even for relatively low photoelectron energies the CQSFA orbits behave like rescattered ATI. They undergo hard collisions, which take place very close to the core, with similar ionisation and rescattering times. This is the reason why many low-energy structures can be explained by standard rescattered SFA orbits [64, 127, 151]. Additionally, we find that the forward scattered trajectory orbit 3 and the back scattered trajectory orbit 4 would contribute to the low energy structures, which agrees with the results in [127, 151].

We verified that the orbits in the CQSFA become degenerate along the axes, and exploited this property to find solutions for the corresponding saddle point equations. This is what enabled a solution of orbit 4 and also made it easier to find multi-pass orbits. However, the degeneracies at the boundaries will also invalidate the use of the standard saddle point approximation, which is only applicable for well separated

saddles. However, the size of the region for which the approximation is no longer valid is possibly quite small, as these boundaries can be asymptotically approached without any visible defects in the PADs.

Our analysis also shows that the classification introduced in [99] for Coulomb-corrected methods, which singles out four types of orbits, is an over-simplification. We have in fact identified several topologically different orbits that would fit under a single type. These include multi-pass orbits that leads to cusps in the low-energy ATI region. These orbits have some correspondence to the HATI orbits found in [64, 127, 151]. In this work the directly recolliding orbits are similar to L orbits, in that both trajectories recollide with the core after less than half a cycle after ionisation. One should also note that, while in the rescattered SFA the orbits occur in pairs, which are defined around a field crossing as long and short and almost merge at local energy maxima [132], the presence of the Coulomb potential disrupts this pattern and introduces additional complexities that are not fully understood. It would seem that a single CQSFA orbit contains the information of both the long and short orbits from HATI. The correspondence is non trivial though as we solve the equations of motion with the Coulomb potential, while in SFA models of HATI the Coulomb potential is included as part of a Born series.

There are some similarities between the PADs computed with the standard rescattered SFA and the CQSFA. The HATI cutoffs, as found in [64], for orbits 3 and 4, lie within similar ranges. This is expected as both types of orbits share key features that will influence the momentum regions identified by both types of distributions. This is possibly the reason why a Coulomb-distorted scattering prefactor such as that employed in [64] reproduces key features encountered in experiments. The cutoffs found in the CQSFA seem to indicate topological changes in the orbits, where the current asymptomatic expansion will most like fail. This is also the case for the cutoffs in HATI orbits [64] and higher order asymptotic expansions such as the uniform approximation have been employed for such case [132, 151]. It is unclear if these sorts of method could easily be used in the CQSFA due to the differences between the two methods, particularly, as the CQSFA uses a functional integral.

We plotted all possible intracycle interference types for the CQSFA and understood how the dynamics of the orbits and recollision plays a role in forming these patterns.

We identified diverging fringes that will lead to interference relating to difference orbit dynamics and interaction with core. This could be very important in the context of electron holography, as if these orbits could be isolated then it would make extracting topological information about a target atom or molecule much easier. Additionally, if we know that the converging interference derives from a different amount of time spent in the continuum of two orbits it would be possible to analytically remove these features from experimental data revealing 'hidden' interference structure which would yield information about the core.

Part II

Non-Sequential Double Ionisation

Chapter 8

Introduction

In the previous sections we discussed processes involving single electrons. As such we have not observed any effects due to electron-electron correlation. In fact most methods for strong field ionisation will typically use the single active electron approximation, in which the effect of any remaining core electrons on the ionised electron is neglected. In our case we have considered hydrogen so far, thus this holds exactly as there is only one electron. In general, however, for typical atomic targets undergoing processes such as ATI or HHG this has been shown to work well [152][1]. Nevertheless, for some higher order processes, for example non-sequential double ionisation (NSDI), strong electron-electron correlation is observed. NSDI is the process where the recollision of an ionised electron with its parent ion, causes the ejection of both the original and an additional electron. This falls under the description of the three step model. Recent reviews on NSDI and electron correlation in strong field physics can be found here [154, 155].

8.1 Background

Historically, the first evidence for NSDI and non-sequential multiple ionisation (NSMI) came in the early 1980s [156]. When, for lower laser intensities, the multiple ionisation yield of xenon atoms was found to be many orders of magnitude different from predictions for sequential ionisation, specifically, for intensities less than around

[1] Except for some recently identified cases, for example, particular recolliding ATI orbits that undergo inelastic collisions [153]

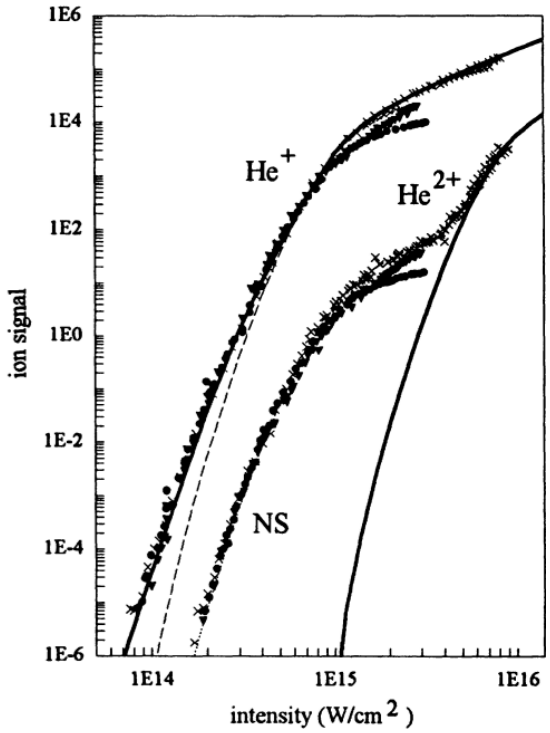

FIGURE 8.1: Singly and doubly charged ion yields for He vs laser intensity for a wavelength of $\lambda = 780$ nm. Showing the 'knee' structure associated with the transition from NSDI to SDI. Taken from [159].

1.5×10^{12} W/cm^2 the ionisation rate diverged from that predicted from sequential ionisation. So for these lower intensities it was surmised that another non-sequential mechanism must be dominant. Above the stated intensity agreement was found with sequential double ionisation (SDI). Non-sequential ionisation is a general effect, which was observed in all nobel gases [156–160] and also molecules [160–162]. The change in mechanism from NSDI to SDI, from low to high laser intensities, gives rise to the famous knee structure visible in the double ion yields vs laser intensity shown in Fig. (8.1) taken from [159]. This feature gave the first clear evidence of a double ionisation alternative mechanism.

Initially, there was much speculation and disagreement on the precise process that leads to NSDI. There were three main contenders for the ionisation of the two electrons. Firstly, shake-off ionisation [157], where the disruption to the core after the first electron is 'violently' ripped out by the field leads to the excitation of the second. Subsequently, the second electron is ionised via the laser field. Secondly, collective tunnelling [163], where both electrons tunnel together in a single step. Thirdly, the three-step model as

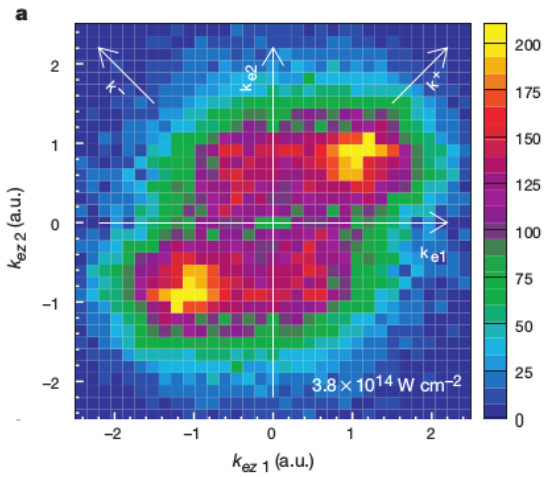

FIGURE 8.2: Example of NSDI for argon, showing the two photoelectrons yield over momentum components parallel to the laser field polarisation. With a laser field peak intensity of 3.8×10^{14} W/cm^2 and a wavelength of $\lambda = 800$ nm. Taken from [165].

described above [44], which today is the accepted description. The three steps here are similar to those in the model with the same name for high harmonic generation (HHG), tunnel ionisation of the first electron, propagation in the continuum and recollision causing a second electron to be ionised. Ultimately, the three step model was accepted as the other models were unable to explain two features in NSDI experiments: A reduction in the NSDI yield with increasing ellipticity in the laser field polarisation [164] and the off-centre maximum in the momentum spectra of the ions/ ionised electrons [165, 166]. As can be seen in Fig. (8.2), where the NSDI probability distribution has two off centre peaks along the diagonal in the yield over momentum components parallel to the laser field polarisation. Both are strong indicators of recollision, the first because recollision is much more likely with a linear field as opposed to an elliptical one and the second because recollision is most probable at a laser field crossing, which would lead to the off centre peaks.

The prevalence of the three-step model was much aided the by cold-target recoil ion momentum spectroscopy (COLTRIMS) technique [24, 53], which allowed the measurement of the momentum dependent yield/ momentum distributions of the ion and two electrons. Given momentum conservation of the ion and the two electrons, only two of the three momenta need to be considered to get the whole picture. Typically, the yield as a function of the two photoelectron momentum components parallel to the

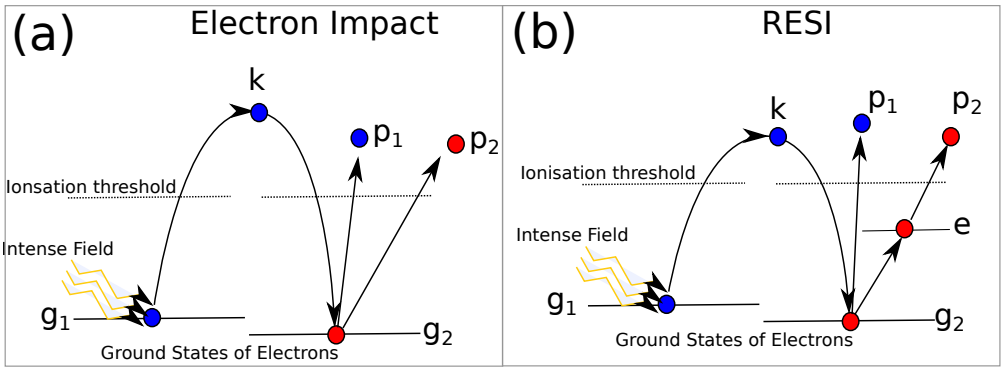

FIGURE 8.3: Schematic of the two main mechanisms in NSDI. In panel (a) electron impact ionisation is shown, while in panel (b), the recollision excitation with subsequent ionisation (RESI) mechanism is shown.

laser field polarisation is used, in both experiment and theory, which encapsulates a lot of important information about the electron dynamics and the bound states (as shown in [167–169]) from which they were ionised. While, the remaining momentum components perpendicular to the laser field polarisation are usually summed over. Originally this was because only a subset could be observed in the experimental setup, so the alternative momentum components would be traced out/ integrated over. However, often today the full set of coordinates can be measured but the integration is performed in order to easily visualise the data in a 2D density plot. An example of this can be seen in Fig. (8.2). Given the two electrons are indistinguishable there will always be symmetry around the diagonal, $p_{1\|} = p_{2\|}$. In fact, most experiments will use this and sometimes other symmetries to their advantage, symmetrising about specific axes, allowing a more restricted range of momenta to be measured. A similar symmetrisation is generally used in a theory as well.

8.2 Mechanisms

There are two mechanisms prevalent in NSDI, a schematic of both can seen in Fig. (8.3):

1. Direct, a.k.a. electron impact (EI), NSDI, this occurs when the energy of the recolliding electron is sufficient to directly ionise the second electron, causing simultaneous ejection of electrons.

2. Time-delayed NSDI a.k.a. recollision with subsequent ionisation (RESI), which occurs when the energy of the recolliding electron is not sufficient to ionise the

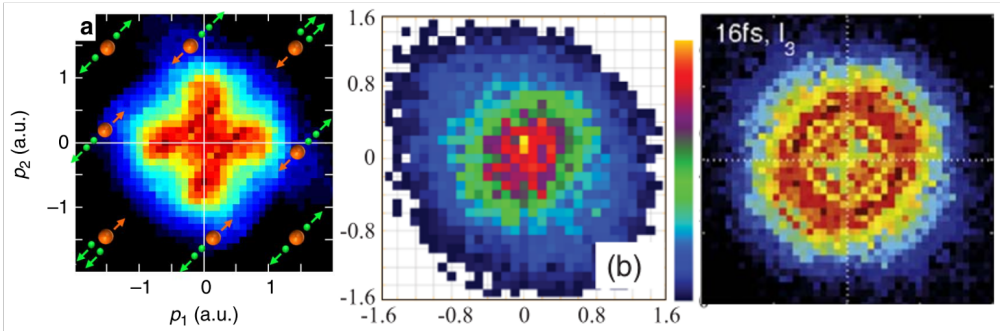

FIGURE 8.4: Experimental data from [171] (left), [172] (centre) and [173] (right), demonstrating the range of shapes possible in the momentum distributions, due to the RESI mechanism of NSDI. The targets and peak laser intensity and wavelengths used were, argon $I = 3 \times 10^{14}$ W/cm^2 and $\lambda = 750$ nm, Xenon $I = 1.6 \times 10^{14}$ W/cm^2 and $\lambda = 790$ nm and argon $I = 1.4 \times 10^{14}$ W/cm^2 and $\lambda = 790$ nm, from left to right, respectively.

second electron and it is only excited. The first electron leaves the atom and the second electron is ionised from the excited state by the field, via tunnelling ionisation (or possible over-the-barrier ionisation), after a time delay.

An estimate of which the dominant mechanism will be, is given by comparing the classical maximum return energy of the first electron [44], $3.17\mathrm{U_p}$, where $\mathrm{U_p}$ is the ponderomotive energy given by $\mathrm{U_p} = E_0/(4\omega^2)$, with the ionisation potential E_{2g} of the second electron. If $3.17\,\mathrm{U_p} > E_{2g}$, then the first electron will have enough energy to full ionise the second and the EI mechanism will most likely be dominant. Otherwise, the first electron will only have enough energy to excite the second electron and the RESI mechanism will be dominant.

Electron impact ionisation being the simpler of the two mechanisms has received the most attention. As the electrons leave the target simultaneously, which leads to side-by-side emission. This means the signal is almost entirely in the first and third quadrants of the momentum distributions. The peaks in signal tend to lie at round $p_{1\parallel} = p_{2\parallel} = \pm 2\sqrt{\mathrm{U_p}}$ but it has been shown the final momentum of the two electrons may extend much beyond this [170].

For the RESI mechanism, the situation is not so simple. Initially, it was expected that due to the time delay between the ionisation of the two electrons, there would be back-to-back emission of the two electrons with most of the signal in the second or fourth quadrants. Some early experimental findings supported this [165, 174–176]. However,

more recent results suggest that a range of shapes in the momentum distribution are possible. For example, results using a few-cycle laser pulse for argon have revealed cross-shaped distribution for short pulses, which collapse to more evenly spread distributions for longer pulse lengths [171, 173]. Other results using xenon [172] found similarly that the distribution equally occupied all quadrants. A collection of these results can be seen in Fig. (8.4) These results are in contradiction with the claim that the time-delay leads exclusively to back-to-back emission. Additionally, some early experiments mentioned [56, 174–176], using a peak laser intensity below the EI threshold, dismissed the signal in the first quadrant as EI (due to a lowering of the threshold), while it could in fact be due to the RESI mechanism. The range of shapes in experimental results are backed by theoretical findings using a variety methods such as the SFA and related methods [167, 177, 178] and classical-trajectory [172, 179–181] computations. Although back-to-back emission was highlighted, in many classical-trajectory studies cross- or ring-shaped distributions spreading across all quadrants have been identified [172, 179–181]. This behaviour has even been found for intensities far below the threshold, for which electron-impact ionisation can definitely be ruled out [180]. Hence, a complete description of what causes the different shapes in the momentum distributions in RESI is lacking. However, in what follows we provide a framework and a thorough analysis that can be used to explain the variety of different regions occupied in the momentum distributions.

8.3 Classical-Quantum Correspondence

For the case of electron impact ionisation classical models have reproduced experimental results quite well. As can be seen in the comparison between experiment and theory using a classical model in Fig. (8.5) showing NSDI of He via the electron impact mechanism. Classical models reproduce many of the key features in experiments, such as the shapes and maxima of the electron-momentum distribution and finer details such as the V-shaped structure that is a fingerprint of the long-range electron interaction [176, 182], for a review see [183]. The classical models are able to reproduce these features

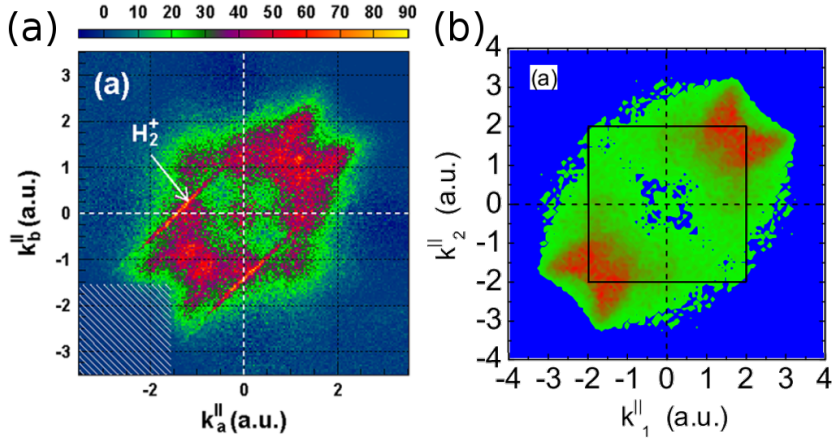

FIGURE 8.5: Comparison between experiment (panel (a) [184]) and classical theory (panel (b) [185]) for NSDI of He. Where the electron impact mechanism is dominant. The photoelectron signal is plotted over the momentum components parallel to the laser field polarisation of both photoelectrons and the perpendicular components have been integrated over. For a laser with a wavelength of $\lambda = 800$ nm and a peak intensity of $I = 4.5 \times 10^{14}$ W/cm^2.

without considering interference of the electron trajectories, and studies of classical-quantum correspondence in NSDI [155] have suggested that the interference does not survive integration over the momentum components perpendicular to the polarisation of the laser-field. This amounts to firm evidence that EI NSDI is predominantly classical, besides an initial quantum tunnelling step.

It was also extrapolated that for the RESI mechanism, interference would again be lost after integration over the perpendicular components of momentum. However, little direct evidence for this was provided. Given the range of shapes possible for RESI distributions, this suggests that both the assumptions that the electrons are ejected back-to-back and that there is no interference are oversimplified.

In initial attempts at modelling RESI distributions using semi-analytical methods such as the SFA [167, 168, 177] or the quantitative rescattering theory [178], exclusively fourfold symmetric distributions were identified for RESI, in agreement with rigorous momentum constraints [177]. That is, the momentum distributions are symmetric about both the $p_{1||}$ and $p_{2||}$ axes. This is in contradiction with experiments, where in general only the symmetry due to the indistinguishably of electrons is present. One should note, however, that in none of the SFA computations was interference between electron

trajectories or excitation channels incorporated. More recently, in 2014, SFA computations using inter-channel interference demonstrated that the fourfold symmetry can be broken [186]. Indeed, it has been argued that quantum interference is paramount, and that it can lead to anti-correlated distributions more similar to some of those found in experiment. In this study only one type or interference was explored. It is not much of a leap to assume there may be more types of interference and that it could be this interference that leads to the wide range of shapes present in RESI. For instance, no attention has been paid to interference related to symmetries present in RESI that previously lead to fourfold symmetry in the SFA, and no explicit conditions have been provided for any interference fringes. Another open question is if, given a RESI distribution of a particular shape, can we use this information for imaging purposes such as bound state reconstruction?

In the following chapters, the work I did from [169, 187] is presented, which tackles the issue of interference and addresses many of the above questions/ problems. This includes: 1) A systematic analysis of all the interference effects possible in RESI, employing the SFA. 2) Deriving analytic expressions for the interference fringes encountered and demonstrated how one can generate a multitude of RESI distributions using interference effects, paying particular attention to the role the geometry of the bound electronic states. 3) This knowledge is extended to reproduce recent experimental results [173], using a superposition of channels of excitation of the second electron. To ensure better agreement with experiment the distribution of intensities of the laser pulse in space and time, is accounted for using focal averaging. Hence, it is shown that the interference effects survive focal averaging as well as integration of the momentum components perpendicular to the polarisation of the laser field. An argument is also provided, as to why the cross-shaped distributions are observed for short pulses.

Chapter 9

NSDI Theory

In this chapter we present the existing theory that is necessary to understand non-sequential double ionisation (NSDI) in terms of the strong field approximation (SFA). In the previous part of this thesis (7.1.1) we derived the general S-matrix transition amplitude for strong field ionisation with a single rescattering event, high-order above threshold ionisation (HATI), Eq. (7.1). This describes the dynamics of the first electron in NSDI, except the collision will be inelastic in NSDI. Hence, we can use Eq. (7.1) as a starting point and generalise this to two electrons. The ground state can be approximated by the composition of two single electron bound state wavefunctions $|\psi_g(t')\rangle = |\psi_{g_1}(t')\rangle \otimes |\psi_{g_2}(t')\rangle$. Given we have two indistinguishable electrons we will have to account for exchange symmetry. We will consider the electrons to be from the same orbital (in a singlet state), so that the wavefunction will be antisymmetric due to the spin part of the wavefunction. Spin-coupling effects are weak in comparison to interaction with the field. An approximate correction to the tunnel rate, to account for spin effects, was given in [188]. For the typical field intensities used here and using the magnetic moment for an electron bound in a hydrogen-like system this give a correction of $\approx 10^{-4}\%$. This kind of effect would be well below experimental uncertainties and thus, we will not consider spin effects any further. The final state of the electrons will be given by the composition of two momentum scattering states $|\psi_{\mathbf{p}}(t)\rangle = |\psi_{\mathbf{p}_1}(t)\rangle \otimes |\psi_{\mathbf{p}_2}(t)\rangle$. This neglects both the ion-electron and electron-electron Coulomb interactions for the continuum states, except for in the recollision, as we are using the SFA. Within this approximation both the EI and RESI mechanisms for NSDI can be written in terms of a Feynman diagram, see Fig. (9.1). For the case of EI NSDI, panel (a), the first electron ionises from its ground state g_1 at time t' into momentum state k. From this state it then

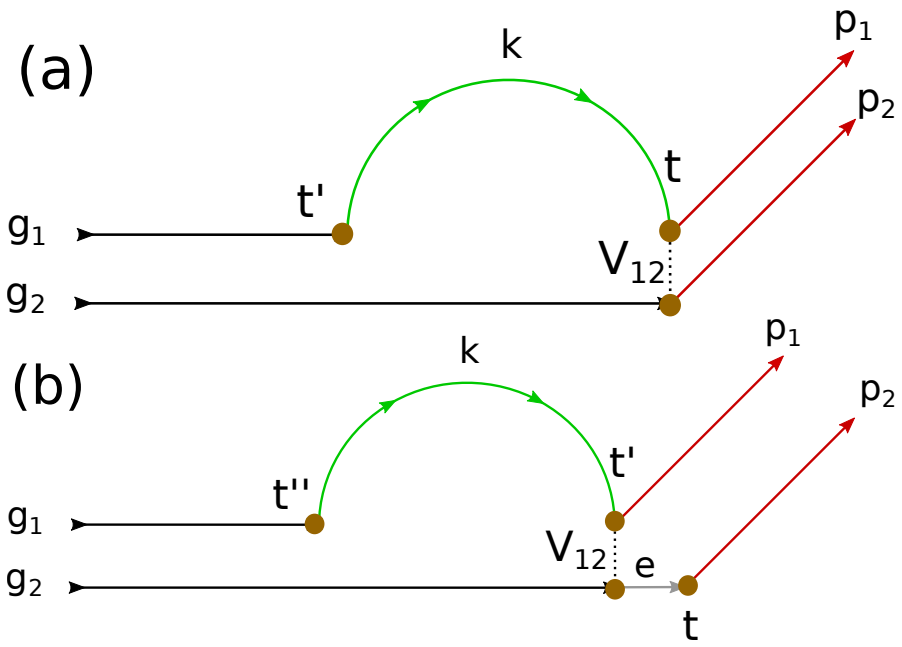

FIGURE 9.1: Feynman diagrams of the EI and RESI pathways for NSDI, panel (a) and (b), respectively.

recollides with the ion at time t, so that both the first and the second electron ionise into final momentum states p_1 and p_2. For the case of RESI NSDI, panel (b), the first electron ionises from its ground state g_1 at time t'' into momentum state k. From this state it then recollides with the ion at time t', exciting the second electron from its ground state g_2 to its excited state e. The first electron is then in its final momentum state p_1, subsequently the second electron ionises via tunnel ionisation into its final momentum state p_2.

The S-matrix transition amplitudes will be composed of the same state evolution as that used in the Feynman digram. The transition amplitude associated with direct, electron-impact ionisation reads

$$M_{\mathrm{EI}}(\mathbf{p}_1,\mathbf{p}_2) = -\int_{-\infty}^{\infty} \mathrm{d}t \int_{-\infty}^{t} \mathrm{d}t' \, \langle \psi^v_{\mathbf{p}_1}(t), \psi^v_{\mathbf{p}_2}(t) | V_{12} U(t,t') V_1 | \psi_{g_1}(t'), \psi_{g_2}(t') \rangle \,. \quad (9.1)$$

Here, $H_{\mathrm{int}}(t')$ has been replaced by the atomic potential of the singly charged ion V_1, which is valid within the SFA, as first shown in [130]. With, $U(t',t) = U_{v_1}(t',t) \otimes U_{g_2}(t',t)$, where, $U_{v_1}(t,t')$ is the Volkov time evolution operator for the first electron, $U_{g_2}(t,t')$ is the time evolution operator for ground state of the second electron and V_{12} is the electron-electron interaction potential. This transition amplitude describes

the electron impact mechanism in NSDI, where the first electron ionises at time t' and propagates until time t, where it recollides with the ion and the first second electrons end in final Volkov states with momentum $\mathbf{p}_1$ and $\mathbf{p}_2$, respectively. The Volkov time evolution operator $U_{v_1}(t,t')$ can be written in terms of an integral over Volkov states,

$$U_1^v(t,t') = \int \mathrm{d}^3\mathbf{k}\, |\psi_{\mathbf{k}}^v(t)\rangle \langle\psi_{\mathbf{k}}^v(t')|$$

Inserting this into Eq. (9.1) gives

$$M_{\mathrm{EI}}(\mathbf{p}_1,\mathbf{p}_2) = -\int_{-\infty}^{\infty}\mathrm{d}t\int_{-\infty}^{t}\mathrm{d}t'\int \mathrm{d}\mathbf{k}\,\langle\psi_{\mathbf{p}_1}^v(t),\psi_{\mathbf{p}_2}^v(t)|V_{12}|\psi_{\mathbf{k}}(t),\psi_{g_2}(t)\rangle\,\langle\psi_{\mathbf{k}}(t')|V_1|\psi_{g_1}(t')\rangle\,. \tag{9.2}$$

This can be re-expressed in terms of a semi-classical action and prefactors to give

$$M_{\mathrm{EI}}(\mathbf{p}_1,\mathbf{p}_2) = -\int_{-\infty}^{\infty}\mathrm{d}t\int_{-\infty}^{t}\mathrm{d}t'\int \mathrm{d}^3\mathbf{k}\, V_{\mathbf{p}_1\mathbf{p}_2,g_1,g_2}V_{\mathbf{k}g_1}\exp(iS(\mathbf{p}_1,\mathbf{p}_2,\mathbf{k},t,t')), \tag{9.3}$$

where the action reads,

$$\begin{aligned} S(\mathbf{p}_1,\mathbf{p}_2,\mathbf{k},t,t')) = E_{1\mathrm{g}}t' + E_{2\mathrm{g}}t - \int_{t'}^{t}\frac{[\mathbf{k}+\mathbf{A}(\tau)]^2}{2}\mathrm{d}\tau - \int_{t}^{\infty}\frac{[\mathbf{p}_1+\mathbf{A}(\tau)]^2}{2}\mathrm{d}\tau \\ - \int_{t}^{\infty}\frac{[\mathbf{p}_2+\mathbf{A}(\tau)]^2}{2}\mathrm{d}\tau \end{aligned} \tag{9.4}$$

and the prefactors are given by

$$V_{\mathbf{k}g_1} = \langle\tilde{\mathbf{k}}(t')|V|\psi_{g_1}\rangle \quad \text{and} \quad V_{\mathbf{p}_1\mathbf{p}_2,g_1,g_2} = \langle\tilde{\mathbf{p}}_1(t),\tilde{\mathbf{p}}_2(t)|V_{12}|\tilde{\mathbf{k}}(t),\psi_{g_2}\rangle\,, \tag{9.5}$$

and using different expressions $\tilde{\mathbf{p}}_n(\tau)$ for they can be written in either the length or velocity gauge. For the length gauge $\tilde{\mathbf{k}}(\tau) = \mathbf{k}+\mathbf{A}(\tau)$ and $\tilde{\mathbf{p}}_n(\tau) = \mathbf{p}_n+\mathbf{A}(\tau)$ ($\tau = t,t',t''$), and in the velocity gauge $\tilde{\mathbf{k}}(\tau) = \mathbf{k}$ and $\tilde{\mathbf{p}}_n(\tau) = \mathbf{p}_n$, with $n = 1,2$. In [167] it was verified that, in practice, the results obtained in both gauges lead to qualitatively similar results. Here we employ the latter gauge in order to avoid bound-state singularities. This is the general form of the transition amplitude for electron impact ionisation, for

more details see [154]. In order to formulate the RESI mechanism of NSDI transitions to intermediate excited states must be included for the second electron. This yields the following transition amplitude,

$$M_{\mathrm{RESI}}(\mathbf{p}_1,\mathbf{p}_2) = -\int \mathrm{d}^3t\, \langle \psi_{\mathbf{p}_1}(t), \psi_{\mathbf{p}_2}(t)|V_{\mathrm{ion}}\tilde{U}(t,t')V_{12}|U(t',t'')V|\psi_{g_1}(t''), \psi_{g_2}(t'')\rangle\,. \tag{9.6}$$

Where,

$$\int \mathrm{d}^3t \equiv \int_{-\infty}^{\infty}\mathrm{d}t \int_{-\infty}^{t}\mathrm{d}t' \int_{\infty}^{t}\mathrm{d}t'',$$

$U(t',t'') = U_{v_1}(t',t'') \otimes U_{g_2}(t',t'')$ and $\tilde{U}(t,t') = U_{v_1}(t,t') \otimes U_{e_2}(t,t')$. Here $U_{v_1}(t',t'')$ is the Volkov time evolution operator for the first electron, while $U_{g_2}(t',t'')$ and $U_{e_2}(t',t'')$ are the time evolution operators for the ground and excited states of the second electron, respectively. Expressing the first electron's intermediate time evolution operator in terms of an integral over intermediate momenta and collecting terms into a semi-classical action and prefactors terms gives

$$M(\mathbf{p}_1,\mathbf{p}_2) = \int \mathrm{d}^3t \int \mathrm{d}^3\mathbf{k} V_{\mathbf{p}_2 e} V_{\mathbf{p}_1 e,\mathbf{k}g} V_{\mathbf{k}g} \exp[iS(\mathbf{p}_1,\mathbf{p}_2,\mathbf{k},t,t',t'')], \tag{9.7}$$

where

$$\begin{aligned} S(\mathbf{p}_1,\mathbf{p}_2,\mathbf{k},t,t',t'') = {} & E_{1\mathrm{g}}t'' + E_{2\mathrm{g}}t' + E_{2\mathrm{e}}(t-t') - \int_{t''}^{t'} \frac{[\mathbf{k}+\mathbf{A}(\tau)]^2}{2}\mathrm{d}\tau \\ & - \int_{t'}^{\infty} \frac{[\mathbf{p}_1+\mathbf{A}(\tau)]^2}{2}\mathrm{d}\tau - \int_{t}^{\infty} \frac{[\mathbf{p}_2+\mathbf{A}(\tau)]^2}{2}\mathrm{d}\tau \end{aligned} \tag{9.8}$$

denotes the semiclassical action, and the prefactors

$$\begin{aligned} V_{\mathbf{k}g} &= \langle \tilde{\mathbf{k}}(t'')|V|\psi_{g_1}\rangle \\ &= \frac{1}{(2\pi)^{3/2}} \int \mathrm{d}^3 r_1 V(\mathbf{r}_1) e^{-i\tilde{\mathbf{k}}(t'')\cdot\mathbf{r}_1} \psi_{g_1}(\mathbf{r}_1), \end{aligned} \tag{9.9}$$

$$\begin{aligned} V_{\mathbf{p}_1 e,\mathbf{k}g} &= \langle \tilde{\mathbf{p}}_1(t'), \psi_{e_2}|V_{12}|\tilde{\mathbf{k}}(t'), \psi_{g_2}\rangle \\ &= \frac{1}{(2\pi)^3} \iint \mathrm{d}^3 r_2 \mathrm{d}^3 r_1 \exp[-i(\mathbf{p}_1 - \mathbf{k})\cdot\mathbf{r}_1] \\ &\qquad \times V_{12}(\mathbf{r}_1,\mathbf{r}_2)[\psi_2^{(e)}(\mathbf{r}_2)]^* \psi_2^{(g)}(\mathbf{r}_2) \end{aligned} \tag{9.10}$$

and

$$\begin{aligned} V_{\mathbf{p}_2 e} &= \langle \tilde{\mathbf{p}}_2(t)|V_{\mathrm{ion}}|\psi_{e_2}\rangle \\ &= \frac{1}{(2\pi)^{3/2}} \int \mathrm{d}^3 r_2 V_{\mathrm{ion}}(\mathbf{r}_2) e^{-i\tilde{\mathbf{p}}_2(t)\cdot\mathbf{r}_2} \psi_{e_2}(\mathbf{r}_2) \end{aligned} \tag{9.11}$$

incorporate all information about the interactions and electronic bound states. Specifically, Eqs. (9.9), (9.10) and (9.11) are related to the ionisation of the first electron, the recollision of the first electron with excitation of the second electron, and the tunnel ionisation of the second electron, respectively. Therein, $V(\mathbf{r}_1)$ and $V_{\mathrm{ion}}(\mathbf{r}_2)$ denotes the binding potential "seen" by the first and the second electron, respectively, and $V_{12}(\mathbf{r}_1, \mathbf{r}_2)$ gives the electron-electron interaction. The momenta $\tilde{\mathbf{k}}$ and $\tilde{\mathbf{p}}_n$ (with $n = 1, 2$) have the same definitions as above and we have again used the velocity gauge versions.

The transition amplitude (9.7) describes a process in which the first electron, initially bound in the ground state $|\psi_{g_1}\rangle$, is released at a time t'' into a continuum state, which is approximated by the Volkov state $|\tilde{\mathbf{k}}(t'')\rangle$. Subsequently, it remains in the continuum from the time t'' to the time t' with intermediate momentum $\mathbf{k}$. At t', it returns to its parent ion and interacts with a core electron via V_{12}. This interaction excites the second electron from the ground state $|\psi_{g_2}\rangle$ of the singly ionised target to the state $|\psi_{e_2}\rangle$. The first electron reaches the detector with final momentum $\mathbf{p}_1$ after rescattering. The second electron remains bound until a later time t, when it is released by tunnel ionisation into a Volkov state $|\tilde{\mathbf{p}}_2(t)\rangle$. It reaches the detector with final momentum $\mathbf{p}_2$. The ground-state energy of the neutral system is given by $E_{1\mathrm{g}}$, and the energies of the

ground and excited states of the singly ionised target are $E_{2\mathrm{g}}$ and $E_{2\mathrm{e}}$, respectively. For details on how this transition amplitude is derived we refer to [167].

9.1 Quantum Orbits

As before, we employ the steepest descent method, a.k.a. the saddle point approximation (SPA), in order to compute the transition amplitude (9.7). In this method, we seek variables t, t' t'' and $\mathbf{k}$ so that the action is stationary. This leads to the following saddle-point equations

$$\left[\mathbf{k} + \mathbf{A}(t'')\right]^2 = -2E_{1\mathrm{g}}, \tag{9.12}$$

$$\mathbf{k} = -\frac{1}{t' - t''}\int_{t''}^{t'} \mathrm{d}\tau \mathbf{A}(\tau), \tag{9.13}$$

$$\left[\mathbf{p}_1 + \mathbf{A}(t')^2\right] = \left[\mathbf{k} + \mathbf{A}(t')\right]^2 - 2(E_{2\mathrm{g}} - E_{2\mathrm{e}}), \tag{9.14}$$

and

$$\left[\mathbf{p}_2 + \mathbf{A}(t)\right]^2 = -2E_{2\mathrm{e}}. \tag{9.15}$$

Eqs. (9.12) and (9.15) give the energy conservation of the first and second electron at the instant of tunnel ionisation. For the former, this occurs from the ground state at the time t'', while the latter tunnels from an excited state at a later time t. The solutions for all the times and momentum $\mathbf{k}$ are in general complex, which reflects the fact that quantum tunnelling has no classical counterpart. Eq. (9.13) restricts the intermediate momentum of the first electron so that it returns to the core, which is assumed to be located at the origin. Finally, Eq. (9.14) states that, upon return, the first electron gives part of its kinetic energy upon return to "bridge" the gap $E_{2\mathrm{g}} - E_{2\mathrm{e}}$ and promotes the second electron to an excited state. We use both the standard saddle point approximation and a uniform asymptotic expansion whose only applicability requirement is that the orbits occur in pairs. For details on these methods see [132].

The real part of the times of first ionisation, recollision and second ionisation, $\mathrm{Re}[t'']$, $\mathrm{Re}[t']$ and $\mathrm{Re}[t]$ can be approximated by solutions of the simple man model [44]. This

is a fully classical model where, in most implementations, the electrons will ionise with zero drift momentum, which leads to ionisation occurring at field extrema and recollisions at field crossings. We also know that because of the causality of the process, $\mathrm{Re}[t''] < \mathrm{Re}[t'] < \mathrm{Re}[t]$, so within two field cycles this gives a limited set of possible solutions. These possibilities can be seen in Fig. (9.2) panel (a) where all the times of ionisation and recollision are marked. We will consider that the first electron recollides approximately 1.5 cycles after the initial ionisation. For recollision times after this the first electron will have already revisited the core previously so it would be unphysical for no scattering to have occurred. For the recollision time before this, at around 0.5 cycles after the initial ionisation, there is a possible solution, which is similar to the directly rescattered orbits discussed in section 7.2 and the L orbits from [150], but the electron would have to have a high initial momentum that works against the field. Hence, we consider this is a low probability event and discount it for this work. In the SFA, for which the electrons will ionise with non-zero momenta and similar to ATI, there are two solutions for each time, long and short and both have been marked on Fig. (9.2). This leaves four possible solutions, marked in panel (b), long and short solutions starting from both the first and second field extrema. The long and short solutions will generally be combined into a single transition amplitude, which we will call an event and interference will occur between different events[1]. The events can be linked by two symmetry operations, a half cycle translation in all times $(t, t', t'') \rightarrow (t + T/2, t' + T/2, t'' + T/2)$, where $T = 2\pi/\omega$ is a field cycle, and inversion of the parallel momentum coordinates $p_{1,2||} \rightarrow -p_{1,2||}$. This is due to the fact that we are using a monochromatic field and $\mathbf{A}(t \pm T/2) = -\mathbf{A}(t)$, so the action is invariant under the combination of both these symmetry operations. If we were using a pulse this symmetry would be lost. However, over two cycles there would still be events corresponding to both those identified in panel (c) but they would not have dynamics related by these symmetries and their overall signal may significantly vary meaning one could dominate [52].

[1]There will also be interference between long and short orbits, as previously stated but this will be washed out upon integration over momentum coordinate perpendicular to the laser field polarisation.

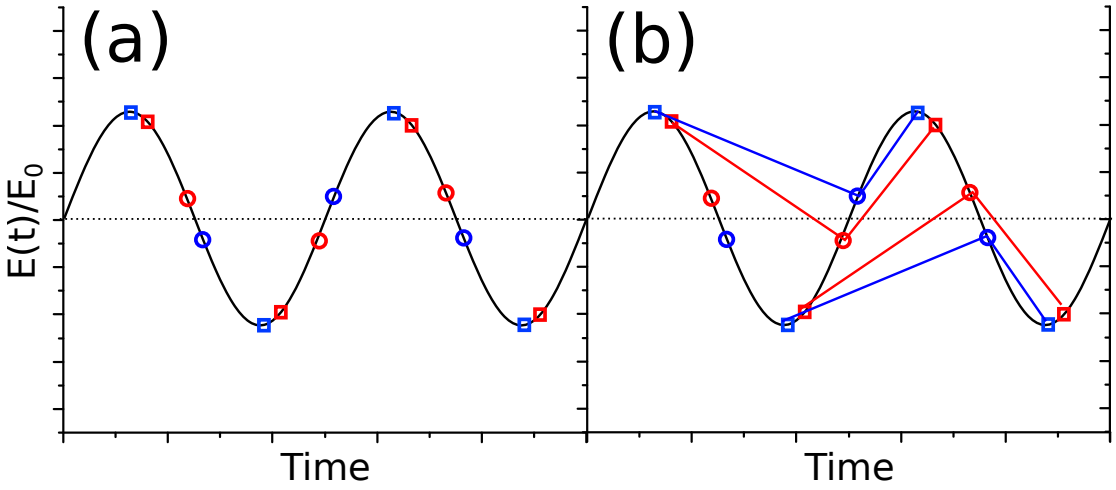

FIGURE 9.2: Possible solutions for the times in the RESI process superimposed on the electric field, this has been plotted over 2 field cycles. Panel (a), shows the possible solutions for ionisation (squares) and recollision (circles) , where long and short orbits correspond to blue and red, respectively. In panel (b) all possible solutions have been marked by blue (long) and red (short) lines.

9.2 Saddle Point Approximation and Uniform Approximation

Despite the fact we can identify approximately where the solutions will be, the saddle-point equations are still non-linear, complex valued and do not have analytic solutions, therefore they have to be solved numerically. However, the solutions can be used to create a transition amplitude of a known analytic form. Hence, it is known as a 'semi-analytic' method. Once we have the solutions we can proceed calculating the transition amplitude using the method of steepest descent as described in Sec. 2.3. The transition amplitude will become

$$M(\mathbf{p}_1, \mathbf{p}_2) = \sum_s A_s(\mathbf{p_1}, \mathbf{p}_2) \exp\left(iS_s(\mathbf{p_1}, \mathbf{p}_2)\right), \tag{9.16}$$

with

$$S_s(\mathbf{p_1}, \mathbf{p}_2) = S(\mathbf{p_1}, \mathbf{p}_2, t_s, t'_s, t''_s, \mathbf{k}_s). \tag{9.17}$$

Using a quadratic expansion of the action the coefficents A_s can be calculated using Eq. (2.42) from Sec. 2.3

$$A_s(\mathbf{p_1}, \mathbf{p}_2) = (2\pi)^3 \frac{V_{\mathbf{p}_2 e} V_{\mathbf{p}_1 e, \mathbf{k}_s g} V_{\mathbf{k}_s g}}{\sqrt{\det(S''(\mathbf{p_1}, \mathbf{p}_2, t_s, t'_s, t''_s, \mathbf{k}_s))}}. \tag{9.18}$$

Here s runs over the relevant saddle points calculated and $\det(S''(\mathbf{p}_1, \mathbf{p}_2, t_s, t'_s, t''_s, \mathbf{k}_s))$ denotes the determinant of the 6×6 Hessian matrix of $S(\mathbf{p}_1, \mathbf{p}_2, t_s, t'_s, t''_s, \mathbf{k}_s)$, with derivatives taken for the variables t,t',t'' and $\mathbf{k}$.

These solutions are known as 'quantum orbits', and come in pairs, long and short, as previously mentioned. The long orbits tunnel earlier than short and recollide later, hence they correspond to the electron spending a longer time in the continuum. For each orbit there is a region of momenta known as the classical region. For these momenta the orbit has a classical counterpart that describes the real motion of the electron between tunnelling and recollision. At the boundary of this region the long and short orbits coalesce and beyond this region is the classically-forbidden region, where the '*quantum orbits*' have no classical counterpart. The imaginary parts of the pairs of solutions quickly change in the classically-forbidden region and one of the orbits diverges becoming unphysical. The classical boundary marks a Stokes transition of the solutions, where $\mathrm{Re}[S_i] = \mathrm{Re}[S_j]$, where S is the action and the labels i and j denote the different orbits. The SPA requires the solutions to be well separated and breaks down at and beyond the classical boundary. However, there is a way around this, a higher order expansion can be taken called the uniform approximation [132]. The uniform approximation uses all the same parameters as in the SPA but the contribution of a pair of orbits is now described by a diffraction integral, which reduces to the SPA when the orbits are well separated. It is defined within the classical boundary as,

$$M_{i+j} = \sqrt{\frac{2\pi\Delta S}{3}} \mathrm{e}^{i(\bar{S}+\pi/4)} \left\{ \bar{A} \left[J_{\frac{1}{3}}(\Delta S) + J_{-\frac{1}{3}}(\Delta S) \right] + \Delta A \left[J_{\frac{2}{3}}(\Delta S) - J_{-\frac{2}{3}}(\Delta S) \right] \right\} \tag{9.19}$$

and ouside classical region

$$M_{i+j} = \sqrt{\frac{2i\Delta S}{\pi}} \mathrm{e}^{i\bar{S}} \left[\bar{A} K_{\frac{1}{3}}(-i\Delta S) + i\Delta A K_{\frac{2}{3}}(-i\Delta S) \right] \tag{9.20}$$

where,

$$\Delta S = \frac{S_i - S_j}{2} \qquad \bar{S} = \frac{S_i + S_j}{2}$$
$$\Delta A = \frac{A_i - iA_j}{2} \qquad \bar{A} = \frac{iA_i - A_j}{2}$$

and J and K denote the Bessel J and K functions respectively. The uniform approximation combines long and short pairs to given the events identified in Fig. (9.2) panel (c).

9.3 Momentum Constraints

Approximate momentum constraints can be derived for the probability distribution associated with the quantum orbits. For simplicity, we will be considering a monochromatic field throughout this part unless specified otherwise. As previously stated the choice of field means events whose times are displaced by half a cycle are related by momentum inversion. Furthermore, since both electrons are indistinguishable, one must also exchange $\mathbf{p}_1$ and $\mathbf{p}_2$ in Eq. (9.7) and add the corresponding amplitudes.

Estimates for the regions in the parallel momentum plane to be populated follow from the saddle-point equations. For the first electron, Eq. (9.14) gives

$$\frac{(p_{1\parallel} + A(t'))^2}{2} = \frac{(k + A(t'))^2}{2} + E_{2e} - E_{2g} - \frac{p_{1\perp}^2}{2} \tag{9.21}$$

where recollision occurs approximately at the electric field crossing so $A(t') \approx 2\sqrt{\mathrm{U_p}}$ leading to the inequality,

$$\pm 2\sqrt{\mathrm{U_p}} - \sqrt{2\triangle E} \leq p_{1\parallel} \leq \pm 2\sqrt{\mathrm{U_p}} + \sqrt{2\triangle E}, \tag{9.22}$$

where $\triangle E = E_{\mathrm{kin}}(t', t'') - \tilde{E}_{\mathrm{exc}}$ yields the energy difference between the kinetic energy

$E_{\rm kin}(t',t'')$ of the first electron upon return and the energy $\tilde{E}_{\rm exc} = E_{2\rm g} - E_{2\rm e} + p_{1\perp}^2/2$. The above-stated inequality indicates that the region where rescattering has a classical counterpart, which is largest if $\mathbf{p}_{1\perp} = 0$. For the second electron, one must bear in mind that Eq. (9.15) is formally identical to that describing tunnel ionisation in direct ATI, hence the probability over $p_{2\parallel}$ will be centred about $p_{2\parallel} = 0$ and the region will be given by the direct ATI cutoff [189], $\pm 2\sqrt{\rm U_p}$, which leads to the following inequality

$$-2\sqrt{\rm U_p} \leq p_{2\parallel} \leq 2\sqrt{\rm U_p}. \tag{9.23}$$

In this latter estimate, we have considered $\mathbf{p}_{2\perp} = 0$. Hence, the distributions will be located around $(\mathbf{p}_1, \mathbf{p}_2) = \left\{(\pm 2\sqrt{\rm U_p}, 0),\ (0, \pm 2\sqrt{\rm U_p})\right\}$. Detailed explanations of these constraints are given in [167, 177, 183]. This gives four symmetry related events whose transition amplitudes occur in four different regions of the parallel momentum distributions: the left, upper, right and downwards parts. Thus, they are labelled $M_{\rm l}$, $M_{\rm u}$, $M_{\rm r}$ and $M_{\rm d}$, respectively (as shown in Fig. (10.1)). These may be combined coherently or incoherently and will form the starting point for the investigation into interference in NSDI.

9.4 Coherence Sums of Events and Channels

The coherent sum of M_l, M_r, M_u and M_d integrated over the transverse momentum components reads

$$\Omega^{(c)}(p_{1\parallel}, p_{2\parallel}) = \iint {\rm d}^2 p_{1\perp} {\rm d}^2 p_{2\perp} \left| M^{(c)} \right|^2, \tag{9.24}$$

with $M^{(c)} = \sum_\nu M_\nu^{(c)}$, and $\nu = l, r, u, d$. If the events are summed incoherently, the amplitudes are replaced by probabilities, i.e., $\sum_\nu |M_\nu^{(c)}|^2$ is used instead. In the RESI mechanism there are multiple channels of excitation for the second electron. The corresponding expression for more than one channel is

$$\Omega(p_{1\parallel}, p_{2\parallel}) = \iint {\rm d}^2 p_{1\perp} {\rm d}^2 p_{2\perp} \left| \sum_c M^{(c)} \right|^2. \tag{9.25}$$

Eq. (9.25) assumes that each excitation represents a path, which the second electron can take. Hence, the amplitudes corresponding to each path must be summed.

Chapter 10

Interferences in NSDI

In this chapter a thorough analysis of all possible interference types is performed. From the previous chapter we have already identified four symmetry related events. These events may be combined to give the first type of interference effects in NSDI, known as event interference. Aside from this the second electron may be ionised via multiple excited states for most atomic targets. These each constitute as alternative paths or channels of excitation for the process and may also interfere, referred to as channel interference. There is also interference between the different long and short 'orbits' that the electrons may follow. Although this interference is included, it has previously been shown that any effects will be washed out over integration of perpendicular momentum coordinates [167, 190]. In this chapter we will be considering the effect of both event and channel interferences, employing the SFA. The SFA, when used in conjunction with the steepest descent method, provides a very intuitive interpretation in terms of electron orbits, and retains quantum interference and tunnelling. This makes it an ideal tool for analysing different types of interference. Additionally, we will investigate the role of the prefactors, which imprint the bound state geometry on the final momentum distributions, in the interference. In all cases the target atom considered is argon.

10.1 Event Interference

Here we will analyse interference between events displaced by half a cycle and those present due to the particle exchange symmetry of the system. This leads to four transition amplitudes, $M(\mathbf{p}_1, \mathbf{p}_2)$, $M(\mathbf{p}_2, \mathbf{p}_1)$, $M(-\mathbf{p}_1, -\mathbf{p}_2)$ and $M(-\mathbf{p}_2, -\mathbf{p}_1)$, which must

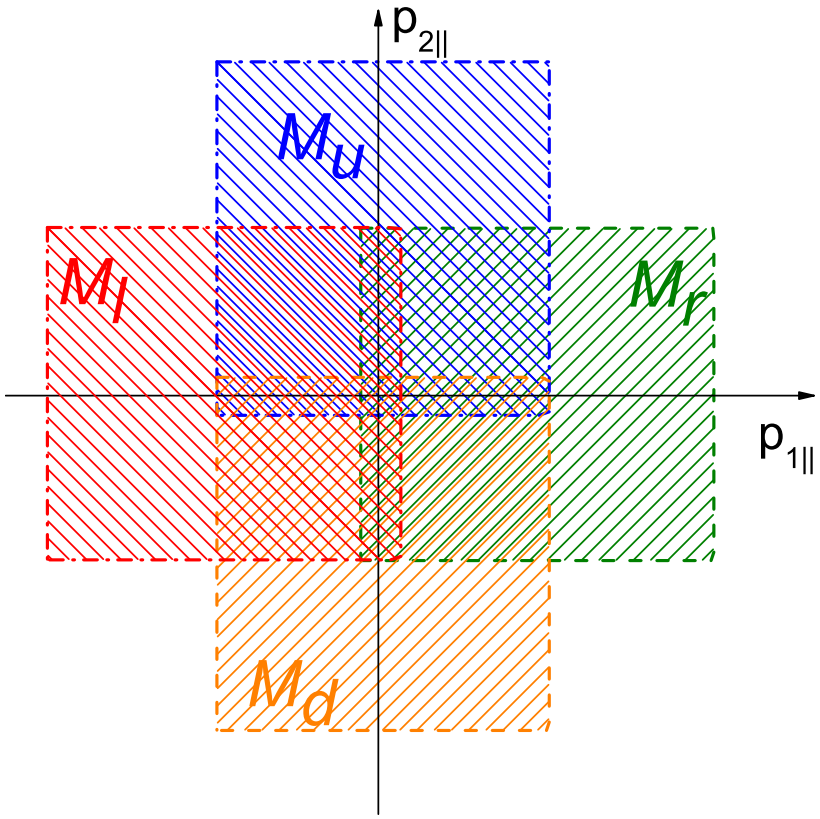

FIGURE 10.1: Schematic representation of the momentum regions occupied by the transition amplitudes M_l, M_u, M_d and M_r, which are displayed as the rectangular patterned regions. The overlap regions indicate areas within these constraints for which quantum interference may occur. The intensity represented in the figure is high enough to allow some interference at the origin $(p_{1\|}, p_{2\|}) = (0, 0)$.

be combined. Due to the localisation of these transition amplitudes, derived in the previous chapter, near the negative $p_{1\parallel}$ half axis, positive $p_{2\parallel}$ half axis, positive $p_{1\parallel}$ and negative $p_{2\parallel}$ half axis, i.e., occupying the left, upper, right and lower regions in the parallel momentum plane, we label them M_l, M_u, M_r and M_d, respectively. A schematic representation of the momentum regions occupied by the different transition amplitudes is provided in Fig. (10.1).

Throughout this analysis we will compare coherent and incoherent sums of these amplitudes integrated over momentum components perpendicular to the laser field, which are given by

$$W(p_{1\parallel}, p_{2\parallel}) = \iint \mathrm{d}^2\mathbf{p}_{1\perp}\mathrm{d}^2\mathbf{p}_{2\perp}|M_l + M_u + M_r + M_d|^2 \tag{10.1}$$

and

$$W(p_{1\parallel}, p_{2\parallel}) = \iint \mathrm{d}^2\mathbf{p}_{1\perp}\mathrm{d}^2\mathbf{p}_{2\perp}\left(|M_l|^2 + |M_u|^2 + |M_r|^2 + |M_d|^2\right), \tag{10.2}$$

respectively.

Quantum interference occurs predominantly in the overlap regions in Fig. (10.1). Apart from the region around $(p_{1\parallel}, p_{2\parallel}) = (0, 0)$, in which, potentially, all amplitudes may interfere, due to the constraints discussed in the previous section, we expect that M_l and M_u will interfere predominantly in the second quadrant and that M_l and M_d will overlap in the third quadrant of the $p_{1\parallel}p_{2\parallel}$ plane. Similarly, interference between M_r and M_u is expected to occur in the first quadrant, and between M_r and M_d will take place mostly in the fourth quadrant. For simplicity, throughout this section we will neglect the prefactors in Eqs. (10.1) and (10.2). This will help us identify how the phases determined by the corresponding actions interact without further momentum bias. The prefactors will be reintroduced in Sec. 10.2.

In Fig. (10.2), we display the coherent and incoherent sum of the transition amplitudes for three driving-field intensities for a target atom of argon. The figure shows that the interference between different events survives the integration over the transverse momentum coordinates, as there are obvious differences between coherent and

incoherent sums of events. Clearer features can be outlined from the difference of the two probability maps. There are maxima along the diagonal and anti-diagonal at all intensities and hyperbolic fringes whose presence becomes more obvious as the intensity increases. For higher intensities the patterns become more complicated.

These features can be explained by looking at the integrand of the coherent sum, which can be rewritten in terms of the actions S_l, S_r, S_u and S_d associated with the above-stated amplitudes. A common factor can be taken out, leaving terms that will contribute to the interference. Explicitly,

$$\begin{aligned}\Omega(p_{1\parallel}, p_{2\parallel}) &= \int \mathrm{d}^4\mathbf{p}_\perp \left| \int \mathrm{d}^3t \, (e^{iS_l} + e^{iS_r} + e^{iS_u} + e^{iS_d}) \right|^2 \\ &= \int \mathrm{d}^4\mathbf{p}_\perp \left| \int \mathrm{d}^3t \, e^{iS_l}(1 + e^{i\alpha_{lr}} + e^{i\alpha_{lu}} + e^{i\alpha_{ld}}) \right|^2, \end{aligned} \tag{10.3}$$

where the action $S_l = S(\mathbf{p}_1, \mathbf{p}_2, \mathbf{k}, t, t', t'')$ is associated with the matrix element $M_l = M(\mathbf{p}_1, \mathbf{p}_2)$ giving the left peak. The integrals over time and momenta have been abbreviated as

$$\int \mathrm{d}^3t = \int_{-\infty}^{\infty} \mathrm{d}t \int_{-\infty}^{t} \mathrm{d}t' \int_{-\infty}^{t'} \mathrm{d}t'', \tag{10.4}$$

and

$$\int \mathrm{d}^4\mathbf{p}_\perp = \iint \mathrm{d}^2\mathbf{p}_{1\perp}\mathrm{d}^2\mathbf{p}_{2\perp}, \tag{10.5}$$

and the phase differences between the actions read

$$\begin{aligned}\alpha_{ld} &= \frac{1}{2}\left(p_1^2 - p_2^2\right)(t - t') \\ &\quad + \frac{2\sqrt{\mathrm{U_p}}}{\omega}(p_{1\parallel} - p_{2\parallel})(\sin(\omega t) - \sin(\omega t')), \end{aligned} \tag{10.6}$$

$$\begin{aligned}\alpha_{lu} &= \frac{\pi}{2\omega}\left(4\mathrm{U_p} + 2\mathrm{E}_{2e} + 2\mathrm{E}_{1g} + p_1^2 + p_2^2\right) \\ &\quad + \frac{1}{2}\left(p_1^2 - p_2^2\right)(t - t') \\ &\quad - \frac{2\sqrt{\mathrm{U_p}}}{\omega}(p_{1\parallel} + p_{2\parallel})(\sin(\omega t) - \sin(\omega t')) \end{aligned} \tag{10.7}$$

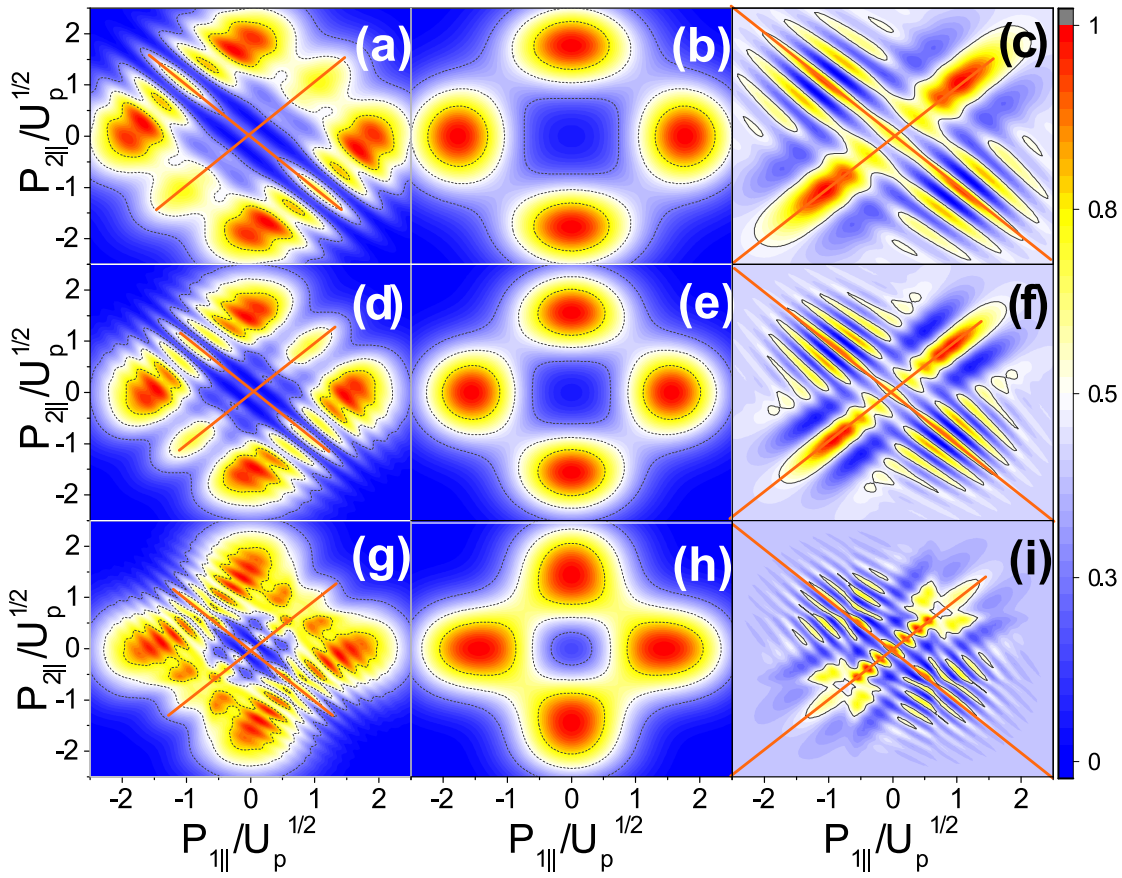

FIGURE 10.2: Coherent and incoherent sums of all amplitudes integrated over the perpendicular momenta as given by Eqs. (10.1) and (10.2). The columns from left to right show a coherent sum of amplitudes [panels (a), (d) and (g)], an incoherent sum of amplitudes [panels (b), (e) and (h)], and the difference between the two [panels (c), (f) and (i)]. The rows show different laser intensities of $I = 2.28, 4.56$ and 6.84 ($\times 10^{13}$ W/cm^2) from top to bottom with values for U_p of 0.05, 0.1 and 0.15 a.u. corresponding to an angular frequency $\omega = 0.057$ a.u. The distributions are computed considering an argon target. The RESI channel corresponds to a ground state valence orbital $3s$ and an excited orbital $3p$ for the second electron. The ionisation potentials of the ground state of the first and second electron and the excited state of the second electron are $I_{1g} = 0.58$, $I_{2g} = 1.02$ and $I_{2e} = 0.52$ a.u. respectively. The diagonal and anti-diagonals $p_{1\|} = \pm p_{2\|}$ are indicated with the orange lines in the figure. The signal in each panel has been normalised with regard to its maximum.

and

$$\alpha_{lr} = \frac{\pi}{2\omega}\left(4\mathrm{U_p} + 2\mathrm{E}_{2e} + 2\mathrm{E}_{1g} + p_1^2 + p_2^2\right) - \frac{4\sqrt{\mathrm{U_p}}}{\omega}\left(p_{1\parallel}\sin(\omega t') + p_{2\parallel}\sin(\omega t)\right). \tag{10.8}$$

In Eq. (10.6)-(10.8), the general form α_{ij} has been adopted, where the indices i, j refer to the interfering amplitudes. Constructive interference requires that the integrand in Eq. (10.3) is maximised, which will occur when $\alpha_{ij} = 0$, or as small as possible. We will start by investigating the "left-down" phase difference (10.6), between the actions associated with the left and lower peak. This phase vanishes for all times t, t' if conditions

$$p_1^2 - p_2^2 = 0 \tag{10.9}$$

and

$$p_{1\parallel} = p_{2\parallel} \tag{10.10}$$

are satisfied.

Condition (10.9), if written as a function of the parallel and perpendicular momentum components for $p_{2\perp}^2 - p_{1\perp}^2 \neq 0$, give the hyperbola

$$\frac{p_{1\parallel}^2}{p_{2\perp}^2 - p_{1\perp}^2} - \frac{p_{2\parallel}^2}{p_{2\perp}^2 - p_{1\perp}^2} = 1 \tag{10.11}$$

whose asymptotes lie at the diagonal and anti-diagonal $p_{1\parallel} = \pm p_{2\parallel}$ and whose vertices and transverse axis will depend on whether $p_{2\perp}^2 - p_{1\perp}^2$ are positive or negative. The former and latter case will lead to a hyperbola with transverse axes along $p_{1\parallel}$ and $p_{2\parallel}$, respectively. For equal transverse momenta, instead, condition (10.9) will give $p_{1\parallel} = \pm p_{2\parallel}$, i.e., the diagonal and the anti-diagonal. In this case, the interference condition is independent of the transverse momenta, so that they are expected to survive when the integration over these variables is performed. The hyperbola, on the other hand, depend on the transverse momentum coordinates, but may survive integration. If this happens, however, integration may influence their transverse axes, vertices and foci.

The analysis performed above suggests that there will be maxima along the diagonal and the anti-diagonal, and that there could be hyperbolic fringes in the coherent sum of the two-electron transition amplitudes, in agreement with Fig. (10.2). In Fig. (10.3), we have a closer look at this interference, and plot a partial distribution in which only M_l

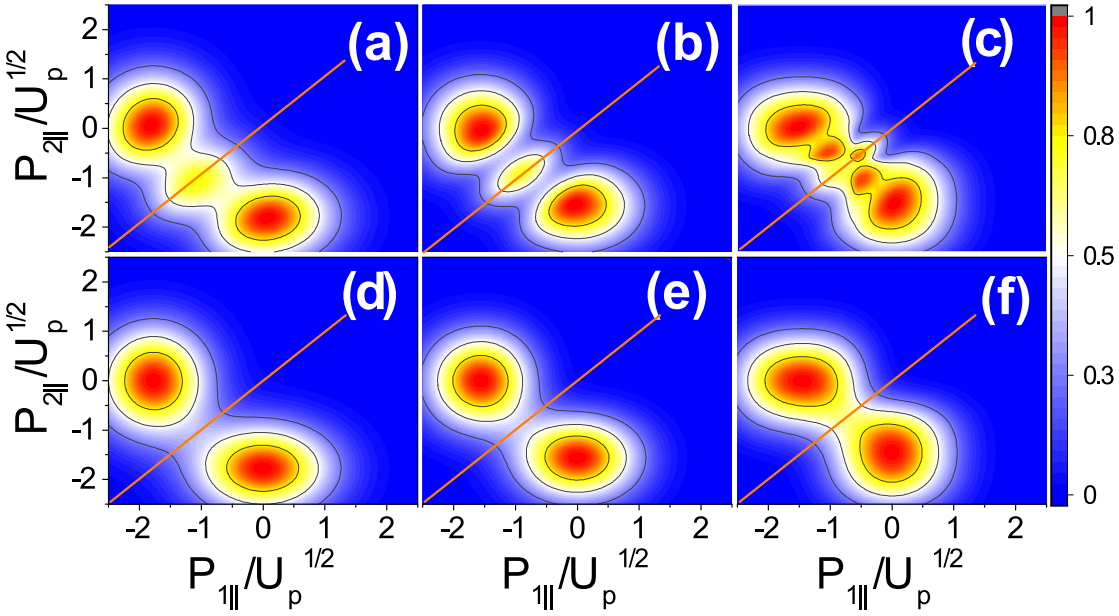

FIGURE 10.3: Correlated electron-momentum distributions obtained by combining the transition amplitudes M_l and M_d, isolating the effect of α_{ld}, integrated over the transverse-momentum components. The left, middle and right columns have been computed for laser intensities of $I = 2.28$, 4.56 and 6.84 ($\times 10^{13}$ W/cm^2), with values for $\mathrm{U_p}$ of 0.05, 0.1 and 0.15 a.u., respectively. Panels (a), (b) and (c) show the coherent sum $\Omega_{coh}^{ud} = |M_l + M_d|^2$, while in panels (d), (e) and (f) the incoherent sum $\Omega_{in}^{ud} = |M_l|^2 + |M_d|^2$ is displayed. The intensities and ionisation potentials are the same as in Fig. (10.2). The diagonals $p_{1\parallel} = p_{2\parallel}$ are indicated with the orange lines in the figure. The signal in each panel has been normalised with regard to its maximum.

and M_d summed, coherently and incoherently (upper and lower panels, respectively). The strongest feature in the figure is the maximum along the diagonal, which comes from condition (10.10) and also from the case $p_{1\perp} = p_{2\perp}$ related to the hyperbolic condition (10.9). Parallel to the diagonal, there are also interference fringes, whose number increases with the driving-field intensity. The interference maxima along the anti-diagonal cannot be seen as the partial sum employed in the figure is vanishingly small in the second quadrant of the parallel momentum plane.

An estimate for the position of the fringes can be obtained by considering the coherent superposition of M_l and M_d, and expanding the momenta in the vicinity of the diagonal, i.e., $p_{1\parallel} = p_{2\parallel} + \delta$. Fringes will occur for $\exp[i\alpha_{ld}] = \pm 1$, i.e., for $\alpha_{ld} = n\pi$, where even and odd n give maxima and minima, respectively. Assuming small momenta $\mathbf{p}_n(n = 1, 2)$, rescattering times at field crossings and ionisation times at the subsequent field crest [$t' = n\pi/\omega$ and $t = (2n + 1)\pi/(2\omega)$], the fringe spacing can be approximated as

$$|\delta| \simeq \frac{\omega n \pi}{2\sqrt{\mathrm{U_p}}}. \tag{10.12}$$

The above-stated equation shows that the spacing between the fringes is inversely proportional to the driving-field strength, in agreement with what has been observed in the previous figures.

The interference patterns are highlighted in Fig. (10.4), where we display the difference between the coherent and the incoherent sum, for the two lower driving-field intensities in the previous figure. Overall, for small momenta the fringe spacing exhibits a very good agreement with Eq. (10.12). Furthermore, all panels in the figure exhibit clear hyperbolic structures, whose number increases with the driving-field intensity. One should note that their transverse axis is not located along $p_{n\parallel} = 0$ $(n = 1, 2)$. This displacement is probably related to the integration over the transverse momenta, which influence the direction of the hyperbola. Furthermore, the last diagonal term will act to shift the centre of the hyperbolae along the diagonal, which can be observed by the fact the hyperbolae are opening, instead of exhibiting asymptotic behaviour towards the diagonals. As the laser intensity increases the hyperbolae should be shifted further from $(p_{1\parallel}, p_{2\parallel}) = (0, 0)$ and the number of fringes increases, as indicated by Eq. (10.12).

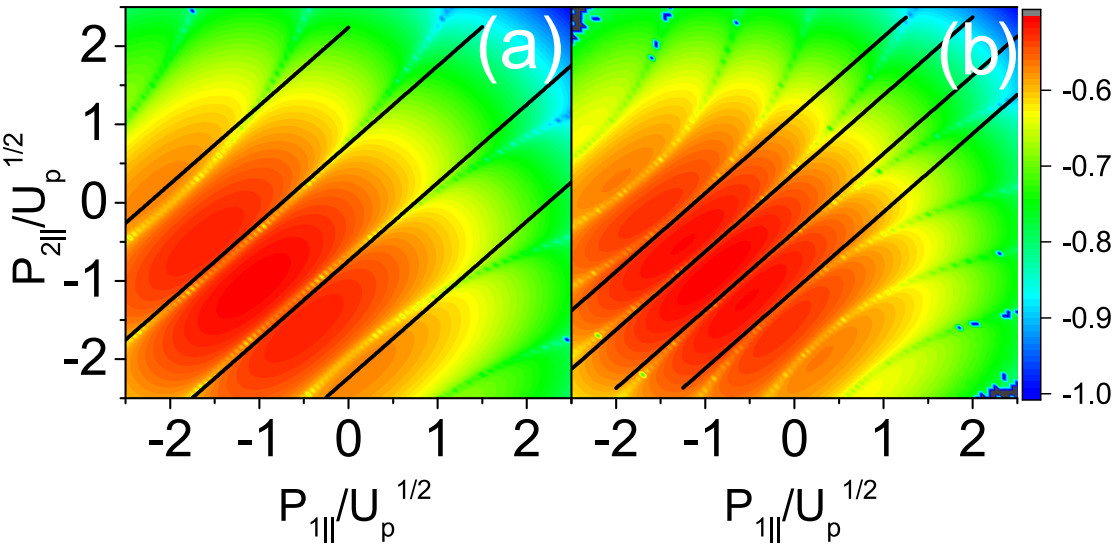

FIGURE 10.4: Absolute value of the difference between the sums from the upper and lower panels in Fig. (10.3). Panels (a) and (b) correspond to $U_p = 0.05$ and $U_p = 0.1$ a.u.respectively. The approximate fringes given by Eq. (10.12) are marked by black lines. The panels have been plotted in a logarithmic scale ($\log(|\Omega^{ud}_{coh} - \Omega^{ud}_{in}|)$) and the signal in each has been normalised with regard the maximum absolute value.

The remaining phase shifts, α_{lr} and α_{ld}, will not vanish. However, by an adequate choice of parameters one may identify momentum regions in which they are smallest, which will give rise to interference maxima. The exponent α_{lu}, which gives the interference between the left and the upper peaks, behaves in a similar way as α_{ld}, with the main difference that Eq. (10.7) shows an additional phase, with regard to Eq. (10.6) giving the left-down phase difference. This phase depends on $p_1^2 + p_2^2$ and has a constant factor. Furthermore, the last term in Eq. (10.7) causes a strong enhancement along the anti-diagonal.

The coherent and incoherent sums of M_l and M_u are presented in Fig. (10.5). The figure shows a very clear maximum along the anti-diagonal $p_{1\|} = -p_{2\|}$, and interference fringes with a richer substructure than the previous partial map. These effects are caused by the additional phases mentioned above. An estimate of the position of the fringes is not straightforward. However, we have verified that their spacing, for small momenta, is approximately one fourth of that given by Eq. (10.12). It also decreases with driving-field intensity.

Finally, we display the partial sum between the left and right amplitudes M_r and M_l (Fig. (10.5)). In this case, the interference effects are minimal and only present close to

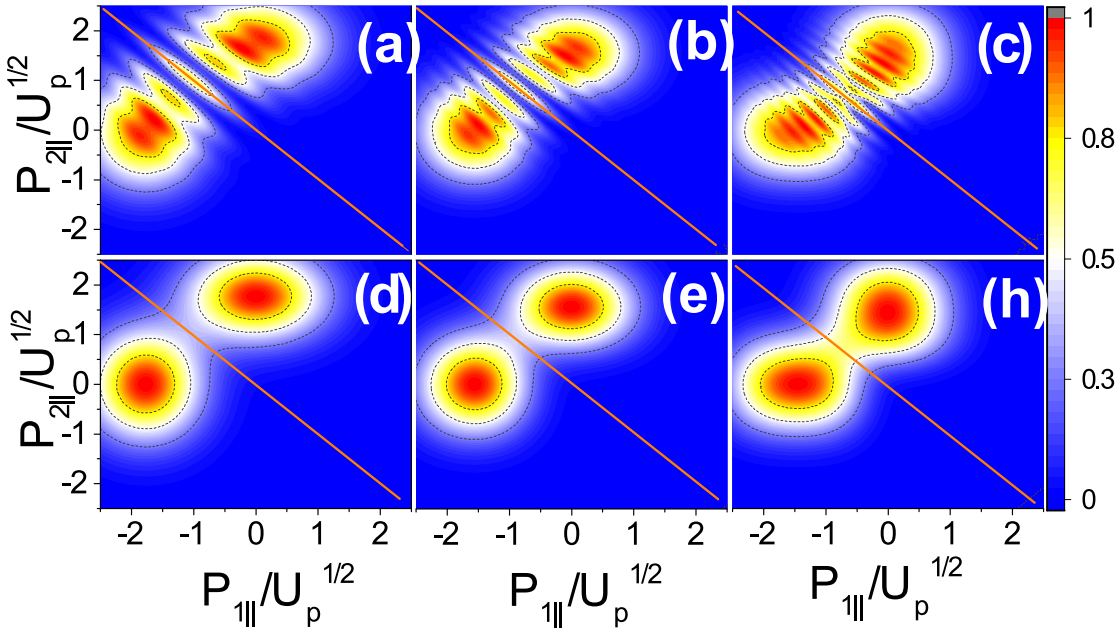

FIGURE 10.5: Correlated electron-momentum distributions obtained by combining the transition amplitudes M_l and M_u, isolating the effect of α_{lu}, integrated over the transverse-momentum components. The driving-field parameters and ionisation potentials are the same as in Fig. (10.3). We have also employed the same normalisation and labelling as in Fig. (10.3), with the coherent and incoherent sums in the upper and lower panels, respectively. The anti-diagonals $p_{1\parallel} = -p_{2\parallel}$ are indicated with the orange lines in the figure.

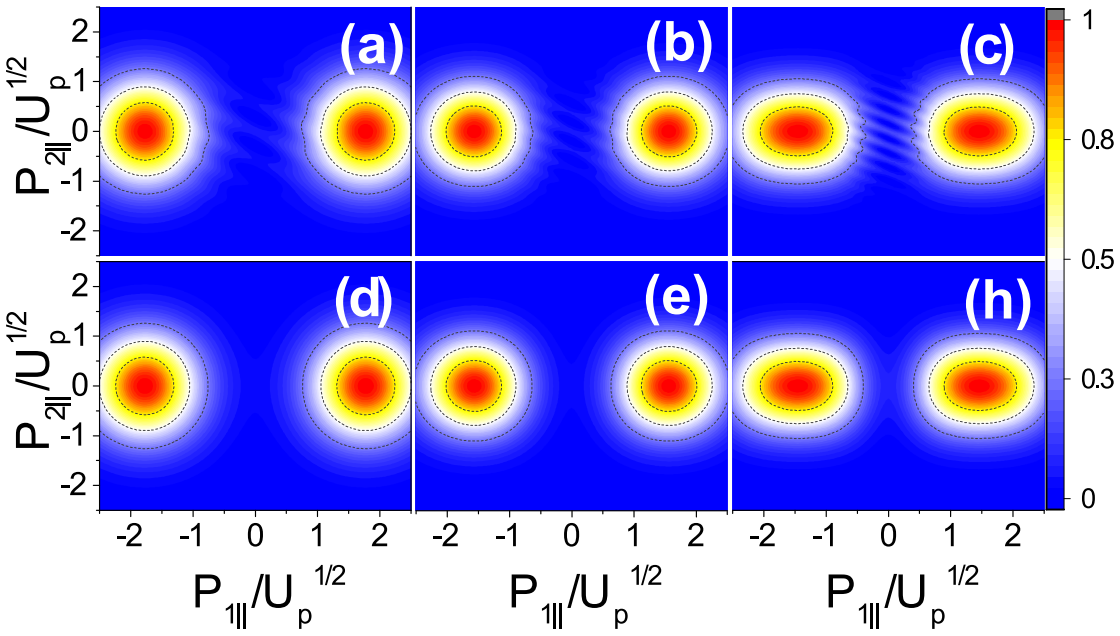

FIGURE 10.6: Correlated electron-momentum distributions obtained by combining the transition amplitudes M_l and M_r, isolating the effect of α_{lr} and integrating over the transverse momentum. The field parameters, ionisation potentials and plotting style are the same as in Fig. (10.3).

the origin $(p_{1\parallel}, p_{2\parallel}) = (0, 0)$. This is expected as according to the constraints the overlap between both amplitudes is vanishing in the other momentum regions. In the case of α_{lr} there is no obvious condition on the parallel momentum, independent of time or the perpendicular components, other than $p_{1\parallel}$ and $p_{2\parallel}$ being close or equal to zero. A time-dependent condition can be extracted,

$$p_{2\parallel} = -\frac{\sin(\omega t')}{\sin(\omega t)} p_{1\parallel}. \tag{10.13}$$

These trajectories will overlap for very low values of parallel momenta. In this case, for the dominant trajectories t' is near a crossing and t is near the next maximum [177]. These trajectories are located close to the axis. Near a crossing, $\sin(\omega t') \simeq \omega t'$ and near a maximum $\sin(\omega t) \simeq 1$. This strongly suggests that the slope in the overlap region will be constant as the rescattering time will not vary substantially. This is approximately the behaviour observed in Fig. (10.6).

Channel	Excited-State Configuration	E_{2e} (a.u.)
1	$3s3p^6$ ($3s \rightarrow 3p$)	0.52
2	$3p^5 3d$ ($3p \rightarrow 3d$)	0.41
3	$3p^5 4s$ ($3p \rightarrow 4s$)	0.40
4	$3p^5 4p$ ($3p \rightarrow 4p$)	0.31
5	$3p^5 4d$ ($3p \rightarrow 4d$)	0.18
6	$3p^5 5s$ ($3p \rightarrow 5s$)	0.19

TABLE 10.1: Relevant excitation channels for Ar^+, ordered according to principal and orbital quantum numbers for the second electron's excited state. From left to right, the columns give the number associated with the channel, the electronic configurations for the sub-levels involved in the excitation and the absolute value E_{2e} of the excited-state energy, respectively. For clarity, the excitation pathway for the second electron is given in brackets.

10.2 The Prefactors

Additionally to the interference effects studied above, the prefactors (9.10) and (9.11) will introduce a momentum bias, which influences the shapes and, in principle, the quantum interference between events or channels. In the specific problem addressed in [186], the target chosen is argon, as there are many experimental results to make a comparison with. The first and second ionisation potentials of argon are $E_{1\mathrm{g}} = 0.58$ a.u. and $E_{2\mathrm{g}} = 1.02$ a.u., respectively. For the parameter range of interest, the condition $3.17\mathrm{U_p} < E_{2\mathrm{g}}$ is satisfied, which leads to exist six relevant excitation channels that are provided in Table 10.1 and involve excitations to states of very different spatial geometry. Hence, they will give us a fairly good idea about the role of the prefactors. Throughout, we will restrict our studies to $m = 0$, in order to facilitate a comparison with the results in [186].

10.2.1 Derivation

Here we provide the full derivation to obtain analytic expressions of all the prefactors given in Eqs. (9.9), (9.10) and (9.11). These prefactors were first derived in [167] in the context of a qualitative analysis, so that only their functional form has been emphasised. In the present work, we have gone beyond those qualitative expressions and include all normalisation constants and phases, as they will be necessary for computing coherent superpositions.

Second Electron Ionisation Prefactor

Here we derive $V_{p_2,e}$, the prefactor related to the second electron tunnelling from an excited state, given in Eq. (9.11). This expression can also be used for V_{kg}, which differs only by the specific bound and momentum state, ψ_{g_1} instead of ψ_e and $|\mathbf{k}\rangle$ instead of $|\mathbf{p}_2\rangle$. The potential will be also be singly rather than doubly charged but this will only introduce an overall factor of $1/2$. From Eq. (9.11) we had,

$$\begin{aligned} V_{p_2,e} &= \langle \tilde{\mathbf{p}}_2(t)|V_{\text{ion}}|\psi_{e_2}\rangle \\ &= \frac{1}{(2\pi)^{3/2}}\int \mathrm{d}^3\mathbf{r}_2 V_{\text{ion}}(\mathbf{r}_2)\mathrm{e}^{-i\mathbf{p}_2\cdot\mathbf{r}_2}\psi_{e_2}(\mathbf{r}_2). \end{aligned} \tag{10.14}$$

We proceed by using hydrogenic states for ψ_{e_2} and expanding the plane wave into spherical harmonics,

$$\psi_{e_2}(\mathbf{r}_2) = R_{n_e l_e}(r_2)Y_{l_e}^{m_e}(\theta_{r_2},\phi_{r_2}) \tag{10.15}$$

$$\mathrm{e}^{-i\mathbf{p}_2\cdot\mathbf{r}_2} = 4\pi\sum_{l=0}^{\infty}(-i)^l j_l(p_2 r_2)\sum_{m=-l}^{l}\bar{Y}_l^m(\theta_{r_2},\phi_{r_2})Y_l^m(\theta_{p_2},\phi_{p_2}) \tag{10.16}$$

Where R_{nl} is the radial part of the wave function, Y_l^m are spherical harmonics and j_l are spherical Bessel functions. Combing these identities we obtain

$$\begin{aligned} V_{\mathbf{p}_2,e} &= \sqrt{\frac{2}{\pi}}\int \mathrm{d}^3\mathbf{r}_2 V_{\text{ion}}(\mathbf{r}_2)R_{n_e l_e}(r_2)Y_{l_e}^{m_e}(\theta_{r_2},\phi_{r_2}) \\ &\quad\times\sum_{l=0}^{\infty}(-i)^l j_l(p_2 r_2)\sum_{m=-l}^{l}\bar{Y}_l^m(\theta_{r_2},\phi_{r_2})Y_l^m(\theta_{p_2},\phi_{p_2}) \qquad (10.17) \\ &= \sqrt{\frac{2}{\pi}}\sum_{l=0}^{\infty}(-i)^l \overbrace{\int_0^\infty \mathrm{d}r_2 r_2^2 V_{\text{ion}}(r_2)R_{n_e l_e}(r_2)j_l(p_2 r_2)}^{Ir_2} \\ &\quad\times\sum_{m=-l}^{l}Y_l^m(\theta_{p_2},\phi_{p_2})\underbrace{\int \mathrm{d}\Omega Y_{l_e}^{m_e}(\theta_{r_2},\phi_{r_2})\bar{Y}_l^m(\theta_{r_2},\phi_{r_2})}_{\delta_{m_e m}\delta_{l e l}}. \\ &= \sqrt{\frac{2}{\pi}}(-i)^{l_e} I r_2 Y_{l_e}^{m_e}(\theta_{p_2},\phi_{p_2}). \qquad (10.18) \end{aligned}$$

Now we calculate Ir_2, we start by writing $R_{n_e l_e}(r_2)$ more explicitly as a sum of associated Legendre polynomials $L_l^m(x)$,

$$R_{n_e l_e}(r_2) = \sqrt{\left(2\sqrt{2E_{n_e}}\right)^3 \frac{(n_e - l_e - 1)!}{2n_e(n_e + l_e)!}} \mathrm{e}^{-\sqrt{2E_{n_e}} r_2} \left(2\sqrt{2E_{n_e}} r_2\right)^{l_e} \times L_{n_e - l_e - 1}^{2l_e+1}(2\sqrt{2E_{n_e}} r_2), \tag{10.19}$$

where the Legendre polynomials are given by

$$L_{n_e - l_e - 1}^{2l_e+1}(2\sqrt{2E_{n_e}} r_2) = \sum_{k=0}^{n_e - l_e - 1} (-1)^k \frac{(n_e + l_e)!}{(n_e - l_e - k - 1)!(2l_e + k + 1)! k!} (2\sqrt{2E_{n_e}} r_2)^k. \tag{10.20}$$

Hence,

$$R_{n_e l_e}(r_2) = \left(\frac{(n_e - l_e - 1)!}{2n_e(n_e + l_e)!}\right)^{\frac{1}{2}} \left(2\sqrt{2E_{n_e}} r_2\right)^{\frac{3}{2}} \mathrm{e}^{-\sqrt{2E_{n_e}} r_2} \times \sum_{k=0}^{n_e - l_e - 1} (-1)^k \frac{(n_e + l_e)! (2\sqrt{2E_{n_e}} r_2)^{k + l_e}}{(n_e - l_e - k - 1)!(2l_e + k + 1)! k!}. \tag{10.21}$$

Substituting this into Ir_2 yields

$$Ir_2 = \sqrt{\frac{(n_e - l_e - 1)!}{2n_e(n_e + l_e)!}} \sum_{k=0}^{n_e - l_e - 1} (-1)^k \frac{(n_e + l_e)! \left(2\sqrt{2E_{n_e}}\right)^{\frac{3}{2} + l_e + k}}{(n_e - l_e - k - 1)!(2l_e + k + 1)!\, k!} \times \underbrace{\int \mathrm{d}r_2 r_2^{l_e + k + 2} \overbrace{V_{\mathrm{ion}}(r_2)}^{\frac{2}{r_2}} \mathrm{e}^{-\sqrt{2E_{n_e}} r_2} j_l(p_2 r_2)}_{I_2}. \tag{10.22}$$

Doing the I_2 integral leads to

$$I_2 = \sqrt{\pi} \frac{p_2^{l_e}}{2^{l_e+1}} \left(\sqrt{2E_{n_e}}\right)^{-2-k-2l_e} \frac{\Gamma(2 + k + 2l_e)}{\Gamma(\frac{3}{2} + l_e)} \times {}_2F_1\left(\frac{1}{2}(2 + k + 2l_e), \frac{1}{2}(3 + k + 2l_e); \frac{3}{2} + l_e; -\frac{p_2^2}{2E_{n_e}}\right), \tag{10.23}$$

where ${}_2F_1(a,b;c;z)$ is the ordinary hypergeometric function. Then we have

$$Ir_2 = \sqrt{\pi}\sqrt{\frac{(n_e-l_e-1)!}{2n_e(n_e+l_e)!}}\sum_{k=0}^{n_e-l_e-1}(-1)^{k+1}\frac{(n_e+l_e)!\,2^{\frac{1}{2}+k}(\sqrt{2E_{n_e}})^{-\frac{1}{2}-l_e}p_2^{l_e}}{(n_e-l_e-k-1)!(2l_e+k+1)!\,k!}\frac{\Gamma(2+k+2l_e)}{\Gamma(\frac{3}{2}+l_e)} \times {}_2F_1\left(\frac{1}{2}(2+k+2l_e),\frac{1}{2}(3+k+2l_e);\frac{3}{2}+l_e;-\frac{p_2^2}{2E_{n_e}}\right). \quad (10.24)$$

Putting it all together gives

$$V_{\mathbf{p}_2,e} = 2(-i)^{l_e}\sqrt{\frac{(n_e-l_e-1)!}{2n_e(n_e+l_e)!}}Y_{l_e}^{m_e}(\theta_{p_2},\phi_{p_2})\sum_{k=0}^{n_e-l_e-1}(-1)^k\frac{(n_e+l_e)!\,2^k(\sqrt{2E_{n_e}})^{-\frac{1}{2}-l_e}p_2^{l_e}}{(n_e-l_e-k-1)!(2l_e+k+1)!\,k!} \times\frac{\Gamma(2+k+2l_e)}{\Gamma(\frac{3}{2}+l_e)}{}_2F_1\left(\frac{1}{2}(2+k+2l_e),\frac{1}{2}(3+k+2l_e);\frac{3}{2}+l_e;-\frac{p_2^2}{2E_{n_e}}\right). \quad (10.25)$$

Recollision Prefactor

Here we derive the prefactor related to the collision of the first and second electron from Eq. (9.10). Its explicit expression is

$$\begin{aligned} V_{\mathbf{p}_1 e,\mathbf{k}g} &= \langle\tilde{\mathbf{p}}_1(t'),\psi_{e_2}|V_{12}|\tilde{\mathbf{k}}(t'),\psi_{g_2}\rangle \\ &= \frac{V_{12}(\mathbf{q})}{(2\pi)^{3/2}}\int \mathrm{d}^3\mathbf{r}_2\mathrm{e}^{i\mathbf{q}\cdot\mathbf{r}_2}\bar{\psi}_e^{(2)}(\mathbf{r}_2)\psi_g^{(2)}(\mathbf{r}_2), \end{aligned} \quad (10.26)$$

where $\mathbf{q}=\mathbf{p_1}-\mathbf{k}$ and using the same identities as before,

$$\mathrm{e}^{-i\mathbf{q}\cdot\mathbf{r}_2} = 4\pi\sum_{l=0}^{\infty}(-i)^l j_l(q\,r_2)\sum_{m=-l}^{l}\bar{Y}_l^m(\theta_{r_2},\phi_{r_2})Y_l^m(\theta_q,\phi_q), \quad (10.27)$$

$$\psi_g^{(2)}(r_2) = R_{n_g l_g}(\mathbf{r}_2)Y_{l_g}^{m_g}(\theta_{r_2},\phi_{r_2}) \quad (10.28)$$

and

$$\psi_e^{(2)}(r_2) = R_{n_e l_e}(\mathbf{r}_2)Y_{l_e}^{m_e}(\theta_{r_2},\phi_{r_2}). \quad (10.29)$$

Hence,

$$V_{\mathbf{p}_1 e,\mathbf{k}g} = \sqrt{\frac{2}{\pi}} V_{12} \sum_{l=0}^{\infty} \sum_{m=-l}^{l} (-i)^l Y_l^m(\theta_q,\phi_q) \overbrace{\int \mathrm{d}r_2 j_l(qr_2) R_{n_g l_g}(r_2) R_{n_e l_e}(r_2) r_2^2}^{I_r} \times \underbrace{\int \mathrm{d}\Omega \bar{Y}_l^m(\theta_{r_2},\phi_{r_2}) \bar{Y}_{l_e}^{m_e}(\theta_{r_2},\phi_{r_2}) Y_{l_g}^{m_g}(\theta_{r_2},\phi_{r_2})}_{I_\Omega} \tag{10.30}$$

We can use the two following relations for spherical harmonics to simplify I_Ω,

$$\bar{Y}_{l_e}^{m_e}(\Omega) = (-1)^{m_e} Y_{l_e}^{-me}(\Omega) \tag{10.31}$$

$$Y_{l_e}^{-me}(\Omega) Y_{l_g}^{m_g}(\Omega) = \sum_{L=|l_g-l_e|}^{l_e+l_g} \sum_{M=-L}^{L} \sqrt{\frac{(2l_e+1)(2l_g+1)}{4\pi(2L+1)}} \times \langle l_g, l_e, 0, 0 | L, 0\rangle \langle l_g, l_e, m_g, -m_e | L, M\rangle Y_L^M(\Omega), \tag{10.32}$$

where $\langle l_1, l_2, m_1, m_2 | L, M\rangle$ denote Clebsch-Gordon coefficients. Inserting these definitions in to Eq. (10.30) yields,

$$I_\Omega = (-1)^{m_e} \sum_{L=|l_g-l_e|}^{l_e+l_g} \sum_{M=-L}^{L} \sqrt{\frac{(2l_e+1)(2l_g+1)}{4\pi(2L+1)}} \langle l_g, l_e, 0, 0 | L, 0\rangle \langle lg, le, mg, -me | L, M\rangle \times \underbrace{\int \mathrm{d}\Omega \bar{Y}_l^m(\Omega) Y_L^M(\Omega)}_{\delta_{mM}\delta_{lL}}, \tag{10.33}$$

leading to,

$$V_{\mathbf{p}_1 e,\mathbf{k}g} = \sqrt{\frac{2}{\pi}} V_{12}(\mathbf{q}) \sum_{L=|l_e-l_g|}^{l_e+l_g} \sum_{M=-L}^{L} (-i)^L (-1)^{m_e} Y_L^M(\theta_q,\phi_q) \sqrt{\frac{(2l_g+1)(2l_e+1)}{4\pi(2L+1)}} \times \langle l_g, l_e, 0, 0 | L, 0\rangle \langle lg, le, mg, -me | L, M\rangle \times Ir_1. \tag{10.34}$$

Now we compute I_r using a similar approach to the previous case,

$$I_r = \int \mathrm{d}r_2 j_L(q\, r_2) R_{n_g l_g}(r_2) R_{n_e l_e}(r_2) r_2^2 \tag{10.35}$$

$$\begin{aligned} R_{n_g l_g}(r_2) = &\left(\frac{(n_g - l_g - 1)!}{2n_g(n_g + l_g)!}\right)^{\frac{1}{2}} \left(2\sqrt{2E_{n_g}} r_2\right)^{\frac{3}{2}} \mathrm{e}^{-\sqrt{2E_{n_g}} r_2} \\ &\times \sum_{k=0}^{n_g - l_g - 1} (-1)^k \frac{(n_g + l_g)! (2\sqrt{2E_{n_g}} r_2)^{k + l_g}}{(n_g - l_g - k - 1)!(2l_g + k_g + 1)! k!} \end{aligned} \tag{10.36}$$

$$\begin{aligned} I_r = &\\ &\sqrt{\frac{(n_e - l_e - 1)!}{2n_e(n_e + l_e)!}} \sqrt{\frac{(n_g - l_g - 1)!}{2n_g(n_g + l_g)!}} \sum_{k_g=0}^{n_g - l_g - 1} \sum_{k_e=0}^{n_e - l_e - 1} \frac{(-1)^{k_g + k_e} (n_g + l_g)!\, (n_e + l_e)!}{k_g!\, k_e!\, (n_g - l_g - 1)!\, (n_e - l_e - 1)!} \\ &\times \frac{\left(2\sqrt{2E_{n_g}}\right)^{3/2 + l_g + k_e}}{(2l_g + k_g + 1)!} \frac{\left(2\sqrt{2E_{n_e}}\right)^{3/2 + l_e + k_e}}{(2l_e + k_e + 1)!} \int_0^\infty \mathrm{d}r_2 r^{2 + k_e + k_g + l_e + l_g} j_L(q\, r_2) \mathrm{e}^{-\xi r_2}, \end{aligned} \tag{10.37}$$

where $\xi = \sqrt{2E_{n_g}} + \sqrt{2E_{n_e}}$. Computing the integral gives

$$\begin{aligned} I_r = &\\ &\sqrt{\pi \frac{(n_e - l_e - 1)!}{2n_e(n_e + l_e)!}} \sqrt{\frac{(n_g - l_g - 1)!}{2n_g(n_g + l_g)!}} \sum_{k_g=0}^{n_g - l_g - 1} \sum_{k_e=0}^{n_e - l_e - 1} \frac{(-1)^{k_g + k_e} 2^{2 + l_g + l_e + k_g + k_e - L} (n_g + l_g)!\, (n_e + l_e)!}{k_g!\, k_e!\, (n_g - l_g - 1)!\, (n_e - l_e - 1)!} \\ &\times \frac{\left(\sqrt{2E_{n_g}}\right)^{3/2 + l_g + k_e}}{(2l_g + k_g + 1)!} \frac{\left(\sqrt{2E_{n_e}}\right)^{3/2 + l_e + k_e}}{(2l_e + k_e + 1)!} \left(\frac{q^2}{\xi^2}\right)^{L/2} \xi^{-3 - k_g - k_e - l_g - l_e} \frac{\Gamma(3 + k_g + k_e + l_g + l_e + L)}{\Gamma(\frac{3}{2} + L)} \\ &\times {}_2F_1\left(\frac{1}{2}(3 + k_g + k_e + l_g + l_e + L), \frac{1}{2}(4 + k_g + k_e + l_g + l_e + L); \frac{3}{2} + L; -\frac{q^2}{\xi^2}\right). \end{aligned} \tag{10.38}$$

Putting it all together we get,

$$V_{\mathbf{p}_1 e,\mathbf{k}g} = \frac{1}{\sqrt{2\pi}} V_{12}(\mathbf{q}) \sum_{L=|l_e-l_g|}^{l_e+l_g} \sum_{M=-L}^{L} (-i)^L (-1)^{m_e} Y_L^M(\theta_q,\phi_q) \sqrt{\frac{(2l_g+1)(2l_e+1)}{(2L+1)}}$$
$$\times \langle l_g, l_e, 0, 0|L, 0\rangle \langle lg, le, mg, -me|L, M\rangle \times I'_r,$$

where

$$I'_r =$$
$$\sqrt{\frac{(n_e-l_e-1)!}{2n_e(n_e+l_e)!}} \sqrt{\frac{(n_g-l_g-1)!}{2n_g(n_g+l_g)!}} \sum_{k_g=0}^{n_g-l_g-1} \sum_{k_e=0}^{n_e-l_e-1} \frac{(-1)^{k_g+k_e} 2^{2+l_g+l_e+k_g+k_e-L} (n_g+l_g)!\,(n_e+l_e)!}{k_g!\,k_e!\,(n_g-l_g-1)!\,(n_e-l_e-1)!}$$
$$\times \frac{\left(\sqrt{2E_{n_g}}\right)^{3/2+l_g+k_g} \left(\sqrt{2E_{n_e}}\right)^{3/2+l_e+k_e}}{(2l_g+k_g+1)!(2l_e+k_e+1)!} \left(\frac{q^2}{\xi^2}\right)^{L/2} \xi^{-3-k_g-k_e-l_g-l_e} \frac{\Gamma(3+k_g+k_e+l_g+l_e+L)}{\Gamma(\frac{3}{2}+L)}$$
$$\times {}_2F_1\left(\frac{1}{2}(3+k_g+k_e+l_g+l_e+L), \frac{1}{2}(4+k_g+k_e+l_g+l_e+L); \frac{3}{2}+L; -\frac{q^2}{\xi^2}\right). \tag{10.39}$$

Below in Eqs. (10.40) and (10.41), we give more compact forms of the general expressions for the excitation and ionisation prefactors, respectively.

$$V_{\mathbf{p}_1 e,\mathbf{k}g} = \sum_{L=|l_e-l_g|}^{l_e+l_g} \sum_{M=-L}^{L} (-i)^L A_1 Y_L^M(\theta_q,\phi_q) \frac{\langle l_g, l_e, 0, 0|L, 0\rangle \langle lg, le, m_g, -m_e|L, M\rangle}{\sqrt{(2L+1)}} I''_r \tag{10.40}$$

$$I''_r = \sum_{k_g=0}^{b_{n_g l_g}} \sum_{k_e=0}^{b_{n_e l_e}} \frac{(-1)^{k_g+k_e} 2^{a_1-1-2L} \xi^{L-a_1} \Xi_{l_g k_g}^{n_g} \Xi_{l_e k_e}^{n_g} \Gamma(a_1)}{k_g!\,k_e!\,(b_{n_g l_g})!\,(b_{n_e l_e})!\,\Gamma(\frac{3}{2}+L)} d_{l_g k_g}^{n_g} d_{l_e k_e}^{n_e} \left(\frac{q^2}{\xi^2}\right)^{L/2}$$
$$\times {}_2F_1\left(\frac{1}{2}a_1, \frac{1}{2}(a_1+1); \frac{3}{2}+L; -\frac{q^2}{\xi^2}\right),$$

where

$$A_1 = (-1)^{m_e} C_{n_g l_g} C_{n_e l_e} \frac{V_{12}(\mathbf{q})}{\sqrt{2\pi}} \sqrt{(2l_g+1)(2l_e+1)}$$

$$C_{nl} = \sqrt{\frac{(n-l-1)!}{2n(n+l)!}} \qquad \Xi^n_{lk} = \left(\sqrt{2E_n}\right)^{\frac{3}{2}+l+k}$$
$$d^m_{lk} = \frac{(n+l)!}{(2l+k+1)!} \qquad \xi = \sqrt{2E_{n_g}} + \sqrt{2E_{n_e}}$$
$$a_1 = 3 + k_g + k_e + l_g + l_e + L \qquad b_{nl} = n - l - 1$$

Now here is the expression for $V_{\mathbf{p}_2 e}$ again with all normalisation constants and phases.

$$V_{\mathbf{p}_2,e} = A_2 \sum_{k=0}^{b_{n_e l_e}} (-1)^k \frac{2^k (\sqrt{2E_{n_e}})^{-\frac{1}{2}-l_e} p_2^{l_e}}{(b_{n_e l_e} - k)!\; k!} d^{m_e}_{l_e k} \frac{\Gamma(a_2)}{\Gamma(\frac{3}{2}+l_e)} \times {}_2F_1\left(\frac{1}{2}a_2, \frac{1}{2}(a_2+1); \frac{3}{2}+l_e; -\frac{p_2^2}{2E_{n_e}}\right), \tag{10.41}$$

where,

$$A_2 = 2(-i)^{l_e} C_{n_e l_e} Y^{m_e}_{l_e}(\theta_{p_2}, \phi_{p_2}) \quad \text{and} \quad a_2 = 2 + k + 2l_e.$$

10.2.2 Effect on Distributions

The above-stated prefactors have radial and angular nodes. The prefactors $V_{\mathbf{p}_1 e,\mathbf{k}g}$, Eq. (10.40) and V_{kg} depend on the intermediate momentum $\mathbf{k}(t'', t')$, which will vary with regard to $\mathbf{p}_1$. This will lead to the nodes being washed out to a great extent. We have verified that this happens even if the integration over $\mathbf{p}_{1\perp}$ is not performed. In general, transverse momentum integration will cause further blurring. Mostly, the prefactor $V_{\mathbf{p}_1 e,\mathbf{k}g}$ will cause a shift in the peaks of the electron momentum distribution from $p_{1\parallel} = \pm 2\sqrt{\mathrm{U_p}}$ and alter their width. The prefactor for the first electron excitation has no explicit dependence on the final momenta V_{kg}, hence it plays almost no role in the overall shape of the distributions.

The effects caused by the prefactor $V_{\mathbf{p}_2 e}$ are much more dramatic. This has been observed in previous publications [167, 168] for atoms and molecules, but has not been investigated systematically. Similarly to what is observed for hydrogenic wave functions, the number of radial nodes is given by $b_{n_e l_e} = n_e - l_e - 1$, and angular nodes by l_e. This

Channel and State	$b_{n_e l_e}$	Numerator	Roots
1 $3p$	1	$2E_{2e} - p_2^2$	$p_2 = \sqrt{2E_{2e}}$
2 $3d$	0	const.	no roots
3 $4s$	3	$8E_{2e}^3 - 28E_{2e}^2 p_2^2 + 14E_{2e} p_2^4 - p_2^6$	$p_2 = \sqrt{2E_{2e}}$, $p_2 = \sqrt{(6 \pm 4\sqrt{2})E_{2e}}$
4 $4p$	2	$20E_{2e}^2 - 28E_{2e} p_2^2 + 5p_2^4$	$p_2 = \sqrt{\frac{2}{5}\left(7 \pm 2\sqrt{6}\right) E_{2e}}$
5 $4d$	1	$2E_{2e} - p_2^2$	$p_2 = \sqrt{2E_{2e}}$
6 $5s$	4	$80E_{2e}^4 - 480E_{2e}^3 p_2^2 + 504E_{2e}^2 p_2^4 - 120E_{2e} p_2^6 + 5p_2^8$	$p_2 = \sqrt{\left(2 \pm \frac{4}{\sqrt{5}}\right) E_{2e}}$, $p_2 = \sqrt{\left(10 \pm 4\sqrt{5}\right) E_{2e}}$

TABLE 10.2: Number of radial nodes $b_{n_e l_e} = n_e - l_e - 1$ and the numerator polynomials (and their associated roots) that give rise to these nodes. Note that $p_2^2 = p_{2\parallel}^2 + p_{2\perp}^2$, so that the expressions in the third column describe circles in the $(p_{2\parallel}, p_{2\perp})$ plane.

is because, formally, the prefactor is the Fourier transform of a hydrogenic excited state $\psi_{n_e l_e m_e}(\mathbf{r}_2)$ modified by the interaction $V_{\rm ion}(\mathbf{r}_2) = 1/r_2$. Since $V_{\rm ion}$ and $\exp(i\mathbf{p}_2 \cdot \mathbf{r}_2)$ have no nodes, the number of nodes will be preserved but their energy positions will be different, if compared to the momentum-space wave function $\psi_{n_e l_e m_e}(\mathbf{p}_2)$. Their number and position with regard to the momentum $p_2 = \sqrt{p_{2\parallel}^2 + p_{2\perp}^2}$ are given in Table 10.2.

According to Table 10.2, the radial nodes will manifest themselves as circles in the $p_{2\parallel} p_{2\perp}$ plane. They are clearly seen if we fix the momentum of the first electron at $(p_{1\parallel}, p_{1\perp}) = (2\sqrt{\rm U_p}, 0)$ and plot the probability distribution as a function of the momentum components $p_{2\parallel}$ and $p_{2\perp}$ of the second electron. This procedure is similar to the computation of partial momentum maps employed in the publications [183, 190], and provide a wealth of detail which is lost if the transverse momentum integration is performed.

Fig. (10.7) displays these distributions for the six channels in Table 10.1. The panel labels each correspond to the channel number, which is detailed in Table 10.1. The circle $p_{2\parallel}^2 + p_{2\perp}^2 = 4{\rm U_p}$ indicates the direct ATI cutoff, according to the condition (9.23). Changes in the shapes of the distributions will be caused by nodes within this region. The radial nodes will then be particularly important for highly excited states, as in this case E_{2e} is small. Physically, this is related to the fact that high localisation in momentum space corresponds to a large position-space spread. The smaller the binding energy, the more delocalised $\psi_{n_e l_e m_e}(\mathbf{r}_2)$ will be.

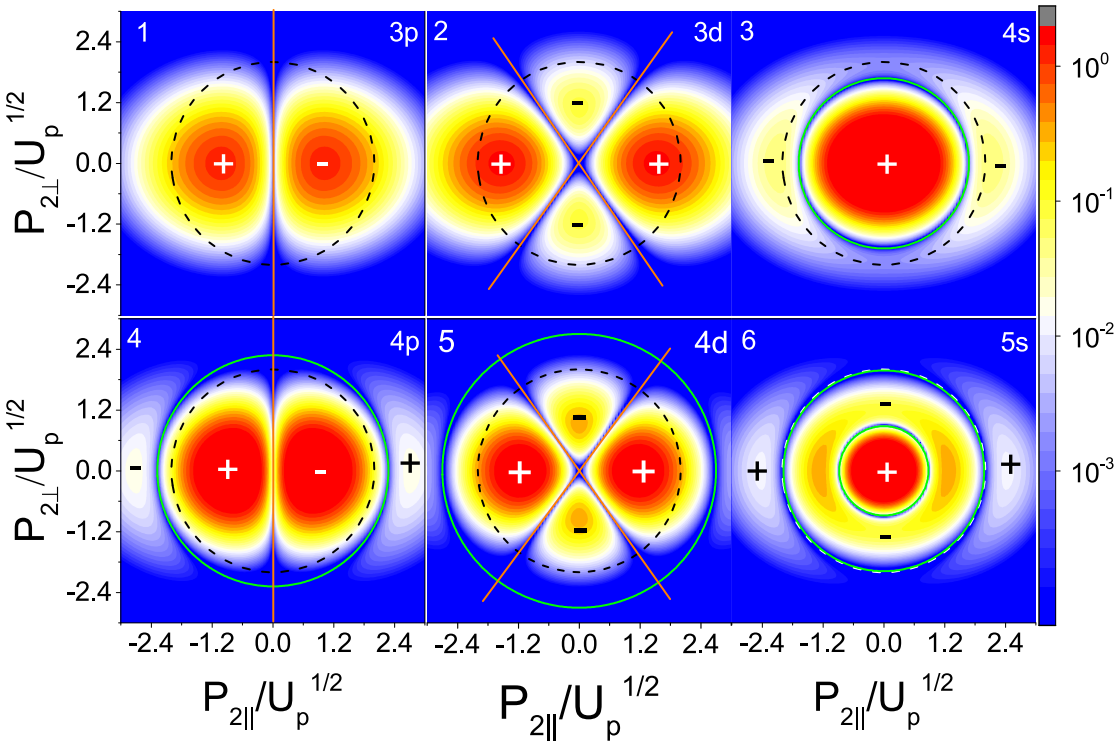

FIGURE 10.7: Cross-section of the total probability distribution with p_1 fixed at $(p_{1\parallel}, p_{1\perp}) = (2\sqrt{\mathrm{U_p}}, 0)$, which gives an effective partial probability distribution over p_2. The ponderomotive energy is given by $\mathrm{U_p} = 0.1$ a.u.($I = 4.56 \times 10^{13}$ W/cm^2). A logarithmic scale has been used to highlight the orbital-geometrical features. The radial and angular nodes resulting from the second ionisation prefactor are marked by green circles and red line respectively. The direct ATI cutoff $p_{2\parallel}^2 + p_{2\perp}^2 = 4\mathrm{U_p}$ is marked with a dashed circle. Beyond this point the probability distribution decays exponentially. Phases for each prefactor are indicated by + and - signs, with a change in sign indicating a flip. The signal in each panel has been normalised with regard to its maximum value.

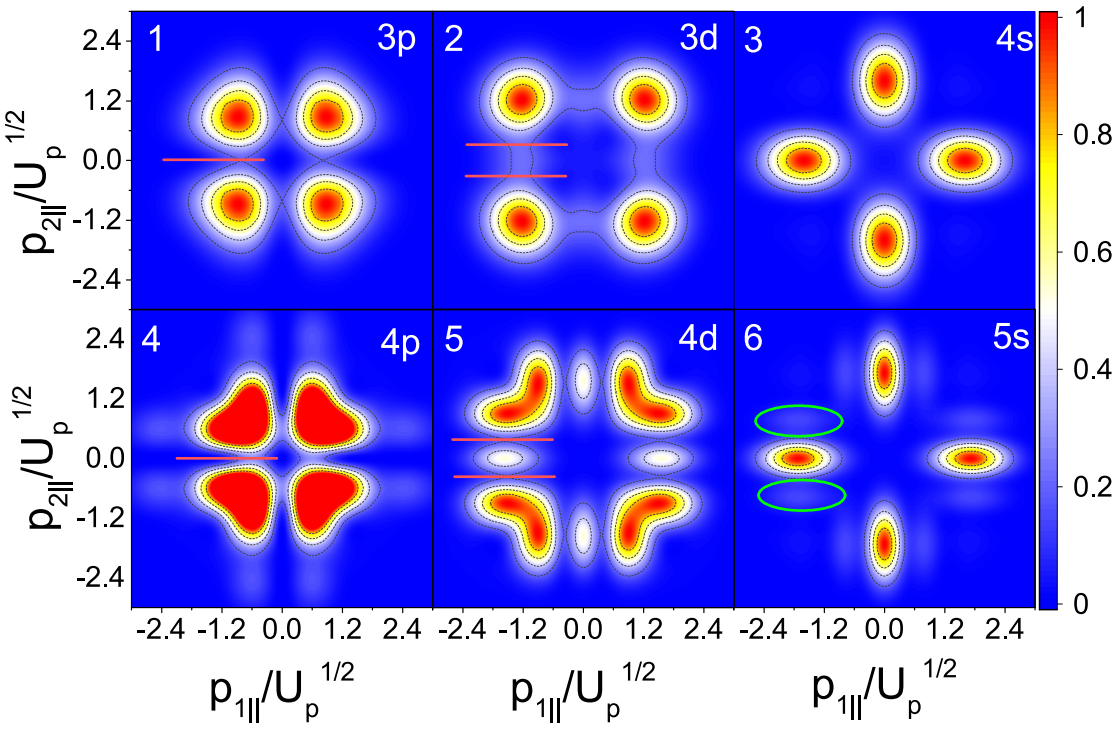

FIGURE 10.8: Full probability distribution with all prefactors included, an incoherent sum of events has been used. The panels are marked with the channel number and excitation state (top left and right corners, respectively). Red lines have been used to show the splitting caused by angular nodes and green circles mark the secondary peaks due to radial nodes. The ponderomotive energy is given by $\mathrm{U_p} = 0.1$ a.u.($I = 4.56 \times 10^{13}$ W/cm^2). The yield in channel four has been over-exposed in order to show the secondary nodes.

The effect of the radial nodes can be seen by comparing channels 3 and 6, which involve s-states. For channel 3, there is only one radial node in the momentum region of interest, while for channel 6 the two existing nodes influence the electron momentum distributions. This will lead to an overall narrowing in momentum space. In the remaining channels, in addition to this effect, there are also angular nodes, which behave in very distinct ways. For $l_e = 1$ (channels 1 and 4) they lead to a strong suppression in the electron-momentum distributions for $p_{2\|} = 0$. Since these nodes occur for all $p_{2\perp}$, they will survive the transverse-momentum integration. This will cause the correlated two-electron distributions to move away from the axes. For d-states, there are x-shaped nodes which intersect at $(p_{2\|}, p_{2\perp}) = (0, 0)$. We have verified that these nodes will also survive the integration over the transverse momentum components, but will lead to a secondary, much weaker maximum at the axes instead of a complete suppression.

In Fig. (10.8), we plot the incoherently symmetrised, correlated distributions, for

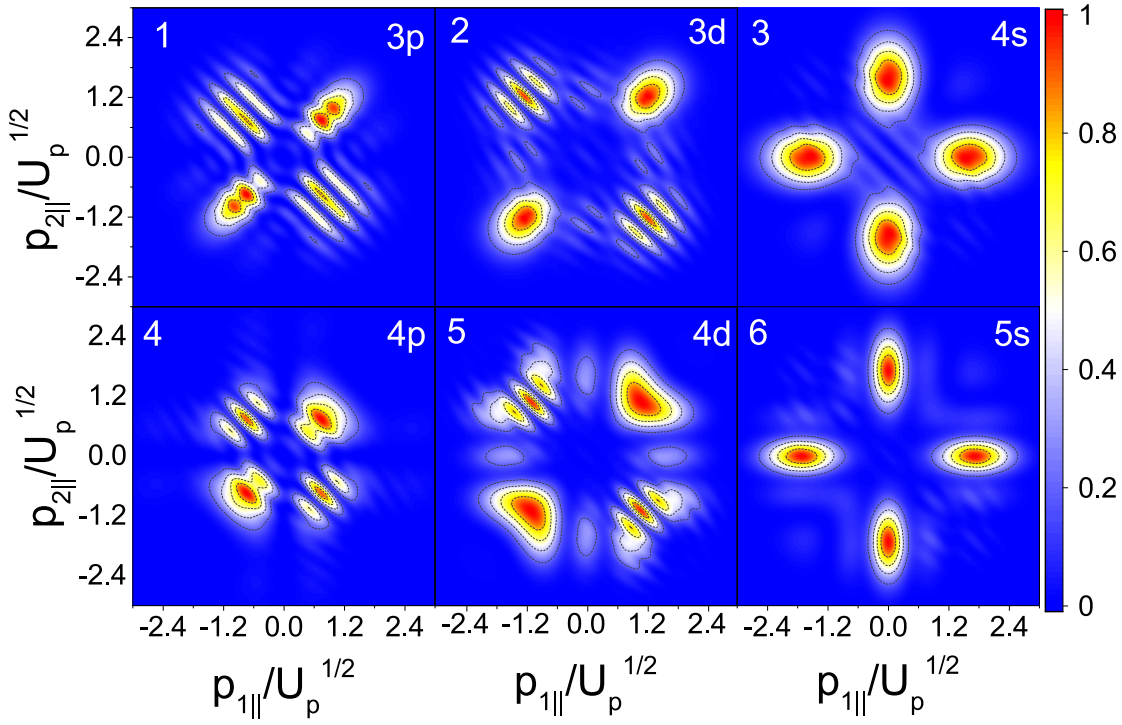

FIGURE 10.9: Full probability distribution with all prefactors included, for identical parameters as in Fig. (10.8), except that a coherent sum of events has been used. The same panel labels are used as in Fig. (10.8). The signal in each panel has been normalised with regard to its maximum value.

the same channels as in Fig. (10.7). The figure in fact shows an overwhelming influence of the prefactor $V_{\mathbf{p}_2 e}$. Angular nodes in $p_{2\|}$ are clearly visible as cuts marked by orange lines and radial nodes can be seen by small secondary peaks marked by green circles. Only for very loosely bound states does the excitation prefactor lead to some substructure (see channel 4), although it is an order of magnitude below the main peak. This figure establishes which substructure comes from the prefactors themselves, so that they cannot be attributed to the interference between different events.

If a coherent sum is considered upon symmetrisation, Fig. (10.9), the same diagonal fringes can be seen as in Fig. (10.2). There will not be interference for s-states as the localisation of the states causes the prefactor to narrow the distribution on to the axis, away from the diagonal regions where the interference mostly occurs. For p- and d-states, there is a lot of interference as the effect of the angular nodes is to split the distribution apart, widening it causing much of it to be along the diagonal. The actual type of interference is unchanged from Fig. (10.2), we verified this by looking at the phase information from the prefactor. For the second ionisation prefactor, looking a the phase plotted over p_2, the nodes represent a phase shifts of π (see Fig. (10.9)). If this is applied to the partial momentum distribution there is little change in the resulting phase map and the affect of this after integration over $p_\perp$ will be lost entirely. Hence the prefactors effect the interference only by limiting the signal to specific regions in the probability momentum distributions and all the effects derived, discussed earlier, are still valid.

10.3 Channel Interference

We will now study the quantum interference between the different excitation channels in Table 10.1. A uniform superposition of channels is used, which can be justified if one views each channel as a path the second electron can take from its ground state to the final Volkov state. Hence, the final transition amplitude should sum over the possible channels, leading to $|\sum_c M_c|^2$, where M_c is the transition amplitude calculated for each channel.

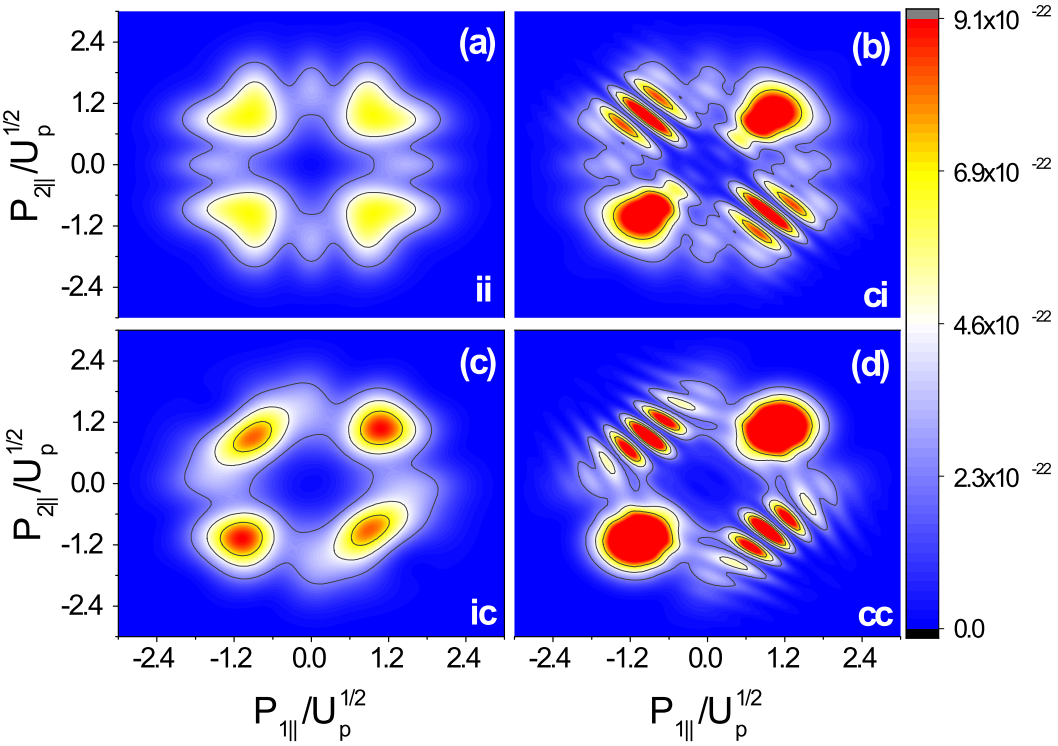

FIGURE 10.10: Full coherent and incoherent superpositions of all channels in Table 10.1, for the same field parameters as in Fig. (10.8). Panel (a) is an incoherent sum of all the channels and their events, panel (b) is an incoherent sum of channels with a coherent sum of events, panel (c) is a coherent sum of channels with an incoherent sum of events and panel (d) is a coherent sum of channels and events. The symbols i and c in the bottom right corners denote incoherent and coherent sums for event and channel, respectively, with event preceding channel. All panels use the same arbitrary scale.

$U_p = 0.05$		$U_p = 0.1$		$U_p = 0.15$	
1	3.49×10^{-28}	5	2.95×10^{-22}	5	4.67×10^{-19}
4	2.02×10^{-28}	4	1.31×10^{-22}	4	1.02×10^{-19}
5	1.54×10^{-28}	1	9.91×10^{-23}	2	5.43×10^{-20}
2	1.01×10^{-28}	2	7.62×10^{-23}	1	3.26×10^{-20}
3	7.78×10^{-29}	3	4.94×10^{-23}	3	2.52×10^{-20}
6	6.17×10^{-30}	6	1.21×10^{-23}	6	1.94×10^{-20}

TABLE 10.3: Mean values of the two electron parallel momentum probability distribution of each channel for different laser intensities, within the parameter range of interest. These distributions have been computed for a monochromatic field.

In Fig. (10.10) we plot the full sum of channels 1 to 6, using different combinations of coherent and incoherent superpositions for events and channels. The figure shows that a fourfold momentum symmetry only occurs if the channels and events are summed incoherently [panel (a)]. Once quantum interference is introduced, only the reflection symmetry with regard to the diagonal or anti-diagonal remains, as shown in panels (b) to (d). In this case, the features along the diagonal and the anti-diagonal differ. However, only channel interference [panel (c)] exhibits a diagonal enhancement. The anti-diagonal fringes only come from event interference [see panel (b)]. The diagonal enhancement and breaking of symmetry in panel (c) is consistent with what was found in [186].

A legitimate question is whether one may identify dominant channels and/or features related to the channel type in the superpositions presented above. The shapes of the superpositions in Fig. (10.10) suggest that excitations involving p- and d-states prevail. Table 10.3 shows the mean values of the correlated electron momentum distributions for each channel, which are comparable. Since one channel does not dominate significantly over the rest, interference is expected to be important. This is contrary to the results in [186], where channels 1-3 were found to dominate.

More insight is obtained by considering superpositions of two channels, which may be incoherent or coherent. The former and the latter case are given by

$$\Omega_{In}(p_{1\|}, p_{2\|}) = ||M_1||^2 + ||M_2||^2 \tag{10.42}$$

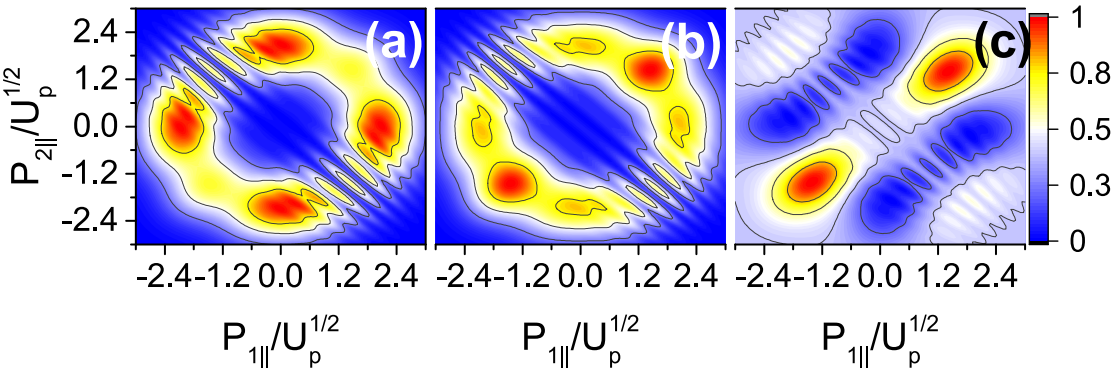

FIGURE 10.11: Channel sum 1 and 4 without prefactors. Panel (a) shows an incoherent sum of channel and a coherent sum of events, panel (b) shows a coherent sum of channels and events, panel (c) is the difference between the two. The driving-field parameters are the same in Fig. (10.8). The signal in each panel has been normalised to its maximum value.

and

$$\Omega_{Coh}(p_{1\|}, p_{2\|}) = ||M_1 + \mathrm{e}^{i\phi} M_2||^2, \tag{10.43}$$

respectively. In the coherent sum (10.43), we have included a phase ϕ that can be used to manipulate interference effects such as diagonal or anti-diagonal enhancement.

Without the effect of prefactors there is little qualitative difference between the possible channel sums, given that the actions only differ by the term $E_{2g}t$ (see panels (a) and (b) in Fig. (10.11)). Nonetheless, in the difference between the coherent and incoherent sums we can see hyperbolic fringes (Fig. (10.11)(c)). We have verified empirically that the position of the fringes is determined by the value of the phase ϕ and the thickness of the fringes is inversely related to $E_{2e_1} - E_{2e_2}$. Due to their location in the $p_{2\|}p_{1\|}$ plane, the most significant interfering terms will be equivalent events between channels, e.g., M_{1l} and M_{2l}, but the terms related by particle exchange such as M_{1l} and M_{2d} will also be important. The prefactors add a momentum-dependent phase difference between the two channels. In the case of the second ionisation prefactor, which mainly determines the interference effects, the phase is constant but inverts when a nodal line is crossed. The other prefactors depend on $\mathbf{k}$, which has a complex phase relation determined by the saddle point equations.

Fig. (10.12) shows a selection of particular interference phenomena occurring in two-channel sums. In panel (a) the recollision and second ionisation prefactor both cause phase inversion, which cancels overall. The diagonal enhancement comes from

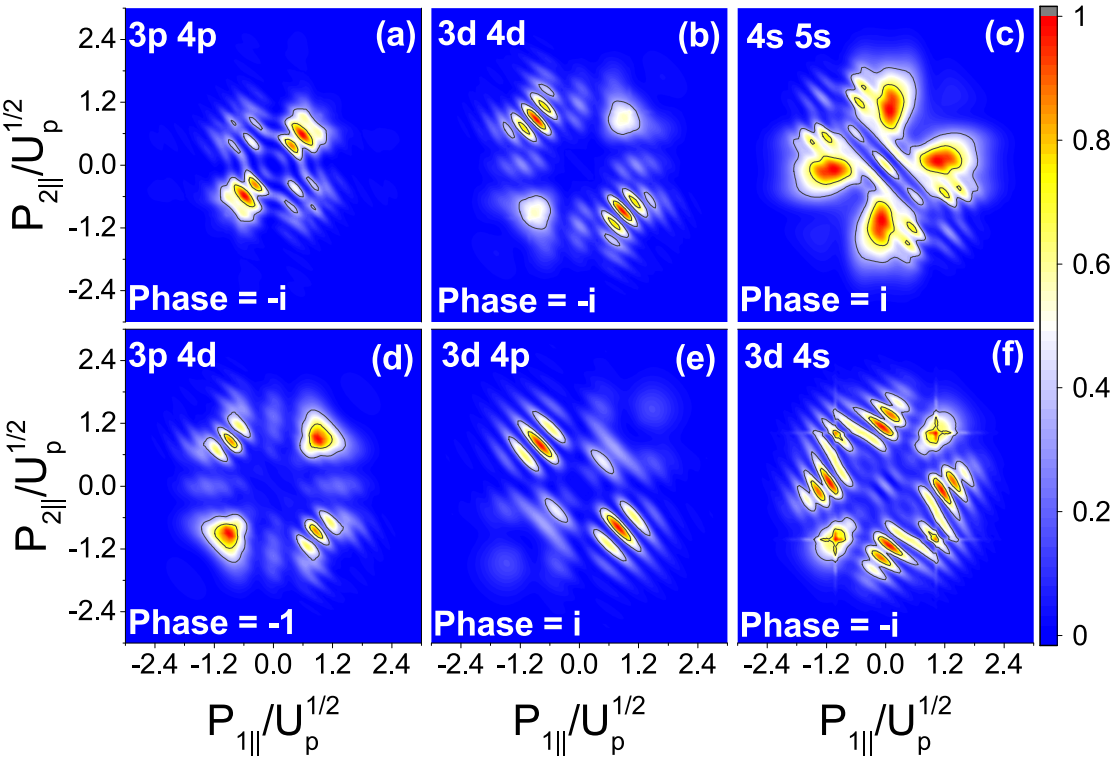

FIGURE 10.12: Two-channel sums with prefactors, for the same driving-field parameters in Fig. (10.8). The numbers at the top left in each panel labels the excited states used in the superposition, with the phase difference given in the bottom left. The signal in each panel has been normalised to its maximum value.

the fringes related to channel interference, which have been shifted by a phase of $-i$, whereas i would cause an anti-diagonal enhancement. For panel (b) the total effect of the prefactors is to cause an inversion in the channel-interference fringes. This leads to a suppressed signal along the diagonal. However, the effect is not as strong as the fringes are distorted by $V_{\mathbf{p}_2 e}$. In both panels (a) and (b), the thickness of the channel-interference fringes are comparable to those associated with the “left-down" interference. There are no significant diagonal effects in panel (c) as both distributions are concentrated near the axes $p_{n\|} = 0 (n = 1, 2)$. This happens because, for the two interfering channels, the second electron is excited to an s-state. However, there are some interference effects breaking the fourfold momentum symmetry.

The remaining panels show some implications of channel interference involving energetically very close and distant excited states. For the interference of channels 1 and 5, shown in panel (d), there is a large difference in the excited-state energies. This causes small inter-channel fringes, so that suppression along the diagonal or anti-diagonal is not possible. In contrast, for panel (e), the excited bound states are energetically very close. This implies that fringes stemming from channel interference are too thick to cause a diagonal or anti-diagonal suppression. However, the prefactor does this instead (see below). For panel (f) the channel-related fringes are even thicker, so that the substructure is determined by the event interference and the prefactors.

Fig. (10.13) shows the same coherent sums of channels as in Fig. (10.12), but, instead, incoherent sums of events. All the diagonal and anti-diagonal effects remain and are in general stronger without the phase information and fringes from different events. The influence of the combined prefactors can also be seen more clearly. For instance, in panels (a) to (c) the features related to p-, d- and s-states are very evident, with a further bias introduced by the inter-channel interference. These features are (a) probability densities concentrated at the diagonal and anti-diagonal; (b) similar probability distributions as in (a), but with secondary maxima at the axes; (c) distributions concentrated mostly at the axes, respectively. This happens because the angular momentum quantum number l_e of the excited states are the same for the two interfering channels.

The situation becomes more complex in the lower panels, in which channels with

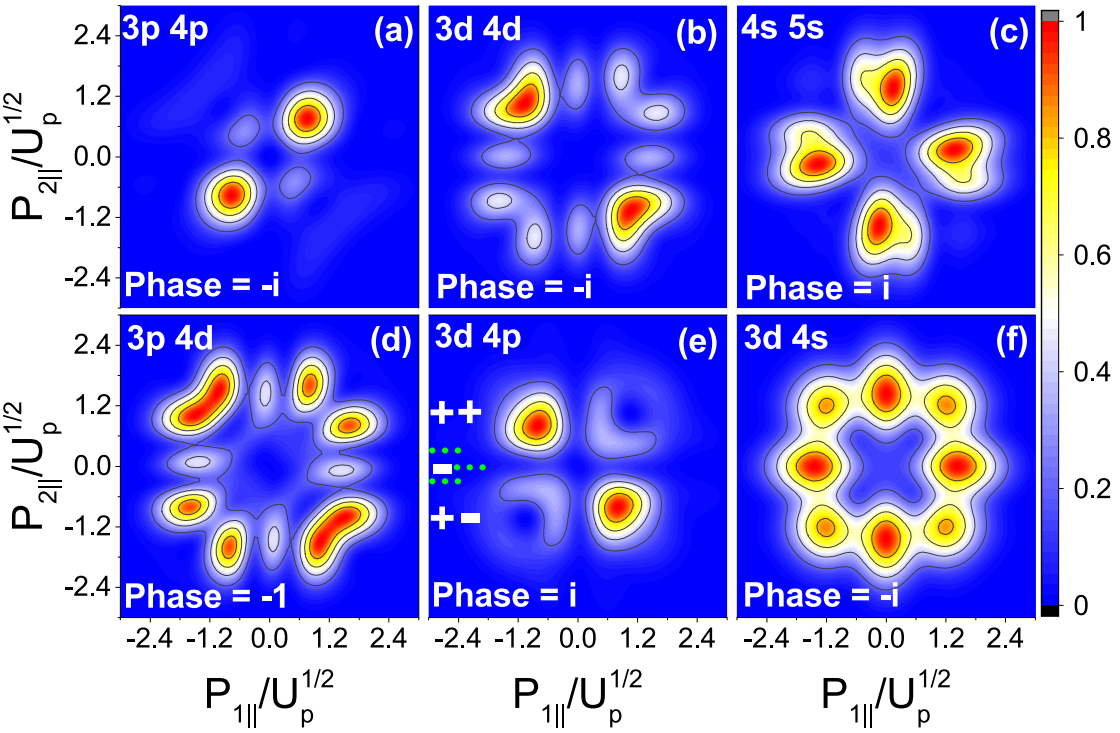

FIGURE 10.13: Same two-channel sums as Fig. (10.12), except that the events have been summed incoherently. For clarity, the prefactor phase information has been marked on panel (e) in white. This information can be related to panels 2 and 4 in Fig. (10.7). The green dotted lines mark nodal lines. The same logic can be applied to panel (f), with the difference that the $4s$ state does not have angular nodes.

different angular momenta l_e are mixed. In this case, we have identified two very striking scenarios, which occur for energetically close levels [panels (e) and (f)]. Because the inter-channel fringes are very thick in these cases, the shape of the electron-momentum distributions will be mainly determined by the prefactors and their phases. For instance, the clear diagonal suppression for panel (e) can be explained by the phase of the second ionisation prefactors, which flips at every nodal line. The interfering channels involve excitation to $3d$ and $4p$. For a p-state, there is one node at $p_{2\|} = 0$, while for a d-state there are two. This means that, from the top to the bottom of the panel, the phase of the p-state will flip once, while that of the d-state will flip twice. Hence, in the second quadrant the channels interfere constructively, while in the third quadrant destructive interference occurs. The same line of argument can be employed for the first and fourth quadrant, but in this case the interference pattern will be reversed. This shows a case where we have entirely prefactor dependent anti-diagonal enhancement. In panel (f), the phase of the $4s$ prefactor will not flip in the momentum region of interest, while that of the $3d$ prefactor will flip twice. Hence, this will preserve the fourfold symmetry. Furthermore, interference between the channels will not be significant, as d states populate mainly the two diagonals and s states lead to distribution localised along the axes. This leads to a momentum distribution with peaks at the axes and the two diagonals. This distribution is, for practical purposes, fourfold symmetric, unless event interference is considered [see Fig. (10.12)(f)].

To summarise the inter-channel fringes, prefactors and a relative phase can cause a range of interference effects. The prefactors can cause an inversion, which leads to diagonal/anti-diagonal enhancement being swapped. They can also apply a phase shift, such that a different phase between the two channels is needed for diagonal/ anti-diagonal enhancement. Inter-channel interference effects are not washed out by more complex superpositions, as can be seen by directly comparing Figs. (10.10), panels (a) and (c).

10.4 Discussion

In this chapter, we have performed an in-depth, semi-analytical study of quantum interference in recollision-excitation with subsequent ionisation (RESI) using the strong-field approximation (SFA). Our analysis includes interference of symmetry-related features such as electron indistinguishability, and of different excitation channels. Overall, we have found that the electron momentum distributions are greatly influenced by both types of interference. The main effect of quantum interference is to break their fourfold symmetry in $p_{1\parallel}p_{2\parallel}$ plane, while the symmetry with regard to the diagonals is retained. This fourfold symmetry has been encountered in previous RESI studies employing the strong-field approximation [167, 168, 177] or related methods [178].

We have shown, by considering a coherent sum of symmetry-related events, that interference effects previously thought to be washed out from integration over perpendicular momenta are present in the correlated electron-momentum distributions. This influences the RESI distributions even for a single channel of excitation, via enhancement and suppression near the diagonals $p_{1\parallel} = \pm p_{2\parallel}$. We provide fully analytical expressions and estimates for diagonal, anti-diagonal and hyperbolic interference patterns. Similar fringes can be seen, but have not been explained, in [191], where RESI has been modelled using a strong-field quantum-electrodynamical method (see Fig. 7 therein). Additionally, further quantum interference fringes have been found by the same group for NSDI of helium using two-colour IR+XUV fields using a similar method [192, 193]. These fringes are found to exist for both equivalents of the EI and the RESI mechanisms of NSDI for IR+XUV fields. The interference is between channels that arise due to differing numbers of XUV photons absorbed by the electrons across the NSDI process. Different numbers of XUV photons absorbed during the second electron ionisation event could act to create channels similar to the channels of excitation we considered here, by in effect reducing the ionisation potential. Formally, in the ionisation equation used in this work this is exactly what happens as the number of XUV photons absorbed effectively changes the ionisation potential. Thus, a parallel may be drawn between the inter-channel interferences and some interferences found in [193].

We found that inter-channel interference will play an important role in RESI, in

agreement with the results of [186]. We go, however, beyond such studies and show that the shape of the electron-momentum distributions will be determined by a complex interplay of inter-channel and event interference, and the geometry of the excited bound states. This will mainly occur near the diagonal and anti-diagonal in the parallel-momentum plane. This means that it will mainly impact channels involving excitation to p- or d-states, while the influence on those with s-state excitation will be much less critical. In particular, for the parameter range of interest, the contributions from all channels used in this work are comparable.

We also analyse this interference in more detail using two-channel coherent superpositions. In this case, diagonal or anti-diagonal enhancement may occur due to inter-channel fringes and/or geometry-dependent prefactors. The fringes have hyperbolic shape, and their width is inversely proportional to the energy difference between the two channels involved. The prefactors will determine the region in momentum space to be occupied. In particular the nodes of the ionisation prefactor $V_{\mathbf{p}_2 e}$ of the second electron will cause phase shifts, which will influence inter-channel interference in specific momentum ranges. This enhancement can be manipulated using a relative phase. In this context, one should notice that by appropriate choice of channels and relative phase one may obtain anti-correlated distributions without resorting to bound-state depletion. This latter feature has been employed in [186] in order to suppress the signal in the first and third quadrants of the parallel-momentum plane.

Interestingly, depending on how interference occurs, the RESI distributions may exhibit diagonal enhancement (correlation), anti-diagonal enhancement (anti-correlation), or be spread in the four quadrants of the $p_{1\parallel}p_{2\parallel}$ plane. In contrast, for electron-impact ionisation, the probability density is located only in the first and third quadrants and interference effects get washed out by transverse momentum integration. This sheds some light on experimental findings where different atoms give either diagonal or anti-diagonal enhancement [194]. Diagonal enhancement is normally attributed to electron-impact ionisation. However, for low, below-threshold intensities, this could also be related to RESI. Indeed, all possible results found experimentally [174, 176, 194] are achievable if we can find the correct superposition of channels. Furthermore, there exist theoretical studies for which anti-correlation has been obtained without excitation

[195]. This suggests that the ability to manipulate diagonal and anti-diagonal enhancement with a phase opens up the possibility of control over the RESI process, which could lead to various applications.

These results show that quantum interference has a striking influence on the shapes and localisation of the electron-momentum distributions and thus call into question quantum-classical correspondence in RESI. Hence, classical-trajectory methods must be viewed with care. On the other hand, highly excited states may give rise to a quasi-continuum, which would allow the existence of a quasi-classical wave packet. This would justify the success of classical models. For molecules, a larger density of states and enhanced ionisation may increase their predictive power [179, 196, 197].

Furthermore, the SFA considers discrete states and neglects broadening and distortion caused by the field. It could well be that these effects lead to a strong overlap and thus the creation of a quasi-continuum, washing out phase information. However, recent studies of the RESI dynamics in phase space have revealed a highly confined region that can be associated with trapping in an excited state [198]. This would justify using discrete bound states and neglecting depletion, and would render interference important. Recent experimental results [199] report oscillation in the asymmetry of the electron-electron momentum correlation when varying the laser intensity. These results are reported to be only possible through interference effects. Thus, this may be experimental verification of the interference described here. Additionally, recent fully quantum mechanical calculation of NSDI, which neglects the Coulomb potential for continuum electrons (as in this work) [124], reports sub-cycle interference features in the final momentum distributions. Note this calculation did not separate contributions from RESI, the EI or any other mechanism. For a detailed discussion on the advantages and drawbacks of classical and quantum-mechanical approaches in the modelling of RESI see the review article [154]. The present work contributes to this discussion by shedding additional light on the role of interference in this context.

Chapter 11

Pulse Effects and State Reconstruction

In this chapter we use knowledge of interference types coupled with the bound state prefactors to perform a more advanced analysis of experimental results. Using the fact that we can manipulate distributions by changing the phase between two channels, we can extend this argument to all channels. We can include normalisations and phases, to control the dominance and whether the interference is constructive or destructive, between all of the channels. One may include different amplitudes or phases for each channel, which would model channel selection or account for phase effects. This yields a more general sum than Eq. (9.25),

$$\Omega(p_{1\parallel}, p_{2\parallel}) = \iint \mathrm{d}^2 p_{1\perp} \mathrm{d}^2 p_{2\perp} \left| \sum_c N_c e^{i\phi_c} M^{(c)} \right|^2 . \tag{11.1}$$

This method can use experimental data to guide the construction of a superposition of excited states, which should give some information about the excited state the second electron left from. This method is essentially accounting for experimental uncertainty and effects yet to be included in the model that would alter the dominance or phase of different channels.

Experimental results of RESI in argon from [173] (see in Fig. (11.1)), show that increasing pulse lengths from few to many cycle pulses causes a transition from cross-shaped to slightly anti-correlated, correlated or ring-shaped distributions. In Fig. (11.2) we model the results from [173] by selecting specific normalisations as in Table 11.1 to represent the change in channels dominance caused by a pulse. We have also chosen

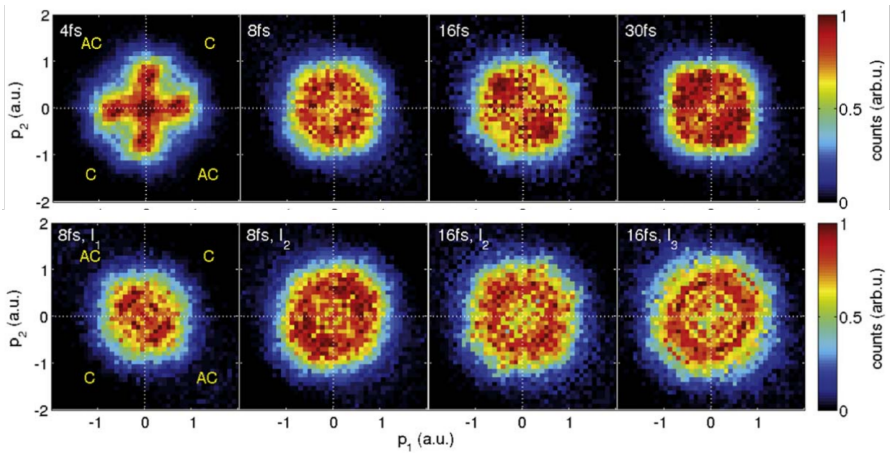

FIGURE 11.1: RESI distributions for argon ($E_{1g} = 0.58$ a.u., $E_{2g} = 1.02$ a.u.). Taken from [173]. In the first row, panels (a)-(d), the peak intensity is 1×10^{14} W/cm^2 with $\omega = 0.057$ a.u. and a ponderomotive energy of $\mathrm{U_p} = 0.22$ a.u. The peak intensities in the second row are as follows: (e) $I = 0.8 \times 10^{14}$ W/cm^2 with $\mathrm{U_p} = 0.18$ a.u., (f) and (g) $I = 1.2 \times 10^{14}$ W/cm^2 with $\mathrm{U_p} = 0.26$ a.u. and (h) $I = 1.4 \times 10^{14}$ W/cm^2 with $\mathrm{U_p} = 0.30$ a.u. These results were averaged over the carrier envelope phase of the laser field.

the phases such that panel (c) matches the corresponding anti-correlated results from [173]. The phases have then been kept the same in all other cases. We find that if a pattern is optimised to be anti-correlated at one driving field strength, changing this will cause it to flip to be correlated. Hence, in panels (e)-(h) we obtain correlated patterns, in agreement with [173]. One should note that, despite this myriad of shapes, all intensities employed in this experiment are well within the below-threshold regime. For the intensities in Fig. (11.2), this energy varies from 0.55 a.u. to 0.86 a.u., i.e., between 54% and 84% of E_{2g}. Hence, RESI is the prevalent NSDI mechanism. Similar superpositions may be used to reproduce the results in [174, 176, 194]. Using this approach allows us to make predictions far beyond that existing for RESI from an SFA model. Later, we also perform focal averaging to make our results more consistent with experiment, see Fig. (11.5). This demonstrates the interference fringes are surprisingly robust and survive integration of perpendicular momentum coordinates and focal averaging.

The features observed in Figs. (11.2) (a) to (d) mark a change from a regime in which excitation to s-states is prevalent, to a scenario in which a coherent superposition of p- and d-states dominates. This statement can be inferred from the different shapes resulting for different channels of excitation. These differences stem from the prefactor

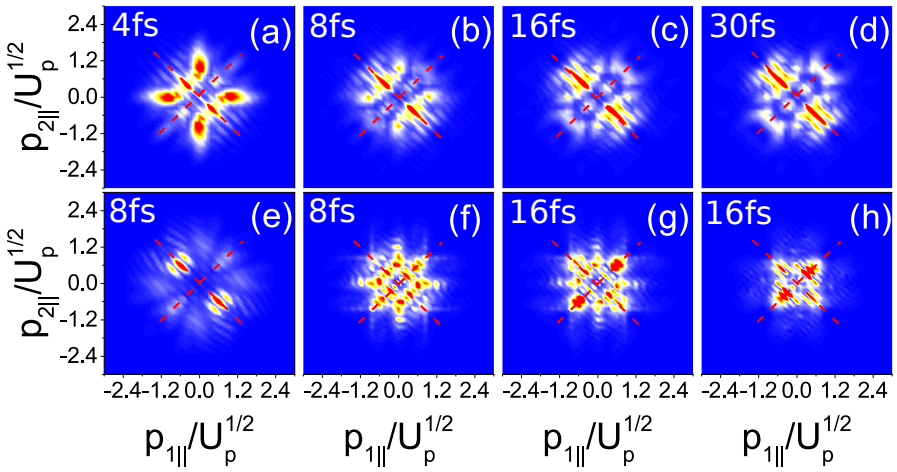

FIGURE 11.2: RESI distributions for argon ($E_{1g} = 0.58$ a.u., $E_{2g} = 1.02$ a.u.) computed using different coherent superpositions of the excitation channels in Table 10.1. The phases and weights employed in these superpositions are provided in Table 11.1, and have been chosen in such a way as to reproduce the experimental data from [173]. In the first row, panels (a)-(d), the peak intensity is 1×10^{14} W/cm^2 with $\omega = 0.057$ a.u. and a ponderomotive energy of $\mathrm{U_p} = 0.22$ a.u. The peak intensities in the second row are as follows: (e) $I = 0.8 \times 10^{14}$ W/cm^2 with $\mathrm{U_p} = 0.18$ a.u., (f) and (g) $I = 1.2 \times 10^{14}$ W/cm^2 with $\mathrm{U_p} = 0.26$ a.u. and (h) $I = 1.4 \times 10^{14}$ W/cm^2 with $\mathrm{U_p} = 0.30$ a.u. The dashed lines in the figure indicate the diagonals $p_{1\parallel} = \pm p_{2\parallel}$. The numbers on the top left corner of the panels indicate the pulse length in [173] we are aiming to reproduce.

Panel (Fig. (11.2))	1 $(3p)$	2 $(3d)$	3 $(4s)$	4 $(4p)$	5 $(4d)$	6 $(5s)$
(a)	$1e^{\frac{i\pi}{4}}$	$1e^{0}$	$4e^{\frac{i7\pi}{8}}$	$1e^{\frac{i7\pi}{8}}$	$0.5e^{\frac{i\pi}{2}}$	$4e^{\frac{i\pi}{2}}$
(b), (e), (f)	$1e^{\frac{i\pi}{4}}$	$1e^{0}$	$2e^{\frac{i7\pi}{8}}$	$1e^{\frac{i7\pi}{8}}$	$0.6e^{\frac{i\pi}{2}}$	$2e^{\frac{i\pi}{2}}$
(c), (g), (h)	$1e^{\frac{i\pi}{4}}$	$1e^{0}$	$1e^{\frac{i7\pi}{8}}$	$1e^{\frac{i7\pi}{8}}$	$0.7e^{\frac{i\pi}{2}}$	$1e^{\frac{i\pi}{2}}$
(d)	$1e^{\frac{i\pi}{4}}$	$1e^{0}$	$0.5e^{\frac{i7\pi}{8}}$	$2e^{\frac{i7\pi}{8}}$	$0.8e^{\frac{i\pi}{2}}$	$0.5e^{\frac{i\pi}{2}}$

TABLE 11.1: Coherent superpositions employed in Fig. (11.1). The letters in the first column indicate the panels in Fig. (11.1) for which a specific superposition have been employed. From the second to seventh column, the numbers in the first row indicate the excitation channel in Table 10.1, and the excited state of the second electron is given in brackets. The numbers $N_c e^{i\phi_c}$ give the weight and the relative phase for each channel.

$V_{\mathbf{p}_2 e}$ related to the ionisation of the second electron, which lead to the shapes seen in Figs. (10.8) and (10.9), i.e. cross-shaped s-states and more homogeneous x-shaped p- and d-states.

11.1 The Effect of Using a Pulse

In order to model the effects of a pulse we have changed the normalisation coefficients in a superposition of channels such that we go from s-states being dominant to d- and p-states as we go from short pulses to long. This leads to the change from cross-shaped distributions to more 'ring'-shaped distributions. We will now justify the choice of normalisations by considering how a laser pulse and its vector potential can be constructed from a sum of sine waves. We use this analysis to estimate the dominant channels by examining the intensity and frequency widths of a pulse. This dominance supports the normalisation coefficients given in the previous section. If the CEP is averaged over, the main difference between a short pulse and a monochromatic laser field is that the pulse will have a spread of intensities and frequencies, which will make a broader momentum region accessible. In contrast, if the CEP is resolved, effects related to the pulse shape become important for few-cycle pulses. This has been investigated by us in previous work, for electron-impact ionisation [136] and for RESI [183, 190]. For pulses longer than ten cycles, we have verified that these effects also become irrelevant even in the CEP-resolved case [52].

The intensity distribution is determined by the weighting of each monochromatic wave in a sum, and the frequency width is inversely proportional to the pulse length. Using the Fourier sine and the Fourier cosine transforms, the vector potential $A(t)$ of any pulse can be reconstructed out of monochromatic fields weighted by its Fourier transform $A(\omega)$. Hence we can think of a pulse as a sum of monochromatic fields weighted by the real and imaginary part of $A(\omega)$. Explicitly,

$$\begin{aligned} A(t) &= \int_0^\infty \mathrm{d}\omega \left(\mathrm{Re}(A(\omega))\cos(\omega(t) + \mathrm{Im}(A(\omega))\sin(\omega t)\right) \\ &\approx \sum_\omega \mathrm{Re}(A(\omega))\mathrm{d}\omega\cos(\omega t) + \mathrm{Im}(A(\omega))\mathrm{d}\omega\sin(\omega t). \end{aligned} \tag{11.2}$$

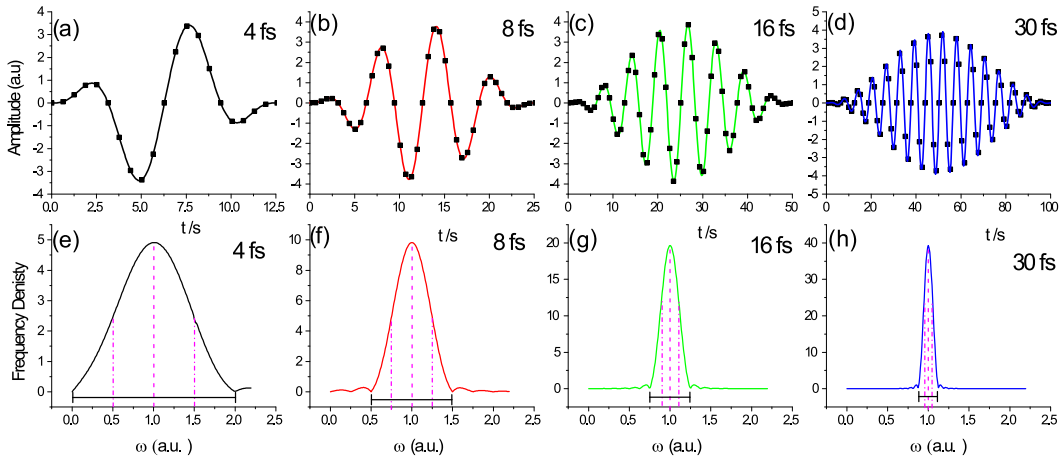

FIGURE 11.3: Temporal vector potential profile and corresponding Fourier transform (upper and lower panels, respectively) for laser pulses of increasing duration τ and central angular frequency $\omega_0 = 0.057$ a.u. The lower panels have been normalised so that the pulse area is kept constant. The panels from left to right correspond to $\tau = 4fs$, $\tau = 8fs$, $\tau = 16fs$ and $\tau = 30fs$ (black, red, green and blue curves) which corresponds to approximately 2, 4, 8 and 16 cycles. The black squares in the upper panels of the figure verify that the expansion given by Eq. (11.5) is correct. The value of the central frequency ω_0 is marked with a dashed purple line and $\omega_\pm$ are marked with dashed-dotted lines on the bottom rows for each pulse length. The frequency width ω_W is shown by a black horizontal line for each Fourier transformed pulse on the lower panels.

In the sum, $d\omega = \omega_i - \omega_{i-1}$ is the difference between the current and previous value of ω. We include the Fourier cosine transform for generality. However, it can be left out as this will only affect the negative t region, which we disregard. This leads to

$$A(t) \approx \sum_{\omega} \mathrm{Im}(A(\omega))\mathrm{d}\omega \sin(\omega t) \tag{11.3}$$

In practice, we found that three monochromatic sine waves dominate Eq. (11.3), so that, for a pulse of n cycles, it can be rewritten as

$$A(t) \approx \beta_0 \sin(\omega_0 t) + \beta_+ \sin(\omega_+ t) + \beta_- \sin(\omega_- t), \tag{11.4}$$

where ω_0 is the central pulse frequency, $\omega_\pm = \omega \pm \frac{1}{4}\omega_W$, and $\omega_W = \frac{4}{n}\omega$ is the frequency width of $A(\omega)$. In the upper panels of Fig. (11.3), we display the exact vector potential time for the range of pulses employed in [173], together with the 'approximate' reconstructions discussed here. For clarity, the frequency widths of such pulses are presented in the lower panels of the figure. For a sine square pulse, Eq. (11.4) is exact as it can be

shown that

$$A(t) = 2A_0 \sin^2\left(\frac{\omega_0 t}{2n}\right)\sin(\omega_0 t+\phi)$$
$$= A_0\left\{\sin(\omega_0 t+\phi)+\frac{1}{2}\left[\sin\left(\frac{n-1}{n}\omega_0 t+\pi+\phi\right)+\sin\left(\frac{n+1}{n}\omega_0 t+\pi+\phi\right)\right]\right\}. \tag{11.5}$$

This means that the vector potential can be exactly constructed out of three monochromatic sine waves of frequencies ω_0 and $\omega_\pm = \omega_0(n\pm 1)/n$, and amplitudes $\beta_0 = A_0$ and $\beta_\pm = \frac{1}{2}A_0$. Using this knowledge, together with the pulse widths in frequency and intensity, one may perform estimates of the parameter range assessed by pulses of different lengths. For these estimates, we will use Eq. (11.5), as we have verified little difference in the distributions obtained with Gaussian and sine squared pulses [52, 136]. For simplicity, we have set the CEP in Eq. (11.5) as $\phi = 0$.

We will now examine the relative dominance of s-, p- or d-channels for a range of frequencies and intensities, which contain the regions important for the pulses. To do this we will average over the momentum probability distributions for channels with specific values of the orbital quantum number l, and compare the values with the overall average to obtain an idea of relative dominance.

When calculating these averages, one must be careful as each channel state will lead to probability distributions occupying different regions of the $p_{1\|}p_{2\|}$ plane. Hence, it may happen that the probability density associated with specific channels are highly peaked in some regions and nearly zero elsewhere. This may lead to an overall bias towards contributions which are less localised in the parallel-momentum plane, such as those from the d-states. In order to avoid this problem, it is a good idea to compute averages restricted to certain momentum regions. Additionally, if the region averaged over is restricted, the channels which will be dominant for specific regions can be inferred.

We perform this averaging technique for the whole distribution, around the axes $p_{n\|} = 0$ $(n = 1, 2)$ and near the diagonals. The momentum ranges used for the axis were $-0.12 \leq p_{n\|} \leq 0.12$ a.u. and $1.2 \leq p_{m\|} \leq 2.4$ a.u., with $n \neq m$. The width of the diagonal region used was 0.24 a.u. around $p_{1\|} = \pm p_{2\|}$.

The regional average of a channel is calculated using

$$Q_R^c(I,\omega) = \iint_R \mathrm{d}p_{1\parallel}\mathrm{d}p_{2\parallel}\Omega(p_{1\parallel},p_{1\parallel},I,\omega), \tag{11.6}$$

where $\Omega(p_{1\parallel},p_{1\parallel},I,\omega)$ is the momentum probability distribution and R is the region being considered. From this we calculate the relative contributions

$$Q_R^l(I,\omega) = \frac{\sum_s Q_R^s(I,\omega)}{\sum_c Q_R^c(I,\omega)}, \tag{11.7}$$

where the sum over s includes channels of excitation that have intermediate states with the same value of l. The sum over c includes all channels.

These averages are plotted in Fig. (11.4), together with the regions assessed by the pulses, indicated by the rectangles, and the three frequencies and amplitudes in Eq. (11.5), indicated by dots. Panel (a) shows that overall s-states do not contribute much. In fact, a direct inspection of the upper panels in the figure leads to the conclusion that, in general, contributions from the d-states are expected to prevail, with a shift in dominance between p- and d-states for high frequencies and intensities. This dominance is expected due to the contributions from p- and d-states being more spread than those from the s-states.

However, in panel (d), where we have restricted the average to the axis region, we see that the latter have a significant effect for low frequencies and intensities. This makes sense, as s-states lead to cross-shaped distributions. These contributions are more localised in momentum space than those from p- and d-states. Hence, they will not appear to be significant in a total average while they might still have the largest peaks. In contrast, contributions from p-states are negligible in the axis region, and contributions from d-states increase in relevance for high frequencies and intensities (see panels (e) and (f), respectively).

Fig. (11.4) (d) also shows that the influence of the s-states will increase for shorter pulses, as they will make the low frequency, low intensity region accessible. This can easily be seen from the circles representing the frequency and ponderomotive energy of each of the monochromatic waves which form the pulse. The black circles represent the shortest $4fs$ pulse and will pick up the most s contributions. One should also note that,

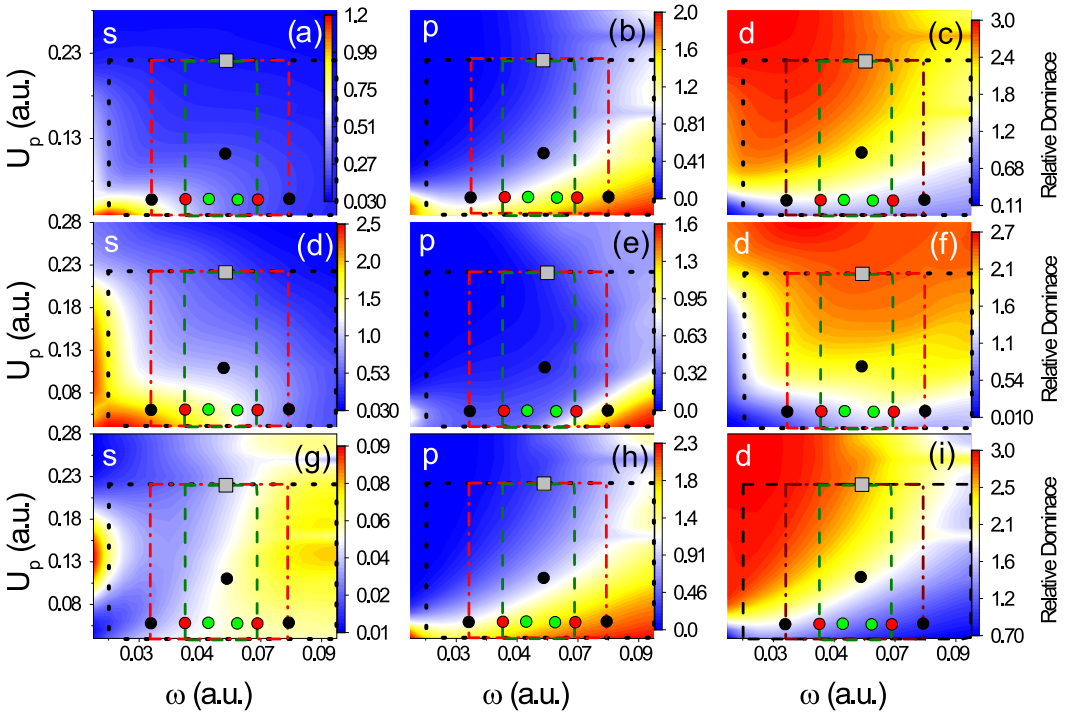

FIGURE 11.4: Relative contributions of channels with different orbital angular momenta l (s-, p- and d-states) computed according to Eq. (11.7), together with the regions in frequency and U_p spanned by different pulses. Panels (a) to (c) show the averages over the whole momentum distribution, panels (d) to (f) give the relative contribution of channels near the axis and (g) to (i) display the contribution of channels around the diagonal. The contributions of s-states are displayed in (a), (d) and (g), those of p-states in (b), (e) and (h) and those of d-states in (c), (f) and (i). The region spanned in frequency and intensity by the 4, 8 and 16 fs laser pulses (shown in Fig. (11.3)) are shown by the black (dotted), red (dotted-dashed) and green (dashed) rectangles, respectively. The frequency ω ranges from 0.02 to 0.1 a.u. and U_p from 0.03 to 0.28 a.u. The original monochromatic field frequency and intensity is represented by the grey square at $\omega = 0.057$ a.u. and $U_p = 0.22$ a.u. The frequencies and ponderomotive energies of the three monochromatic waves forming the pulse according to Eq. (11.5) are represented by the black, red and green circles for the 4 fs, 8 fs and 16 fs pulses respectively, where the central black dot, at $U_p = 0.11$ a.u., corresponds to β_0 and is the same for each pulse. The amplitudes $\beta_\pm$ are calculated for each pulse using Eq. (11.5). The ionisation potentials for the six channels are the same as those used in the main paper.

near the axis, there is swapping between s- and d-state dominance as one moves away from this region.

Near the diagonals, contributions from p- and d-states prevail. However, these contributions are also very much dependent on the field parameters. Comparing panel (h) and (i) in Fig. (11.4) shows that there is swapping between p- and d-state dominance as one moves away from the low-frequency region.

In all cases, be it overall, in the diagonal or in the axes region, as the pulse length increases the contributions associated to d states become dominant for the typical parameter range used in experiments (see Figs. (11.4) (c), (f) and (i), respectively, for the different types of average). The dominance of d-states explains the increasing homogeneity of the distributions in [173] with higher intensity and longer pulse duration. This happens as contributions from d-states are the only that lead to a non-vanishing probability density both near the axes and the diagonals. Furthermore, the on-axis transition from d- to s-states as the pulses shorten successfully explains the cross shapes present in [173], and can be used in support of the normalisation coefficients used to model the pulses

One should note, however, that the estimates provided above do not take the phases associated with the transition amplitudes into account. These phases are important, as they are present in the monochromatic fields that we combine to construct the pulses. They could lead to constructive or destructive interference in the averages performed, and thus alter the maps presented in Fig. (11.4). On the other hand, the fact that the additional phases remain the same across Table II for all the pulse lengths indicates that the amplitudes determine the overall trend. From the points representing the pulse in Fig. (11.4) we can say that, for the short pulse, s-states lead to contributions between three and four times stronger than for the monochromatic case, agreeing with the specific values for normalisation used, thus justifying them.

11.2 Focal Averaging

Focal averaging accounts for the range of intensities present in the laser field beam profile, by integrating over the range of intensities incident on the gas jet sample. For

the experiment we are modelling [173] a narrow gas jet is used with a radius of 0.5 mm while the lasers' Rayleigh length, which is defined as the distance along the propagation direction of a beam from the waist to the place where the area of the cross section is doubled, is $z_0 = 1.7$ mm. Further details on the setup used by [173] are given in [171]. The pulse used is both spatially and temporally short enough such that, in order to perform a realistic comparison with the experiment, we have to incorporate the intensity variation over the beam profile. Hence, we use focal averaging in our model following the derivations previously performed in [200].

We consider an ensemble of atoms in a field of varying intensity. For each atom, we can calculate an ionisation yield for which it emits two electrons via NSDI. Since this ensemble is macroscopic, there are far too many electrons for a coherent state to form. Moreover, electrons ionised from separate atoms are considered to be far enough apart such that they have non-overlapping wavefunctions. Hence, this average must be computed incoherently. Typically, in focal averaging the laser beam profile is taken as a Gaussian, as this simplifies the mathematical treatment. We will consider a field both with and without a temporal envelope. The intensity distribution of a beam of duration τ and wavelength λ as a function of the propagation coordinate z, the time t, and the distance ρ from the z axis reads

$$I(\rho, z, t) = I(\rho, z) \exp\left(\frac{(t - z/c)^2}{\tau^2}\right) \tag{11.8}$$

$$I(\rho, z) = I_0 \frac{d_0}{d(z)} \exp\left(-\frac{2\rho^2}{d(z)^2}\right), \tag{11.9}$$

with

$$d(z) = d_0 \left[1 + (z/z_0)^2\right]^{\frac{1}{2}},$$

where $d_0 = \sqrt{\lambda z_0/\pi}$ is the beam waist (the radius of the narrowest cross section of the beam), I_0 is the peak intensity, z_0 is the Rayleigh length, and c is the speed of light.

We would like to calculate the total electron yield $N(p_{1\parallel}, p_{2\parallel})$ integrated over the focal volume incident on the gas jet for the time of a laser pulse, for specific momenta. For each emitter, the probability of ionising both electrons via the RESI mechanism is

given by $\Omega(p_{1\|}, p_{2\|}, I)$, where I is the driving-field intensity (see Eq. (11.1)). Hence, $\Omega(p_{1\|}, p_{2\|}, I)$ will give the rate of emission of electrons with momenta $p_{1\|}, p_{2\|}$ if multiplied by the relevant number density of atoms and divided by the pulse duration. Thus $\Omega(p_{1\|}, p_{2\|}, I)$ is proportional to $dN(p_{1\|}, p_{2\|})/(d^3\mathbf{r}dt)$, and

$$\frac{dN(p_{1\|}, p_{2\|})}{dt} \propto \int \mathrm{d}^3\mathbf{r}\Omega(p_{1\|}, p_{2\|}, I(\rho, z)). \tag{11.10}$$

The above volume integral needs to be rewritten in terms of the intensity I using Eq. (11.9) before we can proceed, so that $rdr = -d(z)^2 dI/(4I)$. The remaining z integral needs to be calculated considering I constant. Hence, the limits of integration change to the maximum and minimum z coordinates on a surface of constant intensity. This gives

$$\frac{dN(p_{1\|}, p_{2\|})}{dt} \propto 2\pi \int_0^{I_0} \frac{\mathrm{d}I}{4I}\Omega(p_{1\|}, p_{2\|}, I) \int_{-z_0\sqrt{\frac{I_0}{I}-1}}^{z_0\sqrt{\frac{I_0}{I}-1}} d(z)^2 \mathrm{d}z \tag{11.11}$$

$$= \frac{\pi d_0^2 z_0}{3} \int_0^{I_0} \frac{\mathrm{d}I}{I^{\frac{5}{2}}}\sqrt{I_0 - I}(2I + I_0)\Omega(p_{1\|}, p_{2\|}, I), \tag{11.12}$$

which can be used for a monochromatic field. For a pulse we must integrate over time as well, so that the above equation is generalized to

$$N(p_{1\|}, p_{2\|}) \propto 2\pi\tau z_0 d_0^2 \int_0^{I_0} \frac{\mathrm{d}I}{I}\Omega(p_{1\|}, p_{2\|}, I) \int_0^{\eta} \mathrm{d}\eta(1+\eta^2) \ln\left(\frac{I_0}{I(1+\eta^2)}\right)^{1/2}, \tag{11.13}$$

where $\eta = \sqrt{I_0/I - 1}$. For the setup we are considering the gas jet is narrow enough such that the laser intensity varies less than 5% from the peak intensity along the width of the jet. Hence, we do not need to consider the z dependence in η. This leads to

$$N(p_{1\|}, p_{2\|}) \propto \pi\tau z_0 d_0^2 \int_0^{I_0} \frac{\mathrm{d}I}{I}\Omega(p_{1\|}, p_{2\|}, I) \left(\ln\frac{I_0}{I}\right)^{1/2}, \tag{11.14}$$

which is the final focal averaged momentum probability distribution used in this work. In order to improve our description of the experimental results, which uses short pulses,

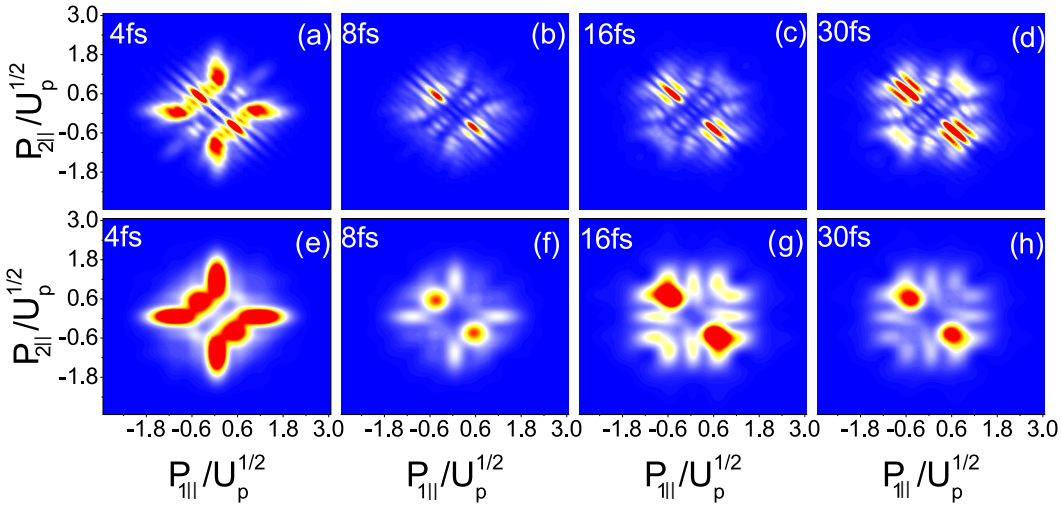

FIGURE 11.5: The parameters and labelling are the same as Fig. (11.2) except the data has been focally averaged. The first and second rows are coherent and incoherent sums of events respectively. To do focal averaging we integrate the expression from 0 to the peak intensity as in Eq. (11.14).

we consider Eq. (11.14) even though we are using a monochromatic field for the computation of $\Omega(p_{1\|}, p_{2\|}, I)$. Nonetheless, apart from a proportionality factor, the number of cycles does not affect the above-stated equation.

The important result to be taken from this section is that the interference fringes survive the integration in Eq. (11.14). This happens because the probability density $\Omega(p_{1\|}, p_{2\|}, I)$ increases exponentially with the driving-field intensity, while the other terms in Eq. (11.14) change much more slowly. Hence, despite the weighting, high-intensity terms dominate. This leads to RESI distributions similar to those obtained for the peak intensity I_0. In Fig. (11.5) we show these results. Remarkably, all interference effects also survive focal averaging. This is shown in Figs. (11.5) (a) - (d), where both types of interference are visible. For incoherent event superpositions, the hyperbolic inter-channel fringes become quite evident (Figs. (11.5) (e) - (h)).

A better analysis of these results can be made if they are compared directly with the experimental results. In Fig. (11.6) we present selected experimental results from [173] for pulses of $\tau = 16fs$ and $\tau = 30fs$ duration, together with a blow up of panels (c) and (d) of Fig. (11.5) (upper and lower rows, respectively).

First, we are able to identify traces of the diagonal hyperbolic fringes due to event and/or channel interference. This is marked on Fig. (11.6) by the black polygon, and

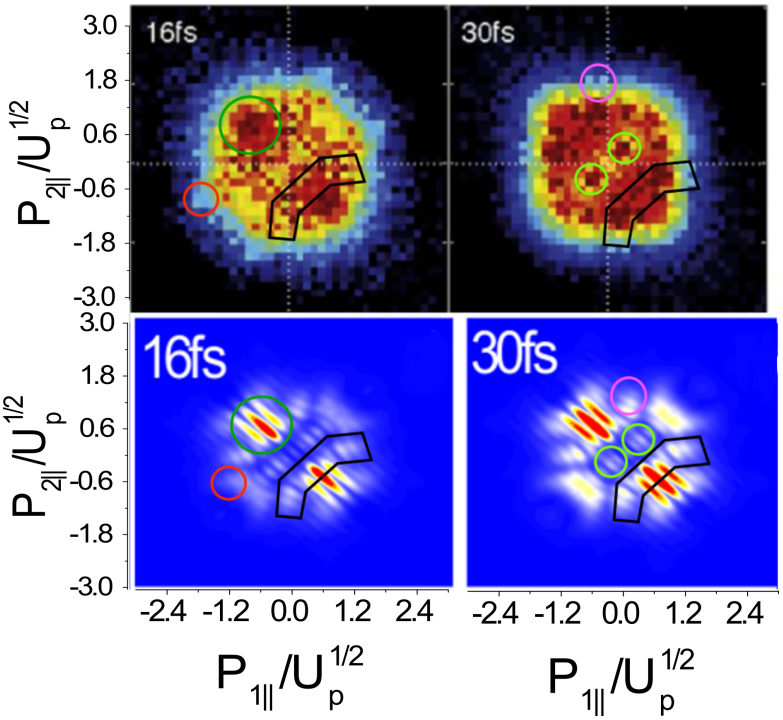

FIGURE 11.6: Comparison of the experimental data from [173] (Fig. (11.1)) with theoretical focal-averaged distributions selected from Fig. (11.5) (top and bottom rows, respectively). In the top row, we show the 16 fs and 30 fs cases from [173] with $\omega = 0.057$ a.u. and $I = 1.0 \times 10^{14}$ W/cm^2 corresponding to $\mathrm{U_p} = 0.22$ a.u. The bottom row gives the focal averaged results taken from Fig. (11.5), with the same field parameters as above. In order to facilitate a comparison, the same panel notation has been kept in the bottom row. Specific features associated with quantum interference are marked by polygons in both upper and lower panels. Both channels and events have been summed coherently.

is good validation of our method as it should be this interference that leads to the shapes that are observed. Second, the dark green circle on the left panels highlights the anti-diagonal blob that we obtain due to constructive interference. This blob is also visible in the experimental data. Third, the red circle on the left panels identifies the tails on the diagonal corners that can be observed both in experiment and theory. This gives rise to flat as opposed to rounded corners in probability densities in the first and third quadrants. Fourth, the pink circles on the right panels also show tails on the anti-diagonal corners that have a similar effect to those on the diagonal. Finally, the light green circles highlight maxima in the diagonal depletion that in our model are due to event interference. These maxima are quite clear both in experiment and theory.

11.3 Discussion

In summary, we have shown that the two types of quantum interference, which survive both transverse-momentum integration and focal averaging, play an important role in reproducing results similar to those in experiments. Inter-channel interference can be used to maximise anti-correlation, correlation, and alter the shape of the electron-momentum distributions, and thus create all distributions found experimentally [173, 174, 176, 194]. In a similar vein, recent experiments have shown that by using a two-colour field and changing the relative phase of the colours the momentum distributions for NSDI below the electron impact threshold can be manipulated from being anti-correlated to correlated [201]. The phases of each channel and event depend strongly on the field as they derive from the action. Hence, it would not be unreasonable to assume this effect came from quantum interference.

The present work, however, invites two main questions: (i) What justifies the use of additional phases and amplitudes? (ii) Why do very short pulses favour excitation to s-states, while longer pulses favour p or d channels? The phases and amplitudes in Table 11.1 make up for several features which are absent in the present model. First, the residual Coulomb potential modifies the action, leading to phase corrections, and also the amplitudes associated to ionisation from specific bound states. In Part I and in

other works, the issue of a single channel in above-threshold ionisation, using Coulomb-corrected forms of the SFA, has been tackled, finding, changes in interference patterns and the topology of the electron orbits in the continuum [79, 80, 94, 99, 102–104]. Second, bound-state depletion and Stark shifts in the bound-state energies enhance ionisation from the weakly bound states and modify the times for which the electrons reach the continuum. Third, a short pulse has a certain width in frequency and intensity. Fourth, there is some experimental uncertainty in the determination of the peak-field intensity. All this will change the phase differences between channels and events, and the dominant channels. The prevalence of s-state contributions for short pulses is related to how the relative contribution of each channel varies with the field frequency and intensity. The s-state contributions dominate for low intensities and frequencies. For the parameters in this work, this regime can only be reached if there is a large frequency spread and a variation in the peak intensity, i.e., for short pulses.

Given the important role quantum interference has in RESI, one should consider the implications this has for classical models. We have shown that interference hugely increases the SFA's descriptive power and can reproduce many of the features seen in experiment. These features are obtained without the need to resort to multiple collisions, and are related to the geometry of specific intermediate bound-state superpositions [1] In [173, 202], this has been related to the prevalence of anti-correlation for longer pulses. Nonetheless, multiple recollisions may not be the only classical mechanism causing anti-correlation, as classical-trajectory computations obtained anti-correlated RESI distributions for much shorter times [179, 203].

In [204] it was reported that due to experimental uncertainties such as laser field intensity, this leaves room to adjust theoretical models to match to experimental results. This is how so many models, classical, semi-classical and fully quantum mechanical can exist with conflicting interpretations. The proposed solution is a full characterisation of NSDI across many intensities and in [204] this is provided for a single cycle pulse. Note the results reported in this chapter give good qualitative agreement across various intensities but could not be considered complete due to the semi-empirical reliance

[1] Within classical models, it has been argued that anti-correlated distributions result from multiple recollisions, which provide the electrons with enough energy so that they can overcome the Stark saddle and reach the continuum.

on additional normalisations and phases. Nonetheless, they provide a powerful way to analyse experiments. In response to [204], a theoretical model using classical trajectories and neglecting interference effects was computed for single cycle pulse and compared to experiment across a complete range of intensities [205]. This model obtained good agreement for higher intensities, where the EI mechanism dominates and worsens for lower intensities as RESI becomes more dominant. Even when the RESI contributions are isolated, the results still fail to reproduce the characteristic cross-shaped distribution. It would seem full agreement with experimental data such as those in [204] would require a complete model that accounts for various features including interference, the Coulomb potential for continuum states, bound-state broadening and accounts for all relevant ionisation pathways such as RESI, EI and others not discussed here. Aside from *ab-initio* solutions of the time-dependent Schrödinger equation, which is numerically intensive and can be nearly as difficult to interpret as experiments, such a model does not exist. However, the work presented in this thesis at least outlines some important ingredients and a potential framework in which such a model could be formed. With the inclusion of Coulomb-distorted trajectories into NSDI, similar to those computed for ATI in Part I, this model would account for nearly every feature highlighted as important in NSDI, except for the laser distortion to the bound states. Hence, good agreement across complete sets of measurements for path based/ quantum trajectory/ semi-classical models such as those employed here may be achievable quite soon.

This work provides a large scope for RESI to be used as an attosecond-imaging tool in order to probe and reconstruct the intermediate state of the second electron, particularly given the range of shapes present in the distributions, which may be used to extract a large amount of information related to the bound states and potential of the parent ion. Furthermore, given that the correlation between the two electrons can be changed and they can be made very strongly correlated, this system could lend itself to creating a controllable amount of entanglement between the two electrons in the momentum coordinates.

Chapter 12

Summary

The main topic of this thesis is quantum interference phenomena in the context of the interaction of atoms with intense lasers fields. The two processes, which are focussed on, above-threshold ionisation (ATI) and non-sequential double ionisation (NSDI), have been dealt with separately in Parts I and II, but the topics are unified by the interference studied in both, analysed using a similar framework.

In Part I, ATI is investigated using the newly developed Coulomb quantum-orbit strong-field approximation (CQSFA). This exploits Coulomb distorted quantum trajectories in order to understand how many interference patterns form. We investigated two previously neglected quantum trajectories [80, 100], known as orbit 3 and 4 and find both contribute to the final momentum distribution and improve agreement with *ab-initio* solutions of the TDSE. Together, these four quantum trajectories provide an in-depth explanation for three main intracycle interference patterns; the fan-like, spider-like and spiral-like structures. The first two have been previously seen in the literature [22, 65, 80, 102, 105, 106] but the latter had not previously been identified. In addition to these patterns there are a range of other combinations and types of interference. We find that each pairwise combination of orbits will have two or three types of interference patterns, which arise from restrictions or transformations on the times of ionisations. These interference types not only allow a better comparison with experimental (e.g. [22]) and theoretical (e.g. [118]) results, where such restrictions have been applied, but also reveals previously hidden structures containing information specific to the interaction of the electron with the core, encoded in the holographic interference patterns. We also derived holographic interference conditions and a semi-analytic model in order to better interpret the interference patterns, which should ultimately aid the extraction

of information in holographic imaging for atoms and molecules using ATI.

Given the importance of the interaction with the residual ion we also investigated the role of recollision in the CQSFA and formulated a new classification for the type of collision for a particular CQSFA orbit. This is required because the previous notion of direct and recolliding orbit is based on a Born expansion with regards to interaction with the core, where the trajectory either has no further interaction with the core (direct) or undergoes a hard collision (recolliding), in which the trajectory will pass through the Coulomb singularity. In the CQSFA a Born expansion is not used, so the trajectories can have any degree of interaction with the core between those two extremes. Thus, a classification is formulated based on the distance of closest approach and used to show the CQSFA trajectories tend to the direct or rescattered SFA orbits for ATI with increasing energy, depending on the final angle the electron is ejected relative to the tunnelling path taken. We also found that the four trajectory classification introduced in [99] does not account for all orbits types and in fact orbit 3 and 4 have two additional subtypes of trajectories.

The CQSFA can be improved by including complex valued trajectories in the continuum, in [92, 94] it was shown including such trajectories could account for the effect of deceleration of electron wavepacket by the Coulomb potential. This would also mean that any integration contours chosen in the CQSFA would give equivalent results, which is desirable as the contour is not an observable so should only be a mathematical choice as discussed in [101]. However, including complex trajectories leads to issues from branch cuts, which emerge in the action and equations of motions due to taking the complex square root present in the Coulomb potential. Some solutions to this problem have been presented for Coulomb-free SFA-like trajectories, where the Coulomb potential is not included in the dynamics [61] and a partial solution for Coulomb-distorted trajectories, where the the Coulomb potential is included in the dynamics [98]. Beyond technical improvements to the CQSFA, much can be gained by extending the CQSFA to molecules. This is where the real power of ultrafast electron holography will lie. Small, e.g. diatomic, molecules should not present a difficult challenge as initial wavefunctions can easily be obtained and added into to the CQSFA description via the prefactor, which should account for many broad features in the photoelectron momentum distributions.

Beyond this there may be some challenges developing the dynamics of the orbits in the presence of an ionised molecule. This will be most relevant for orbits 3 and 4, which will revisit the 'core' close enough for these dynamics to be important.

In Part II, interference patterns present in the momentum distribution from NSDI were investigated for the recollision with subsequent ionisation (RESI) mechanism. This work is the second after [186], to report interference effects in NSDI. Thus, a thorough analysis of all possible types was performed, which includes interference for events due to symmetries in the system and over different channels of excitation for the second electron. Both types of interference break the fourfold symmetry previously seen in the SFA [167, 168, 177] and survive integration over the perpendicular momentum coordinates and focal averaging. Additionally, we derived analytic conditions for the interference fringes and showed that the event interference gives rise to hyperbolic fringes. The interplay of event and channel interference was found to produce a wide range of distributions, which in principle could explain all possible results found in experiments [174, 176, 194] through particular interferences. It was found that the quantum interference plays a significant role in forming the distributions for the RESI mechanism, which calls into question the applicability of models without interference to this problem.

A careful analysis of the effect of different pulses length was performed by changing the superposition of states the second electron is excited to. This enables a comparison and interpretation of experimental data [173], which suggests that for short pulses (in this parameter regime) the electron is preferentially excited to s-states. The additional normalisations used in the superposition of states for each pulse length were justified by decomposing the pulses into monochromatic fields and inferring which states give dominant contributions to the final transition amplitude. This opens up the possibility of using experimental data to work backwards and infer the excited state of the second electron just before ionisation.

As stated in the previous chapter, a complete model of NSDI in term of interfering quantum trajectories, with all possible pathways, the effect of the Coulomb potentials of all particles and bound-state broadening is missing. But this is what brings the two parts of the thesis together. Applying the methods of of Part I to Part II could provide something very close to this. This would not only allow for a fast and accurate model

of NSDI in the context of quantum trajectories but would also allow the holography ideas from Part I to be combined with electron correlation from Part II. The second electron in the RESI mechanism formally undergoes ATI in the final ionisation step. This would presumably mean that all the trajectories explored in the CQSFA treatment of ATI would occur for the second electron in NSDI. Given that these trajectories can give rise to holographic interference patterns this opens up the possibility of using NSDI for photoelectron holography. It has previously been argued that this interference will be lost following integration over the previously unmeasured perpendicular momentum coordinates, but now experimental techniques have progressed to the point where all 3D momentum information can be measured for both electrons [24, 206] in NSDI, so holographic interference features should be accessible. In NSDI there is a lot of electron correlation and we have shown that this correlation is intimately related to the interference that occurs. Hence, it may be possible to exploit the electron correlation to add extra control to the holographic interference of the second electron, potentially restricting the number of pathways to make it easier to exploit this process for imaging. This could be manifested by simply choosing appropriate parameters ranges, where the right correlation and holographic interference occurs. Perhaps the laser field could be tailored in order to enhance the imaging ability. Two colour laser fields have already been used to manipulate and control NSDI distributions [207, 208]. Alternatively, different experimental setups and careful measurement techniques could be performed to exploit the correlation and possibly even entanglement between the electrons to vastly improve the imaging capabilities of this process. Beyond imaging, the possible applications will only increase with our understanding and as experiments allow for more complex and delicate approaches.

Bibliography

[1]A. Einstein, "Über einen die Erzeugung und Verwandlung des Lichtes betreffenden heuristischen Gesichtspunkt", Ann. Phys. **322**, 132 (1905).

[2]A. B. Arons and M. B. Peppard, "Einstein's Proposal of the Photon Concept—a Translation of the Annalen der Physik Paper of 1905", Am. J. Phys. **33**, 367 (1965).

[3]M. Fox, *Quantum Optics: An Introduction* (Oxford University Press, New York, 2006).

[4]C. J. Joachain, N. J. Kylstra, and R. M. Potvliege, *Atoms in Intense Laser Fields* (Cambridge University Press, New York, 2012).

[5]W. Kaiser and C. Garrett, "Two-Photon Excitation in CaF_2:Eu^{2+}", Phys. Rev. Lett. **7**, 229 (1961).

[6]M. Göppert-Mayer, "Über Elementarakte mit zwei Quantensprüngen", Ann. Phys. **401**, 273 (1931).

[7]M. Göppert-Mayer, "Elementary processes with two quantum transitions", Ann. Phys. **18**, 466 (2009).

[8]T. H. Maiman, "Stimulated optical radiation in Ruby", Nature **187**, 493 (1960).

[9]E. K. Damon and R. G. Tomlinson, "Observation of Ionization of Gases by a Ruby Laser", Appl. Opt. **2**, 546 (1963).

[10]R. G. Meyerand and A. F. Haught, "Gas breakdown at optical frequencies", Phys. Rev. Lett. **11**, 401 (1963).

[11]H. R. Reiss, "Absorption of light by light", J. Math. Phys. **3**, 59 (1962).

[12]H. R. Reiss, "A convergent perturbation expansion in first-quantized electrodynamics", J. Math. Phys. **3**, 387 (1962).

[13]A. I. Nikishov and V. I. Ritus, "Quantum processes in the field of a plane electromagnetic wave and in a constant field. I", Sov. Phys. JETP **19**, 529 (1964).

[14]L. V. Keldysh, "Ionization in the field of a strong electromagnetic wave", Sov. Phys. JETP **20**, 1307 (1965).

[15]G. S. Voronov and N. B. Delone, "Many-photon ionization of the Xenon atom by ruby laser radiation", Sov. Phys. JETP **23**, 54 (1965).

[16]G. S. Voronov, G. A. Delone, N. B. Delone, and O. V. Kudrevatova, "Multiphoton Ionization of the Hydrogen Molecule in the Strong Electric Field of Ruby Laser Emission", Sov. Phys. JETP **1**, 377 (1965).

[17]F. H. Faisal, "Multiple absorption of laser photons by atoms", J. Phys. B At. Mol. Phys. **6**, L89 (1973).

[18]H. R. Reiss, "Effect of an intense electromagnetic field on a weakly bound system", Phys. Rev. A **22**, 1786 (1980).

[19]S. V. Popruzhenko, "Keldysh theory of strong field ionization: history, applications, difficulties and perspectives", J. Phys. B At. Mol. Opt. Phys. **47**, 204001 (2014).

[20]A. D. Bandrauk, F. Fillion-Gourdeau, and E. Lorin, "Atoms and molecules in intense laser fields: Gauge invariance of theory and models", J. Phys. B At. Mol. Opt. Phys. **46**, 153001 (2013).

[21]H. R. Reiss, "Theoretical methods in quantum optics: S-matrix and Keldysh techniques for strong-field processes", Prog. Quantum Electron. **16**, 1–71 (1992).

[22]C. M. Maharjan, A. S. Alnaser, I Litvinyuk, P Ranitovic, and C. L. Cocke, "Wavelength dependence of momentum-space images of low-energy electrons generated by short intense laser pulses at high intensities", J. Phys. B At. Mol. Opt. Phys. **39**, 1955 (2006).

[23]Y. Huismans, A. Gijsbertsen, A. S. Smolkowska, J. H. Jungmann, A. Rouzée, P. S.W. M. Logman, F. Lépine, C. Cauchy, S. Zamith, T. Marchenko, J. M. Bakker, G. Berden, B. Redlich, A. F. G. Van Der Meer, M. Y. Ivanov, T. M. Yan, D. Bauer, O. Smirnova, and M. J. J. Vrakking, "Scaling laws for photoelectron holography in the midinfrared wavelength regime", Phys. Rev. Lett. **109**, 013002 (2012).

[24]B. Wolter, M. G. Pullen, M. Baudisch, M. Sclafani, M. Hemmer, A. Senftleben, C. D. Schröter, J. Ullrich, R. Moshammer, and J. Biegert, "Strong-field physics with Mid-IR fields", Phys. Rev. X **5**, 021034 (2015).

[25]H. R. Reiss, "The tunnelling model of laser-induced ionization and its failure at low frequencies", J. Phys. B At. Mol. Opt. Phys. **47**, 204006 (2014).

[26]A. Ludwig, J. Maurer, B. W. Mayer, C. R. Phillips, L. Gallmann, and U. Keller, "Breakdown of the dipole approximation in strong-field ionization", Phys. Rev. Lett. **113**, 243001 (2014).

[27]T. Keil and D Bauer, "Coulomb-corrected strong- field quantum trajectories beyond dipole approximation", J. Phys. B At. Mol. Opt. Phys. **50**, 194002 (2017).

[28]P. L. He, D. Lao, and F. He, "Strong Field Theories beyond Dipole Approximations in Nonrelativistic Regimes", Phys. Rev. Lett. **118**, 163203 (2017).

[29]A. Emmanouilidou and T. Meltzer, "Recollision as a probe of magnetic-field effects in nonsequential double ionization", Phys. Rev. A **95**, 033405 (2017).

[30]A. Emmanouilidou, T. Meltzer, and P. B. Corkum, "Non-dipole recollision-gated double ionization and observable effects", J. Phys. B At. Mol. Opt. Phys. **50**, 225602 (2017).

[31]H. Kleinert, *Path Integrals in Quantum Mechanics, Statistic, Polymer Physics and Financial Markets*, 5th ed. (World Scientific, 2009).

[32]N. B. Delone and V. P. Krainov, *Multiphoton Processes in Atoms: Second Edition* (2000).

[33]P. Agostini and L. F. DiMauro, *Atomic and Molecular Ionization Dynamics in Strong Laser Fields: From Optical to X-rays*, Vol. 61 (Elsevier Inc., 2012), p. 117.

[34]P. Agostini, F. Fabre, G. Mainfray, G. Petite, and N. K. Rahman, "Free-free transitions following six-photon ionization of xenon atoms", Phys. Rev. Lett. **42**, 1127 (1979).

[35]P. Kruit, J. Kimman, H. G. Muller, and M. J. Van Der Wiel, "Electron spectra from multiphoton ionization of xenon at 1064, 532, and 355 nm", Phys. Rev. A **28**, 248 (1983).

[36]S. L. Chin, F. Yergeau, and P. Lavigne, "Tunnel ionisation of Xe in an ultra-intense CO2 laser field (1014 W cm-2) with multiple charge creation", J. Phys. B At. Mol. Phys. **18**, L213 (1985).

[37]A. M. Perelomov, V. S. Popov, and M. Terent'ev, "Ionization of atoms in an alternating electrical field", Sov. Phys. JETP **23**, 924 (1966).

[38]V. S. Popov, "Tunnel and multiphoton ionization of atoms and ions in a strong laser field (Keldysh theory)", Physics-Uspekhi **47**, 855 (2004).

[39]M. Ferray, A. L'Huillier, X. F. Li, L. A. Lomprk, G. Mainfray, and C. Manus, "Multiple-harmonic conversion of 1064 nm radiationin rare gases", J. Phys. B At. Mol. Opt. Phys. **21**, L31 (1988).

[40]A. McPherson, G. Gibson, H. Jara, U. Johann, T. S. Luk, I. A. McIntyre, K. Boyer, and C. K. Rhodes, "Studies of multiphoton production of vacuum-ultraviolet radiation in the rare gases", J. Opt. Soc. Am. B **4**, 595 (1987).

[41]G. G. Paulus, W. Nicklich, H. Xu, P. Lambropoulos, and H. Walther, "Plateau in above threshold ionization spectra", Phys. Rev. Lett. **72**, 2851 (1994).

[42]M. Lewenstein, K. C. Kulander, K. J. Schafer, and P. H. Bucksbaum, "Rings in above-threshold ionization: A quasiclassical analysis", Phys. Rev. A **51**, 1495 (1995).

[43]W. Becker, F. Grasbon, R. Kopold, D. B. Milošević, G. G. Paulus, and H. Walther, "Above-threshold ionization: From classical features to quantum effects", Adv. At. Mol. Opt. Phys. **48**, 35 (2002).

[44]P. B. Corkum, "Plasma perspective on strong field multiphoton ionization", Phys. Rev. Lett. **71**, 1994 (1993).

[45]M. Lewenstein, P. Balcou, M. Y. Ivanov, A. L'Huillier, and P. B. Corkum, "Theory of high-harmonic generation by low-frequency laser fields", Phys. Rev. A **49**, 2117 (1994).

[46]W. Becker, A. Lohr, and M. Kleber, "Light at the End of the tunnel: two- and three-step models in intense-field laser-atom physics.", Quantum Semiclass. Opt. **7**, 423 (1995).

[47]W. Becker, "Higher-harmonic production in a model atom with short range potential", Phys. Rev. A **41**, 4112 (1990).

[48]G. G. Paulus, F. Zacher, H. Walther, A. Lohr, W. Becker, and M. Kleber, "Above-threshold ionization by an elliptically polarized field: Quantum tunneling interferences and classical dodging", Phys. Rev. Lett. **80**, 484 (1998).

[49]P. Antoine, A. L'Huillier, and M. Lewenstein, "Attosecond pulse trains using high–order harmonics", Phys. Rev. Lett. **77**, 1234 (1996).

[50]P. Salières, P. Antoine, A. de Bohan, and M. Lewenstein, "Temporal and spectral tailoring of high-order harmonics", Phys. Rev. Lett. **81**, 5544 (1998).

[51]S. V. Popruzhenko, P. A. Korneev, S. P. Goreslavski, and W. Becker, "Laser-Induced Recollision Phenomena: Interference Resonances at Channel Closings", Phys. Rev. Lett. **89**, 023001 (2002).

[52]X. Liu and C. Figueira de Morisson Faria, "Nonsequential Double Ionization with Few-Cycle Laser Pulses", Phys. Rev. Lett. **92**, 133006 (2004).

[53]J. Ullrich, R. Moshammer, A. N. Perumal, and R. Moshammer, "Reports on Progress in Physics Related content Recoil-ion and electron momentum spectroscopy : Recoil-ion and electron momentum spectroscopy :" Rep. Prog. Phys **66**, 1463 (2003).

[54]W. Quan, Z. Lin, M. Wu, H. Kang, H. Liu, X. Liu, J. Chen, J. Liu, X. T. He, S. G. Chen, H. Xiong, L. Guo, H. Xu, Y. Fu, Y. Cheng, and Z. Z. Xu, "Classical aspects in above-threshold ionization with a midinfrared strong laser field", Phys. Rev. Lett. **103**, 093001 (2009).

[55]C. I. Blaga, F. Catoire, P. Colosimo, G. G. Paulus, H. G. Muller, P. Agostini, and L. F. DiMauro, "Strong-field photoionization revisited", Nat. Phys. **5**, 335 (2009).

[56]C. Liu and K. Z. Hatsagortsyan, "Origin of unexpected low energy structure in photoelectron spectra induced by midinfrared strong laser fields", Phys. Rev. Lett. **105**, 113003 (2010).

[57]W. Becker, S. P. Goreslavski, D. B. Milošević, and G. G. Paulus, "Low-energy electron rescattering in laser-induced ionization", J. Phys. B At. Mol. Opt. Phys. **47**, 204022 (2014).

[58]A. Kästner, U. Saalmann, and J. M. Rost, "Energy bunching in soft recollisions revealed with long-wavelength few-cycle pulses", J. Phys. B At. Mol. Opt. Phys. **45**, 074011 (2012).

[59]N. I. Shvetsov-Shilovski, S. P. Goreslavski, S. V. Popruzhenko, and W. Becker, "Capture into rydberg states and momentum distributions of ionized electrons", Laser Phys. **19**, 1550 (2009).

[60]C. Y. Wu, Y. D. Yang, Y. Q. Liu, Q. H. Gong, M. Wu, X. Liu, X. L. Hao, W. D. Li, X. T. He, and J. Chen, "Characteristic spectrum of very low-energy photoelectron from above-threshold ionization in the tunneling regime", Phys. Rev. Lett. **109**, 043001 (2012).

[61]E. Pisanty and M. Ivanov, "Slalom in complex time: Emergence of low-energy structures in tunnel ionization via complex-time contours", Phys. Rev. A **93**, 043408 (2016).

[62]J. Dura, N. Camus, A. Thai, A. Britz, M. Hemmer, M. Baudisch, A. Senftleben, C. D. Schröter, J. Ullrich, R. Moshammer, and J. Biegert, "Ionization with low-frequency fields in the tunneling regime", Sci. Rep. **3**, 2675 (2013).

[63]W. Quan, X. L. Hao, Y. J. Chen, S. G. Yu, S. P. Xu, Y. L. Wang, R. P. Sun, X. Y. Lai, C. Y. Wu, Q. H. Gong, X. T. He, X. J. Liu, and J. Chen, "Long-Range Coulomb Effect in Intense Laser-Driven Photoelectron Dynamics", Sci. Rep. **6**, 27108 (2016).

[64]W. Becker and D. B. Milošević, "Above-threshold ionization for very low electron energy", J. Phys. B At. Mol. Opt. Phys. **48**, 151001 (2015).

[65]A. Rudenko, K. Zrost, C. D. Schröter, V. L. B. de Jesus, B. Feuerstein, R. Moshammer, and J. Ullrich, "Resonant Structures in the Low-Energy Electron Continuum for Single Ionization of Atoms in the Tunneling Regime", J. Phys. B At. Mol. Opt. Phys. **37**, L407 (2004).

[66]Y. Huismans, A. Rouzée, A. Gijsbertsen, J. H. Jungmann, A. S. Smolkowska, P. S.W. M. Logman, F. Lépine, C. Cauchy, S. Zamith, T. Marchenko, J. M. Bakker, G. Berden, B. Redlich, A. F. G. Van Der Meer, H. G. Muller, W. Vermin, K. J. Schafer, M Spanner, M. Y. Ivanov, O. Smirnova, D. Bauer, S. V. Popruzhenko, and M. J. J. Vrakking, "Time-Resolved Holography", Science **331**, 61 (2010).

[67]F. Mauger, C. Chandre, and T. Uzer, "Recollisions and correlated double ionization with circularly polarized light", Phys. Rev. Lett. **105**, 083002 (2010).

[68]B. Wolter, C. Lemell, M. Baudisch, M. G. Pullen, X. M. Tong, M. Hemmer, A. Senftleben, C. D. Schröter, J. Ullrich, R. Moshammer, J. Biegert, and J. Burgdörfer, "Formation of very-low-energy states crossing the ionization threshold of argon atoms in strong mid-infrared fields", Phys. Rev. A **90**, 063424 (2014).

[69]M. G. Pullen, J. Dura, B. Wolter, M. Baudisch, M. Hemmer, N. Camus, A. Senftleben, C. D. Schroeter, R. Moshammer, J. Ullrich, and J. Biegert, "Kinematically complete measurements of strong field ionization with mid-IR pulses", J. Phys. B At. Mol. Opt. Phys. **47**, 204010 (2014).

[70]D. G. Arbó, K. L. Ishikawa, K. Schiessl, E. Persson, and J. Burgdörfer, "Diffraction at a time grating in above-threshold ionization: The influence of the Coulomb potential", Phys. Rev. A **82**, 043426 (2010).

[71]D. G. Arbó, K. L. Ishikawa, E. Persson, and J. Burgdorfer, "Doubly differential diffraction at a time grating in above-threshold ionization: Intracycle and intercycle interferences", Nucl. Instrum. Methods B **279**, 24 (2012).

[72]Z. Chen, T. Morishita, A.-T. Le, M. Wickenhauser, X. M. Tong, and C. D. Lin, "Analysis of two-dimensional photoelectron momentum spectra and the effect of the long-range Coulomb potential in single ionization of atoms by intense lasers", Phys. Rev. A **74**, 053405 (2006).

[73]D. G. Arbó, S. Yoshida, E. Persson, K. I. Dimitriou, and J. Burgdörfer, "Interference Oscillations in the Angular Distribution of Laser-Ionized Electrons near Ionization Threshold", Phys. Rev. Lett. **96**, 143003 (2006).

[74]D. G. Arbó, J. E. Miraglia, M. S. Gravielle, K. Schiessl, E. Persson, and J. Burgdörfer, "Coulomb-Volkov approximation for near-threshold ionization by short laser pulses", Phys. Rev. A **77**, 013401 (2008).

[75]P. A. Korneev, S. V. Popruzhenko, S. P. Goreslavski, W. Becker, G. G. Paulus, B. Fetic, and D. B. Milosevic, "Interference structure of above-threshold ionization versus above-threshold detachment", New J. Phys. **14**, 055019 (2012).

[76]S. F. C. Shearer and M. R. Monteith, "Direct photodetachment of F by mid-infrared few-cycle femtosecond laser pulses", Phys. Rev. A **88**, 033415 (2013).

[77]O. Hassouneh, S. Law, S. F. Shearer, A. C. Brown, and H. W. Van Der Hart, "Electron rescattering in strong-field photodetachment of F-", J. Phys. Conf. Ser. **635**, 031404(R) (2015).

[78]B. Bergues, Z. Ansari, D. Hanstorp, and I. Y. Kiyan, "Photodetachment in a strong laser field: An experimental test of Keldysh-like theories", Phys. Rev. A **75**, 063415 (2007).

[79]X. Y. Lai, C. Poli, H. Schomerus, and C. Figueira De Morisson Faria, "Influence of the Coulomb potential on above-threshold ionization: A quantum-orbit analysis beyond the strong-field approximation", Phys. Rev. A **92**, 043407 (2015).

[80]X. Lai, S. Yu, Y. Huang, L. Hua, C. Gong, W. Quan, C. Figueira De Morisson Faria, and X. Liu, "Near-threshold photoelectron holography beyond the strong-field approximation", Phys. Rev. A **96**, 013414 (2017).

[81]T. Morishita, A. T. Le, Z. Chen, and C. D. Lin, "Accurate retrieval of structural information from laser-induced photoelectron and high-order harmonic spectra by few-cycle laser pulses", Phys. Rev. Lett. **100**, 013903 (2008).

[82]A.-T. Le, R. D. Picca, P. D. Fainstein, D. A. Telnov, M Lein, and C. D. Lin, "Theory of high-order harmonic generation from molecules by intense laser pulses", J. Phys. B At. Mol. Opt. Phys. **41**, 081002 (2008).

[83]A. T. Le, T. Morishita, and C. D. Lin, "Extraction of the species-dependent dipole amplitude and phase from high-order harmonic spectra in rare-gas atoms", Phys. Rev. A - At. Mol. Opt. Phys. **78**, 023814 (2008).

[84]Z. Chen, A. T. Le, T. Morishita, and C. D. Lin, "Origin of species dependence of high-energy plateau photoelectron spectra", J. Phys. B At. Mol. Opt. Phys. **42**, 061001 (2009).

[85]S. Micheau, Z. Chen, A. T. Le, and C. D. Lin, "Quantitative rescattering theory for nonsequential double ionization of atoms by intense laser pulses", Phys. Rev. A - At. Mol. Opt. Phys. **79**, 013417 (2009).

[86]A. T. Le, R. R. Lucchese, S. Tonzani, T. Morishita, and C. D. Lin, "Quantitative rescattering theory for high-order harmonic generation from molecules", Phys. Rev. A - At. Mol. Opt. Phys. **80**, 013401 (2009).

[87]O. Smirnova, M. Spanner, and M. Ivanov, "Coulomb and polarization effects in subcycle dynamics of strong-field ionization", J. Phys. B At. Mol. Opt. Phys. **39**, S307 (2006).

[88]O. Smirnova, A. S. Mouritzen, S. Patchkovskii, and M. Y. Ivanov, "Coulomb-laser coupling in laser-assisted photoionization and molecular tomography", J. Phys. B At. Mol. Opt. Phys. **40**, F197 (2007).

[89]O. Smirnova, M. Spanner, and M. Ivanov, "Analytical solutions for strong field-driven atomic and molecular one- and two-electron continua and applications to strong-field problems", Phys. Rev. A **77**, 033407 (2008).

[90]L. Torlina and O. Smirnova, "Time-dependent analytical R-matrix approach for strong-field dynamics. I. One-electron systems", Phys. Rev. A **86**, 043408 (2012).

[91]J. Kaushal and O. Smirnova, "Nonadiabatic Coulomb effects in strong-field ionization in circularly polarized laser fields", Phys. Rev. A **88**, 013421 (2013).

[92]L. Torlina, F. Morales, H. G. Muller, and O. Smirnova, "Ab initio verification of the analytical R-matrix theory for strong field ionization", J. Phys. B At. Mol. Opt. Phys. **47**, 204021 (2014).

[93]L. Torlina, F. Morales, J. Kaushal, I. Ivanov, A. Kheifets, A. Zielinski, A. Scrinzi, H. G. Muller, S. Sukiasyan, M. Ivanov, and O. Smirnova, "Interpreting attoclock measurements of tunnelling times", Nat. Phys. **11**, 503 (2015).

[94]L. Torlina, J. Kaushal, and O. Smirnova, "Time-resolving electron-core dynamics during strong-field ionization in circularly polarized fields", Phys. Rev. A **88**, 053403 (2013).

[95]S. V. Popruzhenko, G. G. Paulus, and D. Bauer, "Coulomb-corrected quantum trajectories in strong-field ionization", Phys. Rev. A **77**, 053409 (2008).

[96]S. V. Popruzhenko and D. Bauer, "Strong field approximation for systems with Coulomb interaction", J. Mod. Opt. **55**, 2573 (2008).

[97]S. B. Popruzhenko, V. D. Mur, V. S. Popov, and D. Bauer, "Multiphoton ionization of atoms and ions by high-intensity X-ray lasers", J. Exp. Theor. Phys. **108**, 947 (2009).

[98]A. S. Maxwell, S. V. Popruzhenko, and C. Figueira de Morisson Faria, "Treating Branch Cuts in Quantum Trajectory Models for Photoelectron Holography", Phys. Rev. A (under review) (2018).

[99]T.-M. Yan, S. V. Popruzhenko, M. J. J. Vrakking, and D. Bauer, "Low-Energy Structures in Strong Field Ionization Revealed by Quantum Orbits", Phys. Rev. Lett. **105**, 253002 (2010).

[100]T.-M. Yan and D. Bauer, "Sub-barrier Coulomb effects on the interference pattern in tunneling-ionization photoelectron spectra", Phys. Rev. A **86**, 053403 (2012).

[101]S. V. Popruzhenko, "Invariant form of Coulomb corrections in the theory of nonlinear ionization of atoms by intense laser radiation", J. Exp. Theor. Phys. **118**, 580 (2014).

[102]A. S. Maxwell, A. Al-Jawahiry, T. Das, and C. Figueira de Morisson Faria, "Coulomb-corrected quantum interference in above-threshold ionization: Working towards multi-trajectory electron holography", Phys. Rev. A **96**, 023420 (2017).

[103]A. S. Maxwell, A. Al-Jawahiry, X. Y. Lai, and C. Figueira de Morisson Faria, "Analytic quantum-interference conditions in Coulomb corrected photoelectron holography", J. Phys. B At. Mol. Opt. Phys. **51**, 044004 (2018).

[104]A. S. Maxwell and C. Figueira de Morisson Faria, "Coulomb-free and Coulomb-distorted recolliding quantum orbits in photoelectron holography", J. Phys. B At. Mol. Phys. **51**, 124001 (2018).

[105]M. Li, J. W. Geng, H. Liu, Y. Deng, C. Wu, L. Y. Peng, Q. Gong, and Y. Liu, "Classical-quantum correspondence for above-threshold ionization", Phys. Rev. Lett. **112**, 113002 (2014).

[106]H. Xie, M. Li, Y. Li, Y. Zhou, and P. Lu, "Intra-half-cycle interference of low-energy photoelectron in strong midinfrared laser fields", Opt. Express **24**, 27726 (2016).

[107]M. V. Ammosov, N. B. Delone, and V. P. Krainov, "Tunnel ionization of complex atoms and of atomic ions in an alternating electromagnetic field", Sov. Phys. JETP **64**, 1191 (1986).

[108]N. I. Shvetsov-Shilovski, M. Lein, L. B. Madsen, E. Rasanen, C. Lemell, J. Burgdorfer, D. G. Arbó, and K. Tokesi, "Semiclassical two-step model for strong-field ionization", Phys. Rev. A **94**, 013415 (2016).

[109]N. I. Shvetsov-Shilovski and M. Lein, "Effects of the Coulomb potential in interference patterns of strong-field holography with photoelectrons", Phys. Rev. A **97**, 013411 (2018).

[110]J. Wu, B. B. Augstein, and C. Figueira De Morisson Faria, "Bohmian-trajectory analysis of high-order-harmonic generation: Ensemble averages, nonlocality, and quantitative aspects", Phys. Rev. A **88**, 063416 (2013).

[111]J. Wu, B. B. Augstein, and C. Figueira De Morisson Faria, "Local dynamics in high-order-harmonic generation using Bohmian trajectories", Phys. Rev. A **88**, 023415 (2013).

[112]C. Zagoya, J. Wu, M. Ronto, D. V. Shalashilin, and C. F.D. M. Faria, "Quantum and semiclassical phase-space dynamics of a wave packet in strong fields using initial-value representations", New J. Phys. **16**, 103040 (2014).

[113]C. Symonds, J. Wu, M. Ronto, C. Zagoya, C. Figueira de Morisson Faria, and D. V. Shalashilin, "Coupled-coherent-states approach for high-order harmonic generation", Phys. Rev. A **91**, 023427 (2015).

[114]M. Meckel, D. Comtois, D. Zeidler, A. Staudte, D. Pavicic, H. C. Bandulet, H. Pépin, J. C. Kieffer, R. Dörner, D. M. Villeneuve, and P. B. Corkum, "Laser-induced electron tunneling and diffraction. Supporting Online Material.", Science **320**, 1478 (2008).

[115]J. Itatani, J. Levesque, D. Zeidler, H. Niikura, H. Pépin, J. C. Kieffer, P. B. Corkum, and D. M. Villeneuve, "Tomographic imaging of molecular orbitals.", Nature **432**, 867 (2004).

[116]D. Shafir, Y. Mairesse, D. M. Villeneuve, P. B. Corkum, and N. Dudovich, "Atomic wavefunctions probed through strong-field light–matter interaction", Nat. Phys. **5**, 412 (2009).

[117]O. Smirnova, Y. Mairesse, S. Patchkovskii, N. Dudovich, D. Villeneuve, P. Corkum, and M. Y. Ivanov, "High harmonic interferometry of multi-electron dynamics in molecules.", Nature **460**, 972 (2009).

[118]X. B. Bian, Y. Huismans, O. Smirnova, K. J. Yuan, M. J. J. Vrakking, and A. D. Bandrauk, "Subcycle interference dynamics of time-resolved photoelectron holography with midinfrared laser pulses", Phys. Rev. A **84**, 043420 (2011).

[119]X. B. Bian and A. D. Bandrauk, "Attosecond time-resolved imaging of molecular structure by photoelectron holography", Phys. Rev. Lett. **108**, 263003 (2012).

[120]X. B. Bian and A. D. Bandrauk, "Orientation-dependent forward-backward photoelectron holography from asymmetric molecules", Phys. Rev. A **89**, 033423 (2014).

[121]D. D. Hickstein, P. Ranitovic, S. Witte, X. M. Tong, Y. Huismans, P. Arpin, X. Zhou, K. E. Keister, C. W. Hogle, B. Zhang, C. Ding, P. Johnsson, N. Toshima, M. J. J. Vrakking, M. M. Murnane, and H. C. Kapteyn, "Direct visualization of laser-driven electron multiple scattering and tunneling distance in strong-field ionization", Phys. Rev. Lett. **109**, 073004 (2012).

[122]M. Meckel, A. Staudte, S. Patchkovskii, D. M. Villeneuve, P. B. Corkum, R. Dorner, and M. Spanner, "Signatures of the continuum electron phase in molecular strong-field photoelectron holography", Nat. Phys. **10**, 594 (2014).

[123]M. Haertelt, X. B. Bian, M. Spanner, A. Staudte, and P. B. Corkum, "Probing Molecular Dynamics by Laser-Induced Backscattering Holography", Phys. Rev. Lett. **116**, 133001 (2016).

[124]Q. Liao, Y. Li, M. Qin, and P. Lu, "Attosecond interference in strong-field nonsequential double ionization", Phys. Rev. A **96**, 063408 (2017).

[125]D. Bauer and P. Koval, "Qprop: A Schrödinger-solver for intense laser-atom interaction", Comput. Phys. Commun. **174**, 396 (2006).

[126]M. Möller, F. Meyer, A. M. Sayler, G. G. Paulus, M. F. Kling, B. E. Schmidt, W. Becker, and D. B. Milošević, "Off-axis low-energy structures in above-threshold ionization", Phys. Rev. A **90**, 023412 (2014).

[127]D. B. Milošević, "Low-energy backscattering quantum orbits in above-threshold ionization", J. Phys. B At. Mol. Opt. Phys. **49**, 175601 (2016).

[128]A. Kastner, U. Saalmann, and J. M. Rost, "Electron-energy bunching in laser-driven soft recollisions", Phys. Rev. Lett. **108**, 033201 (2012).

[129]S. A. Kelvich, W. Becker, and S. P. Goreslavski, "Coulomb focusing and defocusing in above-threshold-ionization spectra produced by strong mid-IR laser pulses", Phys. Rev. A **93**, 033411 (2016).

[130]W. Becker, A. Lohr, M. Kleber, and M. Lewenstein, "A unified theory of high-harmonic generation: Application to polarization properties of the harmonics", Phys. Rev. A **56**, 645 (1997).

[131]M. Y. Ivanov, M. Spanner, and O. Smirnova, "Anatomy of strong field ionization", J. Mod. Opt. **52**, 165 (2005).

[132]C. Figueira de Morisson Faria, H. Schomerus, and W. Becker, "High-order above-threshold ionization: The uniform approximation and the effect of the binding potential", Phys. Rev. A **66**, 043413 (2002).

[133]A. C. Wahl, "Analytic self-consistent field wavefunctions and computed properties for homonuclear diatomic molecules", J. Chem. Phys. **41**, 2600 (1964).

[134]D. B. Milošević, "Phase space path-integral formulation of the above-threshold ionization", J. Math. Phys. **54**, 042101 (2013).

[135]A. M. Perelomov and V. S. Popov, "Ionization of Atoms in an Alternating Electric Field: II.", Sov. Phys. JETP **24**, 207 (1967).

[136]C. Figueira de Morisson Faria, X. Liu, A. Sanpera, and M. Lewenstein, "Classical and quantum-mechanical treatments of nonsequential double ionization with few-cycle laser pulses", Phys. Rev. A **70**, 043406 (2004).

[137]V. Mosert and D. Bauer, "Photoelectron spectra with QPROP and t-SURFF", Comput. Phys. Commun. **207**, 452 (2016).

[138]A. Rudenko, K. Zrost, B. Feuerstein, V. L. B. de Jesus, C. D. Schröter, R. Moshammer, and J. Ullrich, "Correlated Multielectron Dynamics in Ultrafast Laser Pulse Interactions with Atoms", Phys. Rev. Lett. **93**, 253001 (2004).

[139]A. M. Perelomov and V. S. Popov, "Ionization of atoms in an alternating electrical field: III", Sov. Phys. JETP **25**, 336 (1967).

[140]G. Porat, G. Alon, S. Rozen, O. Pedatzur, M. Krüger, D. Azoury, A. Natan, G. Orenstein, B. D. Bruner, M. J. J. Vrakking, and N. Dudovich, "Attosecond time-resolved photoelectron holography", Nat. Commun. **9**, 2805 (2018).

[141]M. He, Y. Li, Y. Zhou, M. Li, W. Cao, and P. Lu, "Direct Visualization of Valence Electron Motion Using Strong-Field Photoelectron Holography", Phys. Rev. Lett. **120**, 133204 (2018).

[142]Y. Zhou, O. I. Tolstikhin, and T. Morishita, "Near-Forward Rescattering Photoelectron Holography in Strong-Field Ionization: Extraction of the Phase of the Scattering Amplitude", Phys. Rev. Lett. **116**, 173001 (2016).

[143]S. Patchkovskii, Z. Zhao, T. Brabec, and D. M. Villeneuve, "High harmonic generation and molecular orbital tomography in multielectron systems: Beyond the single active electron approximation", Phys. Rev. Lett. **97**, 123003 (2006).

[144]S. Patchkovskii, Z. Zhao, T. Brabec, and D. M. Villeneuve, "High harmonic generation and molecular orbital tomography in multielectron systems", J. Chem. Phys. **126**, 114306 (2007).

[145]O. Smirnova, S. Patchkovskii, Y. Mairesse, N. Dudovich, D. Villeneuve, P. Corkum, and M. Y. Ivanov, "Attosecond circular dichroism spectroscopy of polyatomic molecules", Phys. Rev. Lett. **102**, 063601 (2009).

[146]R. Santra and A. Gordon, "Three-step model for high-harmonic generation in many-electron systems", Phys. Rev. Lett. **96**, 073906 (2006).

[147]B. B. Augstein and C. Faria, Figueira de Morisson, "Multielectron corrections in molecular high-order harmonic generation for different formulations of the strong-field approximation", J. Mod. Opt. **58**, 1173 (2011).

[148]T. Keil, S. V. Popruzhenko, and D Bauer, "Laser-driven recollisions under the Coulomb barrier", Phys. Rev. Lett. **117**, 243003 (2016).

[149]Y. Li, Y. Zhou, M. He, M. Li, and P. Lu, "Identifying backward-rescattering photoelectron hologram with orthogonal two-color laser fields", Opt. Express **24**, 23697 (2016).

[150]D. B. Milošević and W. Becker, "Role of long quantum orbits in high-order harmonic generation", Phys. Rev. A **66**, 063417 (2002).

[151]D. B. Milošević, "Forward- and backward-scattering quantum orbits in above-threshold ionization", Phys. Rev. A **90**, 063414 (2014).

[152]C. A. Ullrich, U. J. Gossmann, and E. K. U. Gross, "Density-Functional Approach to Atoms in Strong Laser Pulses", Berichte der Bunsengesellschaft für Phys. Chemie **99**, 488 (1995).

[153]C. Yu and L. B. Madsen, "Above-threshold ionization of helium in the long-wavelength regime: Examining the single-active-electron approximation and the two-electron strong-field approximation", Phys. Rev. A **95**, 063407 (2017).

[154]C. Faria, Figueira de Morisson and X. Liu, "Electron-electron correlation in strong laser fields", J. Mod. Opt. **58**, 1076 (2011).

[155]W. Becker, X. Liu, P. J. Ho, and J. H. Eberly, "Theories of photoelectron correlation in laser-driven multiple atomic ionization", Rev. Mod. Phys. **84**, 1011 (2012).

[156]A. L'Huillier, L. A. Lompre, G. Mainfray, and C. Manus, "Multiply charged ions induced by multiphoton absorption in rare gases at 0.53 μm", Phys. Rev. A **27**, 2503 (1983).

[157]D. Fittinghoff, P. Bolton, B. Chang, and K. Kulander, "Observation of nonsequential double ionization of helium with optical tunneling", Phys. Rev. Lett. **69**, 2642 (1992).

[158]K. Kondo, A. Sagisaka, T. Tamida, Y. Nabekawa, and S. Wantanabe, "Wavelength dependence of nonsquential double ionization in He", Phys. Rev. A **35**, R2531 (1999).

[159]B. Walker, B. Sheehy, L. F. DiMauro, P. Agostini, K. J. Schafer, and K. C. Kulander, "Precision Measurement of Strong Field Double Ionization of Helium", Phys. Rev. Lett. **73**, 1227 (1994).

[160]A. Talebpour, S. Larochelle, S.-L. L Chin, C.-Y. Chien, Y. Liang, S. Larochelle, and S.-L. L Chin, "Non-sequential and sequential double ionization of NO in an intense femtosecond Ti:sapphire laser pulse", J. Phys. B At. Mol. Opt. Phys. **30**, 1721 (1997).

[161]C. Cornaggia and P. Hering, "Laser-induced non-sequential double ionization of small molecules", J. Phys. B At. Mol. Opt. Phys. **31**, L503 (1998).

[162]E. Eremina, X. Liu, H. Rottke, W. Sandner, M. G. Schätzel, A. Dreischuh, G. G. Paulus, H. Walther, R. Moshammer, and J. Ullrich, "Influence of molecular structure on double ionization of N2 and O2 by high intensity ultrashort lasre pulses", Phys. Rev. Lett. **92**, 173001 (2004).

[163]U. Eichmann, M. Dörr, H. Maeda, W. Becker, and W. Sandner, "Collective Multielectron Tunneling Ionization in Strong Fields", Phys. Rev. Lett. **84**, 3550 (2000).

[164]P. Dietrich, N. H. Burnett, M. Ivanov, and P. B. Corkum, "High-harmonic generation and correlated two-electron multiphoton ionization with elliptically polarized light", Phys. Rev. A **50**, R3585 (1994).

[165]T. Weber, H. Giessen, M. Weckenbrock, G. Urbasch, A. Staudte, L. Spielberger, O. Jagutzki, V. Mergel, M. Vollmer, and R. Dörner, "Correlated electron emission in multiphoton double ionization", Nature **405**, 658 (2000).

[166]R. Moshammer, B. Feuerstein, W. Schmitt, A. Dorn, C. D. Schröter, J. Ullrich, H. Rottke, C. Trump, M. Wittmann, G. Korn, K. Hoffmann, and W. Sandner, "Momentum Distributions of Ne n+ Ions Created by an Intense Ultrashort Laser Pulse", Phys. Rev. Lett. **84**, 447 (2000).

[167]T. Shaaran, M. T. Nygren, and C. Figueira de Morisson Faria, "Laser-induced nonsequential double ionization at and above the recollision-excitation-tunneling threshold", Phys. Rev. A **81**, 063413 (2010).

[168]T. Shaaran, B. B. Augstein, and C. Figueira De Morisson Faria, "Excitation two-center interference and the orbital geometry in laser-induced nonsequential double ionization of diatomic molecules", Phys. Rev. A **84**, 013429 (2011).

[169]A. S. Maxwell and C. Figueira de Morisson Faria, "Quantum interference in time-delayed nonsequential double ionization", Phys. Rev. A **92**, 023421 (2015).

[170]D. B. Milošević and W. Becker, "Classical cutoffs for laser-induced nonsequential double ionization", Phys. Rev. A **68**, 065401 (2003).

[171]B. Bergues, M. Kübel, N. G. Johnson, B. Fischer, N. Camus, K. J. Betsch, O. Herrwerth, A. Senftleben, a. M. Sayler, T. Rathje, T. Pfeifer, I. Ben-Itzhak, R. R. Jones, G. G. Paulus, F. Krausz, R. Moshammer, J. Ullrich, and M. F. Kling, "Attosecond tracing of

correlated electron-emission in non-sequential double ionization.", Nat. Commun. **3**, 813 (2012).

[172]X. Sun, M. Li, D. Ye, G. Xin, L. Fu, X. Xie, Y. Deng, C. Wu, J. Liu, Q. Gong, and Y. Liu, "Mechanisms of Strong-Field Double Ionization of Xe", Phys. Rev. Lett. **113**, 103001 (2014).

[173]M. Kübel, K. J. Betsch, N. G. Kling, A. S. Alnaser, J. Schmidt, U Kleineberg, Y Deng, I Ben-Itzhak, G. G. Paulus, T. Pfeifer, J. Ullrich, R. Moshammer, M. F. Kling, and B. Bergues, "Non-sequential double ionization of Ar: from the single- to the many-cycle regime", New J. Phys. **16**, 033008 (2014).

[174]E. Eremina, X. Liu, H. Rottke, W. Sandner, A. Dreischuh, F. Lindner, F. Grasbon, G. G. Paulus, H. Walther, R. Moshammer, B. Feuerstein, and J. Ullrich, "Laser-induced non-sequential double ionization investigated at and below the threshold for electron impact ionization", J. Phys. B At. Mol. Opt. Phys. **36**, 3269 (2003).

[175]D. Zeidler, A. Staudte, A. B. Bardon, D. M. Villeneuve, R. Dörner, and P. B. Corkum, "Controlling Attosecond Double Ionization Dynamics via Molecular Alignment", Phys. Rev. Lett. **95**, 203003 (2005).

[176]Y. Liu, S. Tschuch, a. Rudenko, M. Dürr, M. Siegel, U. Morgner, R. Moshammer, and J. Ullrich, "Strong-Field Double Ionization of Ar below the Recollision Threshold", Phys. Rev. Lett. **101**, 053001 (2008).

[177]T. Shaaran and C. F. De Morisson Faria, "Laser-induced nonsequential double ionization: Kinematic constraints for the recollision-excitation-tunneling mechanism", J. Mod. Opt. **57**, 984 (2010).

[178]Z. Chen, Y. Liang, and C. D. Lin, "Quantitative rescattering theory of correlated two-electron momentum spectra for strong-field nonsequential double ionization of helium", Phys. Rev. A **82**, 063417 (2010).

[179]A. Emmanouilidou and A. Staudte, "Intensity dependence of strong-field double-ionization mechanisms: From field-assisted recollision ionization to recollision-assisted field ionization", Phys. Rev. A **80**, 053415 (2009).

[180]D. F. Ye and J. Liu, "Strong-field double ionization at the transition to below the recollision threshold", Phys. Rev. A **81**, 043402 (2010).

[181]L. Zhang, X. Xie, S. Roither, D. Kartashov, Y. Wang, C. Wang, M. Schöffler, D. Shafir, P. B. Corkum, A. Baltuška, I. Ivanov, A. Kheifets, X. Liu, A. Staudte, and M. Kitzler, "Laser-sub-cycle two-dimensional electron-momentum mapping using orthogonal two-color fields", Phys. Rev. A **90**, 061401 (2014).

[182]A Emmanouilidou, "Recoil collisions as a portal to field-assisted ionization at near-UV frequencies in the Strong-Field Double Ionizationof Helium", Phys. Rev. A **78**, 23411 (2008).

[183]C. Figueira de Morisson Faria, T. Shaaran, and M. T. Nygren, "Time-delayed nonsequential double ionization with few-cycle laser pulses: Importance of the carrier-envelope phase", Phys. Rev. A **86**, 053405 (2012).

[184]A. Staudte, C. Ruiz, M. Schöffler, S. Schössler, D. Zeidler, T. Weber, M. Meckel, D. M. Villeneuve, P. B. Corkum, A. Becker, and R. Dörner, "Binary and recoil collisions in strong field double ionization of helium", Phys. Rev. Lett. **99**, 263002 (2007).

[185]D. F. Ye, X Liu, and J Liu, "Classical Trajectory Diagnosis of a Fingerlike Pattern in the Correlated Electron Momentum Distribution in Strong Field Double Ionization of Helium", Phys. Rev. Lett. **101**, 233003 (2008).

[186]X. Hao, J. Chen, W. Li, B. Wang, X. Wang, and W. Becker, "Quantum Effects in Double Ionization of Argon below the Threshold Intensity", Phys. Rev. Lett. **112**, 073002 (2014).

[187]A. S. Maxwell and C. Figueira de Morisson Faria, "Controlling Below-Threshold Nonsequential Double Ionization via Quantum Interference", Phys. Rev. Lett. **116**, 143001 (2016).

[188]V. S. Popov, B. M. Karanakov, and V. D. Mur, "On the Relativistic Theory of Tunneling V.", JETP Lett. **79**, 262 (2004).

[189]G. G. Paulus, W. Becker, W. Nicklich, and H. Walther, "Rescattering effects in above-threshold ionization : a classical model Rescattering effects in above-threshold ionization : a classical", J. Phys. B At. Mol. Phys. **27**, L703 (1994).

[190]T. Shaaran, C. Figueira de Morisson Faria, and H. Schomerus, "Causality and quantum interference in time-delayed laser-induced nonsequential double ionization", Phys. Rev. A **85**, 023423 (2012).

[191]B. Wang, Y. Guo, J. Chen, Z.-C. Yan, and P. Fu, "Frequency-domain theory of nonsequential double ionization in intense laser fields based on nonperturbative QED", Phys. Rev. A **85**, 023402 (2012).

[192]F. Jin, Y. Tian, J. Chen, Y. Yang, X. Liu, Z. C. Yan, and B. Wang, "Nonsequential double ionization of helium in IR+XUV two-color laser fields: Collision-ionization process", Phys. Rev. A **93**, 043417 (2016).

[193]F. Jin, J. Chen, Y. Yang, X. Liu, Z.-C. Yan, and B. Wang, "Nonsequential double ionization of helium in IR + XUV two-color laser fields II : collision- excitation ionization process", J. Phys. B At. Mol. Opt. Phys. **51**, 035601 (2018).

[194]Y. Liu, D. Ye, J. Liu, a. Rudenko, S. Tschuch, M. Dürr, M. Siegel, U. Morgner, Q. Gong, R. Moshammer, and J. Ullrich, "Multiphoton Double Ionization of Ar and Ne Close to Threshold", Phys. Rev. Lett. **104**, 173002 (2010).

[195]D. I. Bondar, W.-K. Liu, and M. Y. Ivanov, "Two-electron ionization in strong laser fields below intensity threshold: Signatures of attosecond timing in correlated spectra", Phys. Rev. A **79**, 023417 (2009).

[196]D. F. Ye, J. Chen, and J. Liu, "Classical trajectory perspective on double-ionization dynamics of diatomic molecules irradiated by ultrashort intense laser pulses", Phys. Rev. A **77**, 013403 (2008).

[197]Y. Li, S. P. Yang, J. Chen, and J. Fan, "Non-sequential double ionization of diatomic molecules: Alignment dependence of electron correlation", J. Phys. B At. Mol. Opt. Phys. **47**, 045601 (2014).

[198]F. Mauger, A. Kamor, C. Chandre, and T. Uzer, "Mechanism of Delayed Double Ionization in a Strong Laser Field", Phys. Rev. Lett. **108**, 063001 (2012).

[199]W. Quan, X. Hao, Y. Wang, Y. Chen, S. Yu, S. Xu, Z. Xiao, R. Sun, X. Lai, S. Hu, M. Liu, Z. Shu, X. Wang, W. Li, W. Becker, X. Liu, and J. Chen, "Quantum interference in laser-induced nonsequential double ionization", Phys. Rev. A **96**, 032511 (2017).

[200]R. Kopold, W. Becker, M. Kleber, and G. G. Paulus, "Channel-closing effects in high-order above-threshold ionization and high-order harmonic generation", J. Phys. B **35**, 217 (2002).

[201]L. Zhang, X. Xie, S. Roither, Y. Zhou, P. Lu, D. Kartashov, M. Schöffler, D. Shafir, P. B. Corkum, A. Baltuška, A. Staudte, and M. Kitzler, "Subcycle control of electron-electron correlation in double ionization", Phys. Rev. Lett. **112**, 193002 (2014).

[202]C. Huang, Y. Zhou, Q. Zhang, and P. Lu, "Contribution of recollision ionization to the cross-shaped structure in nonsequential double ionization.", Opt. Express **21**, 11382 (2013).

[203]B. Yu, D. Zhang, Y. Li, and Q. Tang, "Electron correlations in nonsequential double ionization of helium at intensity below the recollision threshold", J. Mod. Opt. **59**, 679 (2012).

[204]M. Kübel, C Burger, N. G. Kling, T Pischke, L Beaufore, I. Ben-Itzhak, G. G. Paulus, J Ullrich, T Pfeifer, R Moshammer, M. F. Kling, and B Bergues, "Complete characterization of single-cycle double ionization of argon from the nonsequential to the sequential ionization regime", Phys. Rev. A **93**, 053422 (2016).

[205]A. Chen, M. Kübel, B. Bergues, M. F. Kling, and A. Emmanouilidou, "Non-sequential double ionization with near-single cycle laser pulses", Sci. Rep. **7**, 7488 (2017).

[206]A. H. Winney, Y. F. Lin, S. K. Lee, P. Adhikari, and W. Li, "State-resolved three-dimensional electron-momentum correlation in nonsequential double ionization of benzene", Phys. Rev. A **93**, 031402(R) (2016).

[207]C. A. Mancuso, K. M. Dorney, D. D. Hickstein, J. L. Chaloupka, J. L. Ellis, F. J. Dollar, R. Knut, P. Grychtol, D. Zusin, C. Gentry, M. Gopalakrishnan, H. C. Kapteyn, and M. M. Murnane, "Controlling Nonsequential Double Ionization in Two-Color Circularly Polarized Femtosecond Laser Fields", Phys. Rev. Lett. **117**, 133201 (2016).

[208]S. Luo, X. Ma, H. Xie, M. Li, Y. Zhou, W. Cao, and P. Lu, "Controlling nonsequential double ionization of Ne with parallel-polarized two-color laser pulses", Opt. Express **26**, 13666 (2018).